Flame Topology and Thermochemical States in Laminar and Turbulent Biofuel Flames

Vom Fachbereich Maschinenbau
der Technischen Universität Darmstadt

zur Erlangung des Grades
Doktor der Ingenieurwissenschaften (Dr.-Ing.)
genehmigte

D i s s e r t a t i o n

von

Johannes Ludwig Trabold, M.Sc.

aus Waiblingen

Erstgutachter: Prof. Dr. rer. nat. A. Dreizler
Zweitgutachter: Prof. Dr.-Ing. Dirk Geyer

Darmstadt 2023

Abstract

In the pursuit of addressing climate change, biofuels and e-fuels emerge as promising alternatives for powering heavy-duty vehicles, long-distance passenger aircraft, and ships. These sectors account for approximately thirty percent of global carbon dioxide emissions, necessitating effective solutions. This research aims to conduct experiments to capture time and spatially-resolved validation data for these sustainable fuels, while also gaining insights into fuel-specific differences in flames.

This research is dedicated to advancing the understanding of fuel-specific combustion processes by achieving the following three primary objectives. Firstly, it involves the development of vaporized fuel burner systems with well-defined boundary conditions as the foundation for combustion system research. Secondly, it characterizes the flames of the four lowest alcohols stabilized on these burner systems, considering factors such as flame blow-off, size, and topology. Lastly, the research targets ethanol flames through qualitative and quantitative Raman and Rayleigh spectroscopy investigations, addressing the challenge of managing intermediate species associated with complex fuels.

The employed methodologies include OH-Planar laser-induced fluorescence for flame topology characterization, qualitative long-exposure Raman spectroscopy to unveil intermediate species, and single-shot Raman and Rayleigh spectroscopy to provide the first quantitative thermochemical state measurements in laminar and turbulent premixed ethanol flames. Comprehensive comparisons are made between bio- and e-fuels and the established reference fuel methane. One-dimensional numerical flame calculations complement the experimental approaches, providing additional insights.

Key findings include that turbulent alcohol flames exhibit increased wrinkling as the equivalence ratio transitions from lean to rich, accompanied by a decrease in the Lewis number. Qualitative highly-resolved long-exposure Raman spectroscopy reveals methane, formaldehyde, ethylene, and acetaldehyde as major intermediates in ethanol flames, while OME-3 flames predominantly show formaldehyde and methane. Lastly, capturing thermochemical states in ethanol/air flames is made possible through the following two pivotal innovations. Firstly, the traditional calibration role of the flat flame in the Matrix inversion Raman evaluation method is replaced by probing the center of opposed twin flames, overcoming limitations related to vaporized fuels. Secondly, a surrogate signal based on ethanol, carbon monoxide, and temperature is developed, effectively reproducing previously inaccessible intermediates within the ethanol/air flame front. This knowledge enables the quantification of the main flame species and temperatures with significantly enhanced accuracy.

In summary, this work advances the apparatuses to study flames of prevaporized fuels, characterizes flame topology, and improves Raman and Rayleigh flame spectroscopy and its data evaluation. These accomplishments contribute to the understanding of biofuel and e-fuel combustion, play a crucial role in numerical model validation, and promote the use of renewable fuels in the transition to clean energy.

Kurzfassung

Im Streben nach der Bewältigung des Klimawandels erweisen sich Biokraftstoffe und E-Fuels als vielversprechende Alternativen für den Antrieb von Lastkraftwagen, Langstreckenflugzeugen und Schiffen. Diese Sektoren tragen zusammen etwa dreißig Prozent der globalen Kohlenstoffdioxidemissionen bei, was die Notwendigkeit effektiver Lösungen verdeutlicht. Diese Arbeit hat zum Ziel, zeitlich und räumlich aufgelöste Validierungsdaten für diese Brennstoffe zu produzieren und Brennstoff-spezifische Unterschiede sichtbar zu machen.

Um dies zu erreichen, besitzt diese Arbeit drei Schwerpunkte. Erstens umfasst sie die Entwicklung von Brennersystemen mit klar definierten Randbedingungen für vorverdampfte Brennstoffe, die als Grundlage für die Verbrennungsforschung dienen. Zweitens werden die Flammen der vier niedrigsten Alkohole, welche auf diesen Brennersystemen stabilisiert werden, hinsichtlich Faktoren wie Flammen-Blowoff, -Ausdehnung und -Topologie charakterisiert. Schließlich werden Ethanolflammen mit Hilfe von qualitativer und quantitativer Raman-Rayleigh-Spektroskopie genauer untersucht. Dabei wurde mit der Berücksichtigung der verstärkten Präsenz von Zwischenprodukten eine wichtige Herausforderung erfolgreich bewältigt.

Die angewendeten Methoden umfassen die planare laserinduzierte OH-Fluoreszenz zur Charakterisierung der Flammentopologie, die qualitative Raman-Spektroskopie mit langer Belichtungszeit zur Detektion von Zwischenprodukten sowie die Einzelschuss Raman- und Rayleigh-Spektroskopie zur erstmaligen Erfassung des thermochemischen Zustands in laminaren und turbulenten vorgemischten Ethanolflammen. Die Ergebnisse werden stets mit denen des etablierten Referenzkraftstoffs Methan verglichen. Zusätzlich werden mit eindimensionalen numerischen Flammenkalkulationen ergänzende Erkenntnisse gewonnen.

Wertvolle Erkenntnisse sind die deutliche Zunahme der Flammen-Verwinklung turbulenter Alkoholflammen beim Wechsel von mageren zu fetten Bedingungen und abnehmender Lewis-Zahl. Weiterhin können mit Hilfe qualitativer, hochauflösender Raman-Spektroskopie im Langzeitbelichtungsmodus die Zwischenprodukte Methan, Ethylen, Formaldehyd und Acetaldehyd in Ethanolspwie Formaldehyd und Methan in OME-3/Luft-Flammen sichtbar gemacht werden. Zuletzt wird das Erfassen der thermochemischen Zustände in Ethanol/Luft-Flammen durch zwei entscheidende Innovationen ermöglicht: Erstens wird die Flachflamme in der Raman-Matrixinversions-Auswertung durch Gegenstrom-Zwillingsflammen ersetzt, wodurch die Beschränkung hinsichtlich vorverdampfter Kraftstoffe überwunden wird. Zweitens wird ein Ersatzsignal basierend auf Ethanol, Kohlenmonoxid und der Temperatur entwickelt, das bisher unzugängliche Zwischenprodukte in der Ethanol/Luft-Flammenfront effektiv reproduziert und damit die Bestimmung des thermochemischen Zustands mit erhöhter Genauigkeit ermöglicht.

Zusammenfassend hat diese Arbeit Brenner für vorverdampfte Brennstoffe hervorgebracht, Flammentopologien charakterisiert und die Raman- und Rayleigh-Flammenspektroskopie und deren Datenauswertung vorangebracht. Diese Leistungen tragen zum Verständnis der Biokraftstoff- und E-Fuel Verbrennung bei, spielen eine entscheidende Rolle bei der Validierung numerischer Modelle und fördern damit den Einsatz erneuerbarer Kraftstoffe im Übergang zu nachhaltiger Energie.

Danksagungen

Erklärung

Hiermit erkläre ich, dass ich die vorliegende Dissertation selbstständig verfasst und keine anderen als die von mir angegebenen Hilfsmittel verwendet habe. Ich erkläre außerdem, dass ich bisher noch keinen Promotionsversuch unternommen habe.

Darmstadt, den 29.05.2023

(Johannes Trabold)

Der Mensch muss das Gute und Große wollen!
Das Übrige hängt vom Schicksal ab.

Alexander von Humboldt

Contents

Contents

List of Tables

List of Figures

Glossary

Capital Latin letters		Unit
P	Perimeter of spline length	m
A	Area	m^2
D	Diameter	m
$D_{i,j}$	Mass diffusion	$m^2 \cdot s^{-1}$
D_{th}	Thermal diffusion	$m^2 \cdot s^{-1}$
E	Energy	J
E_a	Activation energy	J
F	Bilger mixture fraction	−
H	Enthalpy	$J \cdot mol^{-1}$
H_{fl}	Flame length	m
I_0	Mean turbulent flame stretch factor	−
I_l	Laser fluence	$J \cdot m^{-2}$
ID	Identifier	−
L	Characteristic length	m
Ma_l	Markstein length	m
N	Number density	m^{-3}
P	Power	W
R	Ideal gas constant	$J \cdot mol^{-1} \cdot K^{-1}$
S	Signal	−
T	Temperature	K
$V_{k,i}$	Diffusion velocity	$m \cdot s^{-1}$
X	Mole fraction	−
Y	Mass fraction	−

Lower-case Latin letters		Unit
$\dot{w}$	Reaction rate	$kg \cdot s \cdot m^{-3}$
$\dot{w}_T$	Heat release due to combustion	W
$\overline{w}$	Mean reaction rate	$kg \cdot s \cdot m^{-3}$
C	Matrix with temperature dependent coefficients	−
c	Mean progress variable	−

c_p	Specific heat capacity	$J \cdot K^{-1}$
f	Aperture number	$-$
f_i	Relative population density	$-$
g_i	Degenerate energy level	$-$
h	Planck's constant	$J \cdot s$
h_f^0	Sensible enthalpy	J
k	Kurtosis	$-$
k_B	Boltzmann constant	$m^2 \cdot kg \cdot s^{-2} \cdot K^{-1}$
k_f	Specific reaction rate constant	$kg \cdot s \cdot m^{-3}$
l_0	Integral length scale	m
l_K	Kolmogorov length	m
l_L	Characteristic laminar length scale	m
m	Molecular mass	$g \cdot mol^{-1}$
p	Static pressure	$N \cdot m^{-2}$
r	Radius	m
r_{ss^+}	Small-scale positive radii	m
r_{ss^-}	Small-scale negative radii	m
s	Skewness	$-$
s_d	Flamelet displacement speed	$m \cdot s^{-1}$
s_L	Laminar burning velocity	$m \cdot s^{-1}$
t_0	Macroscopic flow time scale	s
t_L	Reaction time scale	s
u	Velocity	$m \cdot s^{-1}$
u_K'	Kolmogorov velocity	$m \cdot s^{-1}$

Capital Greek letters   **Unit**

Ω	Opening angle	sr
Ω_0	Non-dimensional function of parameter ϵ	$-$
Ω_1	Correction term for thermo-diffusive instabilities	$-$
Φ	Excess to deficient reactants mass ratio	$-$
Σ	Flame surface density	m^{-1}
Σ_{int}	Integrated flame surface density	$-$

Lower-case Greek letters   **Unit**

α	Strain rate	s^{-1}
α_{th}	Thermal diffusivity	$m^2 \cdot s^{-1}$
δ_{ij}	Kronecker Delta	$-$
$\delta_{L,geo}$	Laminar flame thickness based on geometrical considerations	m

$\delta_{L,th}$	Laminar flame thickness based on thermal properties	m
$\delta_{L,Ze}$	Laminar flame thickness based on Zeldovich	m
ϵ	Kinetic energy transfer rate	$J \cdot s^{-1}$
η	Detection efficiency	$-$
γ	Relation between unburned and burned temperatures	$-$
κ	Flame curvature	m^{-1}
κ_{str}	Flame stretch	s^{-1}
λ	Thermal conductivity	$W \cdot m^{-1} \cdot K^{-1}$
λ	Wavelength	m
λ_c	Critical wavenumber	m^{-1}
μ	Dynamic viscosity	$N \cdot s \cdot m^{-2}$
μ_c	Mean curvature value	m^{-1}
ν	Kinematic viscosity	$m \cdot s^{-2}$
ν_l	Laser frequency	m^{-1}
ω	Wavenumber	cm^{-1}
ϕ	Equivalence ratio	$-$
ρ	Density	$kg \cdot m^{-3}$
σ	Standard deviation	$-$
σ_i	Rate of instability parameter	$m \cdot s^{-2}$
$\sigma_{i,j}$	Molecular diameter	m
σ_{phi}	Unburned to burned density ratio	$-$
σ_{Ray}	Rayleigh cross section	m^2
τ	Viscous tensor	$N \cdot m^{-2}$
τ_K	Kolmogorov time	s
τ_L	Characteristic laminar flame time	s

Sub-indices

$\cdot$ad	adiabatic
$\cdot$bulk	bulk flow
$\cdot$b	burned
$\cdot$coflow	coflowing stream
$\cdot$c	critical
$\cdot$D	deficient
$\cdot$eff	effective
$\cdot$E	excess
$\cdot$i,j	species pair
$\cdot$ins	incident
$\cdot$int	integrated
$\cdot$i	direction

Glossary

$\cdot_k$	species index
$\cdot_{l.b./r.b.}$	left and right boundary
$\cdot_L$	laminar
$\cdot_l$	laser
$\cdot_{max}$	maximum
$\cdot_{min}$	minimum
$\cdot_{pilot}$	pilot flow
$\cdot_p$	products
$\cdot_{Ram}$	Raman
$\cdot_{Ray}$	Rayleigh
$\cdot_r$	reactants
$\cdot_{synth}$	synthetic
$\cdot_s$	signal
$\cdot_{ta}$	tangential
$\cdot_{th}$	thermal
$\cdot_t$	turbulent
$\cdot_u$	unburned

Dimensionless quantities

MS	Mixture strength
Da	Damköhler number
Ka	Karlovitz number
Ka_r	Refined Karlovitz number
Le	Lewis number
Ma	Markstein number
Pr	Prandtl number
Re	Reynolds number
Sc	Schmidt number
Ze	Zeldovich number

Abbreviations

Chemical Elements and Compounds

Al_2O_3	aluminum oxide
Ar	argon
C	carbon
C_2	dicarbon
CH	methylidyne
CH*	methylidyne radical
CH_3	methyl
CH_4	methane
C_2H_5OH	ethanol
CH_2O	formaldehyde
C_2H_4O	acetaldehyde
C_2H_4	acetylene
C_2H_4	ethylene
C_2H_6	ethane
CO	carbon monoxide
CO_2	carbon dioxide
DME	dimethyl ether
H	hydrogen
H_2	hydrogen gas, here 'hydrogen'
H_2O	water
He	helium
HCs	hydrocarbons
KrF	krypton fluoride
NO	nitrous oxide
N_2	nitrogen
O	oxygen
O_2	dioxygen, here 'oxygen'
OH	hydroxyl
OH*	hydroxyl radical
OME-3	3-3-oxymethyl ether (H_3C-O-$(CH_2O)_3$-CH_3)
PTFE	polytetrafluoroethylene

Regular Abbreviations

0D	zero-dimensional
1D	one-dimensional
2D	two-dimensional
3D	three-dimensional
AOI	angle of incidence
BM3D	block-matching and 3D filtering
BG3	background channel
CAD	computer-aided design
CCD	charged-coupled device
CL	chemiluminescence
CMOS	complementary metal–oxide–semiconductor
CNG	compressed natural gas
DL	Darrieus-Landau
DNS	direct numerical simulations
FOV	field of view
FSD	flame surface density
FS	of full scale
FWHM	full width at half maximum
GHG	greenhouse gases
HD	higher-dispersed
HRR	heat release rate
IC	internal combustion
IR	infrared
KDP	potassium dihydrogen phosphate
LDV	laser-Doppler velocimetry
LD	lower-dispersed
LES	large eddy simulation
LIF	laser-induced fluorescence
LTOJ	laminar temperature-controlled opposed jet burner
LG	lens group
LPG	liquid petroleum gas
MFC	mass flow controller
MI	matrix inversion
Nd:YAG	neodymium-doped yttrium aluminum garnet
NI	National Instruments
PAH	polycyclic aromatic hydrocarbons
PDF	probability density function
PID	proportional–integral–derivative
PIV	particle image velocimetry

PLIF	planar laser-induced fluorescence
PMT	photomultiplier tubes
PTV	particle tracking velocimetry
r.m.s.	root mean square
Rd	of reading
ROI	region of interest
sRS	spontaneous Raman spectroscopy
SNL	Sandia National Laboratories
SNR	signal-to-noise ratio
S.A.	Spectrometer A at ODEE Institute, Hochschule Darmstadt
S.B.	Spectrometer B at RSM Institute, Technische Universität Darmstadt
TCJB	temperature-controlled piloted jet burner
TNF	Workshop on Measurement and Computation of Turbulent Flames
TUDa	Technische Universität Darmstadt
UV	ultra-violet

1. Introduction

The introduction to this work is subdivided into three sections. The first part portrays the scientific background on which the work is based, leading from global warming over biofuels and e-fuels to intermediate species. The second part covers the state of literature in the most relevant research fields of fuel effects, flame surface density, and spontaneous Raman spectroscopy. The last part presents the aims, the document structure, and the novelties that this work contains.

1.1. Motivation

Models show that in order to stabilize the global mean temperature increase to $2\,^\circ$C or less compared to preindustrial levels, carbon dioxide emissions need to be net-zero by 2060-2070 and then net-negative from there on [94, 118]. Biofuels, which are produced from biomass instead of fossil resources, can play an essential role in this scenario, as documented in the newest International Panel on Climate Change report [116, pg. 37f and 147f]:

- "Reducing greenhouse gases (GHG) emissions across the full energy sector requires major transitions, including [...] switching to alternative energy carriers [...]"
- "Sustainable biofuels, low-emissions hydrogen, and derivatives (including synthetic fuels) can support mitigation of CO_2 emissions from shipping, aviation, and heavy-duty land transport [...]"
- "Sustainable biofuels, electrolytic hydrogen, and derivatives [...] will ultimately be needed to accommodate large shares of renewables in energy systems."
- "Light industry and manufacturing can be largely decarbonized by switching to low GHG fuels (e.g., biofuels and hydrogen) [...]"

Besides biofuels, so called e-fuels, which are synthetic fuels produced from carbon dioxide and water using electricity, recently received increased attention in the literature. A detailed overview on the topic is provided by Agarwal and Valera [2].

To reduce or mitigate adverse impacts on humans or the environment, the advances of these non-fossil based fuels should be addressed by governmental legislation over time. Therefore, it is a must to increase efficiencies and reduce harmful combustion emissions in internal combustion (IC) engines, gas turbines, or other appliances.

Such optimization is typically done with predictive advanced numerical modeling tools. However, the turbulent combustion complexity on one hand and computing power limitations on the other yield a conflict of objectives. While it is possible to represent the complete physical and chemical process in a numerical simulation via direct numerical simulations (DNS), parameters variation

for optimization quickly exceeds reasonable calculation times and economic requirements from an industrial point-of-view. Therefore, compromises must be made to reduce complexity to the right depth while maintaining essential details of flow and flame interaction.

Transported PDF methods, conditional moment closure, and large eddy simulation (LES) approaches have frequently been used in this case [115]. The underlying models for chemistry and fluid dynamics stem from educated assumptions but need validation through experiments. Therefore, defined test cases under well-known boundary conditions are continuously established, in which thermochemical state scalars (temperature and main species), transport, and flame topography are examined.

In the last two to three decades, the Workshop on Measurement and Computation of Turbulent Flames (TNF) has made great efforts in this regard [6]. With experts from both the experimental and numerical sides, its work surrounds the task of finding suitable benchmark flames which are tailored toward model development. Large databases of different experimental setups or from varying laboratories were created and are freely accessible from research communities worldwide.

As mentioned, one essential validation aspect is the thermochemical state in flames, ideally as scalars for gradient accessibility. Combined Raman and Rayleigh spectroscopy, also referred to as spontaneous Raman spectroscopy (sRS), is the only measurement technique that retrieves all relevant scalars simultaneously in a non-intrusive way. Furthermore, sRS can resolve time and length scales in open flames that have turbulence levels resembling the most practical combustion applications. As presented in the State of the Art Section 1.2.3, it has been applied to many methane or hydrogen flame types, including premixed, non-premixed, partially-premixed, swirled, stratified, or multi-regime.

In contrast, thermochemical state data in flames of more complex fuels are scarce. This is despite the fact that other measurement techniques have recently been applied in considerable amounts to studying fuel effects, which will be shown in Section 1.2.1. The present work will contribute to these available studies by performing a set of measurements, including two using sRS (one qualitative, one quantitative).

A particular interest in complex fuel flames lies in the diverse intermediate species mix compared to methane or hydrogen. This is evident from the example in Figure 1.1, where numerical one-dimensional (1D) Cantera calculations results of counterflowing methane/air against air and ethanol/air against air flames are shown (Section 3.6 for details). In these quantities, intermediates are hypothesized to substantially influence various important flame parameters, such as flame speed, length, wrinkling, and flame-wall interaction (refer to Section 1.2.1). The sRS development towards the capability of measuring these fuels and intermediates, a central subject of this work, is therefore of utmost importance to support combustion model developers.

Before giving more details about the aims, the structure, and novelties in the outline section of the document (Section 1.3), the State of the Art is discussed in the following section. As this work contains laser diagnostic measurements that fall into the fuel effects category on one hand and into sRS development on the other, both have individual sections. The third section is on flame surface density, which is an essential flame topography parameter throughout the discussion of Chapter 5.
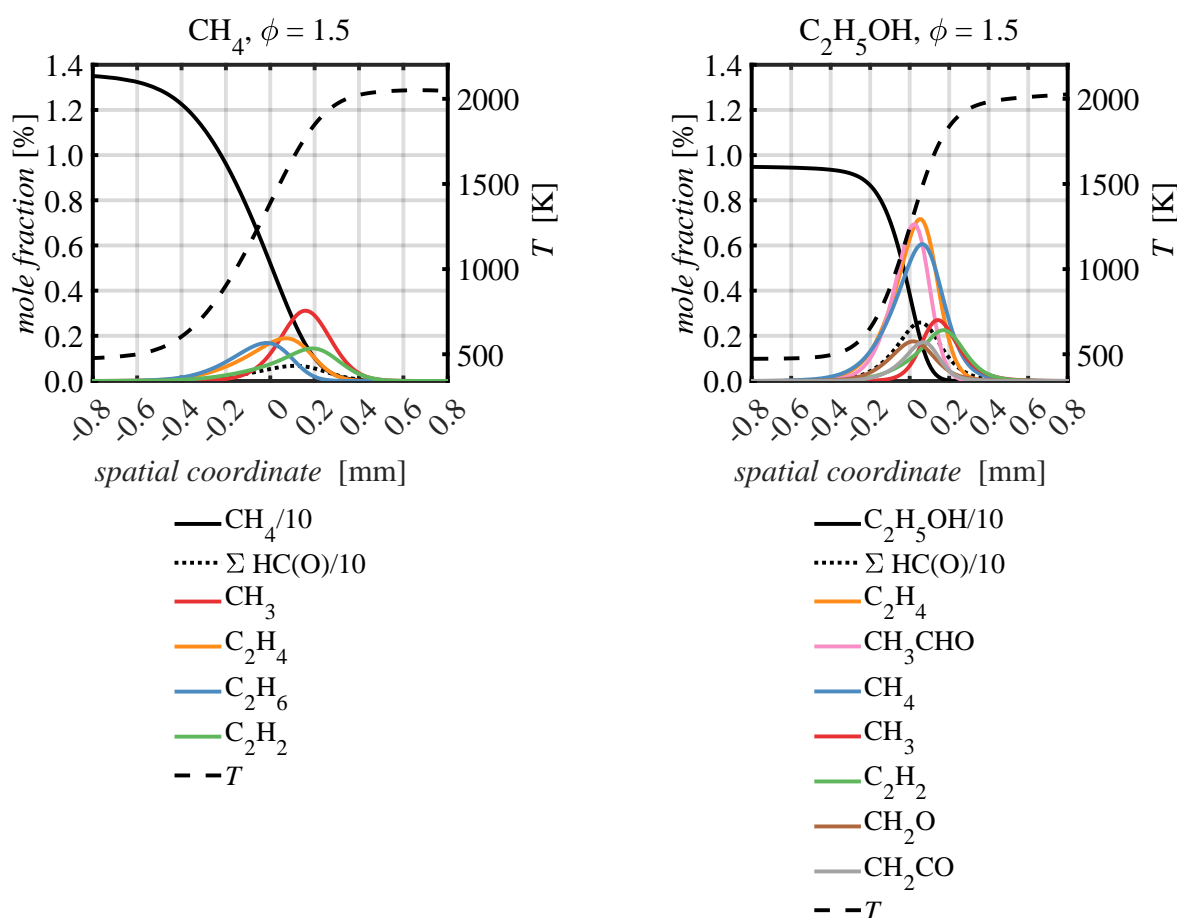
Figure 1.1.: Simulated laminar opposed jet flames of methane/air and ethanol/air against air display the larger number of potentially relevant intermediate species in the more complex fuel.

1.2. State of the Art

1.2.1. Fuel Effects

While fuel effect studies date back several decades, for example in the reaction model development context [107], this section focuses on the more recent studies. They provide experimental and numerical results for major flame parameters, such as laminar burning velocities, extinction strain rates, flame lengths, and flame stability. Furthermore, they contain essential theoretical discussions regarding reaction pathways, intermediate species, and the importance of thermo-diffusive effects.

Veloo et al. [145] compared methanol, ethanol, n-butanol flames, and the respective alkanes in experimental and numerical laminar counterflow setups. Using particle image velocimetry (PIV), they captured laminar flame speeds and extinction strain rates to compare high-temperature flame kinetics. Ethanol, n-propanol, and their alkane counterparts had similar laminar burning velocities. This was attributed to their oxidation mechanisms, including the decomposition reaction products and certain intermediates, namely methyl (CH_3) and hydrogen (H). For these larger fuels, the CH_3 creation, which facilitates chain termination, and H, which facilitates chain branching, are

in balance. In contrast, methane and methanol represent extreme cases where either one or the other dominates.

Tamadonfar and Gülder studied the turbulent premixed methane, ethane, and propane flame structures, stabilized on a piloted Bunsen burner employing PIV and Mie scattering [140]. A very comprehensive flame topography parameter set was derived, including flame lengths, curvatures, flame surface densities, and mean flame stretch factors. Thermo-diffusive effects in turbulent flames at lean, stoichiometric, and rich conditions could be isolated by comparing the mean flamelet consumption speed at similar flow conditions and burning velocities. This also enabled direct fuel comparisons.

Carbone et al. [23] studied fuel variation effects with respect to turbulent premixed flame structures. They investigated all hydrocarbons from methane to octane and utilized PIV and chemiluminescence (CL) measurement techniques. Heat loss effects from the flame to the ambient were accounted for through exhaust gases of an adaptable hydrogen coflow flame. Among larger molecular weight fuels, average flame heights were quite similar. Opposed to that, methane/air flames were substantially longer (shorter) at lower (higher) flame speeds. Carbone et al. [23] connected this to generally higher reactivity and a different behavior to the *Lewis number* (introduced in Section 2.5.1). Lastly, instantaneous high-speed CL showed that fuel effects also influenced flame topology, which was indicated by the fuel pocket sizes.

Smolke et al. [130] compared methane with heavier hydrocarbons by doing PIV and methylidyne radical (CH*) measurements with a piloted jet burner similar to the present work. Furthermore, they attempted to reproduce results using LES calculations. Ethylene, propane, n-heptane, and toluene were studied at constant laminar flame speeds, varying turbulence levels, and heat losses. Methane flames showed consistently larger and ethylene smaller flame heights compared to the longer chained hydrocarbons. Flame length and reactivity were affected by flame heat loss effects to the ambient, which was investigated using the exhaust of a hydrogen coflow. The need to improve models with regard to fuel effects was highlighted.

Watson et al. [147] investigated the lightest four alkanes and their respective alcohol counterparts in a rich premixed laminar stagnation flame setup. Utilizing nitrous oxide (NO) and methylidyne (CH) planar laser-induced fluorescence (PLIF) techniques and results, they discussed the molecular fuel structure influences on NO formation. Compared to their alkane counterparts, alcohol combustion led to less NO through inhibiting CH_3 generation by the alcohols' hydroxyl (OH) group.

Guiberti et al. [61] investigated turbulent flame stability using dimethyl ether (DME), compressed natural gas (CNG), and liquid petroleum gas (LPG) as fuels. They varied the pilot flame's heat release and degree of flow inhomogeneity at the nozzle exit. Both had minor influence compared to the fuel variation.

1.2.2. Flame Surface Density

As a brief introduction, the flame surface density (FSD) (Σ) represents the amount of flame front area in a given volume. As visible from the literature below, it is an important parameter for comparing different turbulent flames and thus a significant part of this work's discussion in Chapter 5. In addition, it has been established that within the flamelet regime, the FSD is a crucial parameter to quantify the mean reaction rate $\overline{w}$ [17, 126, 143, 146]:

$$\overline{w} = s_L \cdot \rho \cdot I_0 \cdot \Sigma \tag{1.1}$$

Therein, s_L is the laminar burning velocity, ρ the premixture density, and I_0 the stretch and curvature influence on the laminar burning velocity. Another important characteristic becomes accessible by transforming the FSD into the mean progress variable c space. The asymmetric appearance of the nominal bimodal distribution indicates whether gradient or counter-gradient diffusion through turbulence is dominant [84, 146].

Trouvé found that in the absence of quenching, the mean consumption speed is widely independent of the overall flow field [143]. Instead, the principal effect is the increased wrinkling through fluctuations, which leads to larger flame surface areas. The results are increased burning rates on a local scale, and decreased flame brush thicknesses and shorter flames on a global scale.

Donbar measured flame brush thicknesses and the FSD using CH-OH PLIF imaging [36]. They found that the FSD scales inversely with the flame brush thickness.

Filatyev et al. [49] studied, among other properties, the FSD and the global consumption speed using CH PLIF and PIV. They concluded that the turbulent burning velocity of a Bunsen flame also depends on its mean burning velocity and the burner width, which affect the residence times of flame-eddy interactions.

Gülder and Smallwood [63] obtained the FSD through OH PLIF on two different Bunsen-type burners. They found that the maximum FSD and the integrated FSD do not depend significantly on turbulence intensity. Instead, they indicate that small-scale transport of heat and species may be more critical, noting that fuel chemistry may not be decoupled from turbulence.

The substantial influence by thermo-diffusive effects on flame wrinkling was also described by Alqallaf et al. [4], who studied curvature evolution in turbulent flames.

Driscoll [37] assessed flamelet structure and turbulent burning velocities from DNS and experimental data to demonstrate their relation. They emphasized a memory of wrinkling, which must be considered when flames of different burners are compared. Furthermore, he concluded that the thin flamelet behavior is widely typical, emphasizing the validity of FSD as a sufficient parameter in most modeling applications.

Tamadonfar and Gülder [139] investigated flame brush characteristics and burning velocities in Bunsen flames. They found that a decrease in turbulent burning velocity to bulk velocity ratio increases flame height.

1.2.3. Spontaneous Raman Spectroscopy

The sRS system at Technische Universität Darmstadt (TUDa) enables the simultaneous temperature and main species quantities measurement in methane and hydrogen flames. However, the technique is still indifferent to small hydrocarbon species that appear as intermediate species in flames of with more complex fuels. Therefore, the system will undergo substantial modifications within this work, enabling the detection of intermediate species within the flame front. The origin and evolution of sRS in flame research, which serve as the background for the present development, are given by highlighting key milestones in the following.

In early experiments, sRS was developed at Sandia National Laboratories (SNL) from a laser-Doppler velocimetry (LDV)-Rayleigh setup. Dibble et al.[31] used a flashlamp-pumped dye laser with a spectrometer and photo multiplier tubes to collect major species Raman signals and Rayleigh scattering in hydrogen flames. Later, this technique was extended to methane and propane diffusion flames with several more species channels [32, 134].

To overcome the limitation of fast gating, Nandula et al.[102], and Chen and Mansour [25] used krypton fluoride (KrF) excimer lasers and intensified charged-coupled device (CCD) arrays to measure scalar dissipation in turbulent hydrogen jet flames. However, the ultra-violet (UV) wavelengths of KrF lasers proved to have comparatively less suitability due to impeded signal-to-noise ratio (SNR) in more luminous hydrocarbon flames [97].

To avoid penalties in dynamic range, SNR, and spatial resolution, high-speed mechanical gating systems in combination with non-intensified, back-illuminated CCD detectors and neodymium-doped yttrium aluminum garnet (Nd:YAG) lasers were used to capture 1D Raman and Rayleigh scattering. Many studies emerged from this breakthrough setup in the SNL [7, 59, 72, 74, 99]. A similar system emerged at TUDa to study opposed-jet diffusion flames and stratified flames [57, 79].

The SNL sRS system underwent another design iteration to improve spatial resolution, optical throughput, gating times, precision, and stability of alignment. It had since been used to study various turbulence-chemistry interaction phenomena and parameters, particularly for methane and hydrogen flames [8–10, 21, 29, 38, 52, 65, 70, 89, 90, 96, 124, 132, 136–138]. Further experimental setup and post-processing improvements were done to study DME flames and their intermediates [47, 54–56, 87, 88]. Thereby, the original spectrometer was duplicated on the opposite side of original detection system. It shall be noted that a similar but improved concept of this dual dispersion sRS setup will be introduced in the present work.

More sRS systems with which flame characteristics were studied emerged in the following. Utsav and Varghese [144] developed a multipass cell concept to capture Raman data from nitrogen in order to determine the temperature in a laminar premixed methane flame. Cessou et al. [3, 24] developed a system with an electro-optical shutter to determine the thermochemical state in a premixed methane flame. Using a combination of Raman, carbon monoxide (CO)-laser-induced fluorescence (LIF), and OH-LIF measurements, turbulent ethanol spray flames have recently been studied by Dunn et al. [40]. However, the data acquisition within the flame was limited to regions without droplets and hence, only rather high axial locations.

As for the most novel sRS evolution, Guiberti et al. [62] introduced a system where the Raman probe volume was extended to a two-dimensional (2D) manifold of 25x8 mm^2. The spectrometer was gated using an electro-optical shutter and four cameras captured the main species individually. Using this system, the temperature and mixture fraction of a non-premixed hydrogen flame at 12 bar were measured. Additionally, the OH mole fraction was simultaneously recorded using OH-PLIF.

This path was recently followed up by Yu et al. [148]. They captured the first 2D Raman images of a hydrogen/air diffusion flame at ambient pressure using a Fiber-bundle-based 2D Raman and Rayleigh imaging system. These 2D studies, despite slightly decreased accuracy and precision compared to the established 1D sRS systems, open up new possibilities in flame-specific research.

However, due to the high accuracy and precision, 1D sRS remains an important tool, particularly with the increased interest in studying flames of more complex fuels. As mentioned, that research began with work by Fuest et al. [54] on laminar premixed DME flames. It was continued by Magnotti et al. [88, 89] with their characterization of individual Raman spectra of typical DME intermediate species heated up to 860 K. The present work will continue on this path towards oxygenated liquid fuels, namely ethanol and 3-3-oxymethyl ether (H_3C-O-$(CH_2O)_3$-CH_3) (OME-3).

Like the study by Magnotti et al. [87], the spectrometer described in this work incorporates a higher-dispersed spectrometer arm for the fuel and intermediate species CH-stretch modes between approximately 2548 and 3434 cm^{-1}, which it records simultaneously with all other relevant flame species. However, a distinction is that the spectrometer arm is diverted from the same optical path where the other species are measured, rather than through a duplicate system positioned at the opposite side of the probe volume. This shall reduce detrimental beam steering or thermal drift influences. Furthermore, the calibration process is simplified and the concept offers economic benefits.

1.3. About This Work

1.3.1. Aims

This work aims to expand the current state of knowledge on the laminar and turbulent combustion of complex hydrocarbons. Furthermore, the data shall be usable to validate numerical models in comparative numerical calculations. Lastly, measurement and evaluation methods of new technical apparatuses are developed and tested, upon which future investigations can build.

These aims will be pursued through several independent experiments, which will be complemented by numerical 1D calculations. More concrete research targets to reach the defined aims are given at the beginning of each respective experiment chapter. In the following, the work's structure and contents are explained first, before the hardware and methodological novelties are summarized.

1.3.2. Content

Chapter 2 covers the fundamentals needed for understanding the work, with sections on combustion, transport, fluid mechanics, turbulence-chemistry interaction, flame front stability, and measurement techniques.

Chapter 3 discusses the numerical methods and calculations used to complement the experiments, including the Cantera calculation tool, numerical 1D flame configurations, numerical calculation and experiment symbiosis, and results on flame parameters and intermediate species.

Chapter 4 covers the experiment that detects oxygenated hydrocarbon intermediate species of premixed ethanol/air and OME-3/air flames. The chapter also describes the design process of a new laminar temperature-controlled opposed jet burner (LTOJ) and its periphery, introduces the spectrometer extension's technicalities, and provides details on the measurement methodology and post-processing.

Chapter 5 covers three experiments investigating the fuel-influence onto blow-off stability, flame length, and flame topology. The chapter also describes the temperature-controlled piloted jet burner (TCJB) which was commissioned during this work, the diagnostics used, and the post-processing methodologies.

Chapter 6 covers the making of the pilot-experiment in which thermochemical states in laminar and turbulent ethanol/air flames are measured for the first time. The novel methods are validated by comparing the experimental flame results against numerical calculations and furthermore by examining differences to well-known methane/air flames.

Finally, Chapter 7 provides a combined conclusion and outlook.

In Appendix A, supplemental results for thermochemical state discussions can be found. Appendix B provides additional research that did not make it into the dissertation's main text body due to its limited relevance for the discussions.

1.3.3. Novelties

Several novelties were created on the way to achieving the aims defined at the beginning of this section.

First, the hardware-specific novelties are summarized:

1. The LTOJ burner was built to study complex fuel flames and calibrate the sRS system at TUDa. It is the only option for calibrating vaporized liquid fuel flames.

2. An extension for the Raman spectrometer at TUDa was built enabling the simultaneous detection of fuel and intermediate species beside the main species.

3. A third shutter wheel system was built for the sRS system at TUDa, enabling long-exposure studies and extending the iris shutter lifetime.

4. The TCJB burner was commissioned for turbulent premixed combustion of vaporized liquid fuels. It can be heated and controlled up to $250\,^{\circ}\text{C}$ and is able to stabilize jet flames with Reynolds numbers up to 61000 (methanol/air).

5. The complete spectrometer housing was redesigned for more flexibility, temperature stability, and stray light tightness.

6. An improved flat flame burner was built with an improved sealing concept and easier burner matrix replaceability.

7. A pure gas calibration nozzle incorporating a nitrogen coflow was built to drastically reduce the necessary amount of costly calibration gas (previously probed above the flat flame).

8. Several small tools were built for the spectrometer's alignment procedure, including a custom leveling scale and new optical target holders.

Secondly, the methodological and exploratory novelties are summarized:

1. A long-exposure methodology was developed to capture small amounts of intermediate species in stationary flames. The main pillars for this success are the flow-considerate LTOJ burner design and a fine in-situ laser alignment. The experimental technique was complemented by numerical calculations to estimate temperatures within $\pm100\,\text{K}$.

2. A flame surface density study was performed to analyze flame wrinkling in turbulent premixed alcohol/air and methane/air flames. Through an effective Lewis number study, thermo-diffusive effects were found to have a substantial effect on flame wrinkling, being very sensitive to either lean or rich conditions.

3. A methodology was invented to calibrate the hybrid matrix inversion (MI) Raman evaluation method using symmetric LTOJ twin flames. This enabled the first thermochemical state measurements in premixed flames of vaporized liquid fuels.

4. Thermochemical states in premixed laminar and turbulent ethanol/air flames were determined at different turbulence intensities and equivalence ratios. Comparisons with numerical 1D flame calculations frequently back up the gathered results. Furthermore, concurrent methane/air flames serve to investigate differences resulting from fuel effects.

2. Theoretical Background

This chapter contains theory that assists the understanding of the presented work. It is divided into sections about combustion chemistry, transport phenomena, fluid mechanics, turbulence-chemistry interaction, and flame front stability. Furthermore, the fundamentals of combined Raman-Rayleigh spectroscopy, chemiluminescence (CL), and laser-induced fluorescence (LIF) are given.

2.1. Combustion

2.1.1. Global Reaction and Subreactions

The global reaction of an oxygenated hydrocarbon with dioxygen, here 'oxygen' (O_2) can be described using the following equation:

$$C_xH_yO_z + (x + \frac{1}{4}y - \frac{z}{2})O_2 \xrightarrow{k_f} xCO_2 + \frac{y}{2}H_2O \tag{2.1}$$
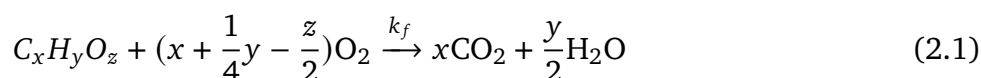
This equation is an abstraction of hundreds of subreactions, also referred to as reaction pathways. Once the global reaction is initiated to produce a stable flame, a radical pool, mainly hydrogen (H), oxygen (O), and hydroxyl (OH), is continuously supplied towards upstream to break down the fuel molecule and its descendants, producing other radicals and less or more active reactants in the process. Finally, the series of reactions reach carbon monoxide (CO) and H, which are oxygenated to carbon dioxide (CO_2) and water (H_2O), respectively.

For a complete picture of the methane or alcohol oxidation subreactions, the reader is referred to Law [83, p. 99ff]. The important takeaway regarding this work is that from a chemical kinetic standpoint, the fuel influence on the particular subreactions is not to be overvalued. Independent of fuel, the reaction pathways generally work hierarchically from big to small molecules using the same main radicals.

Notably, a mechanism for a light fuel molecule such as methane needs to include the reaction pathways of both smaller and larger molecules, such as ethane, ethene, and ethylene. This is because dependent on the fuel-to-air ratio, individual carbon (C)-atom groups may recombine into larger dicarbon (C_2) bond molecules, which have their own reaction pathways.

The specific reaction rate constant k_f in equation 2.1 is expressed as [83, pg. 59]:

$$k_f(T) = A \cdot T^n e^{\frac{-E_a}{RT}}, \tag{2.2}$$

$A \cdot T^n$ make up the pre-exponential factor modified for temperature dependency, E_a the activation energy, and R the universal gas constant. The pre-exponential factor has a minor temperature dependence compared to the exponential term. At higher temperatures, the exponential factor's influence diminishes towards unity, and the pre-exponential factor dominates the rate. The activation energy E_a represents the minimum energy the colliding molecules must possess for a reaction to be possible. This energy must be put into the system first to initiate the break-up of molecules [83, pg. 71f].

Once the hydrocarbon oxidation is initiated, the reaction enthalpy ΔH is released as heat. It can be calculated using *Hess's law*, which states that the sum of product and educt species formation enthalpies H_f at standard conditions equals the reaction enthalpy [68, pg. 68f]. Under consideration of the stoichiometric coefficients ν, the relation is given as follows:

$$\Delta H_r = \sum \nu_p \cdot H_{f(p)} - \sum \nu_r \cdot H_{f(r)} \tag{2.3}$$

2.1.2. Premixed Combustion

Combustion requires oxidizer and fuel mixing on a molecular level. The mixing path leads to the classification into premixed and non-premixed combustion. In non-premixed combustion, the reaction occurs between separate fuel and oxidizer inflows at or near the stoichiometric mixing point. Conversely, fuel and oxidizer are mixed before entering the reaction space in premixed combustion. Typical premixed combustion processes are *Bunsen* burners (laminar), gas turbine combustion, or combustion inside internal combustion engines (both turbulent).

In the following, terms related to premixed combustion are individually discussed.

Flame structure: Figure 2.1 schematically shows the premixed flame structure [83, p. 242]. Upstream, there is a reactant mass fractions supply (Y_r) at unburned temperature T_u. Downstream, the reactants' mass fractions vanish, and the equilibrium temperature T_b is reached. In the outer upstream transport region, referred to as preheating zone, convection and diffusion dominate and balance. In the inner reaction zone, reaction and diffusion balance [83].

The reaction rate displayed is characterized by a strong gradient caused by the activation of the reaction, followed by a steep drop due to rapid reactant depletion. The chemistry is relatively slow before and after this reaction region.

In Figure 2.1, the normalized temperature and reactant mass fraction curves in the preheating zone appear inversely symmetric to one another. This resembles equal diffusion (equidiffusion) of heat and mass, which is not always the case (more in Section 2.5.1).
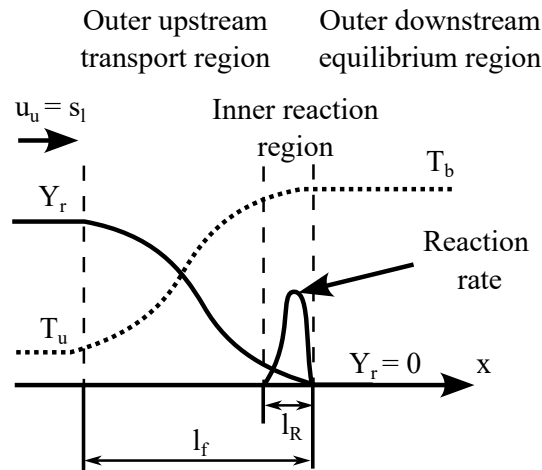
Figure 2.1.: Premixed flame structure including inner reaction region. Adopted from Law [83, pg 242] with some changes.

Equivalence Ratio: An important premixed combustion figure is the equivalence ratio ϕ. It is the ratio between the actual fuel-to-oxidizer ratio and the fuel-to-oxidizer ratio under stoichiometric conditions, at which all fuel and oxidizer molecules react [83, pg. 15]:

$$\phi = \frac{X_F/X_O}{(X_F/X_O)_{st}} = \frac{Y_F/Y_O}{(Y_F/Y_O)_{st}} \tag{2.4}$$

Therein, X_i are the fuel and oxidizer mole fractions and Y_i are the respective mass fractions. The mixture is referred to as lean, stoichiometric, and rich for $0<\phi<1$, $\phi=1$, and $1<\phi<\infty$, respectively.

Within this work, an expression for equivalence ratio that is conserved from unburned to burned mixture species is used. In order to retrieve it, the *Bilger* mixture fraction F is first calculated from the species available through Raman [15]:

$$F = \frac{\frac{2(Y_C-Y_{C,ox})}{w_c} + \frac{Y_H-Y_{H,ox}}{2w_H} + \frac{Y_O-Y_{O,ox}}{w_O}}{\frac{2(Y_{C,fuel}-Y_{C,ox})}{w_C} + \frac{Y_{H,fuel}-Y_{H,ox}}{2w_H} - \frac{Y_{O,fuel}-Y_{O,ox}}{w_O}} \tag{2.5}$$

Therein, the subscripts C, H, and O correspond to the elements, w are the respective atomic masses, and Y the mass fractions.

From this mixture fraction, the equivalence ratio ϕ is approximated using the following equation [15, 137]:

$$\phi \approx \frac{F}{1-Z}\frac{1-Z_s}{Z_s} \tag{2.6}$$

Therein, s denotes the mixture fraction at stoichiometry.

Flammability Limits: Premixtures have equivalence ratio boundaries within which a spark or a flame can ignite or propagate through the mixture. Table 2.1 lists the flammability limits gathered by Naegeli and Weatherford Jr. [101] at atmospheric conditions for fuels relevant to this work. Notably, only the outer range boundaries are given, and the volumetric fractions in air values have been converted to equivalence ratios. Furthermore, these values should be taken as estimates, as they strongly depend on experimental accuracy.

Table 2.1.: Lower and upper flammability limits for fuels studied in this work. The first five are obtained from Naegeli and Weatherford Jr. [101]. The OME-3 values were obtained from Sun et al. [135].

Fuel	Approx. lower limit ϕ	Approx. upper limit ϕ
Methane	0.48	1.43
Methanol	0.43	2.6
Ethanol	0.51	2.71
Isopropanol	0.54	2.57
n-Butanol	0.43	3.22
OME-3	0.7	1.6

Laminar Burning Velocity: The laminar burning velocity characterizes the velocity at which a flame element propagates towards unburned reactants under unstrained conditions (uninfluenced by fluid motion). It is a function of pressure, reactant temperature, and the equivalence ratio:

$$s_L = s_L(p, T_u, \phi) \tag{2.7}$$

Laminar burning velocities can be obtained either experimentally or from numerical 1D laminar flame calculations. While the accuracy of numerically simulated burning velocities depends on the mechanism used, the laminar burning velocity is an essential parameter for which the mechanisms are tested against. As all mechanisms used in this work are from peer-reviewed sources, the laminar burning velocities derivation from calculations is deemed appropriate.

Notably, the laminar burning velocity as a flame analysis parameter is not limited to the laminar flame regime. Within certain boundaries (Section 2.4.2), turbulent flames can be viewed as connected individual laminar flame front elements (*flamelets*), which each behave like laminar flames.

Laminar Flame Thickness: The thermal diffusion D_{th}, calculated from the thermal conductivity λ, the density ρ, and the specific heat capacity c_p, divided by the laminar burning velocity s_L, yields the laminar flame thickness, or *Zeldo'vich thickness* [83, 113]:

$$\delta_{L,Ze} \cong \frac{D_{th}}{s_L} = \frac{\lambda}{\rho \cdot c_p \cdot s_L} \tag{2.8}$$

However, the flame thickness may also be estimated from geometrical considerations by using the temperature [83], which is the definition mainly applied in this work:

$$\delta_{L,geo} = \frac{T_b - T_u}{(dT/dx)_{max}} \tag{2.9}$$

Partially-premixed Combustion: Sohrab et al. [131] created a scenario of an opposed jet flame, where two flames of different premixtures opposed each other. They found that when one was rich and the other lean, the abundance of either fuel or oxidizer led to the transfer of heat and reactants onto the other flame. The result is that diffusion-type characteristics will develop on top of the premixed flame zones, hence the name partially-premixed.

This phenomenon can also be seen in scenarios where a very rich premixed flame is in close proximity of an oxidizer stream. The two will create a secondary flame fueled by left-over hydrocarbons and radicals. In this work, this applies either with an opposed air nozzle (laminar counterflow burner) or an air coflow (turbulent jet flame case).

2.1.3. Flame Types, their Stabilization Mechanisms, and Use Cases

Several flame types are used for different purposes in this work, namely flat flames, *Hencken* flames, laminar opposed flames, and piloted turbulent jet flames. Notably, the *V flame* is another used flame type, but it is in the end replaced by laminar opposed flames. Brief descriptions of these flames are given in the following. More elaborate descriptions of the flat flame and the Hencken burner were given by Schneider [123] and Butz [20] and are therefore spared here.

Flat Flame: The flat flame is a premixed flame for methane/air mixtures or other gaseous fuels. Stabilization usually occurs a few millimeters above a sintered metal structure where laminar burning velocity and premixture gas velocity are balanced. A nitrogen coflow shields the flame against external influences.

The very defined conditions in the flat flame exhaust cone at different equivalence ratios are frequently used to calibrate the single-shot Raman evaluation method, which is called *hybrid MI* (Section 2.6.3).

Notably, the flat flame burner was redesigned for more robust sealing and easier serviceability. A cross-section of the modified burner is shown in Appendix C.2.

Hencken Flame: The Hencken flame is a quasi-premixed flame for hydrogen/air mixtures. Stabilization occurs slightly above the burner's surface, comprised of 100 tubes with hydrogen flow, each surrounded by six air flows in a honeycomb-structured element. Again, the flame exhaust cone region provides well-known conditions, and a nitrogen coflow shields it against external influences. This burner is also used to calibrate the MI.

V Flame: The V flame is a modified premixed Bunsen flame for methane/air mixtures. The flame is split and stabilized by a ceramic rod from aluminium oxide (aluminum oxide (Al_2O_3)). The gradient of one of the two flame branches is used to match the axial position of the Raman and Rayleigh images in single-shot Raman measurements. Again, shielding against external influences is done by a nitrogen coflow.

Laminar Opposed Flame: The laminar opposed flame is a very flexible setup to produce a variety of flames, including non-premixed, premixed, and partially-premixed flames. Stabilization occurs between two opposing nozzles at the conjunction of streams, with nitrogen coflows shielding them from external influences. The different streams from the nozzles can either be from the same mixture, referred to as a twin flame, or of a different kind to produce more complex flames. A detailed description of opposed flames and an overview of possible flame types is given by Sohrab et al. [131].

Within this work, laminar opposed flames from premixed vaporized ethanol or OME-3 fuels are generated using a newly designed burner (Section 4.2.1). This provides an essential capability to calibrate ethanol/air flames for the single-shot Raman and Rayleigh measurements in Chapter 6.

Piloted Turbulent Jet Flames: The piloted jet flame is a jet nozzle that can produce non-premixed or premixed flames. Stabilization at slower bulk velocities can occur at the nozzle rim, where heat losses reduce flame speeds enough to stay balanced with the flow velocities. However, at too high bulk velocities, the flame lifts and vanishes, a phenomenon referred to as *blow-off* (see Section 5.4.1 for measurements). Notably, the opposite occurs when the laminar burning velocity is too large. The flame will rapidly propagate towards the unburned mixture into the burner; an unwanted phenomenon referred to as *flashback*.

Stabilization of the jet flame at higher bulk velocities is provided by using the hot exhaust gases of a much smaller surrounding flame, the *pilot* flame. Large bulk velocities and turbulence levels are possible depending on the heat it provides. A well-studied burner of this type is the *Sydney burner*, which was a significant part of the TNF workshop mentioned in the introduction. A similar burner that can also be heated was built before the beginning of this work, but utilized here for the first time. Its design is introduced in Section 5.2.1.

2.2. Transport

Transport refers to diffusion and convection processes, which will be introduced in the following.

2.2.1. Diffusion

Any system will attempt to restore spatial uniformity in regions with molecular energy, concentration, or momentum gradients [83, pg. 141]. While these properties represent random collisions on an atomic level between individual gas molecules, they even out non-uniformity on the macroscopic scale, nevertheless.

The individual diffusion modes are heat conduction, mass diffusion, and viscous motion, which all go under the diffusion term umbrella in this work. In practice, when considering diffusion within a flame, the higher concentration in the fresh mixture constantly supplies reactants to the flame. In contrast, the hot part of the flame preheats the mixture and thereby delivers the activation energy [83, pg. 142].

Coefficients and Diffusional Fluxes Laws   Rates of the diffusion modes differ and are functions of the gradient's magnitude and the respective diffusion coefficients $D_{i,j}$, $\mu_{i,j}$, $\lambda_{i,j}$. These are used to find the diffusional fluxes via *Fick's law of mass diffusion*, *Newton's law of viscosity*, and *Fourier's law of heat conduction*, respectively, which are given in the following [83, pg. 144]:

$$F_{species,i} = -D_{i,j}\nabla\rho_i, \quad D_{i,j} = \frac{2(8m_{i,j}k^oT/\pi)^{1/2}}{\rho(\pi\sigma_{i,j}^2)} \tag{2.10}$$

$$F_{momentum} = -\mu_{i,j}\nabla\nu_y, \quad \mu_{i,j} = \frac{2(8m_{i,j}k^oT/\pi)^{1/2}}{\pi\sigma_{i,j}^2} \tag{2.11}$$

$$F_{energy} = -\lambda_{i,j}\nabla T, \quad \lambda_{i,j} = \frac{2(8m_{i,j}k^oT/\pi)^{1/2}c_\nu}{\pi\sigma_{i,j}^2} \tag{2.12}$$

Therein, ρ is the density, T the temperature, ν the kinematic viscosity, m the molecular masses, $\sigma_{i,j}$ the molecular diameters, and k^o the Boltzmann constant. The indices i and j stand for individual species pairs. Note that in momentum and energy balance (see Section 2.3.1), the system is often assumed as a one-component gas ($m_{i,j} = m/2$). However, in the case of mass diffusion, the species indices need to be retained [83, pg. 144].

Diffusion Rates and Non-dimensional Numbers   Each diffusion process has a characteristic rate of spreading [83, pg. 145]. For mass diffusion, it is simply the coefficient $D_{i,j}$. For viscous spreading, it is the kinematic viscosity $\nu = \frac{\mu}{\rho}$, and for thermal conduction, its the thermal diffusivity $\alpha_{th} = \frac{\lambda}{c_p\rho}$.

The ratios of spreading rates yield commonly used non-dimensional numbers, namely the Schmidt number (Sc), the Prandtl number (Pr), and the Lewis number (Le) [83, pg. 145f]:

$$Sc_{i,j} = \frac{\nu}{D_{i,j}} = \frac{\mu}{\rho D_{i,j}} \tag{2.13}$$

$$Pr = \frac{\nu}{\alpha_{th}} = \frac{\mu c_p}{\lambda} \tag{2.14}$$

$$Le_{i,j} = \frac{\alpha_{th}}{D_{i,j}} = \frac{Sc_{i,j}}{Pr} = \frac{\lambda}{c_p\rho D_{i,j}} \tag{2.15}$$

For methane/air flames, the assumption is frequently made that heat and mass diffusion are approximately even (Le$\approx$1 *assumption*). However, this is not the case when fuel species are much smaller or larger than the oxidizer. For larger fuel molecules, such as larger-than-methane alkanes or alcohols, Le$>$1 is given in lean, while Le$<$1 is given in rich conditions. The opposite is true for a smaller fuel molecule, for example hydrogen (more details in Section 2.3).

2.2.2. Convection

Convection refers to the media and diffusion properties carried along by the bulk movement of the fluid medium [83, pg. 141]. Notably, convection may facilitate or retard diffusive transport at the same rate for all diffusion modes, as it depends only on fluid motion.

The convective and diffusional transport in laminar or turbulent combustion environments can be mathematically described by fluid dynamics, which will be covered next.

2.3. Fluid Mechanics

This section covers the essential pieces to describe reacting flows: conservation equations, the ideal gas equation, and the turbulence phenomenon.

2.3.1. Conservation Equations

Reacting flows can be numerically captured by solving a system of conservation equations, the Navier-Stokes equations. While these governing equations are not directly applied in this work, the interrelation of the involved quantities is undoubtedly important in the discussions.

The presented versions are taken from Poinsot et al. [113, pg. 13 ff]. They are given on the applicable assumptions that the Mach number is low, pressure is constant, body forces are zero, and viscous heating is negligible.

Conservation of Mass: The conservation of mass is defined as for a non-reacting case:

$$\frac{\partial \rho}{\partial t} + \frac{\partial \rho u_i}{\partial x_i} = 0, \tag{2.16}$$

where ρ is the density, and u_i is the velocities vector.

Conservation of Momentum: Momentum is also conserved in the same way as for a non-reacting case:

$$\frac{\partial}{\partial t}\rho u_j + \frac{\partial}{\partial x_i}\rho u_i u_j = -\frac{\partial p}{\partial x_j} + \frac{\partial \tau}{\partial x_i}, \tag{2.17}$$

where p is the static pressure and $\tau_{i,j}$ the viscous tensor (shear forces). By changing the density with the temperature increase across the flame, combustion strongly influences momentum. This will also influence the viscous tensor by changing the viscosity:

$$\tau_{i,j} = \mu \left(\frac{\partial u_i}{\partial x_j} + \frac{\partial u_j}{\partial x_i} \right) - \frac{2}{3}\mu \frac{\partial u_k}{\partial x_k}\delta_{ij}, \tag{2.18}$$

with δ_{ij} being the *Kronecker-Delta*.

Conservation of Species: The conservation of species can be assumed for each partaking species k:

$$\frac{\partial \rho Y_k}{\partial t} + \frac{\partial}{\partial x_i}(\rho(u_i + V_{k,i})Y_k) = \dot{w}_k \tag{2.19}$$

Therein, Y_k are the species mass fractions and $V_{k,i}$ are the diffusion velocities in the directions i. Because species can be created and consumed during combustion, there exists a source term $\dot{w}_k$, which represents the reaction rate of species k.

Conservation of Energy: Lastly, energy conservation can be applied:

$$\frac{\partial \rho E}{\partial t} + \frac{\partial}{\partial x_i}(\rho u_i E) = \dot{w}_T - \frac{\partial q_i}{\partial x_i} \tag{2.20}$$

Therein, the heat release due to combustion $\dot{w}_T$, or heat release rate (HRR), is defined as:

$$\dot{w}_T = -\sum_{k=1}^{N} \Delta h_{f,k}^0 \dot{w}_k, \tag{2.21}$$

where $h_{f,k}^0$ is species k's sensible enthalpy.

2.3.2. Ideal Gas Equation of State

The ideal gas equation of state applies to the frequently made assumption that the inner energy (viscosity and thermal conductivity) is pressure or volume independent:

$$p = \rho R \sum_{i=1}^{N} X_i m = \rho R \sum_{i=1}^{N} \frac{Y_i}{m} = \frac{\rho R T}{\bar{m}} \tag{2.22}$$

Therein, ρ is the density, R the ideal gas constant, T the temperature, X_i the mole fraction, and m the molecular weight.

However, it depends majorly on the temperature. This can be utilized to calculate the temperature based on Rayleigh scattering (Section 2.6.1).

2.3.3. Turbulence

The order of a fluid's flow is distinguished between either laminar or turbulent. Laminar flow has sheet-like properties, where perturbations in initial conditions, boundary conditions, and material properties have little effect. However, that sensitivity towards perturbations increases drastically once a narrow threshold, the critical *Reynolds number* (Re), is surpassed. The Reynolds number relates the destabilizing inertia forces and the stabilizing viscous forces:

$$\text{Re} = \frac{\rho u L}{\mu} \tag{2.23}$$

Therein, ρ is the density, u is the velocity, L is the characteristic length, and μ is the dynamic viscosity.

Laminar stationary flows have deterministic solutions to the conservation equations. In turbulent flow, only in-deterministic solutions exist and probabilistic values need to be given due to the chaotic flow conditions [114, pg. 37ff].

A common turbulence thought model is the energy cascade. The main stream kinetic energy (e.g., pipe stream) is transferred onto turbulent flow structures, referred to as *eddies*, which are initially of the system's integral length scale size l_0 (e.g., pipe diameter). These large eddies are unstable and disintegrate into smaller and eventually isotropic ones in a cascade manner.

The turbulent kinetic energy transfer rate is ϵ. Finally, the viscosity dominates, and the smallest eddies' energies dissipate fully into heat. The final structures can, by derivation through dimensional analysis, be described by the non-dimensional *Kolmogorov time* τ_K, *Kolmogorov length* l_K, and *Kolmogorov velocity* u'_K numbers [114, pg. 185]:

$$\tau_K \approx \left(\frac{\nu}{\epsilon}\right)^{1/2} \qquad l_K \approx \left(\frac{\nu^3}{\epsilon}\right)^{1/4} \qquad u'_K \approx (\nu\epsilon)^{1/4} \tag{2.24}$$

In the following, some more dimensionless numbers are introduced, which, beyond flow information, include information from the chemistry side. One is the *turbulent Reynolds number* $\mathrm{Re_t}$, which is defined as follows [83, pg. 496]:

$$\mathrm{Re_t} = \frac{u'l_0}{s_L \delta_f} \tag{2.25}$$

Therein, u' is the characteristic velocity fluctuation at the integral length scale l_0, s_L the laminar burning velocity, and δ_f the laminar flame width.

The next is the turbulent *Karlovitz number* $\mathrm{Ka_L}$, which relates the flame thickness to the Kolmogorov scale [83, pg. 497]. It makes a statement as to whether a laminar flame front can be entered by a turbulent structure of Kolmogorov length size:

$$\mathrm{Ka_L} = \frac{\tau_L}{\tau_K} = \left(\frac{l_L}{l_K}\right)^2 = \left(\frac{u'_L}{s_L}\right)^2 \tag{2.26}$$

Therein, $\tau_L = \frac{D}{s_L^2}$ and $l_L = \frac{D}{s_L}$ are the characteristic laminar flame time and length scales (commonly referred to as flame thickness).

A refined Karlovitz number $\mathrm{Ka_R}$ can be found if not the whole flame thickness is regarded, but only the reaction zone's:

$$\mathrm{Ka_R} = \frac{\tau_R}{\tau_K} \tag{2.27}$$

The *Damköhler number* Da relates the macroscopic flow time scales t_0 to the reaction time scales t_L [68]:

$$\mathrm{Da} = \frac{t_0}{t_L} = \frac{l_0 s_L}{u' \delta_f} \tag{2.28}$$

2.4. Turbulence-chemistry Interaction

An integral part of understanding combustion phenomena is the bidirectional interaction between the oftentimes turbulent flow structures and the hydrocarbon oxidation reactions. This field is referred to as *turbulence-chemistry interaction*, and its important aspects are given in the following.

2.4.1. Flame Stretch and Strain Rate

When a flamelet moves in a non-uniform flow field, it is subject to being both strained and curved. The combination is called *flame stretch* κ_{str} [113, pg. 63f], which describes the fractional change rate of the flame surface A:

$$\kappa_{str} = \frac{1}{A}\frac{dA}{dt} = \nabla_{ta} \cdot \vec{u} + s_d \nabla_t \cdot \vec{n} \tag{2.29}$$

Therein, ta in the subscript stands for the differential operator tangential part, $\vec{u}$ is the unburned gas velocity, s_d the displacement speed, and $\nabla_t \cdot \vec{n}$ the flame element curvature:

$$\nabla \cdot \vec{n} = \frac{1}{R_1} + \frac{1}{R_2} \tag{2.30}$$

As it will be frequently used here, the global strain rate α is defined for on-axis opposing flows, with streams emitting from nozzles separated at a distance L with velocities u_1 and u_2:

$$\alpha = \frac{u_1 + u_2}{L} \tag{2.31}$$

Locally, the strain rate varies significantly over the spatial axis, as the gas expands rapidly within the flame. However, the strain rate defined here describes the mean planar (non-curved) flame stretch rather well and is a useful comparative measure for the flames discussed in this work.

When different mixtures are used for the opposing streams, their axial momenta can be balanced by adjusting the velocities relative to the different densities [122]:

$$\rho_1 \cdot u_1^2 = \rho_2 \cdot u_2^2 \tag{2.32}$$

2.4.2. Borghi-Peters Diagram

How turbulent flow and chemical reaction interact depends, among other factors, on whether their characteristic length scales are far apart or in the same order [83, pg. 496ff].

A categorization of the respective effects is given by the Borghi-Peters diagram in Figure 2.2, which was adopted from Law [83, pg. 497] with minor changes.

Therein, the abscissa shows the characteristic length scale (here: nozzle diameter) divided by the laminar flame thickness (here: Zeldo'vich thickness, Section 2.1.2). The ordinate is the velocity root mean square (r.m.s.) divided by the laminar burning velocity.
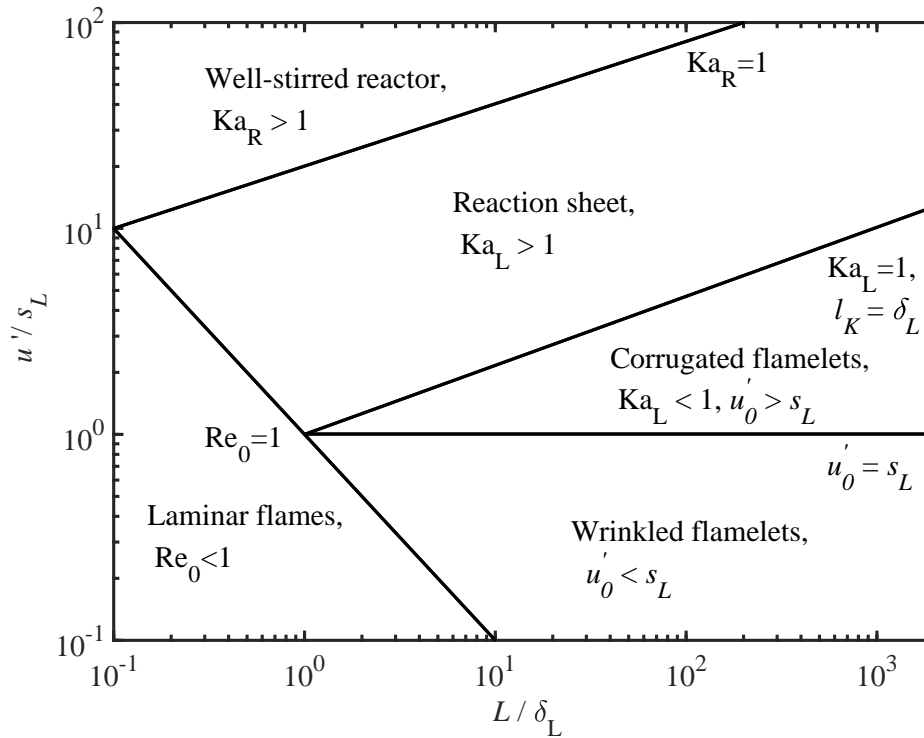
Figure 2.2.: Borghi-Peters regime diagram. Adopted from Law [83, pg. 497] with minor changes.

The following regimes can be categorized based on the non-dimensional numbers derived in section 2.3.3 [83, pg. 498f].

Laminar flames: If $Re_t < 1$, the flame is propagating in a laminar flow.

Wrinkled flamelets: If $Re_t > 1$, $Ka < 1$, and u'<s_L, the turbulent fluctuations will alter the flame front only on a larger scale. The propagation remains determined by small laminar strained flamelets.

Corrugated flamelets: Since $Ka_L < 1$, the flame remains in its laminar structure. However, as u'>s_L, the flamelet will be corrugated when trespassing similar-sized eddies, and the resulting surface increase will influence the flame propagation. As the smallest eddies are still larger than the flame fronts, they will stay intact. The folding flamelets will form unburned fuel and burned mixture pockets.

Reaction-sheet regime: With $Ka_L > 1$, the flame preheating zone will now be penetrated by the smallest eddies. This will enhance heat and mass transfer rates, broadening the flame as a result. As $Ka_R < 1$, the reaction sheet remains only wrinkled.

Well-stirred reactor: The smallest eddies are now on the reaction zone thickness order and will penetrate the flame structure's core. Diffusion and heat transfers to the preheating zone increase, which reduces the flame temperature and consequently extinguishes the flame. No distinct structures remain. Therefore, it behaves as a well-stirred reactor.

The regime boundaries will vary with the fuel studied [140]. This can be captured by multiplying the constant Karlovitz lines (s_L/u') with the Schmidt number 2.2.1.

Several considerations weaken the effect of boundaries between regimes [83, pg. 499]. First, the density increase across the flame front is increasing the normal flow velocity. At the same time, the tangential velocity is continuous across the flame. This can reduce the efficiency of rolling up a flame by a vortex.

Secondly, the characterization assumes stationary flamelets. However, in reality they may adjust their location dependent on upstream motion, thereby resisting wrinkling and possibly extinction.

Thirdly, there might be *diffusional-thermal instabilities* or *hydrodynamic instabilities* mechanisms at play that act upon the flamelet by altering flame wrinkling or inducing it, respectively. Both mechanisms are particularly relevant for this work and are described in the following section.

2.5. Flame Front Stability

The wrinkling initiated by mild to medium turbulence may increase or decrease dependent on three mechanisms. These are based on either thermo-diffusive effects (also referred to as *curvature effects* or *Lewis number effects*), hydrodynamic instabilities (also referred to as *Darrieus-Landau (DL) instability*), and *buoyancy-driven instabilities* (Rayleigh–Taylor instability).

Explanations of the former two, based on the comprehensive description and discussion by Law [83, pg. 456ff], are given in the following. The buoyancy-driven instabilities are not described in detail. This is because they are assumed not to play a significant role in either turbulent flames or among fuel variations, which are at the center of this work.

2.5.1. Thermo-diffusive Effects

Thermo-diffusive effects describe the combination of pure curvature and Lewis number effects. These can have a stabilizing or destabilizing effect on a wrinkled flame front.

In the simplest case, heat and mass diffusions are equal, as schematically shown in Figure 2.3 (center). This is referred to as a pure curvature effect. The concave segment (relative to the exhaust) preheats the mixture relatively more by a heat transfer focusing effect, increasing the burning velocity in this segment. Thus, the lagging flame segment can catch up and smooth out in this location. In the convex segment, the opposite happens through heat de-focusing, which retards the advanced flame segment.

In the next step, different mass and heat diffusion strengths are considered, which cover the mentioned Lewis number effects. For Le>1, or when heat exceeds mass diffusion, burning in concave flame segments is enhanced, and burning in convex segments is weakened (Figure 2.3, left). This is again due to increased mixture preheating and increased reaction rates on the one hand and lacking unburned mass diffusion towards the flame on the other.
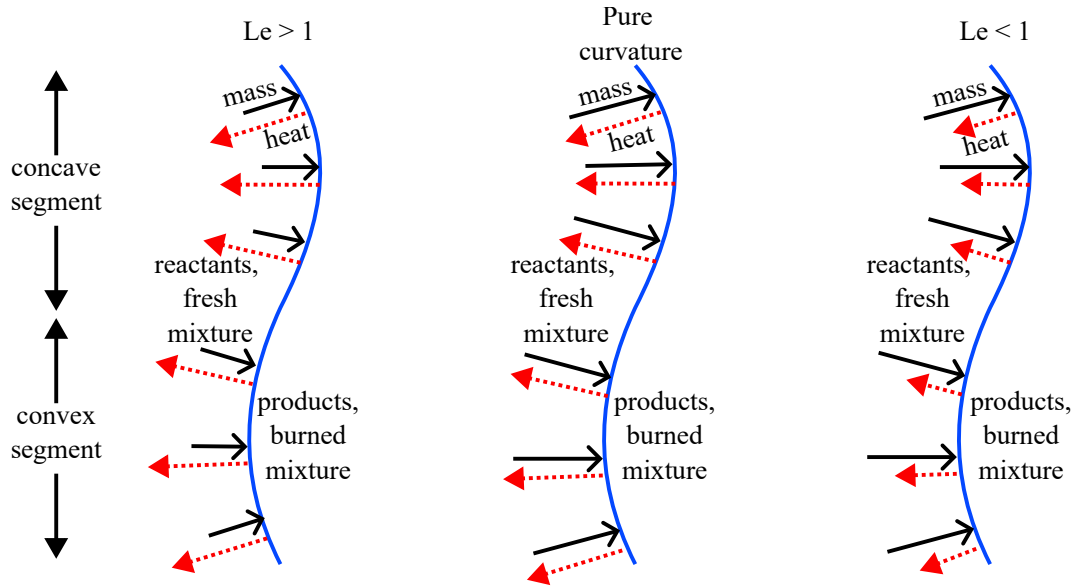
Figure 2.3.: Diffusional-thermal instabilities scheme, which describes non-equidiffusion effects (Le≠1) and pure curvature effects (Le=1). Adopted from Law [83, pg. 458] with some changes.

For Le>1, this results in an overall smoothing of wrinkled flame structures, therefore acting in a stabilizing manner [83, pg. 458]. In contrast, Le<1 weakens the burning rate in concavely curved segments and enhances the burning rate in convexly curved regions, forming even sharper negatively curved cusps (Figure 2.3, right). This results in an unstable cellular flame.

Notably, because of the curvature and Lewis number effects combination, the stability boundary is not at Le=1 but slightly lower at around Le≅0.87 [128].

Thermo-diffusive effects are most prominent at small scales comparable to the flame thickness [83]. Due to the Lewis number effects, they are especially relevant to fuels either lighter (e.g., hydrogen) or heavier (e.g., alcohols) than methane, which itself is close to Le=1 in a mixture with air. While the Lewis number and fuel relation will be covered in more detail in Section 3.5.3, the *effective Lewis number* derivation is described in the following.

Effective Lewis Number Derivation: The effective Lewis number Le_{eff} calculation procedure was obtained from Pareja et al. [108] and Burbano et al. [19], and is summarized in the following.

In the two reactant flame theory, it was demonstrated by Joulin, and Mitani [69] that the reaction rates near stoichiometric conditions are governed not only by the deficient reactant but also by the abundant component of the mixture. Therefore, the Lewis number from the single reactant theory may be exchanged for the more comprehensive effective Lewis number Le_{eff}, which is determined from a weighted average of the two different Lewis numbers of the excess reactant Le_{E} and deficient reactant Le_{D} [1]:

$$\text{Le}_{\text{eff}} = 1 + \frac{(\text{Le}_{\text{E}} - 1) + (\text{Le}_{\text{D}} - 1) \cdot MS}{1 + MS} \tag{2.33}$$

Therein, *MS* stands for mixture strength, expressed as $MS = 1 + Ze\cdot(\Phi\text{-}1)$. Φ is the excess-to-deficient reactants-mass ratio in the fresh mixture relative to their stoichiometric ratio. For fuel-rich mixtures, it is defined as equal to the equivalence ratio ϕ; for fuel-lean mixtures, it is $1/\phi$. Ze is the *Zeldovich number*, which can be calculated according to the following equation [1]:

$$\text{Ze} = E_a \frac{(T_a - T_u)}{R \cdot T_a^2} \tag{2.34}$$

Therein, T_a is the adiabatic temperature, T_u is the unburned mixture temperature, R is the ideal gas constant, and E_a is the activation energy.

The activation energy can be calculated through a methodology provided by Egolfopolous and Law [45]:

$$E_a = -2R \left\{ \frac{d\ln(\dot{w})}{d(1/T_a)} \right\}_p \tag{2.35}$$

Therein, $\dot{w}$ are the mass burning rates at different pressures p and adiabatic temperatures T_a. The varying adiabatic temperatures can be obtained by different inert gas amounts (nitrogen). For near stoichiometric conditions, E_a may be interpolated from off-stoichiometric results, as recommended by Jomaas et al. [67].

In this work, all parameters needed are obtained from unstrained laminar flame calculations, which will be introduced in the numerical 1D flame setups described in Section 3.3.

2.5.2. Hydrodynamic Instability

Hydrodynamic instabilities occur naturally due to the thin nature of a flame. Figure 2.4 displays the phenomenon.
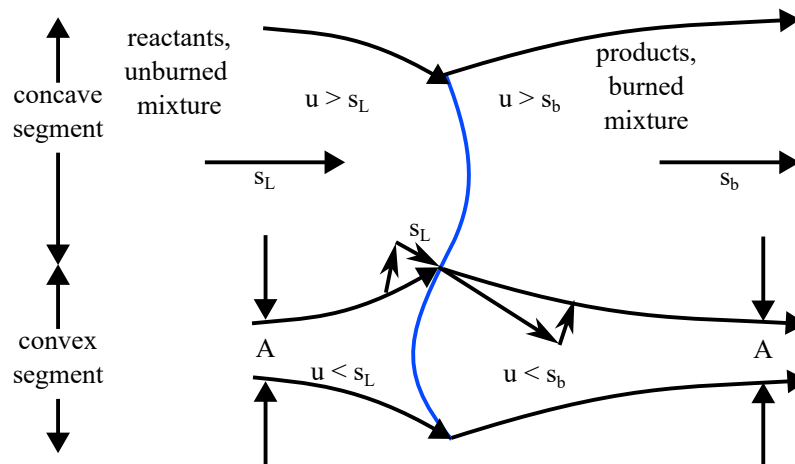
Figure 2.4.: Scheme of hydrodynamic instabilities. Adopted from Law [83, pg. 459] with some changes.

In this mechanism, on the constant density assumption up and downstream of the thin flame, the stream velocity tangential to the flame front is larger downstream than upstream due to thermal

expansion. However, the tangential component needs to be equal, as the stream cone will have the same size *A* far down and upstream. This leads to streamline divergences upstream of convex segments, which results in a slower upstream mixture velocity and facilitates that segment's progression. As the opposite phenomenon happens in the concave segment, flame stability on a local scale decreases.

In the following, hydrodynamic instability assessment parameters are given to judge whether a mixture tends to experience hydrodynamic instability. Notably, some are for laminar or planar flames. Nevertheless, since those are more easily disturbed than in turbulent conditions, it is considered a conservative judgment procedure for turbulent flames.

Markstein Length and Number: Hydrodynamic instabilities do not act on all possible cell sizes, as opposed to initial belief [106]. Markstein found that there is a critical length, nowadays referred to as *Markstein length*, below which a flame is stable and above which it will become unstable [106]. Peters [109, 110] documented that based on Clavin's [26] and Matalon's [93] findings, the Markstein length M_l could be defined as:

$$\frac{M_l}{\delta_f} = \frac{1}{\gamma} \cdot \ln \frac{1}{1-\gamma} + \frac{Ze(Le-1)(1-\gamma)}{2\gamma} \int_0^{\gamma/(1-\gamma)} \frac{ln(1+x)}{x}dx \tag{2.36}$$

Therein, δ_f is the flame thickness, $\gamma = (T_b\text{-}T_u)/T_b$ a relation between unburned and burned temperatures T_u and T_b, Ze the Zeldo'vich number from equation 2.34, and Le the Lewis number from Section 2.5.1.

According to Matalon [92], the *Markstein number* may then be calculated by dividing the *Markstein length* by a characteristic length l_0 (e.g., the jet tube diameter):

$$M = \frac{M_l}{l_0} \tag{2.37}$$

Comparing it to a *critical Markstein number* M_c enables an estimation whether a planar flame front is stable against hydrodynamic instabilities (stable: M>M_c, unstable: M<M_c) [92]. M_c is defined as:

$$M_c = \frac{1}{(2 \cdot \pi)} \cdot \frac{(\sigma - 1)}{(3\sigma - 1)} \tag{2.38}$$

Therein, σ_{rho} is the unburned-to-burned density ratio ρ_u/ρ_b.

Critical Wavelengths: Matalon [92] furthermore described a critical wavenumber λ_c:

$$\lambda_c = \frac{4\pi\sigma M_l}{\sigma - 1} \tag{2.39}$$

Matalon described that in domains where the characteristic length l_0 was smaller than λ_c, stability could be expected in planar flames.

Curvature PDF: Curvature PDFs in flames may also be used to judge whether hydrodynamic instabilities are prominent [73]. Since they promote cusp formation, the curvature PDF should be negatively skewed.

Growth Rate Study: Sivashinsky [128] documented a rate of instability parameter σ_i, which was first established by Frankel and Sivashinsky, as well as Pelce and Clavin:

$$\sigma_i = \Omega_0 \cdot s_L \cdot \kappa_{str} - \Omega_1 \cdot D_{th} \cdot k^2 \tag{2.40}$$

Therein, Ω_0 is a non-dimensional function of the parameter $\epsilon = \rho_b/\rho_u$:

$$\Omega_0 = \frac{\sqrt{\epsilon + \epsilon^2 - \epsilon^3} - \epsilon}{1 + \epsilon}, \tag{2.41}$$

s_L is the laminar burning velocity, κ_{str} the flame stretch, D_{th} the thermal diffusion, and Ω_1 the correction term for thermo-diffusive instabilities:

$$\Omega_1 = \frac{\epsilon(1-\epsilon)^2 - \epsilon \ln \epsilon (2\Omega_0 + 1 + \epsilon)}{2(1-\epsilon)[\epsilon + (1+\epsilon)\Omega_0]} - \frac{\epsilon(1+\Omega_0)(\epsilon+\Omega_0)Ze(1-Le)}{2(1-\epsilon)[\epsilon + (1+\epsilon)\Omega_0]} \int_0^{1/\epsilon-1} \frac{\ln(1+x)dx}{x} \tag{2.42}$$

Therein, Ze is again the Zeldo'vich number and Le the Lewis number.

2.5.3. Buoyancy-driven Instability

This instability acts similarly to hydrodynamic instability, but is driven by a different cause. This time, negative density gradients in a positive force field (e.g., gravity) will lead to converging and diverging streamlines, thus promoting instability.

2.6. Raman and Rayleigh Spectroscopy

Combined Raman and Rayleigh spectroscopy, or sRS, is a non-intrusive laser diagnostic method to capture the species mole fractions and the temperature in dust-free gaseous flows and reaction fields. The reasons for photon scattering are collisions and energy exchanges between the photons and probed molecules, which are described in the following.

Rayleigh scattering results from elastic collisions. Thereby, incident photons lift the molecules to a higher virtual energy state, from which photons with the same energy and frequency are emitted to re-establish equilibrium (i.e., reach the *ground state*). The amount of involved photons is a function of the number density of molecules hit.

In contrast, *Raman scattering* is an inelastic process, meaning the molecules drop to a higher (*Stokes Raman*) or lower (*Anti-Stokes Raman*) state than the initial state. Thus, the scattered photons have
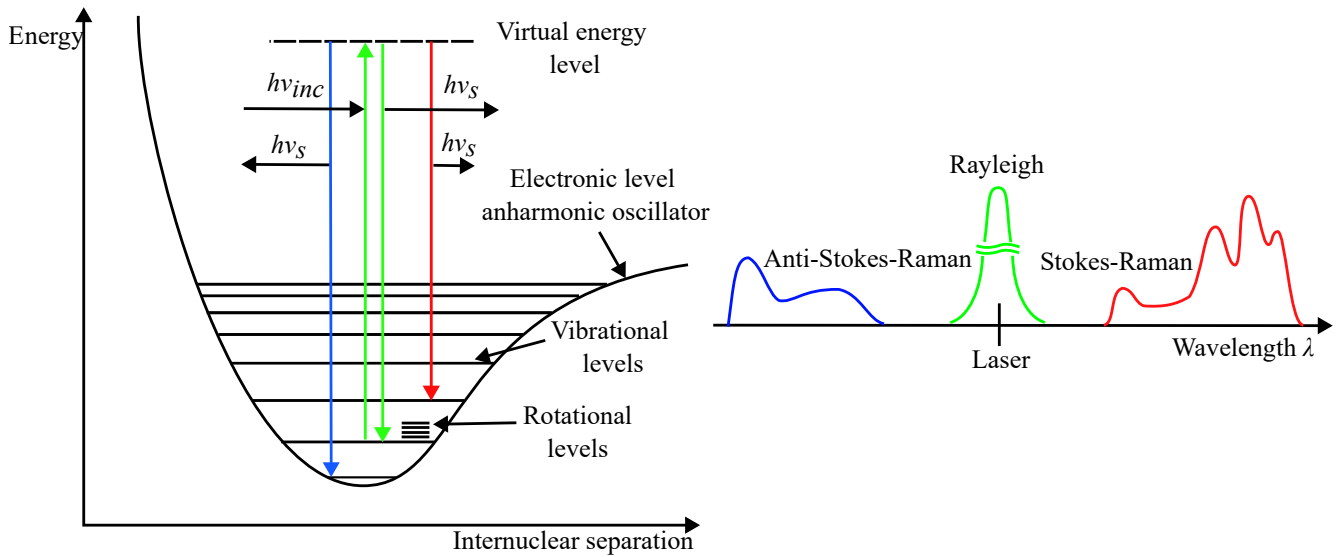
Figure 2.5.: Raman and Rayleigh processes scheme in an exemplary Morse diagram. Adopted from [44] and [132] with minor changes.

lower or higher frequencies, respectively. The processes, including energies, are displayed in the *Morse diagram* in Figure 2.5, which was adopted from Eckbreth [44] and here obtained from Stahler [132] with minor changes. Notably, this work only makes use of Stokes Raman.

The index *inc* stands for *incident* and refers to the laser light. Index *s* stands for *signal*. The black lines schematically show the electronic, vibrational or rotational energy levels (actually present on each vibrational level) that are unique for every molecule type and make up its overall energy state. The quantitative nature of all these levels enables the species determination by measuring the scattered light wavenumber shift to the excitation wavelength.

2.6.1. Mathematical Descriptions

This section is based on descriptions of the topic in several previous works [20, 52, 57, 123, 125, 132].

Rayleigh Scattering: The Rayleigh scattering intensity is calculated using the following relation:

$$S_{Ray} \propto \sigma_{Ray} \cdot I_l \cdot N \tag{2.43}$$

Therein, σ_{Ray} is the Rayleigh cross-section, I_l the laser fluence, and N the number density.

If the mixture composition and individual cross-sections are known, the Rayleigh signal intensity can be used to calculate the temperature:

$$T_{Ray} \propto 1/S_{Ray} \tag{2.44}$$

Raman Scattering: The individual species' number densities are directly proportional to the Raman signal intensity:

$$N_i \propto S_{Ram,j} \tag{2.45}$$

The intensity of each Raman transition $f \leftarrow i$ of a Raman-active species j may thereby be calculated using the following equation:

$$S_{j,f\leftarrow i} = \frac{\frac{\partial \sigma}{\partial \Omega}_{f\leftarrow i}(j,T,\nu_l)}{h\nu_{s,f\leftarrow i}} \cdot E_l \Omega l \eta(h\nu_{s,f\leftarrow i}) \cdot X_j N(T,p) \tag{2.46}$$

The first term divides each transition's differential cross-section, dependent on the species j, the temperature T, and the laser frequency ν_l, by the scattered photon energy. The second term is made up by the laser energy E_l, the detection optics opening angle Ω, the probe volume length l, and the detection efficiency η (optics and detector efficiencies), which is again dependent on the scattered photon energy. Finally, each species's number density is given in the third term. In an ideal gas, it is only temperature and pressure-dependent.

The following equation yields the differential cross-section in the first term:

$$\frac{\partial \sigma}{\partial \Omega}_{f\leftarrow i}(j,T,\nu_l) = \frac{(2\pi)^4}{45} f_i(T) \nu_{s,f\leftarrow i}^4 \Phi_{f\leftarrow i}(\bar{\bar{\alpha}}) \tag{2.47}$$

Therein, $f_i(T)$ is the temperature-dependent relative population density of the initial state i. The function $\Phi_{f\leftarrow i}$ depends on the respective molecule's polarizability.

In the diatomic molecule's case, the relative population density is calculated from the *Maxwell-Boltzmann distribution*:

$$f_i(T) = \frac{g_i exp(-\frac{E_i}{k_B T})}{\sum_i g_i exp(-\frac{E_i}{k_B T})} \tag{2.48}$$

Therein, k_B is the Boltzmann constant and g_i is the initial state degenerate energy levels factor. The latter is equivalent to the amount of quantum numbers with the same energy, which depends on molecular symmetry.

2.6.2. Raman Spectral Library

Within this work, the RAMSES spectral simulator established by Geyer [57] is used to calculate energy levels and respective Raman shifts. The method is capable of simulating di- or triatomic molecules that take part in methane/air combustion, namely nitrogen (nitrogen (N_2)), oxygen (O_2), carbon dioxide (carbon dioxide (CO_2)), hydrogen (hydrogen gas, here 'hydrogen' (H_2)), water (water (H_2O)), and carbon monoxide (CO). The following ro-vibronic transitions with the vibrational quantum number ν and the rotational quantum number J are simulated within this work:

- CO_2: $\Delta\nu_1{=}1$, $\Delta\nu_2{=}2$, $\Delta J{=}0$, ±1, ±2

- O_2: $\Delta\nu{=}1$, $\Delta J{=}0$, ±1, ±2

- CO: $\Delta\nu{=}1$, $\Delta J{=}0$, ±2

- H_2: $\Delta\nu{=}1$, $\Delta J{=}0$, ±2 and $\Delta\nu{=}0$, $\Delta J{=}2$

- H_2O: $\Delta\nu_1{=}1$, $\Delta\nu_3{=}1$

Notably, the simulated shifts are quantified and thus infinitesimally thin. These *stick spectra* are convoluted with the spectrometer optic's *transfer function*, resulting in a broader imaging of the transitions that resemble a *Voigt* distribution (combination of *Cauchy-Lorentzian* and *Gaussian* distribution). This distribution will be determined during calibration to prepare the RAMSES results for the hybrid MI (Section 2.6.3).

For larger molecules, such as methane (CH_4) and ethanol (C_2H_5OH), the Raman shifts cannot be calculated due to their complexity and instead need to be experimentally determined. Alternatively, their *response function*, which is a temperature-dependent polynomial describing their scattering effect, may be tuned. This is covered in more detail in Section 6.2.4.

2.6.3. Data Reduction

Three main strategies exist to evaluate data from the most prominent sRS systems: Polynomial MI, hybrid MI, and *Spectral fitting*. While this work employs the hybrid MI, the polynomial MI is introduced first, as it is the base of the more advanced hybrid MI. Both MI procedures, including a broad discussion on uncertainties, are well-described by Fuest [53] and are only summarized here. The spectral fitting approach was described by Geyer [57], but was not a part of this work.

Polynomial Matrix Inversion

In the polynomial MI, the Raman spectra are quantized into an array of species-individual values, the Raman channels, by integrating spectral regions of the CCD sensor chip (*hardware binning*). Binning is mainly done to minimize the read-out noise and to increase the CCD imaging frequency. The relation between the resulting signal array S_i and the quantity of interest, the number density N_i, can then be expressed as the following matrix equation:

$$S_i = C(T) \cdot N_i \tag{2.49}$$

Therein, C is a matrix with temperature-dependent calibration factors c_{ii} and c_{ij}. The diagonal elements c_{ii} regard the individual species dependence and the off-diagonal elements c_{ij} describe

how one species may affect another (*crosstalk*). When attempting to find the number density in a target flame, the above equation is inverted:

$$
\begin{bmatrix} N_{CO_2} \\ N_{O_2} \\ N_{CO} \\ N_{N_2} \\ N_{HCs} \\ N_{H_2O} \\ N_{H_2} \\ \widetilde{N}_{C_2} \\ \widetilde{N}_{BG3} \end{bmatrix} = \begin{bmatrix} c_{1,1} & c_{1,2} & & & c_{1,5} & c_{1,6} & c_{1,7} & & c_{1,9} & c_{1,10} \\ c_{2,1} & c_{2,2} & & & c_{2,5} & c_{2,6} & c_{2,7} & & c_{2,9} & c_{2,10} \\ & & c_{3,3} & c_{3,4} & c_{3,5} & & c_{3,7} & & c_{3,9} & c_{3,10} \\ & & c_{4,3} & c_{4,4} & c_{4,5} & & & & c_{4,9} & c_{4,10} \\ & & & & c_{5,5} & c_{5,6} & & & c_{5,9} & c_{5,10} \\ & & & & & c_{6,6} & c_{6,7} & & c_{6,9} & c_{6,10} \\ & & & & & c_{7,6} & c_{7,7} & & c_{7,9} & c_{7,10} \\ & & & & c_{9,5} & & c_{9,7} & & c_{9,9} & c_{9,10} \\ & & & & & & & & & c_{10,10} \end{bmatrix}^{-1} \cdot \begin{bmatrix} S_{CO_2} \\ S_{O_2} \\ S_{CO} \\ S_{N_2} \\ S_{HCs} \\ S_{H_2O} \\ S_{H_2} \\ S_{C2} \\ S_{BG3} \end{bmatrix}
$$

$$(2.50)$$

Because some species do not have *crosstalks* (spectrally overlapping signal), the *C* matrix is sparse. Furthermore, signal channels are also used for non-Raman signals, like the background from C_2 LIF interference and background stray light (BG3).

Notably, in the polynomial MI, the c_{ij} elements have a polynomial shape. The elements' strengths are calibrated based on additional measurements, in which *Raman calibration factors m_{ij}* are tuned:

$$ c_{ij}(T) = m_{ij} \circ c_{ij}^{base}(T) \tag{2.51} $$

These calibration measurements are done in the following environments:

- O_2 and N_2: Ambient air

- CO_2, CO, H_2O, H_2, and their crosstalks: Laminar flames with varying equivalence ratios

- Fuel molecule: Mixture with N_2 or argon (Ar), depending on the fuel molecule used

- Interference from C_2: Rich laminar jet flames

As indicated, the *c* elements in the above equation are temperature-dependent. Although temperatures might also be calculated effectively from the ideal gas law, smaller uncertainty can be reached when deriving it from the Rayleigh signal. However, the effective Rayleigh cross-section σ_{Ray} required to calculate the temperature is a linear combination of the species' individual cross-sections in the probe volume:

$$ \sigma_{Ray} = \sum_i \sigma_{Ray,j} \cdot N_j \tag{2.52} $$

Because the species number densities N_j are also unknown initially, a reference signal $S_{Ray,ref}$ first needs to be acquired in a known mixture. Typically, particle-filtered air is used, of which

the temperature is measured with a thermocouple reference. Subsequently, the initial Rayleigh temperature can be calculated through:

$$T_{Ray} = T_{Ray,ref} \cdot \frac{S_{Ray,ref} \cdot \sigma_{Ray}}{\sigma_{Ray,ref} \cdot S_{Ray}} \tag{2.53}$$

Afterwards, the temperature and species number densities can be solved iteratively. About ten iterations are sufficient to obtain temperature differences of less than 1 K.

The polynomial MI suffers from the following three problematic aspects:

- When Raman scattering is captured from a 1D probe volume, the *bowing* effect appears [149]. Thereby, the Raman lines near the optical axis bow towards the spectrum's red side. However, since the hardware binning is fixed on a linear grid, it is indifferent to this shift. As a result, systematic errors in crosstalks are made in neighboring species channels, for example, oxygen and carbon dioxide.

- The exciting laser inherently has pointing uncertainty, which leads to spectral shifts. This will also shift the spectra relative to the fixed hardware binning channels, yielding another systematic error.

- When the laser passes large density gradients that inherently exist in flames, it is steered in the direction with a greater density. The result is another shift in spectral direction, leading to additional systematic errors.

While these effects could theoretically be accounted for in the polynomial MI by varying the laser position during the calibration, that is unfeasible from an operational standpoint. Therefore, the hybrid MI was developed by Fuest et al. [52], described in the following.

Hybrid Matrix Inversion

In the hybrid MI, rather than calibrating the c elements experimentally, the calibration sources are simulated spectra from the Raman spectral library RAMSES (Section 2.6.2).

First, the library is generated at temperatures ranging from 290 to 2500 K. Next, the resulting stick spectra are convoluted with the spectrometer apparatus function, which is typically obtained for each axial spacing from frequently taken Rayleigh images in dry air. The channel boundaries are then shifted relative to the calculated spectra to compensate for the polynomial MI drawbacks listed in the previous section.

Binning within the spectral channels is done similarly to the polynomial MI. The results are tabulated and normalized to zero shift and 290 K, yielding the temperature and location dependent *response functions* and crosstalks.

The Raman calibration factors m_{ij} are tuned in well-known pure gas and flame conditions. During the iterative procedure, it is being interpolated between the tabulated results that are in 20 K-steps and one-pixel spacing, respectively. During the evaluation, the necessary pixel shift is determined via the laser position on the Rayleigh scattering image.

2.6.4. Raw Data Preparation

Before entering the hybrid MI, the following steps are applied to the Raman data.

Dark Frame Correction: In order to rectify images for the camera's dark current noise and to reduce non-signal light from the ambient, a series of 100 background images are recorded approximately every hour during the measurement program, but with the flame and laser turned off. The *non-signal* is captured on each channel individually and the mean can be subtracted from the regular images taken over the next hour.

Energy Reference: In order to deal with laser shot energy variation, every laser shot's energy is captured with an energy measurement head. The result is then normalized, and each image's intensity is multiplied by the respective energy's reciprocal.

Background Noise Correction: Throughout the day, readout noise within the camera will vary due to CCD sensor temperature variations. Therefore, non-signal is captured during the frequently taken air images to counter this systematic bias. Assuming that the background noise is equal across the entire sensor, the methane channel noise amount is subtracted from all channels while considering their respective sizes. The methane channel is suitable, as there is no crosstalk on it during air images and due to its relatively large size.

A further noise source corrected with air images is the laser stray light, which may reach the camera without passing the primary signal path within the spectrometer. The dedicated background channel BG3 captures this noise in every image taken. As the noise will vary with laser intensity, air images with reduced laser energy are captured at the beginning of the day. A linearly interpolated factor between the signal in the background channel during air images at reduced laser energy and the signal at full laser power is then used to determine the expected background noise amount on other channels. Again, the channel sizes are considered in the process.

Flat Field Correction: All images taken undergo a *flat-field correction*, which is required because there is increasing vignetting towards the spectrometer optics' outer radii. Additionally, the laser is decreasingly focused at the probe volume edges.

The correction is done through images captured during the calibration, in which objects that should have a uniform signal throughout the respective channel's spatial dimension are imaged. The media used for the respective channels are listed in the following:

- Nitrogen and oxygen: Ambient air
- Water and carbon monoxide: Rich methane flame
- Hydrogen: Pure Hydrogen
- Carbon dioxide: Carbon dioxide and nitrogen mixture

Because of their proximity and the lack of a better option, the carbon dioxide channel correction is also used for the C_2 channel, and the hydrogen channel is used for the background channel (BG3) channel.

Dust Correction: Due to the necessary large exhaust gas duct, dust acquisition into the lab space and the probe volume is an inherent problem. As a result, there will be *Mie scattering* on the particles on the same wavelength as the Rayleigh scattering. Fortunately, because of its strength, it can generally be easily identified visually in those images. In order to deal with them on an automated basis, a gradient-based filter operation is applied in this work that was introduced by Butz [20].

Raman images do not capture this Mie scattering due to that wavelength not trespassing the grating. However, the Raman image is rendered completely unusable in a plasma generation incident due to excessive fluence on a dust particle. Furthermore, the CCD chip may also be over-exposed for the following laser shots because of the immense intensity. Therefore, the plasma event image, detected by the laser energy being outside three sigmas of the mean, and ten shots after it are excluded from the data reduction in this work.

Cosmic Ray Correction: Cosmic rays may affect the sensitive CCD sensor at random frequencies and positions. However, this phenomenon is limited to one pixel and leads to its saturation, which can also be easily identified. Therefore, images with saturated pixels are excluded from the data reduction.

2.7. Other Measurement Techniques

Next, two more laser diagnostic measurement techniques applied in Chapter 5 are introduced. These are OH-LIF to capture flame front topologies on the one hand and CH* CL to measure flame lengths on the other.

2.7.1. Laser-induced Fluorescence (LIF)

LIF is a resonant process during which the laser is finely tuned to excite a specific absorption transition. Subsequently, the molecule is in an excited state, from which it falls back to its ground state after a short residence time (ca. 1 to 10 ns). An exemplary Morse diagram, adopted from Eckbreth [44] and Butz [20] with minor changes, is given in Figure 2.6.

The signal intensity is proportional to the number density:

$$S_{OH-PLIF} \propto N_{OH} \tag{2.54}$$

From an experimental standpoint, LIF is a non-intrusive laser diagnostic method to capture radicals' or minor species' quantities, such as the OH, NO, or CO. As discussed in Section 2.1.1, OH is
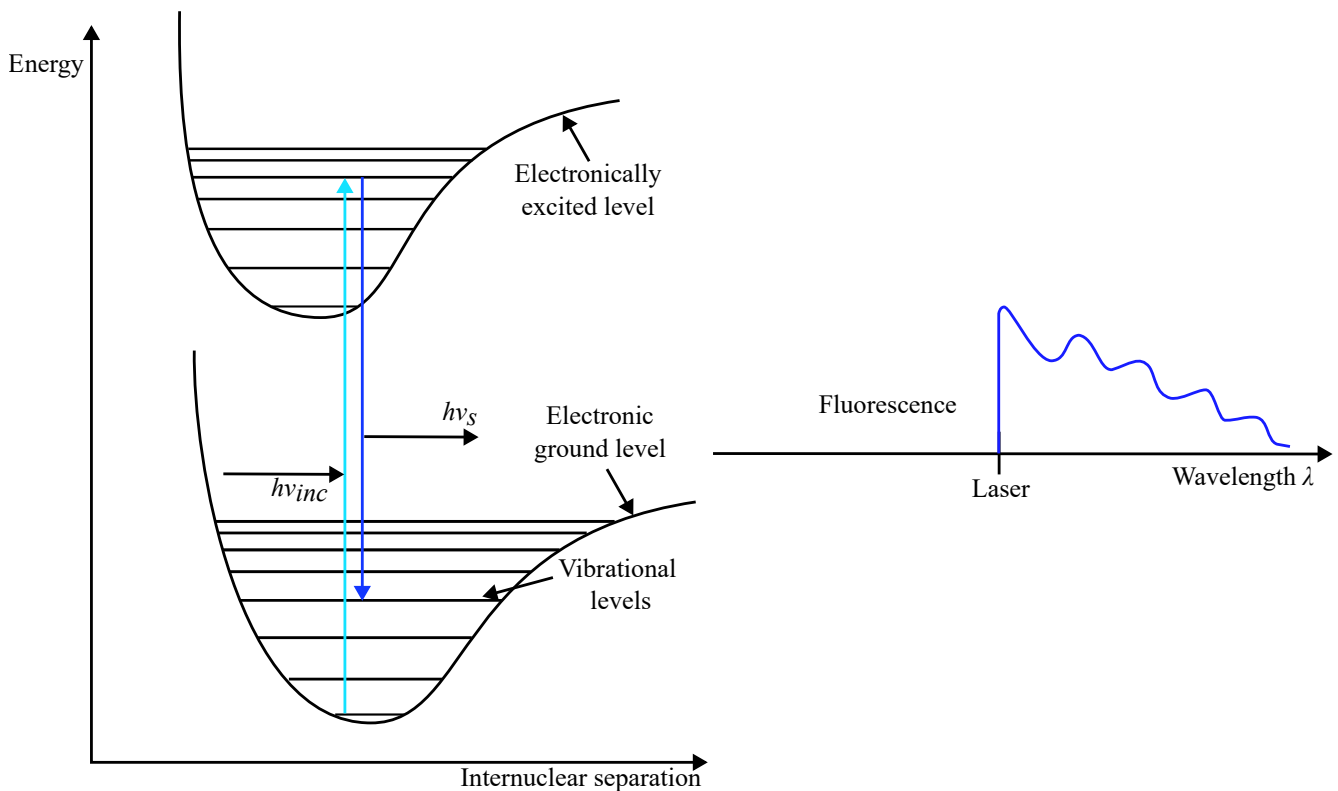
Figure 2.6.: LIF process scheme in an exemplary Morse diagram. Adopted from [44] and [20] with minor changes.

formed immediately within the hydrocarbon flame front and persists in the post flame region [83, pg. 95ff]. Due to its high production rate and intense fluorescence signal, it is commonly used as a reaction zone marker [120].

Within this work, the flame front is captured by evaluating the strongest OH gradient in a 2D sheet. After edge detection, the data can be evaluated statistically using parameters like curvature or flame surface density (Chapter 5).

Notably, other species' *photon quenching processes* compete with the actual LIF signal. However, for this qualitative study, no further measures are deemed necessary to correct these influences.

2.7.2. Chemiluminescence

CL describes the light spectrum emitted by chemically excited radicals [35]. The main radicals that produce substantial CL for hydrocarbon flames are CH*, hydroxyl radical (OH*), and C_2*. With these species, it is possible to estimate where the flame front is located.

Within this work, this method is used to measure the flame length. An advantage of this technique are the few necessary measurement equipment items, for example when capturing the strong CH* $A^2\Delta \rightarrow X^2\Pi$ Q(0-0) transition as done in this work. They are limited to a CMOS camera with a regular photography lens, as well as an interference filter at 434±17 nm.

3. Numerical Simulations

3.1. Introduction

Numerical calculations offer crucial insights into parameters that are difficult or infeasible to capture experimentally. Therefore, they are an important assisting factor in the flame data analysis in Chapters 4, 5, and 6.

This chapter first briefly introduces Cantera, the calculation platform used to compute reactors and 1D flames. It then covers the numerical flame setups and obtained parameters, which include fluid density, viscosity, laminar burning velocity, extinction strain rate, and Lewis number. The computational data is subsequently used to derive synthetic Raman and Rayleigh signals as numerical equivalents to experimental signals. Finally, the study examines the occurrences of intermediate species in ethanol/air and OME-3/air flames.

Parts of this chapter are published in Trabold et al. [141, 142].

3.2. Cantera

Cantera is a software that handles chemical kinetics, thermodynamics, and transport processes [58]. It offers classes of objects for steady 1D reacting flows, including phases, interfaces, reaction managers, and reactor networks. Chapter 2 introduced the essential equations for these objects, which can be solved by Cantera in C++, Python, Fortran, or Matlab (used in this work).

Reactors and Reacting Flows   Cantera has two major model suites for reactors and flames, both utilized in this work

- *Reactors* are zero-dimensional (0D) models that calculate a mixture's *steady state*. After reactions are initiated at given initial and boundary conditions, the calculations are run at constant pressure or volume, before finally reaching equilibrium.

- Cantera also models steady state, quasi-1D *reacting flows* to numerically calculate common flames [58].

This work adapts open-source code examples of a freely propagating laminar premixed flame and a strained laminar premixed counterflow flame to suit respective needs. The latter is also modified to calculate twin flames, in which identical mixtures enter from both counterflow configuration ends.

Mechanism Choices   Dependent on the fuel type, different mechanisms may be chosen to calculate the problem efficiently and accurately. The different mechanisms chosen for the respective fuels are given in Table 3.1. All kinetic mechanisms used in this work present the current state of research.

Table 3.1.: Source for the respective fuels' mechanisms for numerical calculations.

Fuel	Mechanism	Source
Methane	GRI30	[129]
Methanol	Li	[86]
Ethanol	ELTE	[105]
2-Propanol	POLIMI/CRECK	[51]
2-Butanol	POLIMI/CRECK	[51]
OME-3	Sun	[135]

Diffusion Treatment   The diffusion treatment within a calculation may occur with different levels of detail. Molecular diffusion is calculated either *multi-component,* i.e., individually between all species pairs, or *mixture-averaged,* as an overall mixture average value. Due to the relatively large fuel molecules and the respective intermediates, thermo-diffusive effects are expected. To capture as much detail as possible in this regard, all numerical calculations in this work were finally calculated using the multi-component diffusion approach.

3.3. Numerical 1D Setups

3.3.1. Unstretched Flames

In freely propagating flame calculations, a fuel and oxidizer mixture enters a 1D domain from one side. Since the inflow velocity is set to the flame propagation speed, the flame is kept at a constant position in the computational domain. The burnt mixture exits the domain on the opposite end, where a zero-gradient boundary condition is applied.

This setup provides a means to obtain the unburned mixture kinematic viscosity ν, the unburned mixture density ρ, and the laminar burning velocity s_L. Furthermore, the laminar flame thickness can be calculated using equation 2.9, and the effective Lewis-number Le_{eff} can be derived following the approach introduced in Section 2.5.1.

To assist the experiment in Chapter 5, unstretched methanol, ethanol, propanol, butanol, and methane flames are calculated at atmospheric pressure and premixed with air at equivalence ratios from $\phi=0.8$ to 1.5. For the liquid fuels, the initial mixture temperatures are set to 343 K to match the experiment. Methane/air flames are additionally calculated at the initial temperature 293 K to investigate the influence by pre-heating.

The obtained mixture parameters from the unstretched flame calculations, which are used for the experiment discussion later on, are summarized in Table 3.2 in Section 3.5.4. The resulting

laminar burning velocities and effective Lewis numbers are discussed in Section 3.5.1, and 3.5.3, respectively.

3.3.2. Strained Counterflow Flames

The strained flame calculations, unlike the unstretched premixed flame calculation, is achieved by opposing the fuel/air stream with an air stream. The strained counterflow flame setup is essential for the qualitative Raman study in Chapter 4, as the parameters obtained from the numerical calculations are directly projected onto the experimental results. The investigated mixtures include methane/air, ethanol/air, and OME-3/air, each at various equivalence ratios from lean to partially-premixed.

Additionally, the calculations are utilized to estimate the strain-induced extinction point. This is accomplished by gradually increasing the counterflow flame strain rate until a rapid decline in temperature occurs. Results for varying premixed methanol, ethanol, and methane flame extinction strain rates for three equivalence ratios are discussed in Section 3.5.2. These results support the interpretation of experimentally observed fuel-dependent blow-off limits in Section 5.4.1.

Lastly, this setup is employed to calculate flamelets of opposed jet flames in Section 6.7, where the mixture of fuel and air is opposed either by an air flow or the conditions of flame exhaust gases.

3.3.3. Strained Twin Flames

The twin flame setup consists of two identical mixtures in an opposed flow configuration. This calculation type is used in Section 6.5.4, where the opposed jet flame center is probed to calibrate the sRS system for ethanol flames.

For both the strained counterflow and the strained twin flames, the strain rate has to be fitted onto the one from the experimental data by varying the hot gas region width. The procedure is detailed in the next section.

3.4. Symbioses of Simulation and Experiment

In Chapter 4, highly-resolved complex fuel flame Raman spectra are presented. To estimate the local gas temperatures, a concurrent numerical calculation is used. The necessary steps and the uncertainty thereof are described in the following.

3.4.1. Fitting Strain Rate and Flame Location

The strain rate introduced in Section 2.4.1 is an important parameter for the strained counterflow and twin flame configurations. As initial experiments and concurrent numerical calculations reveal, it is rather sensitive to the respective inflow velocities into the combustion domain on the one hand,

and the combusting mixture volume expansion on the other. The sensitivity becomes evident when even though the same inflow conditions are set, significant deviation in the hot gas region width occur. In order to identify the actual strain rate in the experiment, the calculated flame's width needs to be tuned towards the experimental's by bulk velocity adjustments.

Additionally to the strain rate difference, the flame is usually not at the same axial position. The spatial offset to be corrected for can thereby be found in the distance between the maximum temperature gradients in the experiment's and the numerical calculation's primary reaction zone. When the temperature is unavailable from the experimental side, an alternative can be followed instead, by matching synthetic Raman and Rayleigh signals created from the numerical calculation (described in the following sections).

To test the presented fitting approach, methane/air against air counterflow flame data sets were analyzed at different equivalence ratios. Figure 3.1 shows the good spatial agreement between experimental and synthetic 1D Rayleigh signals for the flames with an $\alpha = 300\,\mathrm{s}^{-1}$ bulk strain rate and $\phi = 0.9$, 1.5, and 3.5 equivalence ratios. This fitting procedure will be utilized in Section 4.4.1, where results for ethanol/air and OME-3/air are shown.

3.4.2. Synthetic Rayleigh Signal

Generally, individual synthetic Rayleigh signals $S_{Ray,synth}$ are calculated along the burner axis using the following equation:

$$S_{Ray,synth} = \frac{\sum_i X_{i,calc}\sigma_{Ray,i}}{T} \tag{3.1}$$

Whereas the local molar fractions X_i ($X_i > 0.1\,\mathrm{mol\,\%}$) and mixture temperatures T are obtained through numerical calculations, all species Rayleigh cross-sections $\sigma_{Ray,i}$ relevant to this work except for OME-3 could be obtained from Fuest [53]. In the case of OME-3, the cross-section is obtained experimentally by dilution with nitrogen. Under the assumption that the calibrated flow controllers define the uncertainty in mixture composition (error approximately 2 %), this results in a $\sigma_{Ray,OME-3} = 50.9 \pm 7$ Rayleigh cross-section relative to nitrogen.

3.4.3. Synthetic Raman Signal

In order to also assign Cantera temperatures to Raman spectra, the captured lower and higher-dispersed Raman images need to be shifted in the axial direction relative to the Rayleigh images (which are already aligned with the Cantera results). This is done by using the strong temperature gradient in the primary reaction zone. While the Rayleigh signal gradient can be obtained through integration perpendicular to the laser sheet and normalization, the Raman signal gradient originates from the spectrally integrated and normalized C-H-stretch region ($\nu = 2670\,\mathrm{cm}^{-1}$ to $3085\,\mathrm{cm}^{-1}$).

In order to verify that this shift is due to actual misalignment and not of natural causes, the situation is again assessed using the numerical calculations. Therefore, a synthetic Raman signal approximation is calculated by multiplying the fuel molecule concentration with its normalized
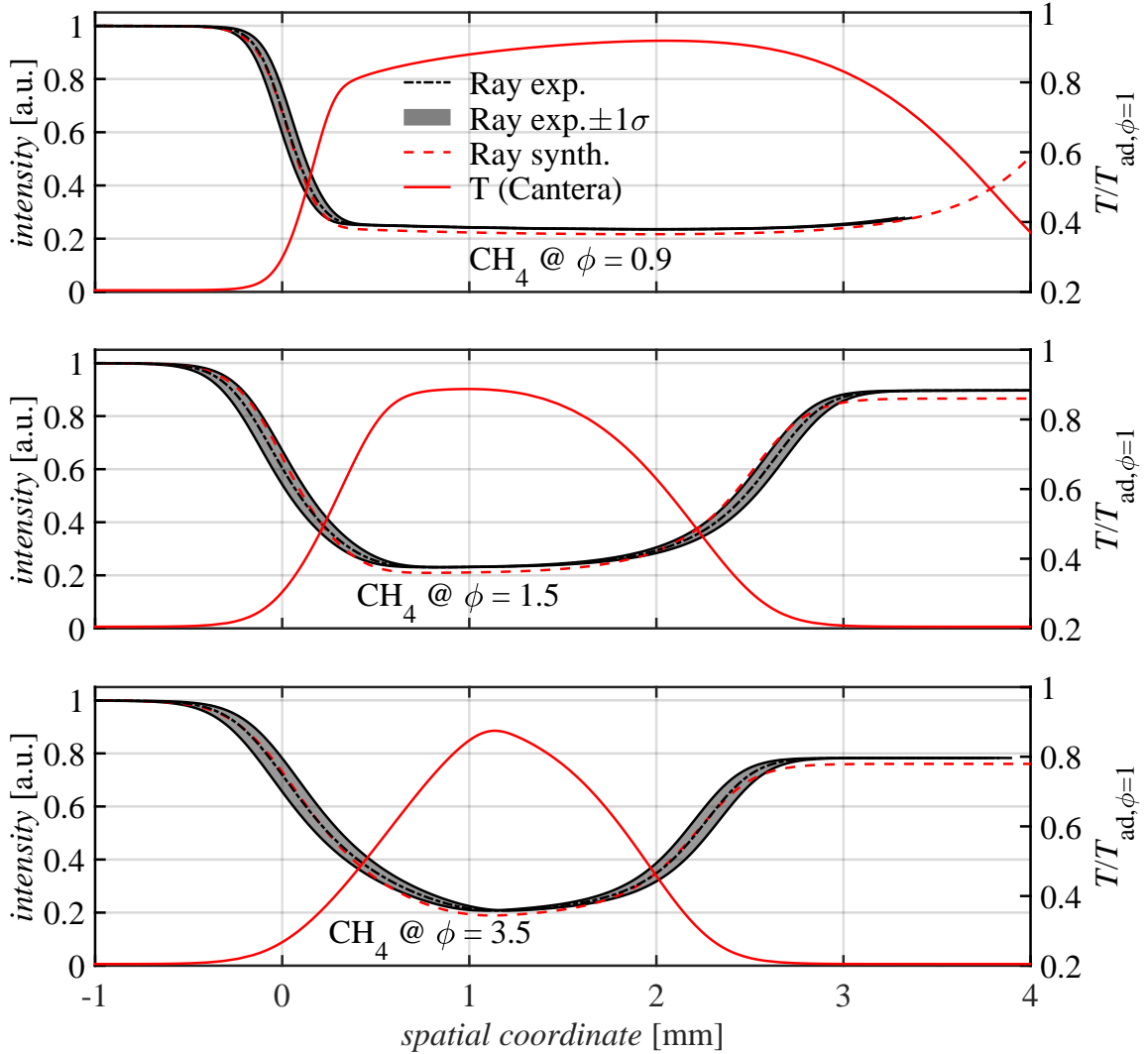
Figure 3.1.: Normalized 1D Rayleigh profiles along the spatial coordinate for methane/air flames at an $\alpha=300\,\mathrm{s}^{-1}$ bulk strain rate. While the premixed mixtures originate from the left, air enters from the right nozzles. The maximum experimental Rayleigh signal gradient on the fuel/air side serves as an anker for the spatial coordinate's origin. Grey shaded is the $\pm1\sigma$ flame motion range, highlighting the low reaction zone fluctuations. The calculated temperature traces T (red) are given on the right ordinate. They are normalized by the mixtures' adiabatic temperatures at stoichiometry $T_{\mathrm{ad,phi=1}}$. Adopted from Trabold et al. [142] with minor changes.

temperature-dependent response function. This synthetic Raman signal's highest gradient location can then be compared with the highest gradient's location of the numerically calculated inverse temperature (synthetic Rayleigh signal). As a result, using opposed methane/air against air flames for verification, the numerically calculated gradients align well for all three equivalence ratios (ϕ=0.9, 1.5 and 3.5). This validates the matching of experimental Raman and Rayleigh through their respective signal gradients.

It has to be mentioned that because the temperature-dependent Raman scattering response functions of ethanol and OME-3 flame intermediate species are currently not available over the whole flame temperature range. Therefore, the temperature-dependency was disregarded for them. Still, satisfying results with similar quality as methane/air were reached. With all mentioned steps, the described shifting procedure finally allows to align calculated temperatures and other numerically calculated parameters to the Raman spectra displayed in Section 4.4.3.

3.4.4. Temperature Assignment Uncertainty

Figure 3.1 shows that the synthetic and experimental Rayleigh data fitting happens within very tight margins. The other factor that defines the temperature assignment uncertainty is the axial fitting accuracy between Raman and Rayleigh signals. This matching's quality was estimated by again studying the synthetic Rayleigh and synthetic Raman signals for methane/air against air flames at lean, rich, and partially-premixed conditions.

This was done by taking the largest spatial fluctuation, which was given in the methane/air against air flame at partially-premixed conditions (Section 3.1), and projecting the temperature trace with an equivalent axial shift. A conservative $\pm 100\,\mathrm{K}$ maximum temperature difference could found. This uncertainty was deemed sufficiently low to claim that the numerical calculation can add valuable information to the Raman spectra results in Chapter 4.

3.5. Results and Discussion

The numerical calculation results for laminar burning velocities, extinction strain rates, and effective Lewis numbers are given and discussed in the following. Furthermore, a Table in Section 3.5.4 summarizes the different mixtures' adiabatic temperatures T_{ad}, unburned mixture densities ρ, kinematic viscosities ν and laminar flame thicknesses δ_f.

3.5.1. Laminar Burning Velocities

Calculated laminar burning velocities s_L for the different fuels are presented in Figure 3.2.

As shown by Veloo et al. [145], the laminar burning velocity is a function of the molecular structure and varies with the combusted fuel and intermediate species. The intermediate species play a major role, with some intensifying chain branching (hydrogen or formaldehyde) and others promoting chain termination (methyl). When it comes to the production of intermediate species, methanol and methane/air flames represent two opposite extremes. In contrast, ethanol/air, 2-propanol/air, and 2-butanol/air flames have more balanced intermediates, with their laminar burning velocities generally falling between those of methane/air and methanol/air flames [145].

Another observation is that the alcohol/air flames' laminar burning velocities peak around equivalence ratios $\phi \approx 1.1$ to 1.15. Methane/air, on the other hand, sees its maximum at $\phi \approx 1.05$. This
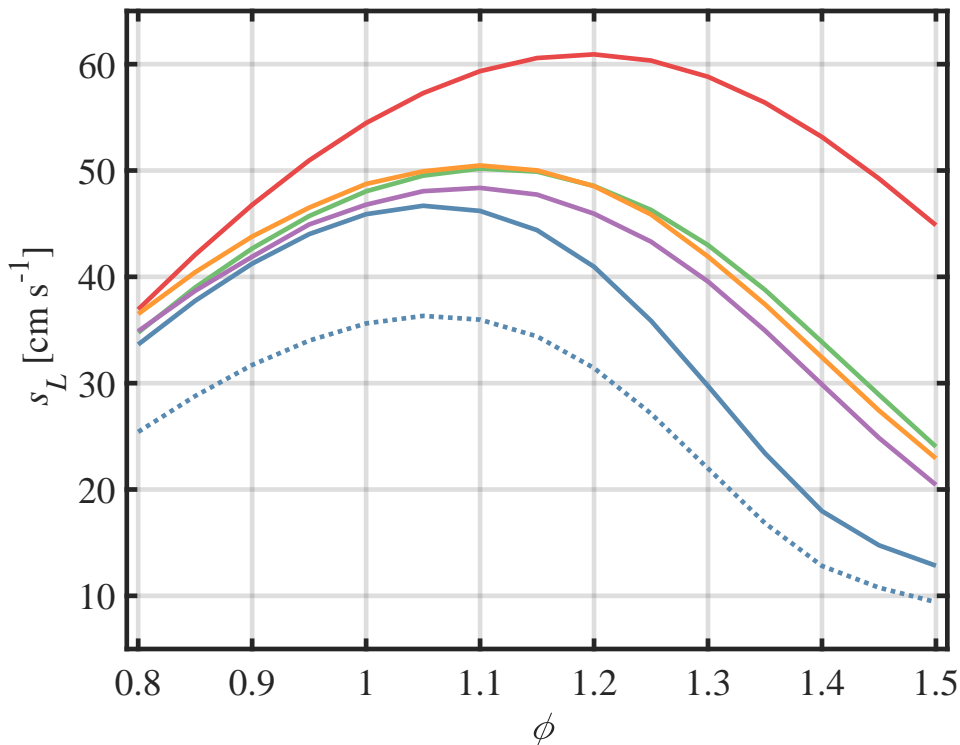
Figure 3.2.: Laminar burning velocity numerical calculation results for various flames and equivalence ratios. Framed are the conditions in which the flame surface density is studied. ■ Methane/air; (- - T_u=293 K, —— T_u=343 K); ■ Methanol/air; ■ Ethanol/air; ■ 2-Propanol/air; ■ 2-Butanol/air. Adopted from Trabold et al. [141] with minor changes.

observation was also made by Veloo et al. [145] and can be explained by different sensitivities with regard to chain branching reactions.

3.5.2. Extinction Strain Rates

Using premixed flames opposed by air streams, a numerical extinction strain rate study is performed. Thereby, the strain rate is incrementally increased and when the temperature suddenly drops significantly, the extinction by strain is postulated. Figure 3.3 shows these extinction strain rate values, which are equivalent to curves' right ends' abscissa values. The data source for the graphs were provided by Dr.-Ing. Sandra Hartl for Trabold et al. [141].

The study incorporated methane (blue), methanol (red), and ethanol (green) under lean, slightly rich and partially-premixed equivalence ratios (dotted, dashed and solid lines, respectively). Rich and partially-premixed mixtures have a higher strain rate resistance, although temperatures are consistently smaller. One explanation is the secondary reaction zone that develops from the primary reaction zone's residual hydrocarbons. Theis zone provides additional heat to the first zone and thereby stabilize the reaction (Section 2.1.2).
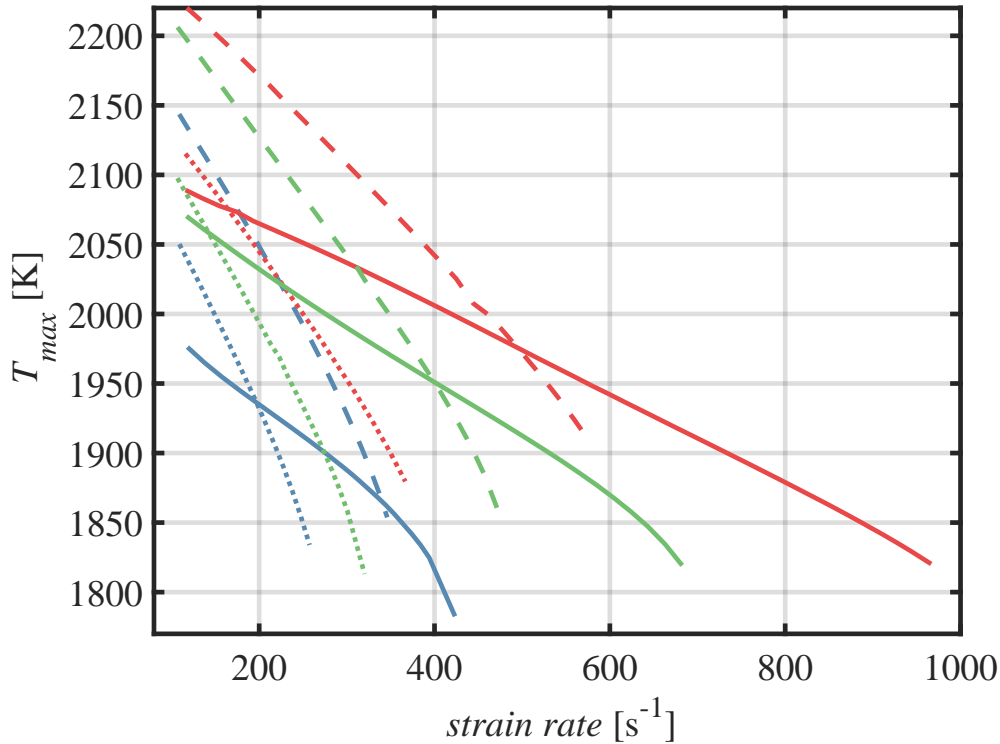
Figure 3.3.: 1D laminar opposed jet flames of premixed fuel/air streams against air were numerically calculated to investigate the maximum flame temperature T_{max}. The strain rate was varied, while the $T_u = 343$ K premixed mixture temperature was kept constant. The extinction strain rates, determined from a sudden temperature drop, are equivalent to the curves' right ends' abscissa values. ■ Methane/air; ■ Methanol/air; ■ Ethanol/air. Dotted lines: $\phi = 0.9$, Dashed lines: $\phi = 1.05$, Solid lines: $\phi = 1.5$. Graphic adapted from Trabold et al. [141] with minor changes.

The results will also be used as arguments in the flame blow-off resistance discussion in Section 5.4.1. There, the secondary reaction zone is formed between the rich jet mixture and the lean pilot flame's products surrounding the jet.

3.5.3. Effective Lewis numbers

The effective Lewis number is calculated according to the procedure described in Section 2.5.1. Figure 3.4 presents effective Lewis numbers for the four alcohol/air and methane/air mixtures that will be relevant to the flames discussed in Chapter 5 and Chapter 6.

Methane/air mixtures have marginally lower Lewis numbers at lean and larger than unity ones at rich conditions. As discussed in Section 2.5.1, the small deviation between thermal and mass diffusion in premixed methane/air flames does not significantly contribute to flame wrinkling by thermo-diffusive effects.

In contrast, the larger alcohol molecules mixed with air have effective Lewis numbers greater than unity at lean and stoichiometric equivalence ratios. The magnitude also positively correlates with the fuels' molecular masses, with the 2-butanol/air having the largest values. Because the values
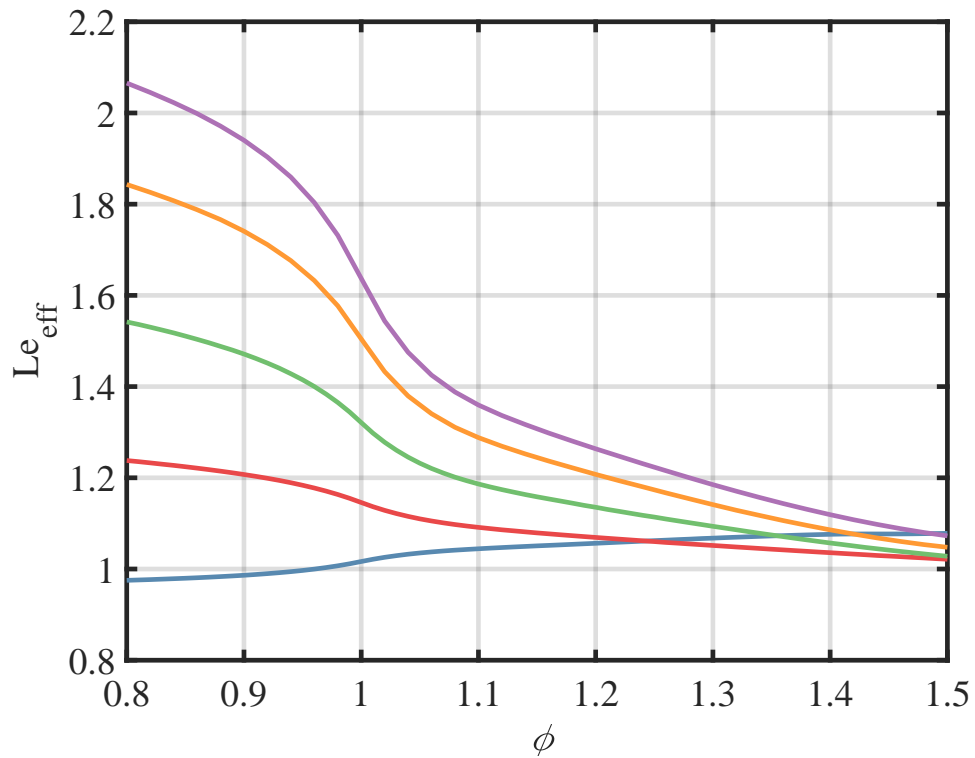
Figure 3.4.: The different fuels' effective Lewis numbers calculated from numerical 1D laminar flame calculations in the equivalence ratio space. ■ Methane/air; ■ Methanol/air; ■ Ethanol/air; ■ 2-Propanol/air; ■ 2-Butanol/air. Adopted from Trabold et al. [141] with minor changes.

are larger than unity, a frame wrinkling dampening is expected (Section 2.5.1). Notably, this flame front stabilizing effect diminishes as the mixtures become more rich.

3.5.4. Further Parameters

For later reference, additional parameters derived from the numerical calculations are given in Table 3.2.

Table 3.2.: Numerical 1D unstretched premixed laminar flame calculations served as a source for more parameters, which are listed together with the laminar burning velocities s_L in the following table. While all mixtures are calculated at a 343 K premixed mixture temperature, methane/air is also shown at 293 K (in brackets). Obtained from Trabold et al [141].

Equiv. ratio	Parameter	Methane/air	Methanol/air	Ethanol/air	2-Propanol/air	2-Butanol/air
$\phi=0.8$	T_{ad} [K]	(1992) 2027	2054	2057	2055	2070
	ρ [kg/m^3]	(1.157) 0.990	1.036	1.058	1.065	1.069
	ν [10^{-5}m^2/s]	(1.539) 2.029	1.852	1.845	1.826	1.832
	δ_f [μm]	(534) 498	404	440	417	443
	s_L [cm/s]	(25.42) 33.64	36.93	34.75	34.51	34.89
$\phi=0.9$	T_{ad} [K]	(2130) 2160	2170	2178	2182	2198
	ρ [kg/m^3]	(1.154) 0.986	1.037	1.061	1.070	1.075
	ν [10^{-5}m^2/s]	(1.540) 2.031	1.836	1.827	1.807	1.808
	δ_f [μm]	(472) 444	347	390	374	398
	s_L [cm/s]	(31.71) 41.24	46.77	42.67	43.80	41.89
$\phi=1.0$	T_{ad} [K]	(2218) 2244	2242	2252	2262	2277
	ρ [kg/m^3]	(1.149) 0.982	1.039	1.065	1.075	1.080
	ν [10^{-5}m^2/s]	(1.542) 2.033	1.819	1.810	1.784	1.790
	δ_f [μm]	(444) 419	314	364	351	373
	s_L [cm/s]	(35.62) 45.89	54.47	48.04	48.74	46.78
$\phi=1.05$	T_{ad} [K]	(2222) 2249	2251	2262	2271	2288
	ρ [kg/m^3]	(1.147) 0.980	1.039	1.067	1.077	1.082
	ν [10^{-5}m^2/s]	(1.542) 2.034	1.812	1.802	1.774	1.784
	δ_f [μm]	(436) 413	302	356	342	364
	s_L [cm/s]	(36.33) 46.68	57.28	49.51	49.92	48.06
$\phi=1.1$	T_{ad} [K]	(2199) 2230	2239	2251	2256	2276
	ρ [kg/m^3]	(1.145) 0.978	1.040	1.069	1.080	1.085
	ν [10^{-5}m^2/s]	(1.543) 2.035	1.805	1.793	1.765	1.772
	δ_f [μm]	(434) 411	291	349	336	357
	s_L [cm/s]	(35.97) 46.20	59.35	50.18	50.48	48.37
$\phi=1.2$	T_{ad} [K]	(2126) 2159	2183	2192	2190	2213
	ρ [kg/m^3]	(1.140) 0.974	1.041	1.072	1.084	1.090
	ν [10^{-5}m^2/s]	(1.544) 2.037	1.790	1.777	1.747	1.755
	δ_f [μm]	(471) 440	277	347	334	356
	s_L [cm/s]	(31.42) 40.95	60.92	48.55	48.53	45.94
$\phi=1.3$	T_{ad} [K]	(2047) 2080	2118	2119	2114	2138
	ρ [kg/m^3]	(1.136) 0.971	1.042	1.076	1.089	1.096
	ν [10^{-5}m^2/s]	(1.546) 2.039	1.775	1.760	1.729	1.732
	δ_f [μm]	(622) 568	277	372	362	389
	s_L [cm/s]	(21.98) 29.74	58.82	42.99	41.91	39.56
$\phi=1.4$	T_{ad} [K]	(1970) 2003	2053	2048	2039	2063
	ρ [kg/m^3]	(1.132) 0.967	1.044	1.080	1.093	1.101
	ν [10^{-5}m^2/s]	(1.547) 2.041	1.762	1.743	1.712	1.716
	δ_f [μm]	(1037) 894	295	443	439	480
	s_L [cm/s]	(12.81) 17.97	53.15	33.87	32.42	29.88
$\phi=1.5$	T_{ad} [K]	(1900) 1933	1991	1978	1966	1990
	ρ [kg/m^3]	(1.126) 0.963	1.045	1.084	1.098	1.106
	ν [10^{-5}m^2/s]	(1.548) 2.043	1.748	1.728	1.695	1.699
	δ_f [μm]	(1374) 1214	336	593	584	655
	s_L [cm/s]	(9.41) 12.83	44.86	24.03	22.93	20.44

3.6. Intermediate Species Study

This section exhibits the numerically derived intermediate species quantities in ethanol/air and OME-3/air flames. These will be relevant to the studies in Chapter 4, where they are probed using long-exposure Raman spectroscopy, and in Chapter 6, where the knowledge of their existence is used to define useful binning channels for single-shot experiments.

Figure 3.5 displays mole fractions with a minimum absolute fraction of 0.1 % along the spatial dimension.

Results are given for ethanol/air and OME-3/air flames at ϕ=0.9, 1.5, and 3.5 equivalence ratios at a $300\,s^{-1}$ strain rate. Note that the parent fuel mole fraction and the summed intermediates species mole fractions are scaled with a factor for improved readability.

Ethanol/air combustion produces alkane/alkene/alkyne intermediates and aldehydes (oxygenated hydrocarbon). In leaner combustion, the aldehyde contents increase at the expense of alkane/alkene/alkyne ones. The opposite is true for richer mixtures. The maximum total intermediates amount constitutes roughly 1.5 % at 1300 K for the lean, 2.8 % at 1480 K for the rich, and 4.5 % at 1450 K in the partially-premixed flame. These are also the approximate temperatures at which the summed intermediates' mole fractions exceed the ethanol mole fraction.

In the OME-3 flames, only formaldehyde substantially exceeds 1 % mole fraction. The next intermediates are methane, ethane, and methyl. The combined intermediates amount is 2.2 % at 1250 K for the lean, 3.4 % at 1250 K for the rich, and 4.4 % again at 1250 K in the partially-premixed flame.
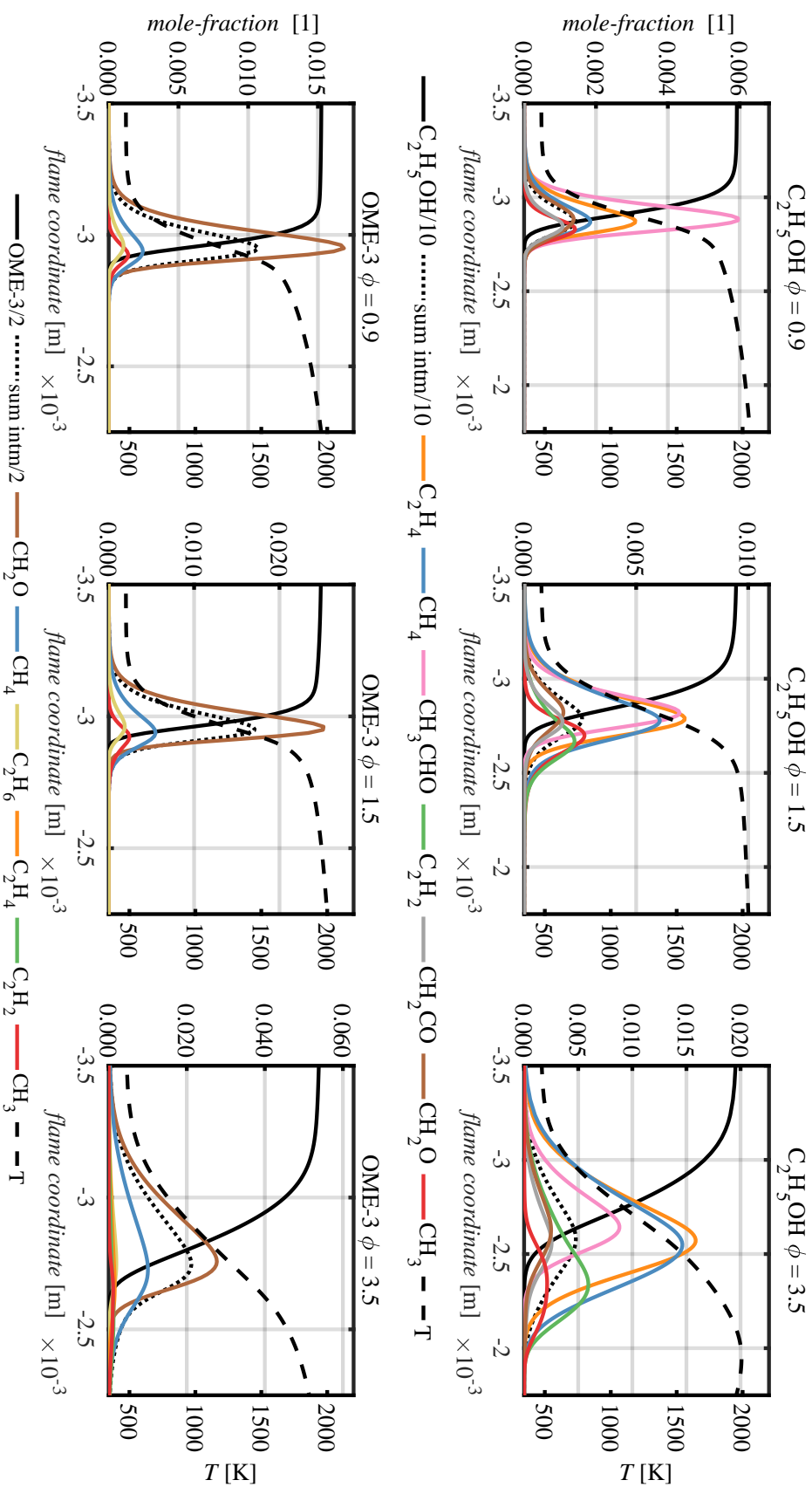
Figure 3.5.: Numerical laminar opposed jet flame calculation results with ethanol/air and OME-3/air emitting from the left nozzle and air from the right. Shown are the most prominent intermediate species' mole fractions at a strain rate of approximately 300 s^{-1}.

3.7. Experimental Turbulent Flow Characterization Study Using LES

In order to estimate the location of all turbulent flames presented in this work within the Borghi-Peters diagram, a basic LES study about the flow properties is performed (provided by Dr.-Ing. Louis Dreßler via personal communication in April 2022). Thereby, an unignited ethanol/air mixture is simulated at three respective bulk flow velocities. From this simulation, the results of other Reynolds numbers are interpolated or extrapolated. Because the different premixed fuel/air mixtures' densities vary rather little, the result for ethanol/air is also used for the other fuels and at various equivalence ratios.

Using this simulation's results, essential flow field parameters for the Borghi-Peters diagram can be estimated, most importantly the mean flow velocity and its r.m.s.. However, given the mentioned strong simplifications and the fact that the study needed to be performed in a short time period, the results and Borghi-Peters diagrams are placed outside the main body of the dissertation and in Appendix B.1.1.

4. Main and Intermediate Species in Ethanol- and OME-3/Air Flames

4.1. Introduction

This chapter covers the experiments to capture highly-resolved Raman spectra of various laminar premixed ethanol/air and OME-3/air flames.

The overarching goal is to increase the understanding of intermediate species formed within the flame fronts. The individual research targets are:

1. To establish a system capable of capturing the intermediates' Raman spectra with a large SNR

2. To capture spectral disparities in flames of different fuels, focusing on intermediate species

3. To evaluate the sensitivity to intermediate species for each individual fuel (e.g., rich versus lean flames)

4. To verify predictions made by numerical 1D flame calculations regarding the intermediate species' presence and amounts

The chapter's structure is divided into the burner introduction and operating points, the acquisition procedure, the processing steps, and finally the results. Notably, it is referred to numerical flame calculation results of chapter 3 at several occasions. Therefore, the reader is guided to read that chapter first in order to receive a complete understanding.

Parts of this chapter are published in Trabold et al. [142].

4.2. Experimental Setup

4.2.1. Laminar Temperature-controlled Opposed Jet Burner

Flames of premixed vaporized liquid fuels have previously not been studied with the here used spontaneous Raman scattering (sRS) system at the RSM institute at TU Darmstadt. Therefore, new custom-designed burners are required. The first of two, the design of which is part of this dissertation, is introduced in the following. The second one, which was commissioned during this work, is presented in Chapter 5. Both utilize the same vaporization periphery, which will also be introduced in the following (Section 4.2.2).

4.2.1.1. Global Requirements

The temperature-controlled laminar opposed jet burner (LTOJ) is designed to provide the sRS system with a flexible calibration flames platform. Furthermore, the burner also provides interesting research target flames, as even laminar and stationary premixed flames present a novelty for vaporized fuels like ethanol. The essential requirements defined during the design process are summarized in the following:

1D Setup   The LTOJ flames need to be optically well-accessible from the achromatic lens capturing the Raman signal (opening angle 13°). Furthermore, the laser needs to intersect the flame perpendicularly to yield experimental data directly comparable to numerical 1D flame calculations. Therefore, it has to enter and traverse the burner on its central axis.

Variability   The burner periphery is designed to enable a wide premixed flame conditions range from gaseous to liquid fuels, low to high equivalence ratios, and low to high strain rates.

Stable Flow Properties   In order to enable stable flow conditions in the probe volume, a large effort is made to homogenize the flow upstream of the nozzles. Furthermore, the nozzle's shape is formed so that the individual nozzle emits the bulk flow with a top-hat velocity profile. Thereby, the highest possible flow stability near the stagnation point between two nozzles is reached.

Defined Thermal Properties   The burner needs to be heated up and be controlled at elevated temperatures, so that vaporized fuel condensation is prohibited.

4.2.1.2. Final LTOJ Design

The detailed design process from concept to the commissioned device is described in different student projects' reports [41–43, 77, 78]. A summary with all important details is presented in the following.

The burner consists of two identical opposing nozzles that are symmetrically aligned and horizontally oriented. One side is shown as a cross-sectional view in Figure 4.1.

The premixed gases enter each burner plenum through 16 holes arranged in the radial direction. From there, the flow is directed axially towards a homogenization section consisting of four screens with a 250 µm mesh size and a honeycomb with a 1/16 inch cell size. Finally, the flow enters a contoured *Morel* nozzle, which contracts the flow with a 9:1 ratio [100].

To produce the final jet flow, a tube made of stainless steel (with a straight exit tube length of 15 mm, a wall thickness of 0.3 mm), and an inner diameter of $D_{jet} = 12$ mm at the exit is attached to the nozzle. The opposing nozzle separation distance L can be flexibly chosen and fine-tuned using electro-mechanically powered spindle wagons located under each burner. In this work, the
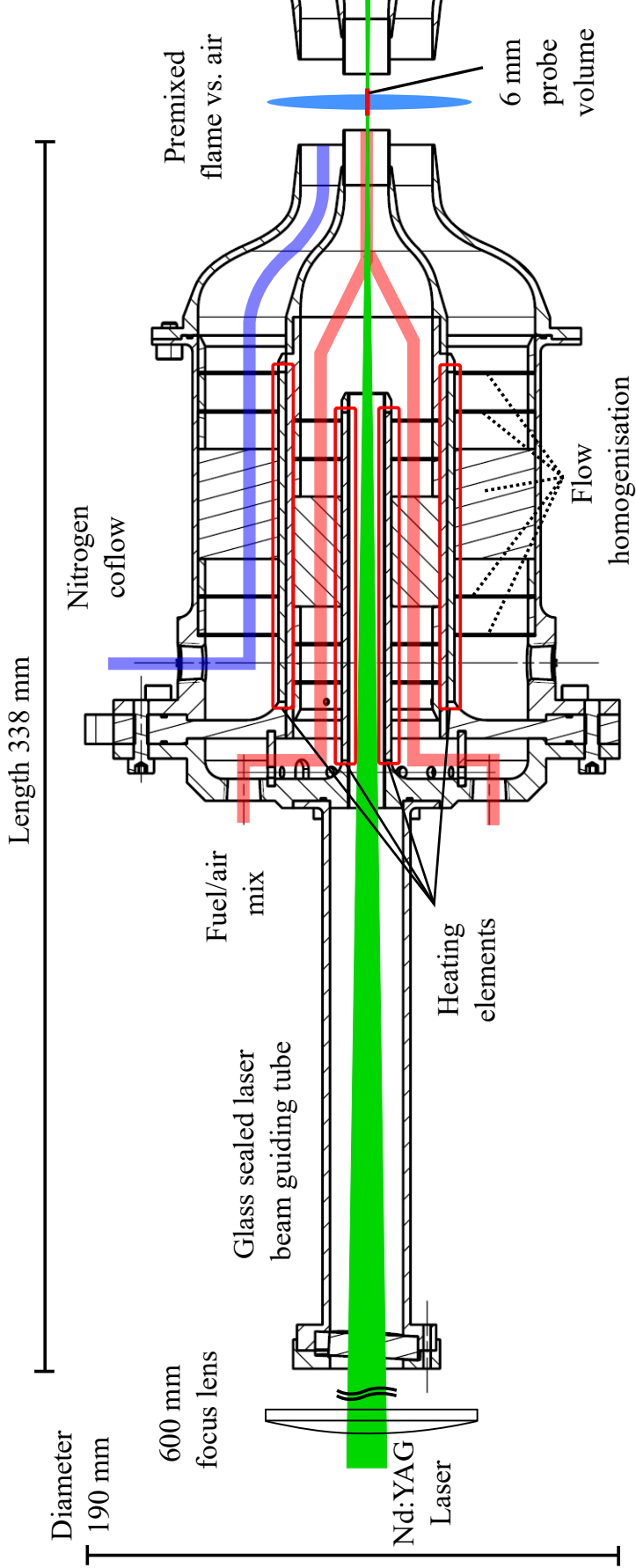
Figure 4.1.: Laminar Temperature-controlled Opposed Jet Burner (LTOJ) cross-sectional view. Adopted from Trabold et al. [142] with minor changes.

distance is fixed at $L=12\pm0.04$ mm for all measurements, resulting in a non-dimensional distance $L/D=1$.

As a well-defined boundary condition, each central jet flow is surrounded by a well-defined nitrogen stream (*coflow*). The burner's annular coflow sections are equipped with four screens and a honeycomb to generate homogeneous velocity profiles in the radial direction. The coflow nozzles are also contoured following the Morel nozzle design principles [100], and have a 6:1 contraction ratio. This results in an $D_{coflow}=31$ mm exit diameter. The coflow bulk velocity is $0.3\,\mathrm{m\,s^{-1}}$ throughout all experiments in this work.

In order to prevent pre-vaporized liquid species condensation and vary the premixed mixture temperature, the nozzles need to be heated in a controlled manner. Each side is equipped with two heating elements (Hotset GmbH, Hotslot Mini 400 W), which are controlled using proportional–integral–derivative (PID) controllers (Jumo, cTron 08). The preheated gas temperatures can be measured in-situ using J-type thermocouples. As verified by K-type thermocouple measurements at the nozzle exit, the maximum reachable gas temperature is 520 K.

In order to align the laser perpendicularly to the vertical flame planes, the LTOJ provides optical access on the central burner axis. Thereby, two cylindrical tubes are mounted co-axially at each burner side's rear end (Figure 4.1). At the tubes' ends, media separation windows are attached far enough away from the laser focus to avoid exceeding their damage threshold. The fused silica windows are slightly tilted to defer harmful reflections into the laser. Media tightness between the cylindrical tube and the window is reached with polytetrafluoroethylene (PTFE) sealant rings.

4.2.2. Pre-vaporization System for Liquid Fuels

A single vaporization system is used to supply the premixed fuel/air mixture to either the LTOJ or the TCJB (which will be introduced in Chapter 5). It is commissioned during this work, but designed beforehand in different student projects [11, 12, 50, 98, 133]. Therefore, the following description is limited to essential details.

Figure 4.2 shows the apparatus scheme with various building blocks, as different configurations are used depending on the experiment. A gear pump (Figure 4.2 (1), Scherzinger GmbH 030-045-DM-25-2) circulates the liquid fuel in a loop. It provides the constant, pulsation-free upstream pressure needed for Coriolis-type mass flow controllers ((2.1), Coriflow MFCs, Bronkhorst, accuracy 0.2 % of full scale (FS)). Three different *Coriolis*-type mass flow controllers (*coriflows*) with flow rates of $200\,\mathrm{g\,h^{-1}}$, $2\,\mathrm{kg\,h^{-1}}$ and $4\,\mathrm{kg\,h^{-1}}$ are used depending on the specific burner and desired liquid mass flows.

Gaseous flows are controlled using calorimetric-type mass flow controllers ((2.2), MFCs, Bronkhorst, accuracy 0.5 % of reading (Rd) plus 0.1 % FS). Notably, these are regularly checked to be within specification for the measurements presented here.

Downstream the flow controllers, the liquid fuel is continuously vaporized in one of the two different vaporizer systems used in this work (3). For the small LTOJ burner, an ADrop DV2-MK-T system is used (400 W vaporizer, 1000 W air heater). That system can vaporize up to $0.2\,\mathrm{kg\,h^{-1}}$ water at vapor temperatures of 520 K and at atmospheric pressure.

Higher rates are possible when the liquid has a lower specific vaporization enthalpy, which is the case for alcohols (methanol: 1.93 times more, ethanol: 2.57 times more). In parallel to the fuel heating section, up to $1.9\,\mathrm{kg\,h^{-1}}$ (26.9 slpm) air are heated (maximum temperature 520 K). Subsequently, vaporized fuel and heated air are mixed using a high-shear static mixer (4).

The combination of vaporizer ((3), ADrop DV4) and gas heater ((5), ADrop NH3) is used for the higher flow rates in the TCJB cases. The ADrop DV4 (4.5 kW electric) reaches vaporization rates of up to 2 kg/h water at atmospheric pressure and with a maximum vapor temperature of 573 K. In parallel, this system can heat up 10 kg/h (140 slpm) air to 423 K.

The ADrop NH3 heating system allows for even higher premixed flow rates, for example for the blow-off experiments described in Chapter 5. This system is capable of heating air mass flows of 80 kg/h up to 493 K. The setup allows running flow rates up to the flame blow-off limits for a wide equivalence ratio range and a variety of fuels.

The present work's operating point with the largest flow rate, demonstrating the capabilities of this system, is a rich methanol/air flame near blow-off ($\mathrm{Re_{bulk}}$=61000 at ϕ=1.5; u_{bulk}=101 m/s). The corresponding fuel flow rate is 6.23 kg/h (0.13 l/min), the air flow rate 29.88 kg/h (644 slpm) and the resulting thermal power is approximately 45 kW.

Between the vaporizer systems and burners, heated hoses prevent gaseous fuel/air mixture condensation (6). Thereby, it was ensured that the partial fuel pressure, defined as $p_{\mathrm{partial}} = X_i \cdot p_{\mathrm{ambient}}$, always remained underneath the saturation pressure. A detailed description of this work's saturation pressure calculations through *Antoine's equation* is given by Becker [11].
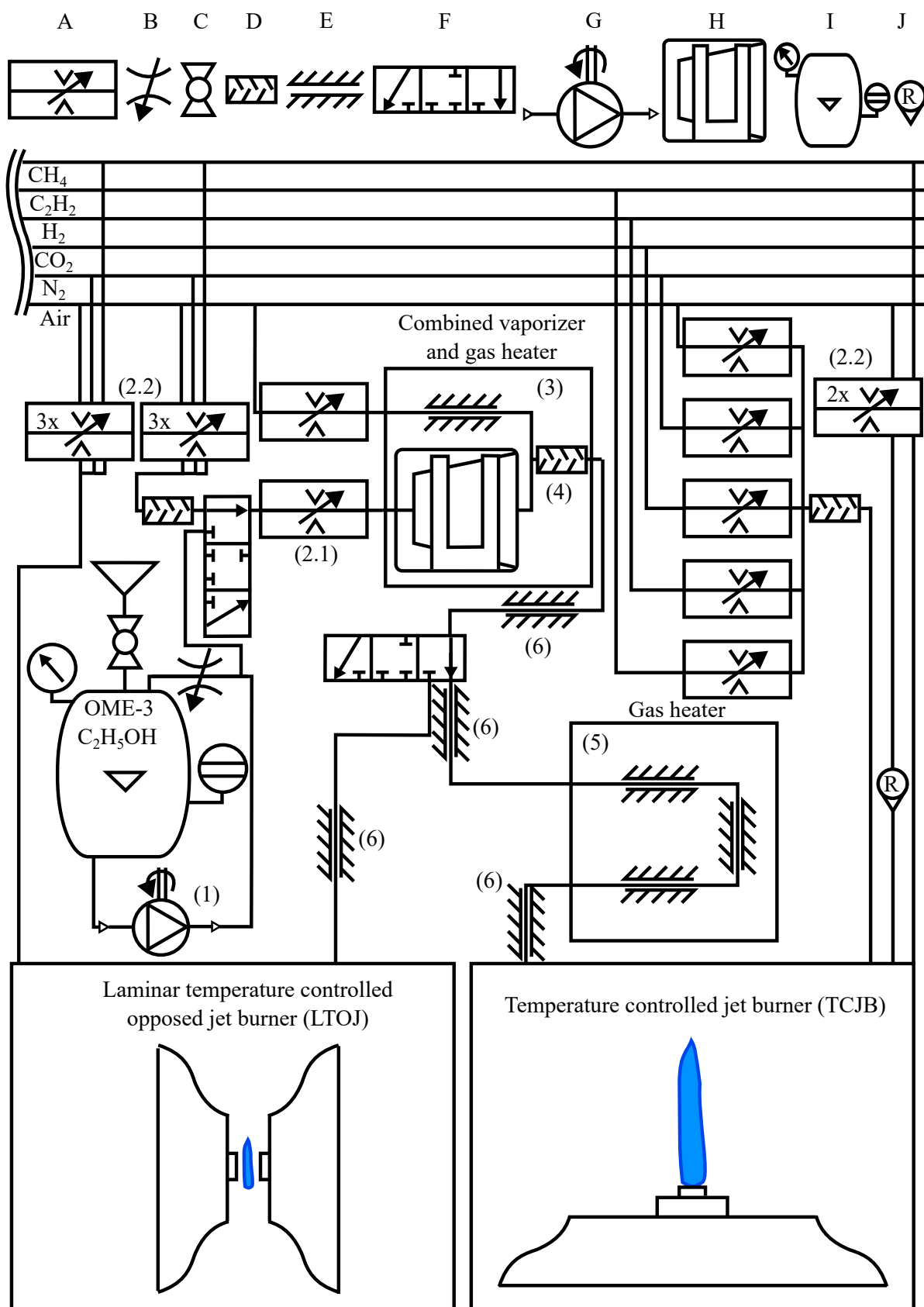
Figure 4.2.: Vaporizer system scheme used to prepare vaporized fuel/air mixtures. Components: (A) Coriflow or mass flow controller, (B) throttle valve, (C) ball valve, (D) static mixer, (E) gas heating appliance, (F) switch valve, (G) electrical gear pump, (H) vaporizer, (I) fuel tank, and (J) rotameter.

4.2.3. Operating Conditions

In this study, ethanol and OME-3 are investigated at the equivalence ratios ϕ=0.9, 1.5, and 3.5. These fuels are chosen as with their vastly different reaction pathways, different intermediate species types and concentrations can be expected within their flame fronts.

The strain rates are experimentally varied in a range of approximately $150\,\mathrm{s}^{-1}$ to $350\,\mathrm{s}^{-1}$, while balancing the axial momenta of both the opposing fuel/air and air streams. An α=$300\,\mathrm{s}^{-1}$ bulk strain rate is finally chosen, as higher strain rates can lead to large radial extents of the partially-premixed flame and lower strain rates can cause the lean premixed flames' flashbacks or extinctions.

The six operating conditions' flow parameters, each with a fixed nozzle distance L=12 mm, are listed in Table 4.1. A relatively high common mixture temperature is chosen to ensure complete OME-3 vaporization.

Table 4.1.: Operating conditions for the laminar counterflow flames including an *ID*, bulk flow velocities u_l and u_r, fuel/air side kinematic viscosities ν, and Reynolds numbers for the respective left and right nozzles (Re$_l$, Re$_r$) at 473 K. The air nozzle's kinematic viscosity was constant at $3.54 \cdot 10^{-5} \mathrm{m}^2\,\mathrm{s}^{-1}$. Table obtained from Trabold et al. [142].

ϕ/fuel	0.9/C$_2$H$_5$OH	1.5/C$_2$H$_5$OH	3.5/C$_2$H$_5$OH	0.9/OME-3	1.5/OME-3	3.5/OME-3
ID	EtOH090	EtOH150	EtOH350	OME090	OME150	OME350
u_l/u_r [m/s]	1.78/1.82	1.77/1.80	1.75/1.85	1.75/1.85	1.72/1.88	1.65/1.95
ν [10^{-5} m^2/s]	3.20	3.04	2.65	2.90	2.61	1.95
Re$_l$/Re$_r$	670/615	700/618	792/627	723/626	792/636	1013/661

Ethanol/air and OME-3/air flame photographs of the captured operating conditions are shown in Figure 4.3. While the premixed fuel/air mixtures enter the combustion space from the left nozzle, air enters from the right. Unburned mixture temperatures are T=473±3 K for all flames. The 532 nm laser enters from the left and is aligned with the burner's axis.
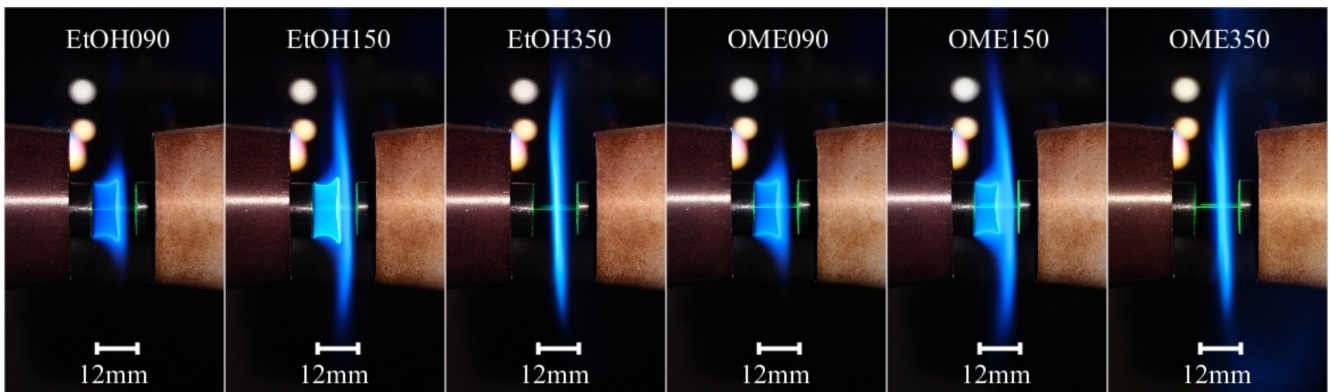
Figure 4.3.: Ethanol/air and OME-3/air flame photographs of the studied operating conditions. Obtained from Trabold et al. [142].

The flames typically stabilize centrally between the nozzles. However, the ϕ=0.9 and 1.5 flames attach to the nozzle due to the low velocities in the nozzle's boundary layer. Notably, it is assumed

that the centrally located flame front probe is not influenced by heat losses to the burner. The reason is that the Raman and Rayleigh signal is obtained in a different section of the stream and spatially far-distanced from the nozzle.

Additionally, because of the short bulk flow residence times (opposing flows with $2\,\mathrm{m\,s^{-1}}$ velocity), sensitivity to buoyancy effects is ruled out (Table 4.1). This is also evident from the rotational symmetric flame appearances near the central axis (Figure 4.3).

The counterflow configuration enables to shorten residence times, even for the richest conditions, which results in bluish flames. Such flames are largely polycyclic aromatic hydrocarbons (PAH)-free and do not produce soot precursors in a substantial amount, which would typically impair Raman scattering detection. Accordingly, this counterflow configuration is well-suited for further 1D Raman and Rayleigh diagnostic developments.

During this chapter's experiments, Raman signals from a varying number of laser shots are integrated on-chip to obtain sufficiently high SNRs. Table 4.2 summarizes the total shot numbers and average laser shot energies. These are calculated from shot-to-shot laser pulse energies measured by an energy meter (Coherent Inc., EnergyMax J-50MB-YAG) after the probe volume. The shot number is maximized to utilize almost the complete Raman CCD sensor's dynamic range. Notably, maximum laser energies for OME-3 are significantly reduced with increasing equivalence ratio in order to avoid optical breakdown.

Due inevitable microscopic movement of the flame, the on-chip averaging of hundreds of signals results in flame front gradient broadening in spatial dimension. This will be discussed in more detail in Section 4.4.1.

Table 4.2.: Mean laser energies and number of shots captured in each long-exposure. The laser energies are reduced for the premixed rich and partially-premixed OME-3/air flames because otherwise optical breakdowns appear. Although measured, the reference cases of methane/air are not listed, as only the respective Rayleigh and not the Raman data was evaluated. Obtained from Trabold et al. [142].

ID	EtOH090	EtOH150	EtOH350	OME090	OME150	OME350
Number of shots	600	3850	2100	12600	21000	21000
Mean laser energy [mJ]	1392	1408	1397	1423	560	275

4.2.4. Excitation and Detection Systems

The excitation and detection configurations of the sRS system used for this experiment, as well as for the one following in Chapter 6, are illustrated in Figure 4.4.

While the excitation system was originally developed by Butz [20], the detection side was developed by Schneider [123].

Throughout the present work, two detection-side subsystems are built. First, the shutter system consisting of two slit wheels and an iris shutter is extended with another slowly rotating slit wheel to allow for better durability in long-exposure and high-sampling measurement campaigns. Second, the detection path is extended with a higher-dispersed (HD) Raman spectrometer arm, with
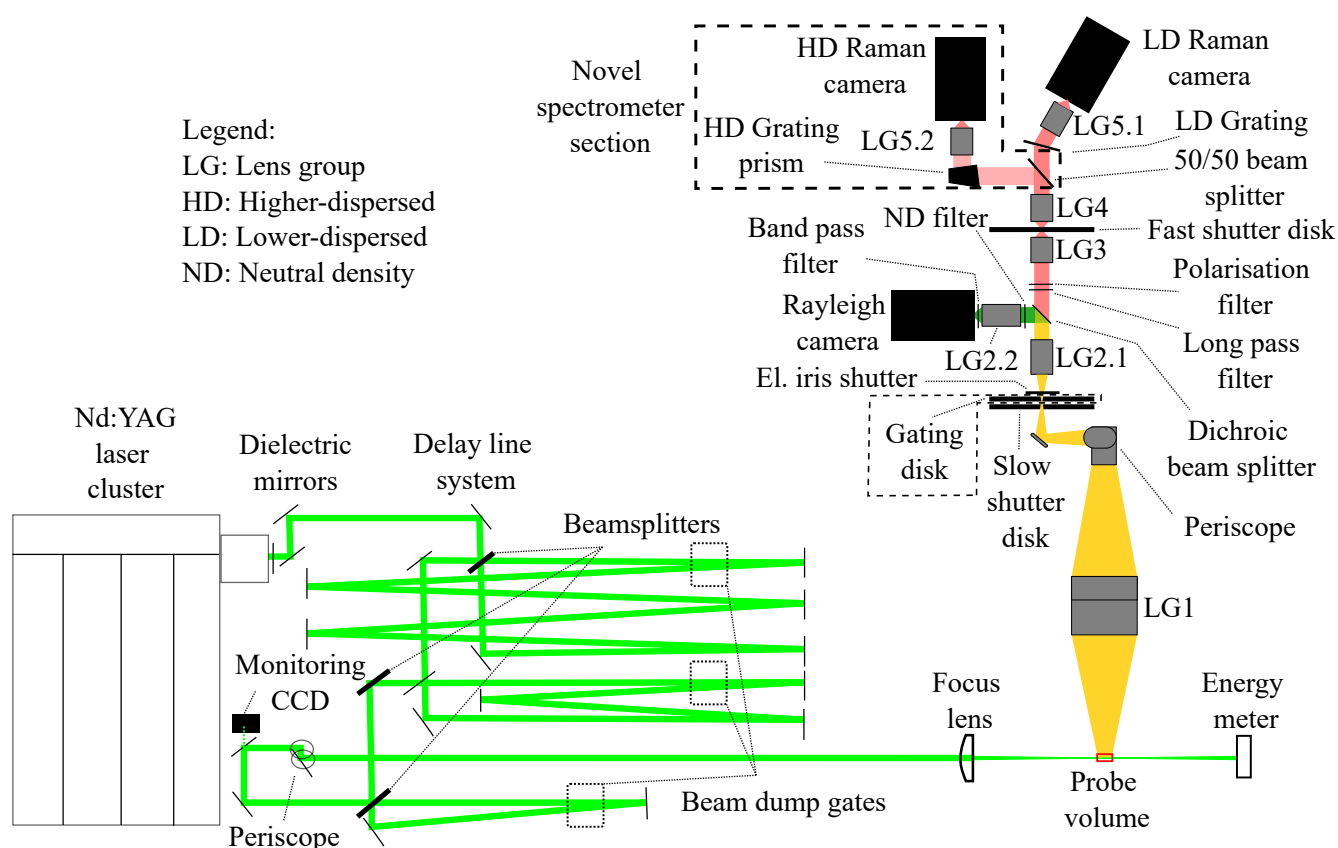
Figure 4.4.: Laser excitation and detection system scheme of the sRS system used in this work. Novelties are the second Raman spectrometer arm, which is indicated by the dashed box, as well as another gating disc. Adopted from Trabold et al. [142] with minor changes.

which the complex hydrocarbon fuels' C-H-stretch bands can be investigated in more detail. As an alternative to this dual-dispersion option, the new spectrometer arm can also be used for a depolarization approach in case background or fluorescence suppression is needed.

The following sections briefly describe the existing laser and spectrometer systems, before the two new subsystems are covered in Section 4.2.4.3 and 4.2.4.4.

4.2.4.1. Laser

A group of four Q-switched Nd:YAG lasers (InnoLas Spitlight 1000) emit laser pulses individually triggered at a 5 Hz repetition rate, separated by 150 ns, and with a pulse energy of approximately 1200 mJ at 1064 nm. Each pulse has a full width at half maximum (FWHM) duration of 7-8 ns.

To achieve spatial beam superposition, the first laser's fundamental frequency is combined with the second laser's second harmonic oscillation using an infrared (IR) transmissive dielectric mirror. The second harmonic is generated by a potassium dihydrogen phosphate (KDP) crystal. The superposed beams pass through the first laser's KDP and exit the laser housing. The same process is repeated to superpose laser three and two, and four on three.

The total pulse energy is adjusted using a combination of a $\lambda/2$ plate and a polarizing beam splitter cube. Optical breakdown in the probe volume is prevented by stretching each pulse at 532 nm to approximately 150 ns (FWHM) using a three-leg optical delay line with segment lengths of approximately 8.4 m, 4.2 m, and 2.1 m. Custom-designed beam splitters (Lattice Electro Optics) in the delay lines transmit approximately 61 % of the laser light with minor losses, while reflecting almost the entire rest.

The delay line alignment is facilitated using a monitoring CCD camera positioned behind a mirror after the delay lines. Additionally, each delay line has remotely controllable beam dump gates to enable individual monitoring during all mirrors' coarse alignment. Fine linear actuators (Newport, New Focus Picomotor) mounted on one mirror in each delay line enable the required highly sensitive mirror alignment (<1″).

A plano-convex lens with a focal length of 600 mm focuses the stretched laser burst into the probe volume. The lens mount is fixed to a three-dimensional (3D) traverse and operated by picomotor actuators, enabling manual in-situ adjustment of the combined lasers' positions with sub-pixel accuracy.

The focused beam has a Gaussian-like profile with a 190±10 µm ($1/e^2$) diameter along the 6 mm long 1D probe volume. The proper laser superposition and delay line alignment are monitored at least every 15 min by using the beams' Rayleigh signal in dry air. After all efficiency losses, the pulse energy in the probe volume amounts to approximately 1600 mJ.

4.2.4.2. Spectrometer

Figure 4.5 shows the dual-dispersion spectrometer and its main components as computer-aided design (CAD) models, excluding lens group (LG)1.

All optical elements within the spectrometer are attached to a custom-designed frame from aluminum. The ones that affect the focusing are traversable by micrometer stages. As part of this work, the complete spectrometer is enclosed within a common housing. This serves the purpose of rejecting stray light more effectively and to provide improved temperature stability for all detection optics in vicinity of high thermal load flames. Constant temperature and purging is provided by a continuous dust-free and dry air flow.

Beam Path As an essential spectrometer part, seven individual lens groups (LGs) are required to guide the signal along the optical elements' path and towards camera sensors. Manufacturer, focal lengths and maximum apertures are given in Table 4.3.

Raman and Rayleigh scattered light is collected with LG1, which is a custom-designed achromatic lens (Linos Photonics) with a 150 mm open diameter and $f/2.0$ and $f/4.0$ apertures at object and image side, respectively. After LG1, a custom-designed periscope rotates the image from horizontal to vertical orientation.

The LG1 backward focus plane lies at the combined aperture of three shuttering devices (refer to Section 4.2.4.3). Subsequently, the focused beam is again collimated with LG2.1. To separate
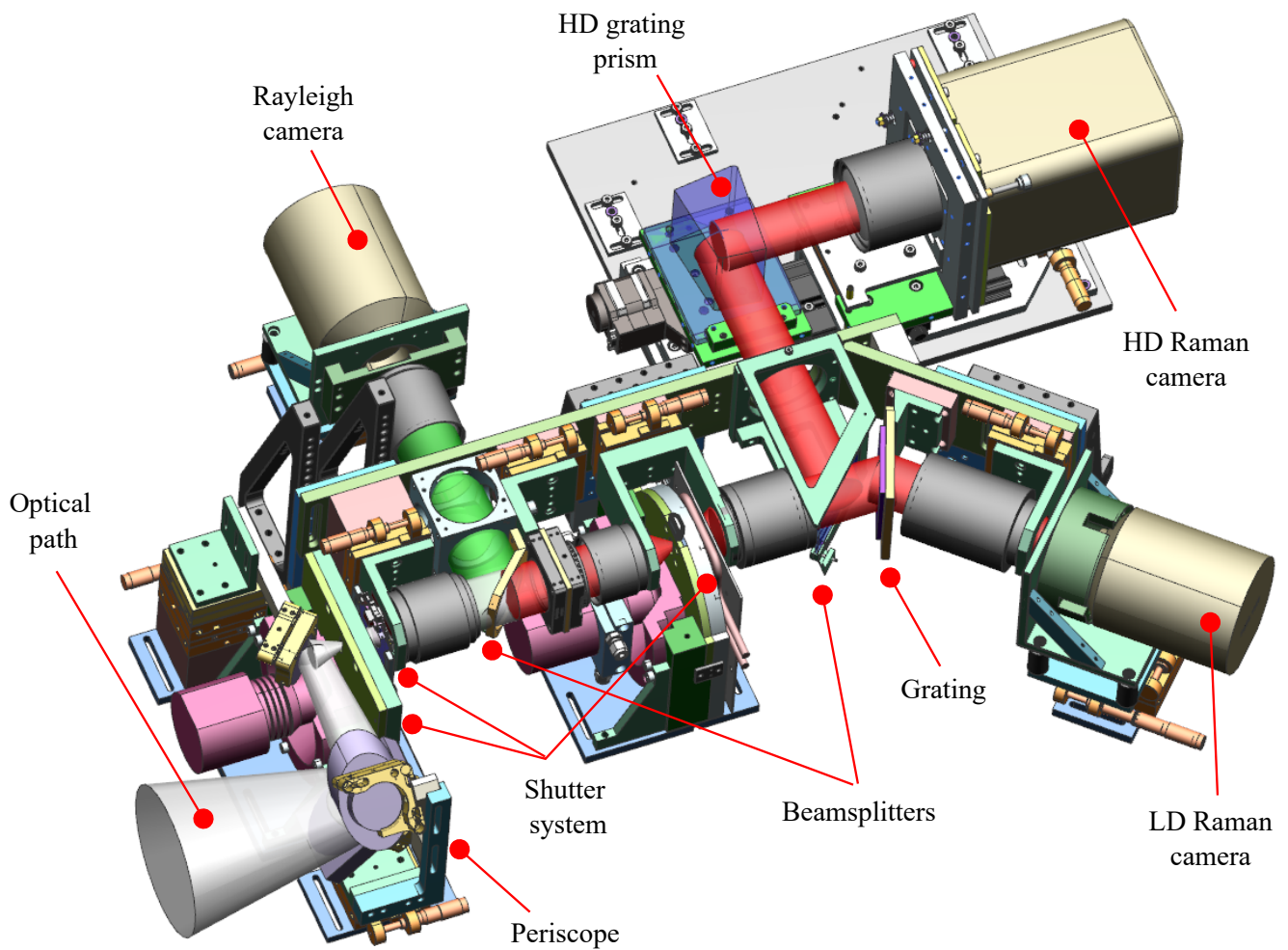
Figure 4.5.: The dual-dispersion spectrometer's CAD model with the optical path indicated in grey (complete signal), green (Rayleigh signal) and red (Raman signal). Adopted from Trabold et al. [142] with minor changes.

the Rayleigh from the Raman signal, a dichroic long pass filter (Barr associates, $D=60$ mm, s-pol, 532/560-700, 38-52° angle of incidence (AOI)) is used. Thereby, the Rayleigh signal is reflected, while the Raman signal is transmitted.

LG2.2 focuses the reflected signal onto the Rayleigh CCD camera (frontside illuminated, Princeton Instruments Pixis 400, operating temperature $T=-55$ °C). Additionally, signals other than Rayleigh scattering are eliminated by a bandpass filter (Semrock 532±2 nm (FWHM), optical density>6 outside of 532±8 nm).

The rotational-vibrational Stokes-Raman that passes the first long pass filter is modified by a second long-pass filter (Semrock EdgeBasic 532 nm, optical density>6 below 535 nm) to omit low wavelength noise. To inhibit overexposure, neutral density filters are added depending on the signal intensity.

Table 4.3.: Lens groups (LGs) in the dual-dispersion spectrometer.

Lens group *ID*	Maker and model
LG1	Linos Photonics $f/2$ and $f/4$ on object and image side, respectively
LG2.1	Canon 100 mm $f/2$
LG2.2	Zeiss 100 mm $f/2$
LG3	Nikon 50 mm $f/1.2$
LG4	Zeiss 85 mm $f/1.4$
LG5.1	Zeiss 135 mm $f/2$
LG5.2	Sigma 135 mm $f/1.8$

Subsequently, the s-polarized part is selectively transmitted by a polarization filter (Codixx ColorPol VIS 700 BC3 CW03, anti-reflection coated, 95 % transmission). LG3 then focuses it onto a rapidly rotating wheel's slit before being collimated again using LG4. The light is subsequently treated in two different ways, which are described next.

Dual Dispersion Setup For the first and original configuration, which is also used in the single-shot (single exposure) measurements in Chapter 6, the Raman scattered light is spectrally dispersed with a custom designed holographic transmission grating (VPH-1200-625, Kaiser Optical Systems Inc., 1200 lines/mm, 76 mm square, 22° incident and refracted angle, diffraction efficiency 78/90/78 % at 565/625/685 nm). Subsequently, after focusing by LG5.1, it is recorded with the lower-dispersed (LD) Raman camera (backside illuminated CCD, Princeton Instruments Pixis 1300B, operating temperature $T = -55\,°C$), resulting in a mean reciprocal linear dispersion of $\delta\lambda/\delta x = 5.94$ nm/mm, as measured with a neon gas lamp and slit combination.

For the long-exposure measurements in Chapter 4, the Raman scattered light is instead split into two partial signals in front of the VPH-1200-625 grating using a 50/50 beam splitter (75x91 mm, 50/50 VIS beamsplitter plate, Edmund Optics, $\Delta\lambda = 400\text{-}700$ nm). The reflected partial signal is spectrally decomposed with a holographic grating prism (HDG-631, Kaiser Optical Systems, Inc., 4165 lines/mm, diffraction efficiency 30/58/58 % at 610.2/631.0/648.1 nm). Subsequently, after focusing by LG5.2, it is recorded with the HD Raman CCD camera (same model as LD Raman camera). This system has a mean reciprocal linear dispersion of $\delta\lambda/\delta x = 0.90$ nm/mm. Further details are given in Section 4.2.4.4.

Calibration, Discretization, and Spatial Resolution A neon gas lamp in combination with a 100 mm wide slit is utilized to spectrally calibrate the dual-dispersion spectrometer's two arms. Therefore, a third-order polynomial is fitted to the wavelength axis in the spectral dimension. The transmission spectrometers *bowing* effect [149] necessitates that each Raman CCD pixel row is analyzed individually.

Furthermore, the optical elements' spectrally dependent transmissions and the Raman CCD cameras' spectrally dependent quantum efficiencies require a spectral-sensitive transmission calibra-

tion. To account for these influences, recordings of a calibrated *Ulbricht sphere* (Gigahertz Optik GmbH) are used for correction.

To calibrate the spatial axis, a custom-designed point mask target is used (Appendix C.1). The point mask has 50 μm wide pinholes, which are arranged as a line pattern in a metal sheet (manufactured by C.F.K. CNC-Fertigungstechnik Kriftel GmbH). For orientation, the holes are distanced differently on the two opposing sides of the central pinhole, either by 0.5 mm or by 1.0 mm. During the calibration process, the target's center is positioned on the achromatic lenses' and the spectrometer's optical axes (which are themselves concentric). The pinholes are horizontally aligned to coincide with the laser direction.

Using the pinhole target, the total magnifications (probe volume to CCD sensors) can be determined at the ±3 mm off-centered holes. The resulting magnifications are 2:1, 1.6:1, and 1.51:1 for the respective Rayleigh, LD, and HD Raman spectrometer arms. Throughout the studies in this work, the 1D probe volume size has a 190±10 μm diameter (defined by the laser diameter on the Rayleigh images ($1/e^2$)) and a 6 mm length (centered between the burner nozzles).

The spatial discretization depends on the individual studies. When using the super-pixel binning for the long-exposure, it is discretized in 20 μm, 25 μm and 26.5 μm blocks on the Rayleigh, LD and HD Raman spectrometer arms, respectively. Those values are defined by the binned pixel sizes and already incorporate any optical magnifications. For the single-shot experiment (Chapter 6), the LD Raman spectrometer arm's spatial discretization is either 50 μm or 125 μm, depending on whether four or ten pixels are spatially binned. The Rayleigh camera's discretization in that experiment is 20 μm.

Notably, the approximately 60 μm spatial resolution reached with the spectrometer is majorly defined by the sharpness of individual lens groups, rather than the sensor resolution. That value was determined using the back-illuminated knife-edge in the probe volume as a step function, and then evaluating the answer's width in spatial direction.

4.2.4.3. Shutter System and Modification

As broadband flame luminosity substantially superimposes over the weak Raman signal as noise, a major effort is done in reducing the spectrometer's gating duration to as close around the signal-inducing laser pulse length as possible. Ideally, the weak Raman signal's CCD sensor should only slightly exceed the 500 ns excitation pulse burst length. In the TUDa Raman spectrometer's original setting by Schneider [123], an electrical iris shutter and a slower rotating slit disc (50 Hz) were positioned after the periscope to realize the laser's 5 Hz frequency and to gate the Rayleigh camera to about 361 μs. Thereby, a 3.4 μs exposure was realized through a fast rotating slit disc (350 Hz) between LG3 and LG4.

As the measurements by Butz [20] showed, the system could reliably gate with the desired exposure and frequency. However, due to the lifetime exceedance by too many repetitions, the long-exposure studies in the present work lead to the iris shutter malfunctioning after only days of operation and needing replacement. Therefore, a shutter hardware and controlling software redesign was

initiated and worked on during a student design project [5]. The essential requirements defined in the beginning are summarized in the following, before the realized system is briefly described.

- Opening and closing of the beam path needs to happen within 39.64 ms, which is the time between two slower rotating wheel's gatings. The opening frequency is 5 Hz.

- The shutter should reach 10-100 million cycles and should not require a replacement in the spectrometer lifetime.

- The slit width should be about 2.5 cm to rule out vignetting effects at the planned location next to the original iris shutter.

- Turning the continuous shutter on or off needs happen within 200 ms, which is the time between two laser shots.

- To be financially viable, the costs should be less than approximately ten original iris shutters (<6000 Euro).

A wide range of solutions fulfilling these requirements was explored in the project's initial concept study [5]. Solutions ruled out after the concept phase included diaphragm iris shutters by other manufacturers, concepts based on shutters being moved by magnetic reluctance, and solutions based on linear electrical motors.

After consideration of all details, the chosen concept is to keep the previous solution's electrical iris shutter, but replace its opening function at the laser's 5 Hz frequency by using a third slit wheel. As a result, the iris shutter only needs to open the beam path once before each imaging series (consisting of 100-20000 images) and close after. Thus, the necessary opening repetitions are reduced by several orders of magnitude and life expectancy greatly increases. At the same time, the new wheel operates almost without wearing, given it is powered directly by a brushless electrical motor. Notably, to be more balanced, it was designed with two slits on opposing sides of the wheel, thereby halving the frequency to 2.5 Hz.

The two original wheels' control system generally remains untouched and serves as a template for the new one. Due to the high rotational velocities, the controlling scheme for them can rely on a single X-encoder signal per rotation. However, because the encoder rates are too slow to control the new wheel's relatively small rotational velocity effectively, the control scheme can not be transferred directly. Instead, an A/B-encoder (Nanotec, NOE2) with 4000 flanks per rotation is added to control the rotational velocity of the new wheel's electrical motor (Nanotec, DB43), and the X-encoder signal is only used to adjust the global slit position after each rotation.

In terms of hardware, the same controller is chosen as for the original wheels (Accelnet, ADP-090-36). From a structural standpoint, the former slow wheel housing is adapted to also hold the new slowest wheel housing. The re-engineered slower wheel shutter system's final CAD design is shown in Figure 4.6.
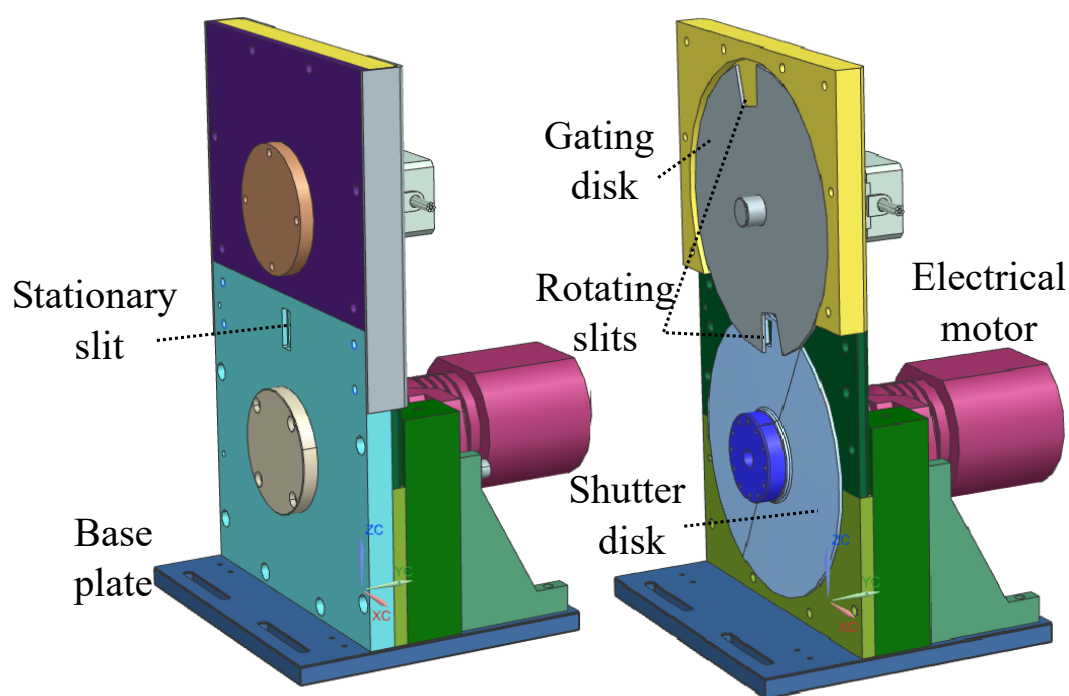
Figure 4.6.: Slower wheel shutter system modification CAD model with enclosure (left) and with discs and slits visible (right).

4.2.4.4. Spectrometer Extension Design

This subsection covers the second spectrometer arm extension's design of the original spectrometer, which is required to study the fuel and intermediate species C-H-stretch bands with a higher dispersion.

Based on the relevant intermediate species identified in Section 3.6, the respective Raman shifts introduced in Section 3.6, and the already available holographic grating prism (Kaiser Optical Systems, HDG-631), the requirements for the spectrometer extension can be defined. While detailed information is given in a thesis work by Bok [16], the most important requirements defined before the design phase are given in the following. Subsequently, the final design is shown in more detail.

- The new system's optical axis height above the optical table shall be 170 mm, which corresponds to the existing LD Raman spectrometer optical axis height.

- To capture the entire signal, the new LG5.2 lens entrance diameter should, at minimum, be 60.7 mm, which is the collimated beam's diameter after LG4.

- The extension should be easily convertible to a polarization separation setup by swapping certain elements and by positioning them flexibly with traversing and rotational mounts.

- The original Raman spectrometer arm calibration should neither be at risk from the spectrometer extension build-up, nor the in-operando switching process between the single and dual dispersion modes.

- The new integrated camera's control should seamlessly be merged into the current triggering system.

Figure 4.7 shows the final system's design, with which all important requirements are met. It incorporates a coarse camera angle alignment towards the grating axis through a sled rotation on the ground plate (1), a fine rotational adjustment by a micrometer screw (2), a fine rotational adjustment of the grating prism using a rotational stage (3), a coarse distance traverse between the camera-lens combination and the grating using a rail (4), and a fine translation stage between LG5.2 and HD Raman camera to adjust focus (5). An option of tilting the camera towards the lens in two axes ((6), *Scheimpflug adapter*) using a custom-designed ball joint was also designed and built. However, adjustment experiments show that the joint's positioning sensitivity is unimportant to imaging quality and it is therefore frozen in a setting perpendicular to the optical axis.
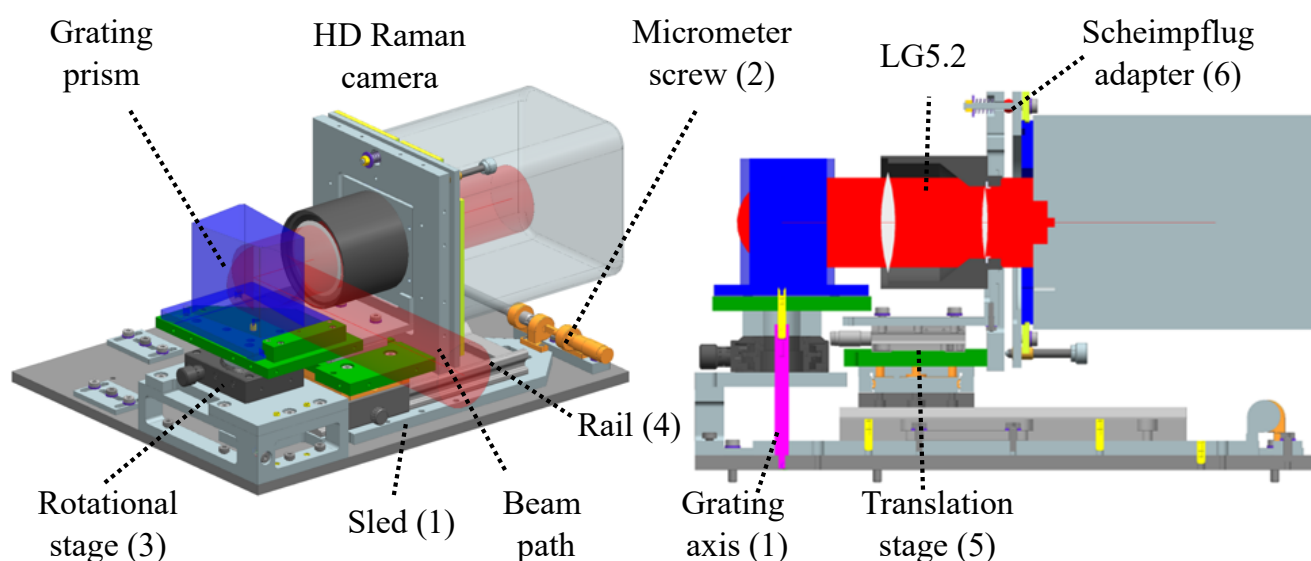
Figure 4.7.: Spectrometer extension CAD design as isometric view (left) and cross-sectional side view (right).

4.3. Acquisition and Data Processing

This section covers acquisition parameters and post-processing steps. After remarks about the pixel discretization, the initial cosmic ray treatment and other noise sources, the SNR derivation is explained.

4.3.1. Binning, Background, Outliers and Axis Calibration

A reasonable balance between resolution and SNR in this experiment is reached by hardware-binning both Raman CCDs in 2-pixel steps in the spatial and spectral directions. This results in 670×650 super-pixels. To ensure proper discretization of relevant gradients in both directions on the CCD chip, additional post-processing binning steps are performed test-wise to confirm that they do not significantly alter the gradients.

To correct for flame luminosity background, images are recorded with the same exposure durations while the laser is turned off and subtracted from each experiment image. A 7×7 super-pixel wide median filter is then applied to remove random cosmic ray phenomena by eliminating outliers more than three local scaled median absolute deviations (MAD) from the local median (Mathworks Matlab® function). The correction is applied only to the affected pixels.

Subsequently, both the spatial and spectral axes are calibrated and linearized (*dewarped*) using the known distances of the point mask and the wavelengths of a 100 µm slit target illuminated by a neon gas lamp (Section 4.2.4.2). It is verified that the spectral shape over wavelength is not altered by the linearization. Intensity normalization and correction of the spectrometer's wavelength-dependent transmission (2D) are then performed using the Ulbricht sphere illumination on a target slit.

4.3.2. Signal-to-noise Ratio and Filtering

The SNR is commonly calculated using a repeated ensemble of measurements at constant process conditions [95]. Because recording one image takes as much 90 min in the currently employed long-exposure mode, an alternative procedure in obtaining an SNR is followed instead. The rationale for the procedure is given in the following.

The raw images are expected to have a shot noise, dark noise, and binary noise combination. On the assumption that a lowpass filter can be tuned to eliminate these visible noise sources and form smooth gradients, a subsequent subtraction of this lowpass filtered noiseless image from the original image creates a residual image solely containing the noise. The signal-to-noise can then be calculated by pointwise division of the original image by the residual image. An important aspect of this procedure is the suitable lowpass filter choice. After unsuccessful attempts with linear and *Fourier*-based filtering, the block-matching and 3D filtering (BM3D) filter by Dabov and coworkers [30] was successful.

For the HD Raman spectrometer arm, Figure 4.8 (top row) exemplarily shows respective lowpass filtered spectra (red) at three temperatures in the primary reaction zone of the EtOH090 ethanol flame (Table 4.1) in comparison to the unfiltered original spectra (black). At the bottom, the residuum generated by subtracting the filtered signal from the original is shown. The filter's suitability is visible by the scattering of values around the zero line. Even at the highest temperatures and lowest signal count levels, this filter's noise exclusion from the original signal is considered accurate. However, as a conservative measure, all result spectra in Section 4.4.3 are still obtained from images that are not lowpass filtered beforehand.

As a result, lowpass filtering is solely applied for two purposes. First, to derive SNR values, which are calculated by dividing the lowpass filtered spectra's maximum in each displayed super-pixel row (at the respective temperature) by the residual image's standard deviation in the same row. Second, to detect outlier signals of unknown origin, which will be described in the following section.
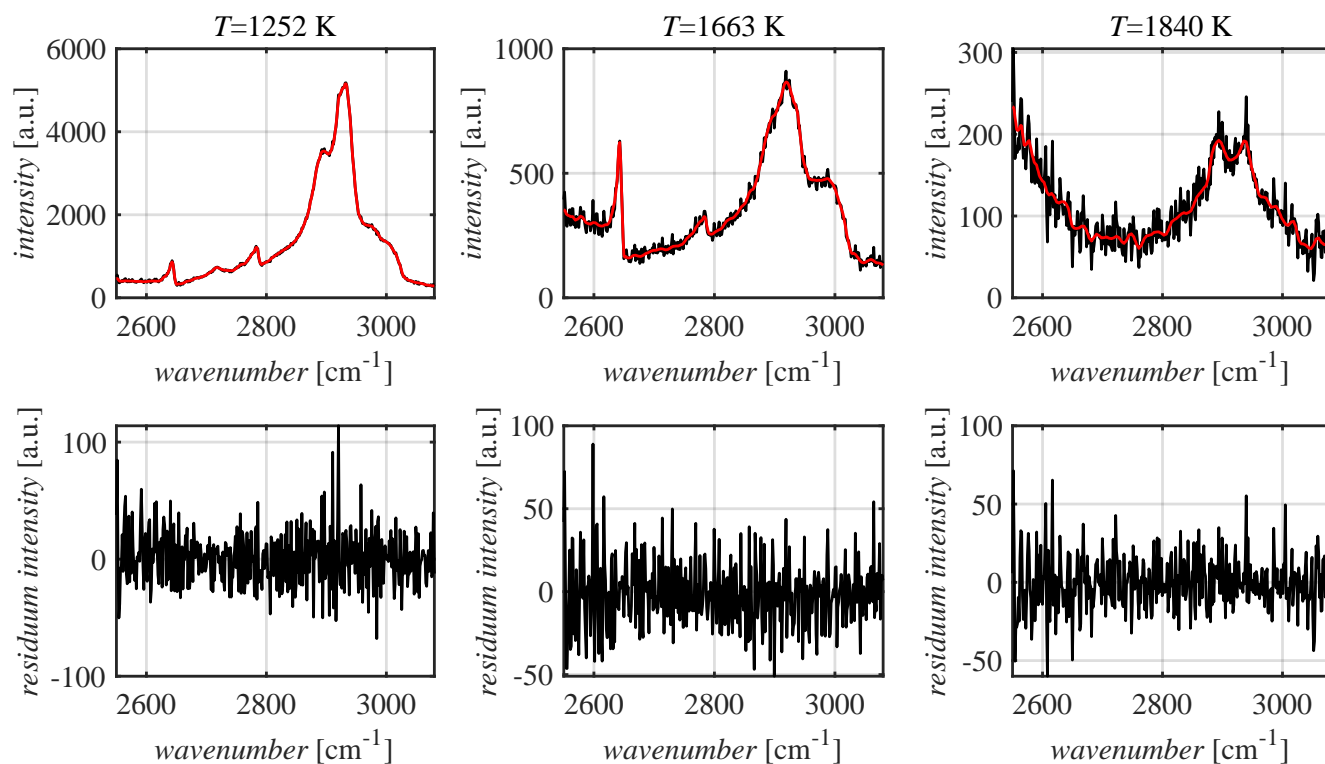
Figure 4.8.: Lowpass filtered Raman spectra (red), non-filtered original Raman spectra (black), and their resulting residua (bottom row). Adopted from Trabold et al. [142] with minor changes.

4.3.3. Erroneous Signal

During the OME150 and OME350 cases (Table 4.1), it is found that on random occasion, excessive signal or over-saturated pixel clusters with a size of 2–3 super-pixels appear (Figure 4.9). This clearly erroneous signal is observed in both pre-heating and reaction zones, and appeared in both the Rayleigh and the Raman images.

The clusters assimilate the *Mie scattering* of dust, when the load and size of particles is under the threshold for optical breakdown. To rule out dust in the present case, the nitrogen coflow was temporally increased three-fold. However, the problem persisted. Another possibility is that the signal's source is the fuel/air mixture itself. Condensation could lead to microscopic small droplets in the liquid phase, which would also increase the signal level drastically due to density spikes. In an attempt to eliminate condensation as an error source, the temperature of all components was increased to the maximum temperature of 473 K. However, the problem still persisted in the same magnitude.

Without further options and because it is a local problem of small spatial scales, the clusters are removed on an automated bases to avoid misinterpretation as spectral features. Before the procedure is explained, examples before and after correction are shown in Figure 4.9.
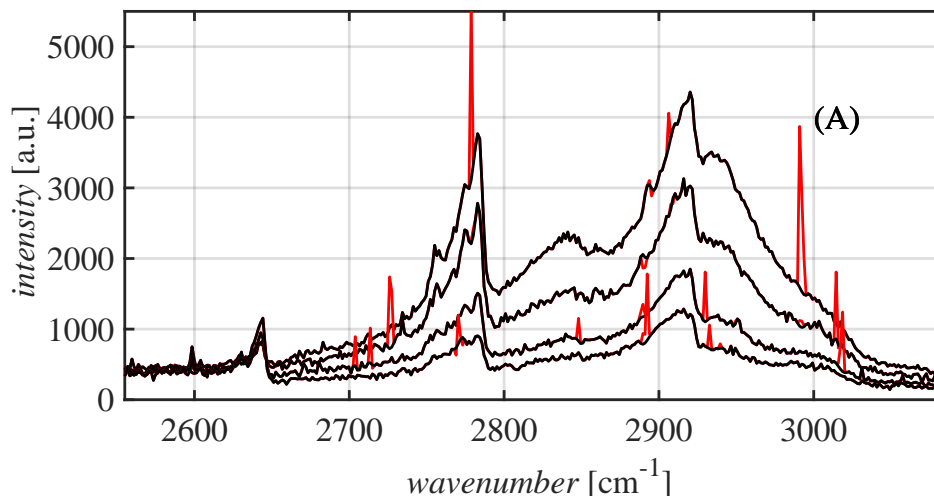
Figure 4.9.: Erroneous signal of unknown origin appeared for the OME150 and OME350 conditions and is shown here exemplarily for the latter. In black, the corrected spectra are shown at four different locations within the flame front. In red, the original error peaks are shown. While they could effectively be removed in the most cases using the procedure described in this section, remaining erroneous peaks needed to be removed manually in very rare cases. Feature (A) is a typical example of such a case. Adopted from Trabold et al. [142] with minor changes.

In the residual images described in Section 4.3.2, the erroneous signals are visible as outliers exceeding each row's 99th percentile. They can subsequently be removed at the same location in the original image, and the resulting gaps are filled with cubic spline interpolations between direct neighborhood super-pixels.

Because the percentile filter is not designed to treat the rarely occurring errors with sizes larger than three super-pixels, such error signals were removed manually instead (example (A) in Figure 4.9).

4.4. Results and Discussion

This section covers the qualitative Raman and Rayleigh experiment results of capturing intermediate species. Section 4.4.1 discusses general observations regarding the measurement system in the applied long-exposure mode. Section 4.4.2 gives insight into the temperature matching from numerical calculations to the experiment. Section 4.4.3 shows the Raman spectra along the probe volume, on which the following detailed spectra within the flame front are based.

4.4.1. Laser Movement, Flame Movement and Actual Strain Rate Influence

A minimum laser and flame movement level is unavoidable during the long-exposure acquisitions. This potentially adversely affects the associated Raman spectra resolution by blurring spatial gradients. Single-shot and mean profiles of integrated 1D Rayleigh signals were analyzed to estimate these effects. Results are given in the following.

Laser Movement: On the one hand, approximately $50\,\mu m$ (1σ) laser position variation due to *beam pointing* were observed using the single-shot Rayleigh images. The resulting bias on the Raman spectra shapes can be investigated on the frequently made assumption that the Rayleigh signal image cross-section in laser-normal direction is representative of the whole spectrometer's transfer function.

Thereby, the transfer function-widening of 5000 overlapped laser shots is inspected. Comparing the mean of all individual Rayleigh signal image cross-sections' FWHM to that of the mean Rayleigh image's cross-section FWHM, the width increase amounts to less than $1\,\%$. That was deemed a negligible factor for the present work's analysis.

The angle deviation from the ideally perpendicularly aligned laser beam towards the flame front was too small to measure. Therefore, any variation thereof was also neglected.

Flame Movement: Variations in the horizontal flame front position are quantified using the maximum axial gradient location in the 1D Rayleigh signal on the fuel/air side. The largest axial flame fluctuations with a *Gaussian*-like distribution and a standard deviation of approximately $67\,\mu m$ is found in the methane/air reference flame at $\phi=3.5$. When comparing the mean individual maximum gradients of all 1D Rayleigh signal realizations with that of all Rayleigh signals averaged, a decrease in the gradient by less than $4\,\%$ can be found. Despite the relatively small effect, the numerical 1D flame calculation that are later fitted onto the experimental results are convoluted with the respective Gaussian distribution to account for these fluctuations.

Actual Strain Rate: As Rolon and coworkers demonstrated [119], counterflow experiments using converging nozzles with large contraction ratios and without screens at the nozzle exit deviate from ideal plug flow velocity profiles. Instead, they form potential flows with velocity minima on the centerline [14, 122]. As a result, the actual strain rate on the centerline differs from the one calculated using the bulk velocities, here referred to as bulk strain rate (Section 4.2.3). In the context of this study, it is not straight forward to match a numerically calculated opposed jet flame with the experiment. Because no velocities are measured, another method needs to be applied to determine the bulk strain rate.

Thereby, the hot gas region widths of the experimental and numerically calculated flames are taken as definite measures for the apparent bulk strain rate. Since the strain rate can easily be varied in numerical calculation, it is changed there incrementally until the width fits that of the experiment. The experiment then has a defined bulk strain rate. To quantify the hot gas region width of the experiment, the Rayleigh signal is suitable. The counterpart for the Rayleigh signal utilized in the numerical calculation is the *synthetic* 1D Rayleigh signal, which is generated with the methodology introduced in Section 3.4.

The accuracy of the bulk strain rate assignment according to the hot gas region width is only limited by the strain rate increments that are numerically calculated. Therefore, it can be claimed that the uncertainty is within $\pm 10\,s^{-1}$ for the most cases. However, difficulties arise when the hot gas region width is on the order of the field of view (FOV) size and barely shows a second gradient on the side

where exhaust gases meet the opposing air stream. This happened for the EtOH150, OME090, and OME150 cases. In those cases, the signal gradient magnitude at spatial coordinate 0 mm (Figure 3.1 and 4.10) is additionally considered for the strain rate determination.

Table 4.4 summarizes the determined strain rates. The initially set bulk strain rate in the experiment was always $\alpha = 300\,s^{-1}$ and the differences from that are up to 33 %. Notably, the methane/air case with equivalence ratio $\phi = 1.5$ exhibits a relatively low deviation in strain rate compared to the ethanol/air and OME-3/air cases. Its larger fitted strain rate can thereby be attributed to the more narrow hot gas region. To investigate the cause of the narrower region, numerical calculations with Cantera are performed (using results from Section 3.4). The calculations reveal that the heat release rates are higher for the ethanol/air and OME-3/air flames, increasing the reacted gases' expansion potential and dampening the inflows from the opposing nozzle. However, this work's scope does not include a detailed strain rate analysis, which would require additional velocity field measurements.

Table 4.4.: Counterflow flame bulk strain rates that are obtained by incrementally fitting the hot gas region widths of equivalent numerically calculated flames to the experimental ones. Obtained from Trabold et al. [142].

ϕ/Fuel or *ID*	0.9/CH$_4$	1.5/CH$_4$	3.5/CH$_4$	EtOH090	EtOH150	EtOH350	OME090	OME150	OME350
Fitted α $[s^{-1}]$	260	290	270	280	200	270	270	200	220

4.4.2. Temperature Assignment

Using the method described in Section 3.4, synthetic 1D Rayleigh profiles are matched with the measured counterparts to estimate local gas temperatures. Figure 4.10 shows the results for ethanol/air and OME-3/air flames. The maximum experimental Rayleigh signal gradient is used to anker the spatial axis at zero. The narrow $\pm 1\sigma$ intervals, shown as a grey shaded area, reflect the well-contained spatial flame fluctuations.

The close matching of the measured and synthetic 1D Rayleigh signal profiles for all operating conditions, which are almost entirely within the flame fluctuations' $\pm 1\sigma$ intervals, indicates very good agreement. As shown in Section 3.4 this leads to temperature assignment uncertainties in the below presented spectra on the order of $\pm 100\,K$ or less, dependent on the fuel and condition.
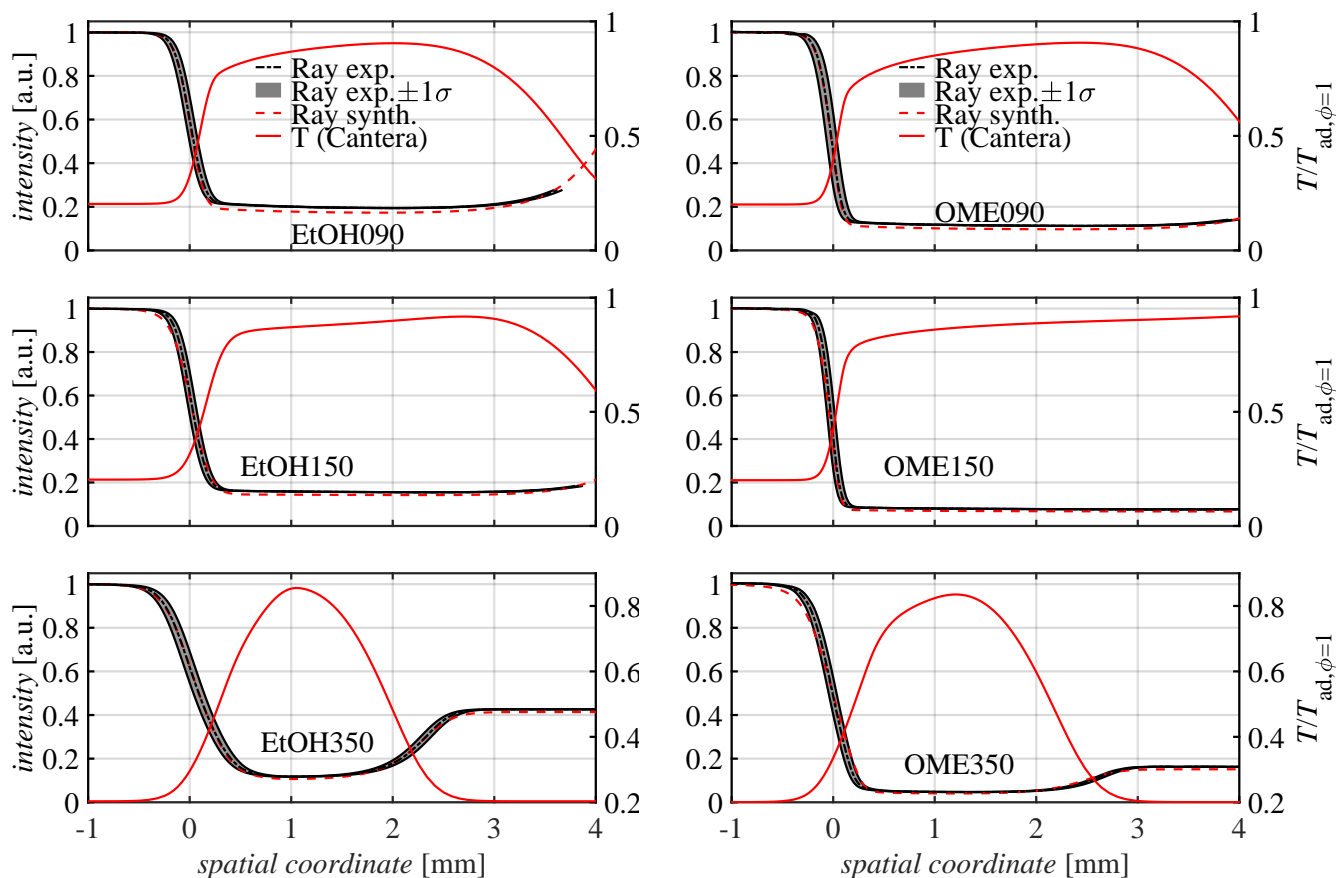
Figure 4.10.: Normalized 1D Rayleigh profiles for ethanol/air (left column) and OME-3/air flames (right column) with a $300\,s^{-1}$ bulk strain rate. The fuel/air premixture originates from the left nozzle, the flow from the right nozzle is air. The grey shaded area marks the narrow $\pm 1\sigma$ range of flame motion. The numerically calculated temperature traces T (red solid lines) normalized to the adiabatic temperature at stoichiometry $T_{ad,\phi=1}$ are given on the right ordinate. Adopted from Trabold et al. [142] with minor changes.

The temperature traces (red solid lines), which are later assigned to the Raman spectra, originate from the numerical 1D flame calculations and are normalized to the respective adiabatic mixture temperatures at an equivalence ratio of one. The strong temperature gradients shown are caused by heat release zones from rapidly occurring chemical reactions. Within these zones, intermediates hydrocarbons (HCs) are produced and consumed. Detecting these intermediates is possible by the present work's long-exposure Raman imaging, the results of which are discussed in more detail next.

4.4.3. Raman Spectra

This section presents and discusses the Raman spectra results captured with the HD Raman camera. After raw data from ethanol/air and OME-3/air flames are compared, the LD Raman spectra are compared to the HD Raman spectra to show the benefit of the setup. Lastly, the flame front spectra, to which temperatures are assigned by concurrent numerical 1D calculations, are displayed.

Raman Image Overview: The center of Figure 4.11 displays the Raman spectra of the partially-premixed ethanol/air flame (EtOH350) on-chip averaged and post-processed (Section 4.3). The vertical axis corresponds to the probe volume's spatial coordinate in Figure 4.10, while the horizontal axis shows the wavenumber range from approximately 700 to $4250\,cm^{-1}$. The Raman image cross-sections located at the top and bottom of Figure 4.11 represent the unburned fuel/air mixture and post-flame zone, respectively, with their exact locations indicated by the dotted horizontal lines at spatial coordinates $-0.8\,mm$ and $1.2\,mm$. In the comparison between these unburned and reacted gases, the number density decline, which is proportional to the signal strength, is evident from the less intense nitrogen bands at high temperatures. In the unburned fuel/air mixture, the ethanol $C-H_2$-bend, C-H-stretch, and O-H-stretch, as well as the rotational-vibrational oxygen and nitrogen Raman bands, are visible. In the post-flame zone, the fuel and oxygen Raman bands disappear, whereas those of carbon dioxide, carbon monoxide, water and hydrogen emerge. The fuel disappearance despite the abundance of fuel in the mixtures is caused by fuel decomposition into carbon monoxide and hydrogen. These have their maximum signal intensity in the close vicinity of the primary reaction zone.

C_2 LIF: A strong signal attributed to the C_2 radical's Swan bands' emissions caused by LIF is observed over a wide spectral range. Spatially, it is restricted to the reaction zone. In the spectrum of EtOH350 at approximately $562\,nm$ (corresponding to $1000\,cm^{-1}$), the intense $C_2(0-1)$ band appears. At the same time, the weaker $C_2(1-2)$ band appears at approximately $557\,nm$ (corresponding to $840\,cm^{-1}$). Both are consistent with the findings of Meier and Keck [97], as well as Brockhinke and coworkers [18]. In addition, at approximately $619\,nm$ (corresponding to an approximately $2630\,cm^{-1}$ Raman shift), $C_2(0-2)$ LIF is observed near the C-H-stretch region. A slight spectral overlap with HC(O) species is visible, particularly in rich and partially-premixed conditions. Ethanol flames are generally more affected by C_2-LIF than the corresponding OME-3 flames, showing such signals not only at rich and partially premixed conditions, but also at lean conditions (EtOH090). The strongest C_2-LIF signal of all considered cases is observed in the EtOH350 case in Figure 4.11.
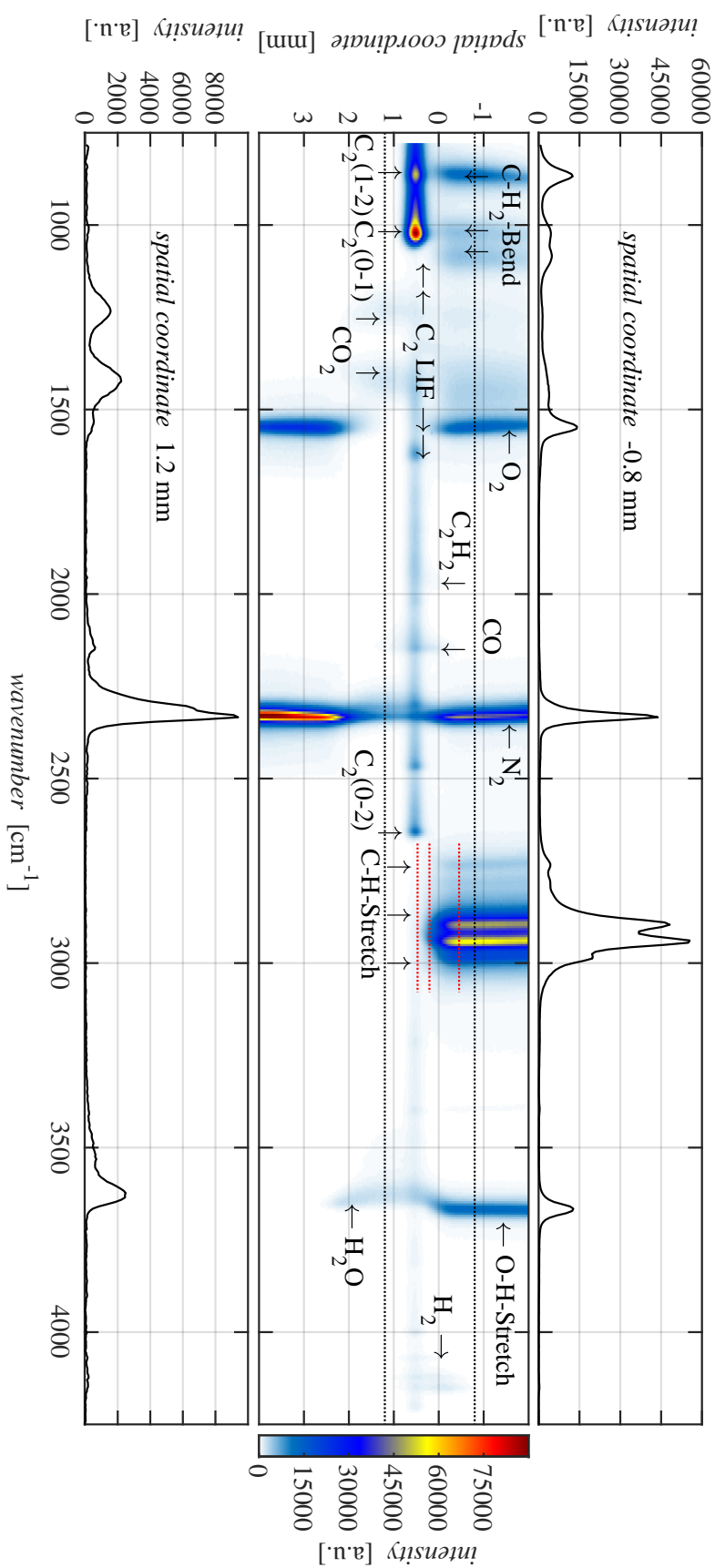
Figure 4.11.: The central graph shows on-CCD sampled LD Raman spectrometer arm spectra for EtOH350 after spatial and wavenumber axis linearization, as well as after intensity calibration. The abscissa displays the wavenumber range corresponding to wavelengths from 553 to 688 nm after excitation at 532 nm. The ordinate displays the spatial coordinate with negative values facing the fuel/air nozzle and zero being located at the previously fitted Rayleigh signal's maximum gradient. The spectra displayed at the top and bottom correspond to unreacted fuel/air mixture and post-flame regions. In the C-H-stretch region, red dotted lines show the locations where the LD and HD spectra will be compared against one another in Figure 4.12. Adopted from Trabold et al. [142] with minor changes.

Comparison of Lower and Higher-dispersed Raman: Three exemplary Raman spectra, which were measured with both the LD (red) and HD (black) spectrometer arms, are shown in Figure 4.12 for comparison purposes. The wavenumber range is the C-H-stretch band region that is located from around 2650 to 3070 cm^{-1} and the target flame is the partially-premixed ethanol/air flame (EtOH350). The spatial positions within the flame structure are indicated by red dotted horizontal lines in the central plot in Figure 4.11. Estimated temperatures at these positions were derived from the fitted numerical calculations and are approximately 480 K, 1000 K, and 1300 K.

The graph clearly displays the dual dispersion setup's benefits. More distinct spectral features are the first visible aspect of the higher spectral resolution that the HD spectrometer arm offers. Furthermore, because the pixel per wavenumber density is much higher in the HD channel (factor of approximately 6.6), the spectra are substantially more robust against the cluster-type noise described in Section 4.3.3 and also against cosmic ray phenomena.

After these first characterizing graphs, the intermediate species spectra in the reaction zone are discussed in the next section.
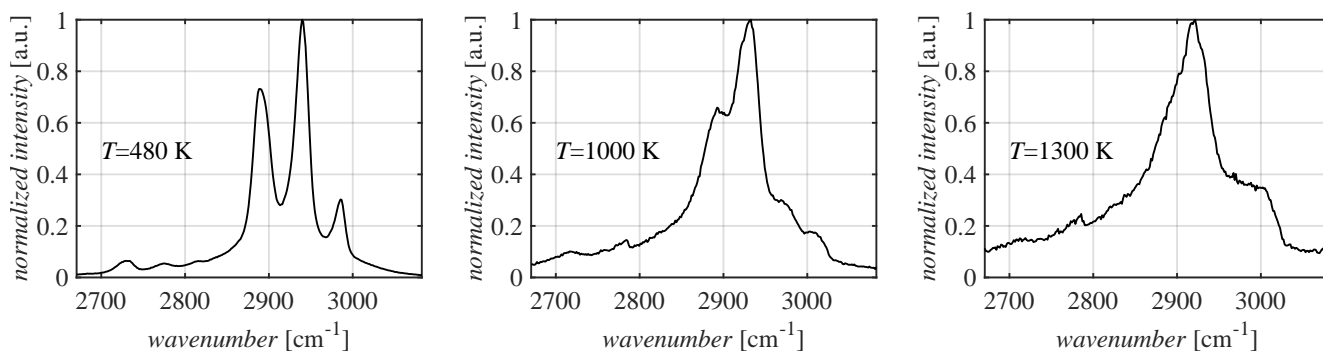
Figure 4.12.: On-CCD sampled Raman spectra measured at three different positions in the EtOH350 flame's reaction zone. Take note that the gas temperatures are estimated from fitted numerical 1D flame calculations (Section 4.4.2). While spectra measured with the LD Raman spectrometer arm are red, HD Raman spectrometer arm spectra are black. Adapted from Trabold et al. [142] with minor changes.

Detailed Flame Front Raman Spectra: The HD spectra for selected ethanol/air and OME-3/air flames, corrected for the local density obtained from concurrent numerical calculations, are shown in Figure 4.13. In each flame configuration, spectra are extracted at four locations to analyze the temperature range from approximately 475 K to 1500 K.

Literature values of the individual species bands' Raman shifts, summarized in Table 4.5 (bold font), are indicated by vertical color-coded bars positioned at the corresponding wavenumber. This helps to identify oxygenated hydrocarbon intermediates formed in the reaction zone, which are underlying the fuel molecules' broad spectra.
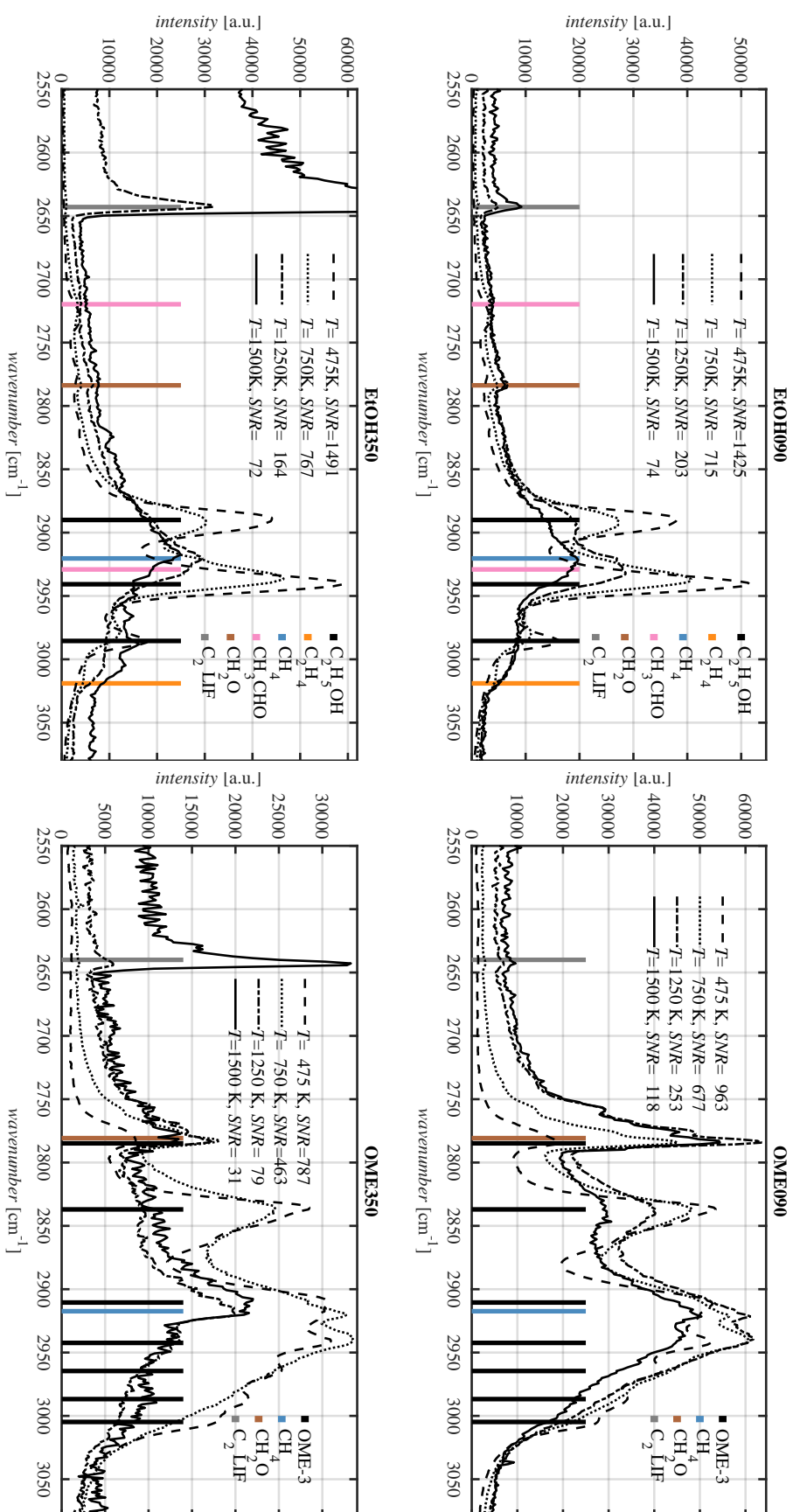
Figure 4.13.: Raman spectra obtained from long-exposure images captured with the HD Raman spectrometer arm. These spectra are corrected for the local number density, which is obtained from the fitted numerical calculations. Lean setpoints are shown at the top, partially-premixed ethanol/air flames at the bottom (left). The same arrangement is given for partially-premixed OME-3/air flames on the right. The spectra are extracted at four different spatial positions within the narrow heat release zone. Temperatures are also assigned from the fitted numerical 1D flame calculations, as detailed in Section 4.4.2. This figure's legend contains the intermediate species that could be identified. Notably, LIF emitted from C$_2$ overlaps with the Raman signal obtained in the C-H-stretch region, particularly at its blue end around 619 nm (Raman shift around 2630 cm^{-1}). Adapted from Trabold et al. [142] with minor changes.

76

For ethanol/air, a characteristic structure with three dominant bands at approximately 2890, 2940 and 2985 cm^{-1} is visible. Due to the larger population of higher rotational-vibrational levels associated with the varying Raman shifts, the Raman bands' widths increase at higher temperatures. Simultaneously and despite the density correction mentioned above, the peak intensity decreases with increasing temperature due to spectral broadening.

The change in population number densities also causes marginal peak position shifts. This is most prominent for the EtOH090 and EtOH350 cases when comparing the temperatures 475 K and 750 K, where the main ethanol peak shifts from approximately 2940 to 2935 cm^{-1}.

With increasing temperature inside the reaction zone, intermediate hydrocarbon species' Raman bands become visible in the fuel spectrum, which itself decreases in magnitude. The SNR values of 30 to 120 even at temperatures up to 1500 K enable to validate the numerical 1D flame calculations' prediction of intermediate species types (Section 3.6).

Upon closer inspection of the ethanol/air flame spectra, the identifiable peaks of acetaldehyde (CH_3CHO), formaldehyde (CH_2O), methane (CH_4), and ethylene (C_2H_4) match with the most prominent species by mole fraction in the concurrent numerical calculation. Acetaldehyde and methane overlap in the most intense ethanol band region. In addition to acetaldehyde, formaldehyde (approximately 2780 cm^{-1}) appears at lower wavenumbers in lean conditions. Ethylene (approximately 3020 cm^{-1}) becomes more visible at higher wavenumbers in partially-premixed conditions.

Compared to ethanol, OME-3 flame Raman spectra are even broader, extending from approximately 2750 to 3030 cm^{-1}. At the lowest temperature, OME-3 exhibits seven bands, of which five overlap on the spectrum's red side, forming a broad peak.

Additionally to those peaks, methane (approximately 2915 cm^{-1}) and formaldehyde (approximately 2780 cm^{-1}) are directly identifiable as the main intermediate species at increased temperatures. This is in line with the numerical OME-3/air flame calculation results presented in Section 3.6, validating the selected mechanism by Cai and coworkers [22]. Formaldehyde, in particular, seems to be an intermediate species with a substantial quantity in the reaction zone at temperatures exceeding 750 K.

Notably, such detailed views would not have been possible using the LD Raman spectrometer arm alone due to its lower spectral discretion. Furthermore, the SNR is proportional to the accumulated laser shots and therefore benefits greatly from the stability level reached with the flames, as well as the excitation and detection systems'.

Table 4.5.: Summary of most important fuel and intermediates' Raman transitions in the C-H-stretch region for temperatures varying between 293 and 473 K (negligible temperature dependence). While more resources for spectral peaks exist in the literature, this table is limited for brevity reasons. Wavenumber peaks listed in bold font are used to indicate peak locations in Figure 4.13 with colored vertical bars. If the sources have slightly varying locations, they are separated by a forward slash. Adapted from Trabold et al. [142] with minor changes.

Species|chemical formula	Approx. peak wavenumbers [cm^{-1}] (bold for most significant)	Literature source/source
Ethanol|C_2H_5OH	2730, 2773, 2812, **2889**, **2939**, **2983**	[33]
OME-3| $H_3CO(CH_2O)_3CH_3$	**2784**, **2837**, **2910**, **2942**, **2966**, **2988**, **3005**	[71]
Acetaldehyde| CH_3CHO	∼/**2716**, ∼/**2748**, 2822/2828, **2917**/**2926**, 3005/3014	[127]/K. Dieter, pers. commun., July 2021
Formaldehyde|CH_2O	**2777**/**2783**, 2843	[127]/K. Dieter, pers. commun., July 2021
Methane|CH_4	**2916**/**2917**, 3020/3021	[112]/K. Dieter, pers. commun., July 2021
Ethylene|C_2H_4	3026/**3016**	[127]/K. Dieter, pers. commun., July 2021

4.5. Summary and Conclusion

This experiment captured spatially and spectrally highly-resolved Raman data in laminar premixed opposed ethanol/air and OME-3/air flames. Since these fuels are liquid under ambient conditions, a vaporization system and a heated burner, the laminar temperature-controlled opposed jet burner (LTOJ), were necessary. While the former was commissioned during this work, the latter was successfully designed, built and commissioned.

On the detection side, the TUDa Raman spectrometer was equipped with a newly designed higher-dispersed spectrometer arm, with which the densely populated C-H-stretch region of complex fuel flames' spectra can be captured in more detail. In combination with the lower-dispersed Raman spectra and the Rayleigh signal, a versatile measurement system was established to simultaneously study main and intermediate species in flames of complex fuels.

To facilitate capturing the intermediates, which is challenging due to very low number densities, a long-exposure mode was applied for the first time. Thousands of laser shots are thereby averaged on-chip before being read out once. This enables detection with the highest possible SNR, even capturing signal that would otherwise be below the read-out noise.

Besides this operational change to the typical single-shot spontaneous Raman spectroscopy, more material changes were made by introducing a third shutter wheel for longer durability and a new housing for the complete spectrometer. Finally, the captured data sets were further enhanced by transferring fitted numerical 1D flame calculation results to the experimental data.

The key data presented in this chapter were the before-mentioned highly resolved spectra of lean and partially premixed ethanol/air and OME-3/air flames at four temperatures from $475\,\mathrm{K}$ to $1500\,\mathrm{K}$. The Raman peaks, which had SNRs greater than 30 even in the flames' hottest regions, validated the existence of intermediates predicted by concurrent numerical 1D flame calculations. As an example, despite the very small amounts of intermediates ($<1\,\mathrm{mol}-\%$ in some cases), even differences between lean and rich flames were clearly visible in the intermediate species peaks.

In summary, all except the last research targets, which claimed to not only identify but essentially quantify the amount of intermediates, were reached. This was not possible yet, because the available individual intermediate species Raman spectra are too far off the flame temperatures to either use them, nor to make valid estimates about their shapes and magnitudes at higher temperatures. However, the methods and equipment presented in this chapter ensure that it will be possible once these spectra become available.

5. Operational Envelope and Flame Topologies of Piloted Turbulent Jet Flames

5.1. Introduction

This chapter covers experiments capturing the sensitivities to equivalence ratio and turbulence intensity of several alcohol/air and methane/air flames.

The overarching goal is to gain an increased understanding of fuel effects on local and global flame characteristics. The steps to reach this target are:

1. To commission the Temperature-controlled Piloted Jet Burner (TCJB) system with alcoholic fuels

2. To evaluate the upper boundaries of the TCJB operational envelope with different fuels

3. To capture data in various flames and develop the post-processing code to evaluate flame topology

4. To identify fuel-dependent differences in the results and possible reasons therefore

Regarding the chapter structure, the TCJB commissioned during this work is introduced first. Next, a series of three experiments are presented and the results are discussed. While blow-off can be investigated by visual and audible perception, chemiluminescence (CL) imaging of electronically excited CH*-radicals is used to capture flame lengths. Flame curvature κ and flame surface density (FSD) are investigated using OH-Planar laser induced fluorescence (PLIF). Notably, it is referred to numerical flame calculation results of chapter 3 at several occasions. Therefore, the reader is guided to read that chapter first in order to receive a complete understanding.

Parts of this chapter are published in Trabold et al. [141].

5.2. Experimental Setup

This section first introduces the TCJB burner and the pre-vaporization system used to vaporize the liquid fuels. Next, the operating conditions under which these systems run at are summarized, before the excitation and detection systems are presented.

5.2.1. Temperature-controlled Jet Burner

Figure 5.1 shows two cross-sectional views of the novel TCJB system that is commissioned during this work. It is designed to operate on gaseous or liquid fuels with the capability to run at low and large turbulence intensities. This is enabled by heating the entire burner and by providing the necessary activation energies for igniting highly turbulent flows using a jet-surrounding pilot flame. The *Sydney burner*-inspired design [39, 91] is covered in more detail in the following.

The burner setup includes a central stainless steel jet tube (depicted in blue in Figure 5.1, right) with an 11.4 mm inner diameter and a 500 mm length. This results in a $L/D_{i,jet}$ ≈ 43 non-dimensional tube length, ensuring that the flow within the tube is fully developed at the nozzle exit.

To control the jet tube wall temperature, three nozzle heaters (Hotslot Mini) with a 150 mm length each are used (depicted in brown in Figure 5.1, right). The premixed fuel/air mixtures enter the burner through 16 holes located at the burner's base. The base is furthermore heated by four custom-designed heating jackets.

To avoid any cold spots and prevent condensation of the pre-vaporized fuel/air mixtures, the temperature is maintained above the due point and controlled within ± 1 K over the whole burner assembly. This is achieved using electrically heated plates regulated by J-type thermocouples and several PID controllers (Jumo cTRON 08). Thermocouple measurements at the nozzle exit and within the pre-vaporized fuel/air stream verify the minor fluctuations of ± 1 K.

The pilot flame configuration consists of an arrangement of 144 individual laminar premixed Bunsen-type flames that originate from a flame holder in a co-annular tube with a diameter of $D_{pilot} = 31$ mm. The flames are circularly evenly distributed in four rings with 36 bore holes each. The bore hole diameters from the inside to outside rings are 0.8, 0.95, 1.1, and 1.2 mm (Figure 5.1, right, depicted in green).

The reactants for the pilot flame, hydrogen, acetylene, carbon dioxide, air, and nitrogen, are mixed upstream of the burner at ambient temperature. The ratio of the first four components is varied to match the C/H/O atom ratio of the jet mixture at a fixed $\phi = 0.7$ equivalence ratio. The adiabatic pilot flame temperature is then adjusted by varying the nitrogen fraction to match the adiabatic temperature of the respective jet mixture at $\phi = 0.7$.

The pilot flame gas mixture composition for each fuel is summarized in Table 5.1, along with the bulk heat releases and adiabatic temperatures. It should be noted that depending on the Reynolds numbers selected, the pilot flames' heat releases do not exceed 1.5 to 10 % of the jet flame's bulk heat release (see Figure 5.2).

A dry and filtered air coflow with a 0.3 m/s bulk velocity surrounds the pilot and jet flames to shield the flame and ensure well-defined boundary conditions. The nozzle has a 260 mm coflow diameter and its contour with a 2.89 contraction ratio is shaped according to Bell/Mehta's design principles [13]. Thereby, a most uniform axial velocity profile can be reached at the coflow exit.
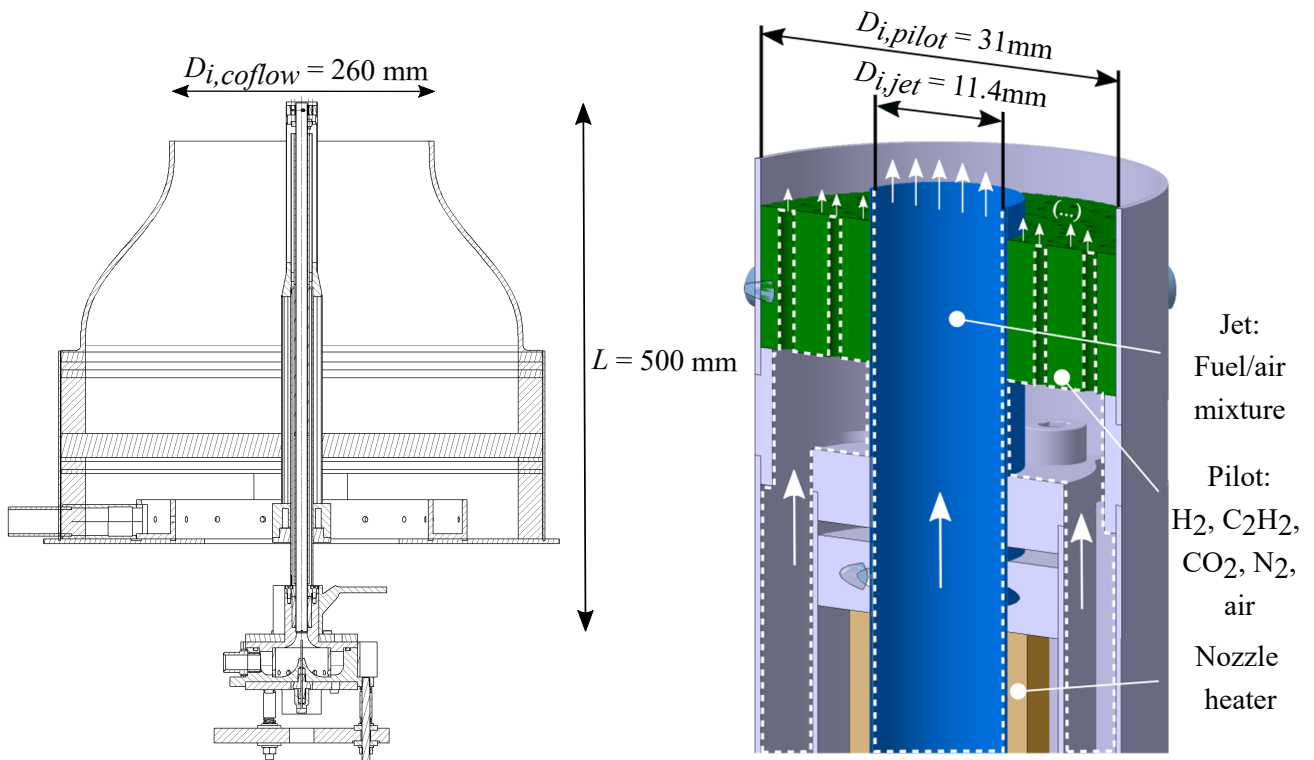
Figure 5.1.: Overall TCJB cross-section including jet, heating, burner base and coflow (left). Detailed cross-sectional view of the jet tube (blue), flame holder (green), and heating elements (brown). Adapted from Trabold et al. [141] with minor changes.

5.2.2. Pre-vaporization System for Liquid Fuels

The dual-purpose vaporization system that is used with both the LTOJ and the TCJB was already described in Section 4.2.2. Notably, for this experiment, the additional gas heater was used to provide the necessary heating power at high flow rates.

5.2.3. Operating Conditions

The four lowest alcohols methanol, ethanol, 2-propanol, and 2-butanol are chosen as potential biofuel additives or surrogates to fossil fuels. The following study will compare global and local flame characteristics of their premixed flames and compare them to the methane/air reference.

In the first experiment, the blow-off limits for each fuel/air mixture are determined as a function of the equivalence ratio, which is varied in 0.05 increments from lean (ϕ=0.8) to rich (ϕ=1.5). Consequently, maximum bulk velocities vary depending on the individual blow-off limit and range from $u_{bulk,bo}$=30 to 95 m/s (equivalent bulk Reynolds number Re_{bulk}=18000 to 61000).

In the second experiment, the non-dimensional flame lengths H_{fl}/D are compared for a fixed 18000 bulk Reynolds number and for the same equivalence ratios. Therefore, the flame CH* CL is used as a marker.

Table 5.1.: Pilot flame gas compositions, heat releases and adiabatic temperatures. Adapted from Trabold et al. [141] with minor changes.

Parameter	Methane/air	Methanol/air	Ethanol/air	2-Propanol/air	2-Butanol/air
Air fraction [mass-%]	76.19	77.84	79.55	80.29	80.55
Nitrogen fraction [mass-%]	8.41	1.66	4.31	5.17	5.72
Hydrogen fraction [mass-%]	10.93	14.22	10.18	8.70	7.96
Carbon dioxide fraction [mass-%]	2.47	4.62	3.48	3.04	2.84
Acetylene fraction [mass-%]	2.00	1.66	2.48	2.79	2.93
Heat release [Watt]	598	639	646	650	651
Adiabatic mixture temperature [Kelvin]	1873	1920	1912	1908	1916

Finally, in the third experiment, curvatures and flame surface densities Σ are evaluated for lean and rich conditions (ϕ=0.9 and 1.05) at two different turbulence levels (Re$_{bulk}$=12000 and 18000) using OH-PLIF.

The bulk flow temperature at the jet exit is 343 K for all alcohol/air mixtures, whereas for methane/air mixtures, the temperatures 293 K and 343 K are investigated. Table 5.2 summarizes the operating conditions. The flame and mixture parameters, which are derived from numerical calculations, are summarized in Table 3.2 in Section 3.5.4.

Table 5.2.: TCJB operating conditions and the respective experiments conducted. Adapted from Trabold et al. [141] with minor changes.

Experiment	Maximum bulk flow	CH* CL	OH-PLIF
Parameter	Blow-off velocity $u_{bulk,bo}$	Flame length H_{fl}/D	Effective Lewis number Le$_{eff}$ FSD Σ_{2D}, Curvature PDF(κ)
Equivalence ratio	0.8...0.05...1.5	0.8...0.05...1.5 0.9, 1.05, 1.5	0.9, 1.05
Reynolds-number (bulk)	CH_4=28000...35000 CH_3OH=21000...61000 C_2H_5OH=18000...55500 C_3H_7OH=18000...45000 C_4H_9OH=18000...48000	18000	12000, 18000
Fuel	Methane, methanol, ethanol, 2-propanol, 2-butanol	Methane, methanol, ethanol, 2-propanol, 2-butanol	Methane, methanol, ethanol, 2-propanol, 2-butanol
Mixture temperature (unburned)	Methane/air: 343 K Alcohols/air: 343 K	Methane/air: 293 K, 343 K Alcohols/air: 343 K	Methane/air: 293 K Alcohols/air: 343 K

To ensure similar turbulence levels, constant Reynolds numbers are maintained across varying fuel/air mixtures in the individual experiments. Therefore, because the methane/air mixture kinematic viscosities at 343 K (293 K) are between 10 and 20% larger (smaller) than those of the alcohol/air mixtures, bulk velocities must also be respectively larger (smaller). Accordingly, the

thermal powers $P_{\text{thermal,bulk}}$ vary distinctively, as displayed in Figure 5.2 for a 12000 Reynolds-number (left) and at blow-off (right). Note that a piloted jet flame's blow-off condition depends heavily on the pilot flame's influence. As done by Coriton et al. [27], the pilot is run at lean conditions to minimize the thermal power output and thus this influence on the jet flame. This also helps to prevent potential heating damage to the directly adjacent jet pipe.
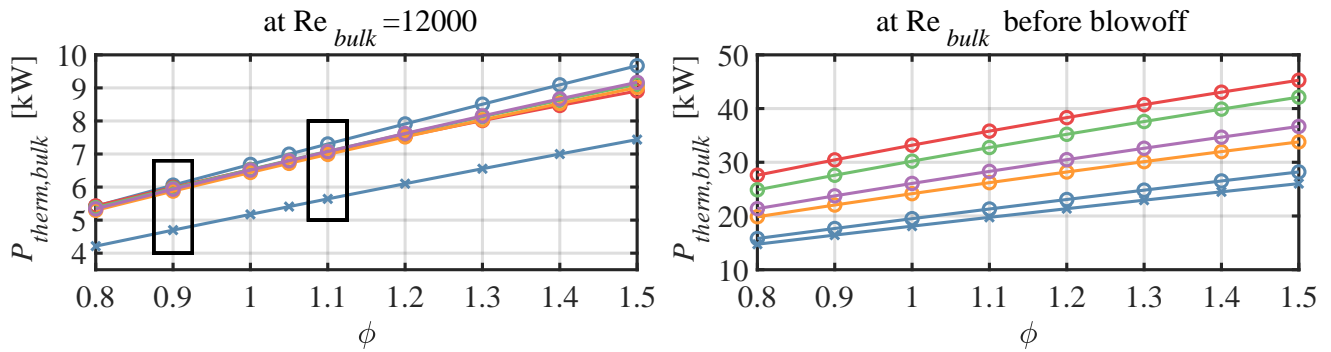
Figure 5.2.: TCJB thermal powers at a 12000 Reynolds number and at blow-off bulk flows. The black boxes locate the equivalence ratios at which the detailed flame topology studies of curvature and flame surface density are conducted. ■ Methane/air; (x T_u=293 K, o T_u=343 K); ■ Methanol/air; ■ Ethanol/air; ■ 2-Propanol/air; ■ 2-Butanol/air. Adapted from Trabold et al. [141] with minor changes.

A characterization into the Borghi-Peters diagram was attempted using a LES study. Because of the small depth of this simulation project and the minor importance to the following discussions, it was decided to place it in Appendix B.1.2.1.

5.2.4. Excitation and Detection Systems

5.2.4.1. Chemiluminescence Imaging

Electronically excited CH* is a common marker for locating reaction zones in hydrocarbon-fueled flames [36, 75]. To capture this CL, the strong A-X(0,0) band emission peak near 431.4 nm is captured using a scientific CMOS camera (LaVision Imager sCMOS) equipped with a 50 mm F1.8 lens (Nikkor). Other radicals' crosstalk, namely OH*, C_2* and CO_2* [75, 121], is reduced by using a 434±17 nm bandpass filter (BrightLine HC).

While the FOV measures 244x206 mm^2 and the pixel discretization reaches 95 μm/pixel, the optical resolution, which is determined using a Siemens star, is approximately 115 μm (8.6 lp/mm). To capture flame fronts from the nozzle to the tip, the burner is axially traversed between the two vertically recorded images. Exposure times at all operating conditions are 250 ms due to the relatively low signal, resulting in time-averaged capturing of flame front features.

In addition to the CH* CL, broadband CL images with color information are captured with a separate digital consumer camera.

5.2.4.2. OH-Planar Laser-induced Fluorescence

Instantaneous flame contours are monitored by OH-PLIF (Section 2.7.1). The measurement scheme is shown in Figure 5.3.
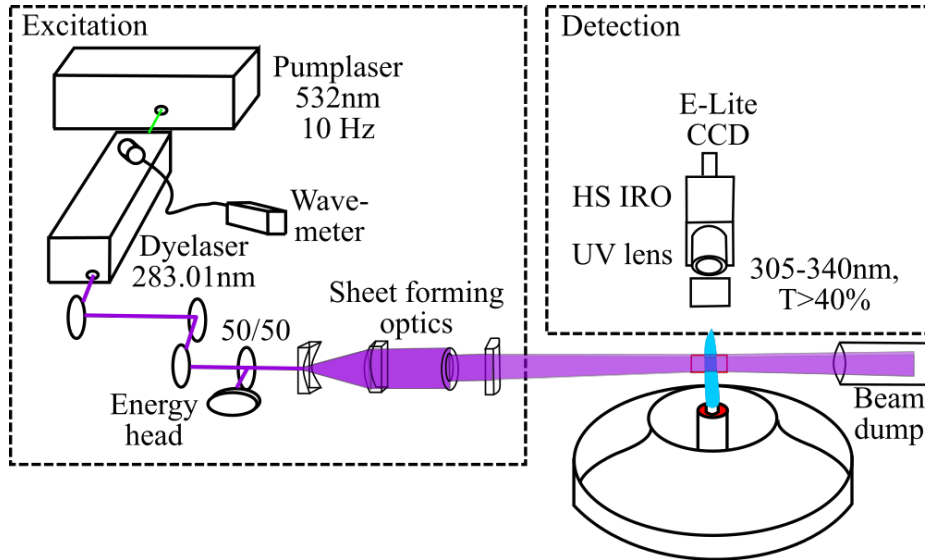
Figure 5.3.: OH-PLIF setup excitation and detection scheme. Adopted from Trabold et al. [141] with minor changes.

To excite the OH A-X(1,0) $Q_1(6)$ line transition at 283.01 nm, a frequency-doubled Nd:YAG laser (Spectra Physics, PIV 400, 300 mJ at 532 nm, 10 Hz) pumps the dye laser (Sirah Lasertechnik GmbH, DoubleDye, Rhodamine 6G). The resulting pulse energies are reduced by beam splitters from approximately 2.9 mJ to 0.3 mJ in order to remain in the linear regime, which was verified before the measurement. From this beam, a cylindrical lenses arrangement forms a laser light sheet with a 25×0.2 mm^2 cross-section. The reported FWHM sheet thickness is thereby measured with a beam monitor (WincamD, DataRay Inc.). On the detection side, a UV lens (Sodern UV 100F/2.8) captures the induced OH fluorescence signal, which is then imaged onto a CCD camera (Imager E-lite, LaVision GmbH) equipped with intensified relay optics (IRO, High-speed, LaVision GmbH).

To ensure only the A–X(0,0) and (1,1) band emissions are recorded, the UV lens is equipped with a bandpass filter (BP300-325, Laser Components GmbH). Gating the intensifier for only 300 ns suppresses the bias by OH* CL and broadband flame luminosity. The PLIF detection system is arranged perpendicular to the laser light sheet and images the whole flame brush horizontally in a 24×32 mm^2 FOV. To capture the flame structures at different heights, the burner is axially traversed to six consecutive locations above the burner ($x/D=1, 3, 5, 7.5, 10, 13$). Notably, while the FOVs at $x/D=1$, 3, and 5 partly overlap, those farther downstream, spanning from $x/D=7.5$ to 13, do not.

The detection system pixel discretization is 23 μm/pixel, and the approximately 110 μm optical resolution (9 lp/mm) is derived from imaging a Siemens star with UV light of similar wavelength. In order to yield a sufficient statistical data base, 2000 images are recorded for each operating condition and axial location. In addition, 200 images for the purpose of background correction are

recorded at each location while the laser is operating outside the mentioned resonance excitation wavelength.

5.3. Acquisition and Data Processing

This section details the data capture and the subsequent post-processing methodologies.

5.3.1. Flame Lengths

To obtain flame lengths, local flame CH* intensities are compared using an average of 100 CL images per fuel and flame condition, while keeping the lens aperture and camera gating time constant. From these averaged images, the flame lengths are derived through several steps. First, the two axial images are stitched together, and outlier pixel data are filtered using a 5x5 pixel median filter. Secondly, an *Abel inversion* is performed to calculate the 2D flame length from the 3D line-of-sight signal [117]. Finally, the flame lengths are defined by the axial location where normalized intensity of the the radially integrated 2D signal drops to 25% of the axial maximum, as proposed by Carbone et al. [23].

5.3.2. Curvature and Flame Surface Density

Figure 5.4 visualizes the post-processing steps to retrieve the wrinkling parameters curvature and FSD from OH-PLIF data.

Figure 5.4 (a-b): After background correction, images are corrected for laser sheet inhomogeneity by using an averaged profile at each flame condition and height [46].

Figure 5.4 (c): Segmenting into unburned and burned mixture (binary image) is done by a maximum OH gradient filter [103].

Figure 5.4 (d): The resulting interface between unburned and burned areas is the flame front position and is fitted with cubic spline segments using the methodology described by Sweeney et al. [136]. The 2D curvature can be directly deduced from these splines.

Figure 5.4 (e): Using the mean of all binary images, the reaction progress variable c can be obtained (not utilized in this work).

Figure 5.4 (f): The 2D flame surface density field Σ_{2D} is calculated according to Donbar et al. [36]:

$$\Sigma_{2D} = \lim_{\Delta x \to \delta_f} \frac{\underline{P}}{\Delta x^2}. \tag{5.1}$$

Next, the FSD derivation process is described in more detail. The above introduced flame front spline length on a sub-pixel scale is represented by the perimeter $\underline{P}$. The pixel-wise sum of $\underline{P}$ is computed across all realizations and subsequently, to calculate the 2D FSD Σ_{2D}, a moving average
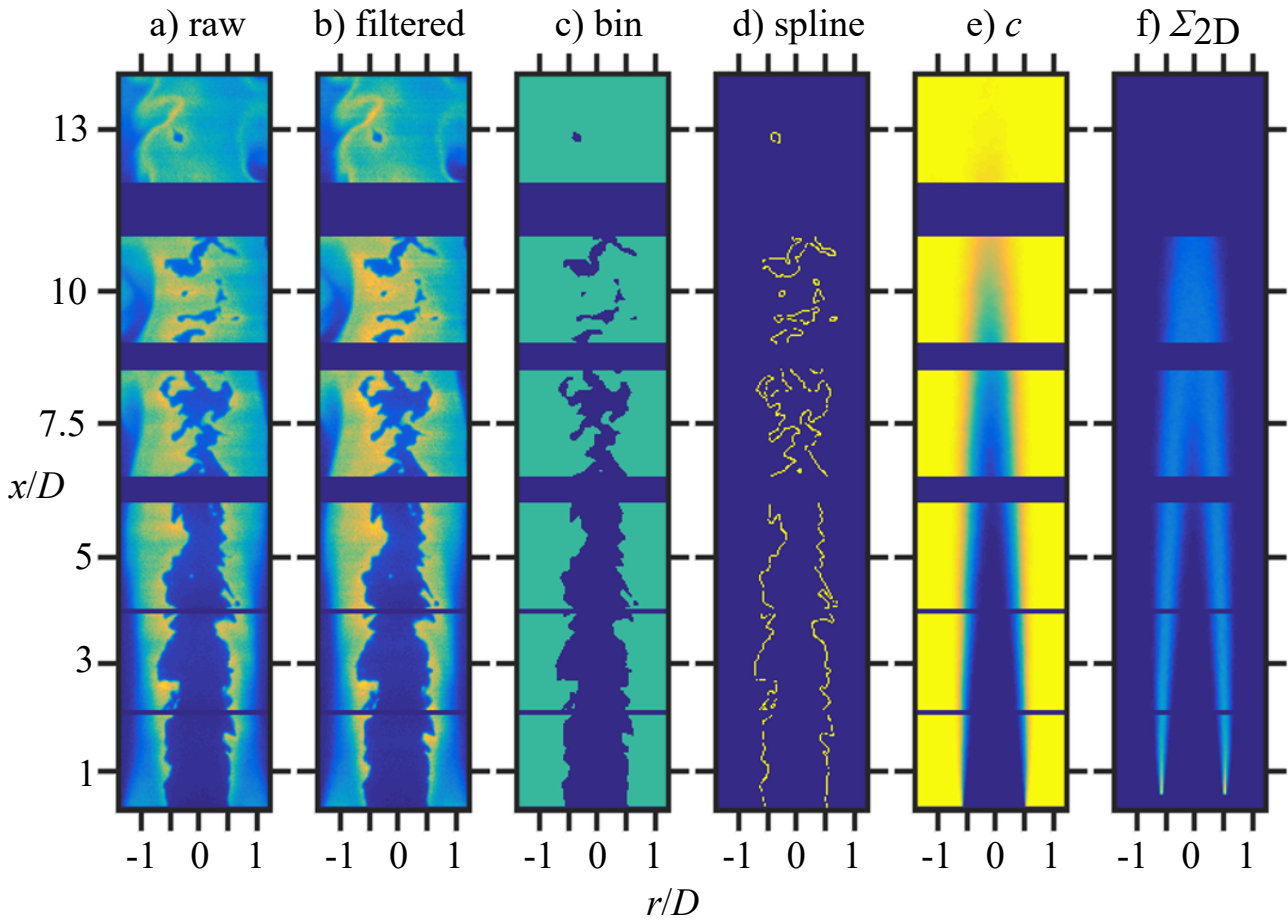
Figure 5.4.: OH-PLIF data processing steps: (a) shows raw stitched individual x/D images, which are corrected for background and laser light sheet inhomogeneity in (b). (c) displays the images in binarized form and (d) the splines that are fitted to the flame flame fronts derived from (c). The reaction progress variable c is shown in (e), which is deduced from all binarized images. The flame surface density field Σ_{2D} shown in (f) is calculated from the spline segments' lengths. Adopted from Trabold et al. [141] with minor changes.

filter is applied to this summed $\underline{P}$ image. The edge length of the moving average filter interrogation window is $\Delta x = 0.5$ mm. This value is chosen because it is larger than the expected flame front thickness δ_f and at the same time, it is five times smaller than the minimum flame brush thickness (refer to Section 2.1.2 for the rationale). Furthermore, a parametric study varying Δx confirms that within the two mentioned limits, Σ_{2D} is insensitive to the interrogation window size.

By dividing the summed and filtered $\underline{P}$ matrix by the number of instantaneous realizations at each FOV, the ensemble-averaged 2D FSD Σ_{2D} is obtained. This parameter is then integrated radially across the flame brush to acquire the integrated FSD ($\Sigma_{2D,int}$) using the following equation (similar to what was done by Filatyev et al. [49] and Shepherd et al. [126]):

$$\Sigma^*_{2D,int} = \frac{1}{2 \cdot n} \sum_{i=1}^{n} \int_{FOV,\,l.b.}^{FOV,\,r.b.} \Sigma_{2D,i}\,dr, \tag{5.2}$$

Here, n represents the number of OH-PLIF image realizations at a given flame condition and FOV containing a flame front, r is the radial coordinate, and $l.b./r.b.$ denote the left and right boundaries of the FOV. The factor $\frac{1}{2}$ is included to account for the two flame branches observed by the intersecting laser light sheet and FOV. The resulting integrated FSD $\Sigma_{2D,int}$ is dimensionless, as it is integrated from the 2D FSD field (unit mm^{-1}) over the radial direction (unit mm).

To yield an ensemble-averaged value, up to 2000 independent statistical realizations are considered depending on the axial position and the operating condition. Sample numbers are reduced from the 2000 images to as low as approximately 400 at higher x/D, when the flame height is reached and a decreasing number of images contains detectable flame structures.

5.4. Results and Discussion

This section presents and discusses the blow-off, flame length and flame topology experiment results.

5.4.1. Blow-off Stability

Blow-off stability defines the upper bulk velocity boundary of a burner's operating envelope. More specifically, if the bulk velocity exceeds a critical value, the flame extinguishes either partly or entirely due flow induced strain. It thus serves as an interesting comparison parameter to classify different fuel mixtures' abilities to sustain high strain.

During the experiment described in the following, the TCJB's jet bulk velocity u_{bulk} is incrementally increased in $0.7 \, m \, s^{-1}$-steps until blow-off occurs. That limit is reached when the flame's blue CL is not sustained downstream of the pilot flame's exhaust region and when the flame's audible rumbling stops. For reference, the pilot region can be seen in the bottom of Figure 5.4 (a).

The blow-off experiment's results are depicted in Figure 5.5, which shows the maximum bulk velocities at blow-off $u_{bulk,bo}$. The equivalence ratios span from $\phi=0.8$ to 1.5 in 0.05-steps.

Independent of the fuel, flames are more blow-off resistant with increasing equivalence ratio. The explanation for this larger stability are the increased extinction strain rate resistances of rich flames in ambient oxidizer, a phenomenon described in Section 3.5.1. In brief, the secondary diffusion flame structure in this particular setup is fueled by excess hydrocarbons from the partially-premixed jet and excess oxygen from the lean pilot flame. This diffusion flame counteracts the heat loss of the stretched shear layer close to the rim [48, 85]. Notably, the inverse setup of a rich pilot and a lean jet was studied by Guiberti et al., yielding similar findings [60, 61].

Next, potential reasons for the blow-off differences among varying fuel/air mixtures are discussed:

Pilot Flame: During this study, the pilot flame was constantly operated at equivalence ratio $\phi=0.7$ (Table 5.1). With the resulting relatively low adiabatic mixture temperature, only minor differences in heat release influence towards the jet are expected. This corresponds with a study by Guiberti
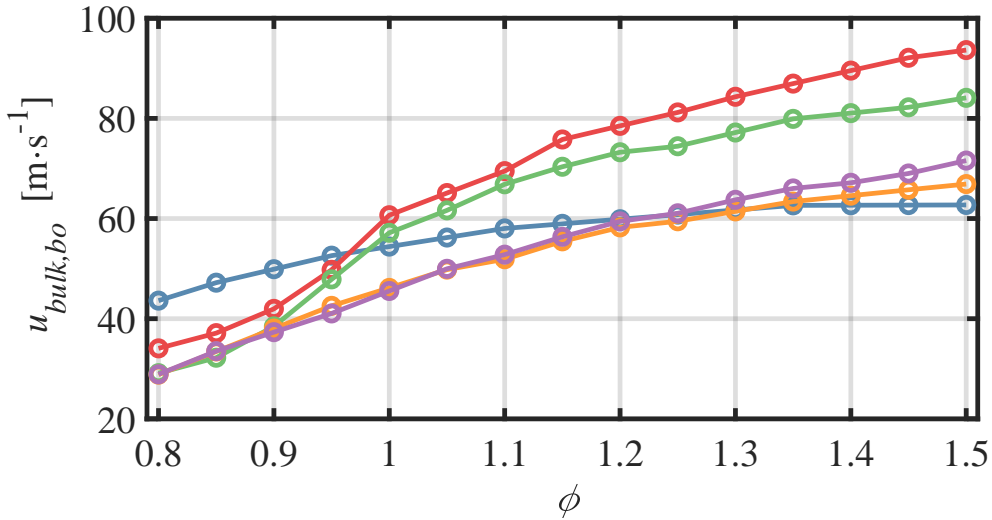
Figure 5.5.: Results for the bulk velocity $u_{bulk,bo}$ at blow-off experiment at a $T_u = 343\,\text{K}$ unburned mixture temperature in equivalence ratio space.   ■ Methane/air;   ■ Methanol/air;   ■ Ethanol/air;   ■ 2-Propanol/air; ■ 2-Butanol/air. Adopted from Trabold et al. [141] with minor changes.

et al. [61], who also find that the pilot does not substantially influence fuel-specific differences in blow-off stability.

Laminar Flame Speed: Among the alcohol/air mixtures, the stability increased with decreasing chain length, with methanol/air being the most stable. Therefore, one hypothesis is that the higher reactivity that comes with the relatively high methanol/air flame speed also increases blow-off resistance. While this might be true, the similar laminar flame speed of ethanol/air and the two larger alcohols (compare Figure 3.2) contradicts with the finding that the latter two are substantially less blow-off resistant. Therefore, additional factors besides must be at play.

Extinction Strain Rates and Temperatures: Comparing the fuel-dependent extinction strain rate study results depicted in Figure 3.3 with the results of the blow-off experiment, a clear correlation can be seen (Section 3.5.1). The relative differences among the three fuels match up with the jet flame blow-off velocities at rich conditions, possibly explaining the different behavior. However, in lean conditions, methane/air mixtures are more resistant against blow-off than alcohol/air mixtures, which is not reflected in the numerical calculation. Therefore, under lean conditions, a different effect may play out with regard to opposing blow-off behavior among the fuels.

Influence of Radicals and Lewis Number Effects: By studying CL, Carbone et al. [23] showed that compared to longer hydrocarbons, methane/air had significantly higher radical concentrations under lean conditions. That would improve stability against blow-off through facilitating chain branching reactions.

Carbone et al. [23] further hypothesized that longer-chained fuels might be at a disadvantage regarding large wrinkling because of their high Lewis number, which was also indicated in Section 3.5.3 for the present alcohol fuels at lean conditions. Especially in the presence of strong shear forces, this could bring a decisively lower reactivity compared to methane/air. Furthermore, methane/air's maximum laminar burning velocity at equivalence ratio $\phi=1.05$ is closer to lean condition compared to the alcohol/air mixtures', which peak between $\phi=1.1$ and 1.2.

The aspect of fuel-dependent reactivity for blow-off is also highlighted by Guiberti et al. [61]. At this state of the discussion, the experiment's results support this hypothesis.

Flame Wrinkling: Despite the findings by Carbone and Guiberti regarding the Lewis number's influence on reactivity, it may still be ruled out as substantial blow-off stability improving mechanism in the closer nozzle region. This is because even in less turbulent flames, flame wrinkling differences among fuels start only as far downstream as $x/D=4$ for lean conditions (refer to Section 5.4.3).

However, below $x/D=4$ is precisely where the most shear forces exist and the blow-off stability is likely decided. Therefore, wrinkling and Lewis number may in fact have limited influence on the results in lean conditions.

In summary, the blow-off differences among the fuels at stoichiometric and rich conditions are likely caused by differing extinction strain rates. At lean conditions, a number of effects take place and their superposition influences the blow-off behavior.

5.4.2. Flame Length

The next flame parameter discussed is the flame length. To provide a visual impression, the photographs in Figure 5.6 (left images) show the slightly lean, slightly rich, and rich flames' broadband CL at the $Re_{bulk}=18000$ bulk Reynolds-number. The Abel-inverted CH* CL images (right) at identical conditions show the reaction zones' mean distributions.

From both image types, it is already visible that the methane/air flame lengths increase with larger equivalence ratios, while the alcohol/air flames' decrease. This opposing trend phenomenon, which was already part of the blow-off stability results in the previous section, is also the main subject of the following quantitative flame length and flame topology discussions.
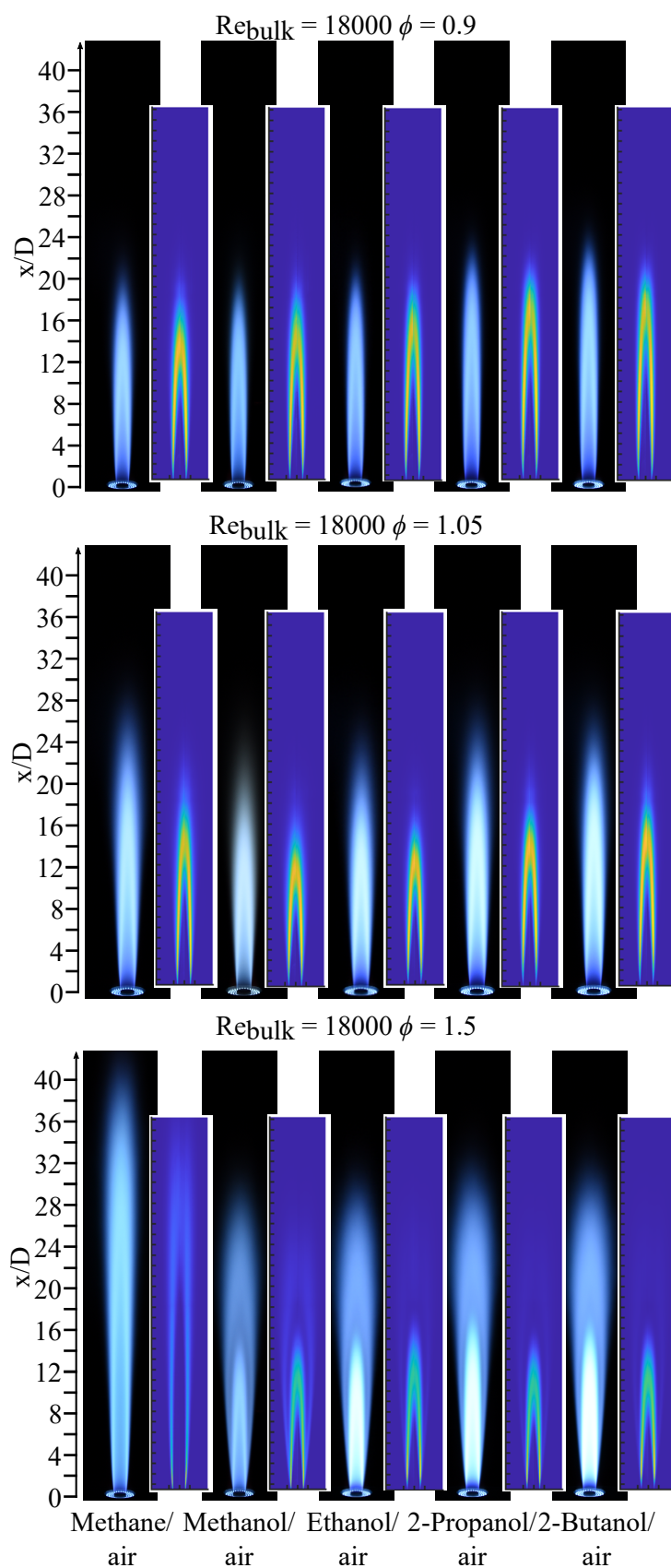
Figure 5.6.: Side-to-side comparison of photographs and Abel-inverted CH* chemiluminescence images for different fuels at one turbulence intensity and three equivalence ratios. Adopted from Trabold et al. [141] with minor changes.

Figure 5.7 shows the normalized flame lengths H_{fl}/D derived from the Abel-inverted CH* CL images. The two different methane/air mixture temperatures only lead to a minor flame length differences, particularly at equivalence ratios lower than $\phi=1.2$. Thus, the missing preheating of methane/air during the following flame topology study is disregarded to have a substantial influence.
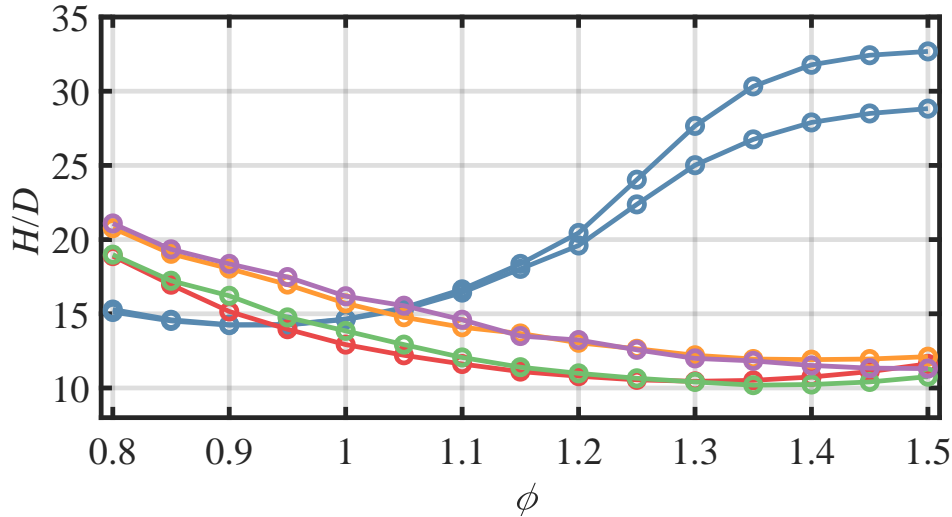
Figure 5.7.: Normalized flame lengths at a $Re_{bulk}=18000$ bulk Reynolds-number in the equivalence ratio space. ■ Methane/air; ■ Methanol/air; ■ Ethanol/air; ■ 2-Propanol/air; ■ 2-Butanol/air. Preheating mixture temperatures are either 293 K (x) or 343 K (o). Adopted from Trabold et al. [141] with minor changes.

Overall, methane/air's minimum flame lengths are located at equivalence ratio $\phi=0.9$, after which they increase towards rich conditions. The alcohol/air mixtures behave differently, with a minimum flame length at rich conditions. Depending on the fuel, the minimum is between $\phi=1.3$ and 1.45. The flame length differences between the different alcohol fuels' flames are minor, when compared to the difference to the methane/air flames.

Corresponding laminar burning velocities can partly explain the much longer methane/air flames under rich conditions, as they are up to 30 % smaller for methane/air than the three larger alcohol/air mixtures at $\phi=1.5$. Additionally, the methane/air viscosity is much larger than the alcohols' (Table 3.2), leading to larger bulk velocities at the same Reynolds number.

To follow up on these two parameters' potential influences, Figure 5.8 (right) displays the corresponding normalized bulk velocities u_{bulk}/s_L.

At the maximum equivalence ratio, methane/air reaches approximately 3.8 times the methanol/air value. The ratio between methane/air and the other alcohol/air mixtures, however, is approximately 1.7-2.0. This offset in the rich conditions between methane/air and the alcohol/air mixtures is similarly excessive as the flame lengths presented before, indicating the bulk velocity and laminar burning velocities' potential relevance.

Notably, methanol's much lower normalized bulk velocity does not translate into equivalent shorter flames lengths compared to the other alcohols. Therefore, no plain flame length scaling based on
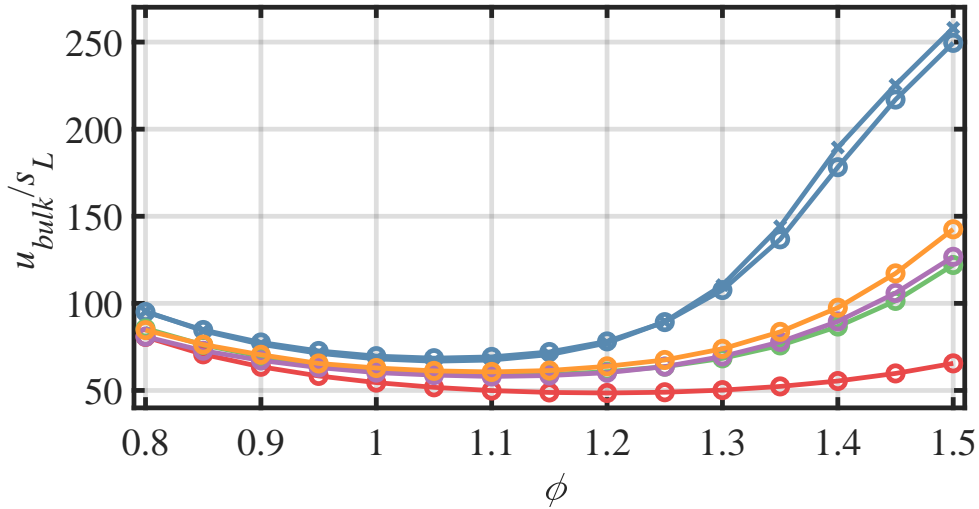
Figure 5.8.: Normalized bulk velocity u_{bulk}/s_L at a $Re_{bulk}=18000$ bulk Reynolds-number in the equivalence ratio space. ■ Methane/air; ■ Methanol/air; ■ Ethanol/air; ■ 2-Propanol/air; ■ 2-Butanol/air. Preheating mixture temperatures are either 293 K (**x**) or 343 K (**o**). Adopted from Trabold et al. [141] with minor changes.

laminar burning or bulk velocities was possible under these turbulent conditions. This is interesting in light of the observations by Carbone et al. [23], who found this was the case for fuels with similar Lewis numbers. However, they were only considering lean conditions.

In summary, the analysis reveals that the numerically derived parameters are not sufficient to yield a proper flame length correlation across all equivalence ratios. Hence, additional physical effects must have an influence. In the following, the local flame wrinkling captured by OH-PLIF is discussed. Its influence on the flame length is anticipated, as literature on the topic showed (Section 1.2.2).

5.4.3. Flame Topology

First, raw OH-PLIF images of the different flames are shown for visualization. Next, extracted contours are statistically analyzed using curvature PDFs (Section 5.4.3.1). These PDFs are global parameters combining information from either every individual axial FOV or all FOVs combined. Lastly, the FSD analysis increases the detail level to every pixel row within a FOV (Section 5.4.3.4). Both approaches are used as these allow for different views on the topology aspect. Lewis number effects and results from Section 3.5.3 are directly referred to during the curvature and FSD analyses. Another potential influence, which are Darrieus-Landau instabilities (hydrodynamic instabilities), were covered in Section 5.4.3.3.

5.4.3.1. Instantaneous Flame Front

Arbitrarily selected instantaneous OH-PLIF images recorded at six axial positions are assembled for each fuel to yield global instantaneous flame structure impressions at equivalence ratio $\phi=1.05$ and bulk Reynolds number $Re_{bulk}=12000$ (Figure 5.9).
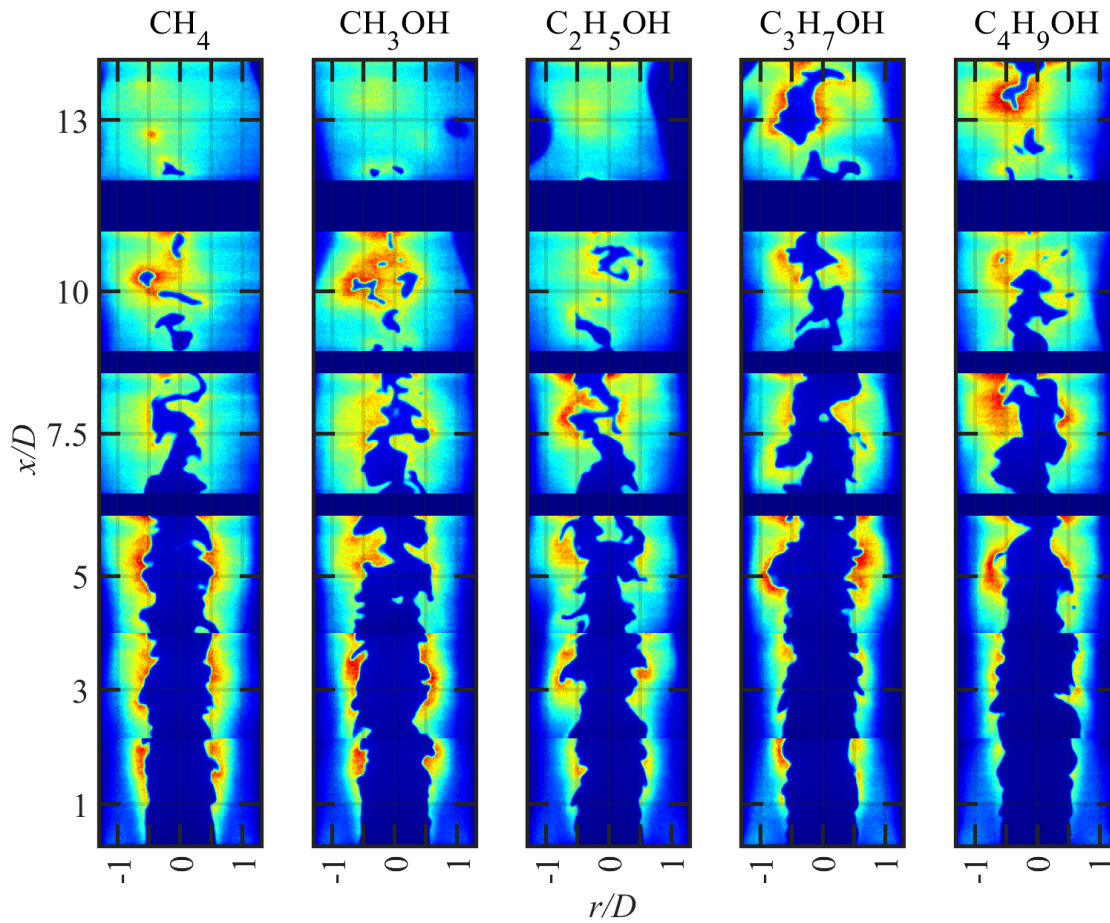
Figure 5.9.: Raw single-shot OH-PLIF images showing the instantaneous flame locations at six axial locations x/D. The operating point was at equivalence ratio $\phi = 1.05$ and bulk Reynolds number $Re_{bulk} = 12000$. The colors shown are arbitrary OH signal intensities from low (blue) to high (red). Adopted from Trabold et al. [141] with minor changes.

Starting at the base of the flame, a thin vertical OH-PLIF region is visible for all flames at and below $x/D = 1$. Concentrically around it, the weak signal (blue) which originates from pilot exhaust gases, forms a slightly contracting cone. The reason therefore could be that the relatively slow emitting pilot exhaust gases are being sucked into the high velocity jet flow. Subsequently, the OH-PLIF signal spreads again into now corrugated flame structures, with the signal and thus temperature becoming more intense in the process.

Downstream until $x/D = 5$, the primary reaction zones of the two visible flame branches are at a distance from one another, each confined to their own turbulent motion band within the PLIF sheet. At $x/D = 7.5$ and higher, the separate branches start to merge and enclosed pockets appear (example for unburned gas pocket: methanol/air flame at $x/D \approx 7.5$; example for burned gas pocket: ethanol/air flame at $x/D \approx 5$). Just like the branches are results of the intersection between the planar laser sheet and a corrugated 3D flame surface, the pockets are intersected 3D structures. Inconsiderate to which flame structure types are captured, all of them are part of the curvature and FSD studies discussed below.

5.4.3.2. Curvature Distribution

This section shows the results from the apparent flame curvature κ by statistically representing all magnitudes of flame wrinkling in curvature PDFs. For visualization and simplified curvature PDF interpretation, Figure 5.10 shows a flame front sketch, including burned and unburned pocket features.

III. Burned mixture consumes residual unburned mixture, increasing positive radii. Unburned pockets detach from flame front and reduce in size, decreasing negative radii further.

II. Burned pockets start to detach from the connected flame front and grow in size, increasing positive radii. Intersected 3D-structures add to this. Radii of unburned areas decrease as negatively shaped cusps form.

I. Long branches increase symmetrically in curvature/decrease in radii by turbulent mixing in shear layer.

Figure 5.10.: Positively (concave towards products, black) and negatively (convex towards products, red) curved flame segment evolution scheme along the axial direction.

The positively and negatively curved segments are drawn in black and red, respectively. Some observations along the axial dimension are directly given as annotations. Note that the pocket number is exaggerated to indicate how unburned pockets decrease in size on average, whereas burned pockets increase.

The first curvature PDF selection in Figure 5.11 shows PDF curvatures derived individually at the $x/D=1$, 5, 7.5, and 10 FOVs. Notably, showing all setpoints is mainly done for documentation purposes. This is because at each FOV, different portions of the flames are represented due to the variation in flame lengths for each fuel. In the following, the each individual fuel's evolution along the flame height is discussed for the $Re_{bulk}=12000$ Reyhnolds number and $\phi=1.05$ equivalence ratio setpoint. That setpoint is chosen because of its relatively short flames, which are entirely captured by the six FOVs.

With increasing axial location, the curvature PDF distributions broaden independent of the fuel. This is mainly due to the turbulence development and the energy cascade of eddies towards the Kolmogorov length scale (Section 2.3.3). Up to approximately $x/D=5$, probabilities of positive and negative curvatures in the PDFs are almost symmetric.
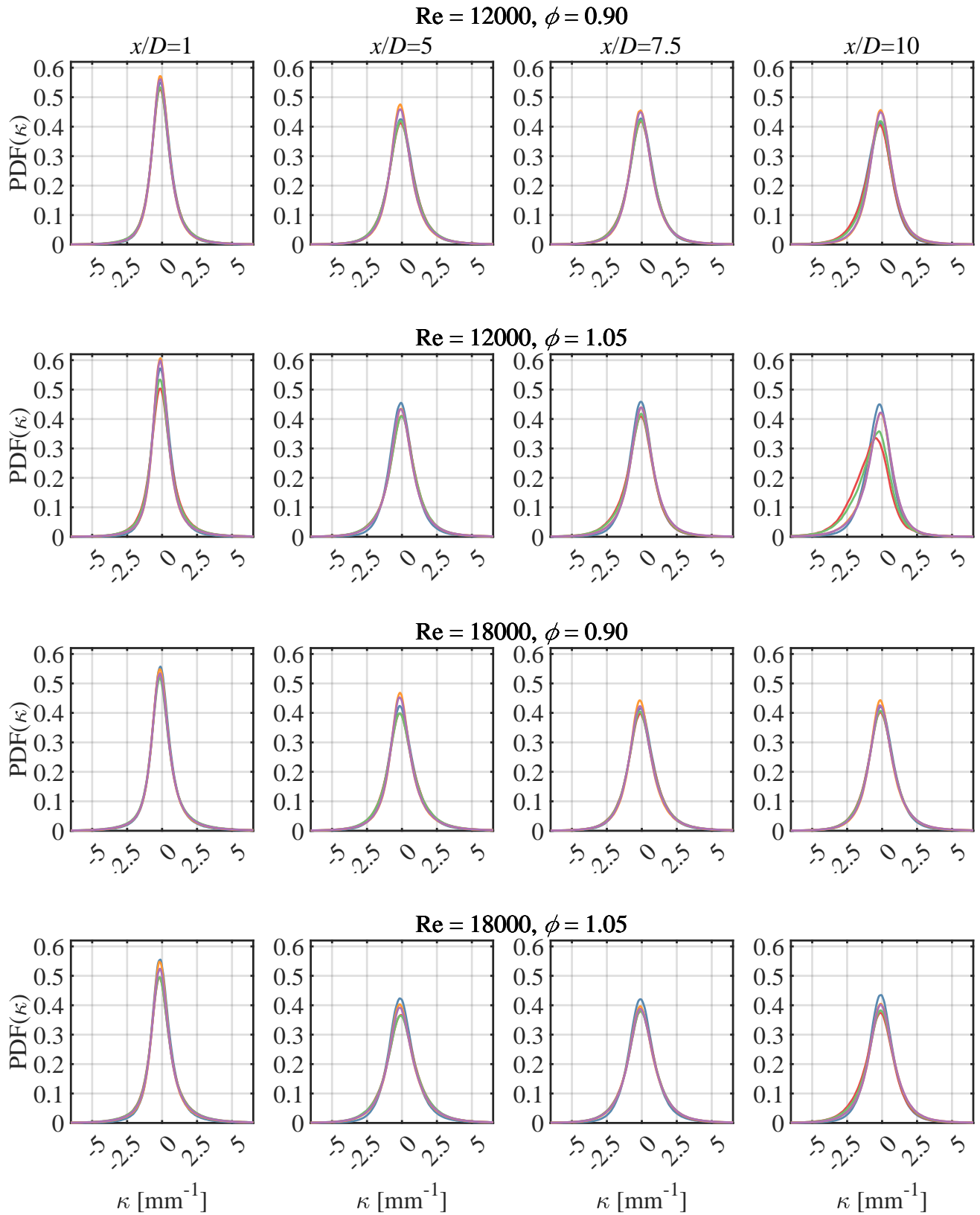
Figure 5.11.: Curvature κ PDFs at equivalence ratios ϕ=0.9 and 1.05 and bulk Reynolds numbers Re_{bulk}=12000 and 18000 at x/D=1, 5, 7.5, and 10. ■ Methane/air; ■ Methanol/air; ■ Ethanol/air; ■ 2-Propanol/air; ■ 2-Butanol/air

The visual appearance, shown in Figure 5.9 and summarized schematically in Figure 5.10 region I, indicates rather straight connected flame front branches containing positively curved bulges and negatively curved cusps. Downstream of that region, the curvature PDFs progress to being positively skewed, meaning the negative curvature likelihood with smaller radii increases, while the one with positive curvature the with smaller radii decreases.

Again, small positive curvatures to some extent result from larger scale concave burned mixture pockets within the unburned fuel/air mixture, as visible in Figure 5.10, region II. These pockets can be caused by 3D effects extending into the 2D laser sheet or pockets separated from the main reaction zone by a strong eddy.

In region III, referring to corner formation by Landau-propagation [83, pg. 400ff], the trend towards a decrease of the largest positive curvatures is enhanced when negatively curved cusps grow to their expense. The overall positive curvature likelihood reduction is also expected, as fresh fuel/air mixture is progressively consumed in decreasingly sized pockets.

Next, Figure 5.12 shows each flames' combined FOVs' curvature PDFs. As this is almost entirely independent of the flame length, it allows for a fuel and setpoint-respective comparison.
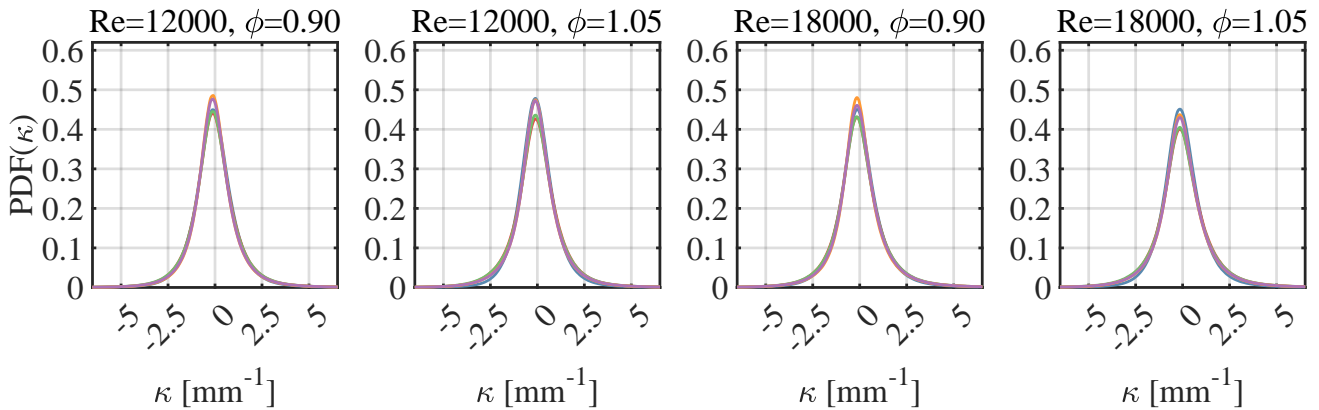
Figure 5.12.: Overall-flame curvature κ PDFs at equivalence ratio ϕ=1.05 and bulk Reynolds number Re_{bulk}=12000 at four x/D locations. ■ Methane/air; ■ Methanol/air; ■ Ethanol/air; ■ 2-Propanol/air; ■ 2-Butanol/air

Visually, curvatures are symmetrically distributed along the different flame conditions. In order to quantitatively evaluate the PDFs in more detail, the four PDF moments are given in Table 5.3.

Skewness and kurtosis are calculated using the following equations:

$$s = \frac{E(x - \mu_c)^3}{\sigma^3}, \qquad k = \frac{E(x - \mu_c)^4}{\sigma^4} \qquad (5.3)$$

Therein, E is the expected value, σ is the standard deviation, and μ_c is the mean curvature value.

The mean curvature is marginally negative, which agrees with recent findings by Alqallaf et al. [4] in a Bunsen flames DNS study. Notably, this was not the case for Tamadonfar and Gülder's curvature PDFs [140]. However, their pixel resolution was more than three times larger (91 μm), and

Table 5.3.: Curvature PDF statistical parameters including third and fourth moments.

Bulk Re	Equivalence ratio	Fuel	Mean	Standard deviation	Skewness	Kurtosis
12000	0.90	CH_4	-0.029	1.222	0.31	7.95
		CH_3OH	-0.027	1.322	0.37	8.07
		C_2H_5OH	-0.031	1.345	0.37	8.23
		C_3H_7OH	-0.025	1.260	0.46	8.53
		C_4H_9OH	-0.031	1.289	0.42	8.48
12000	1.05	CH_4	-0.032	1.135	0.38	7.99
		CH_3OH	-0.033	1.371	0.24	7.80
		C_2H_5OH	-0.042	1.394	0.21	7.89
		C_3H_7OH	-0.029	1.317	0.28	8.15
		C_4H_9OH	-0.024	1.328	0.27	8.23
18000	0.90	CH_4	-0.025	1.309	0.44	8.19
		CH_3OH	-0.025	1.441	0.47	8.28
		C_2H_5OH	-0.017	1.481	0.47	8.41
		C_3H_7OH	-0.006	1.400	0.49	8.68
		C_4H_9OH	-0.004	1.423	0.46	8.61
18000	1.05	CH_4	-0.025	1.243	0.51	8.17
		CH_3OH	-0.010	1.510	0.46	8.15
		C_2H_5OH	-0.026	1.554	0.39	8.28
		C_3H_7OH	-0.019	1.472	0.43	8.37
		C_4H_9OH	-0.018	1.492	0.39	8.42

because their laser sheet thickness was approximately $300\,\mu m$, they capped the PDFs at $3.3\,mm^{-1}$. In contrast, this work's approximately $200\,\mu m$ thick laser sheet thickness allows for the curvatures to be capped only as high as $5\,mm^{-1}$.

The curvature standard deviation is most narrow for methane/air throughout all flame conditions. This is associated with a higher (smaller) amount of small (large) curvatures than alcohol/air mixtures, indicating more small-scale flame wrinkling. Among the different alcohols, the only persistent behavior is that methanol/air and ethanol/air PDFs have a higher curvature standard deviation and, thus, more small-scale flame wrinkling than propanol/air and butanol/air.

Increasing the turbulence level from $Re_{bulk}=12000$ to 18000 also leads to more local wrinkling, which is expected due to more small-scale eddies. For alcohol/air mixtures, an equivalence ratio increase also exclusively leads to a larger standard deviation and, therefore, more wrinkling. Notably, the opposite happens for methane/air, again indicating a contrasting wrinkling behavior compared to the alocohol/air mixtures.

As already indicated by individual axial x/D PDFs in Figure 5.11, the skewness is either neutral or positive. This results in sum in positive skewnesses, as given in Table 5.3. Like the standard deviation, the skewness has an opposing effect between methane/air and the alcohol/air mixtures. For them, the increase in equivalence ratio is associated with smaller skewnesses, while for

methane/air, the skewness increases. This positive skewing represents a higher relative amount of negative curvatures, for example, by fresh mixture pockets surrounded by products.

Lastly, kurtosis, a measure for the number of outliers, does not have a clear trend, except that it is marginally increasing with fuel molecule size.

After having shown differences in the overall size spectrum of wrinkling features between the fuel/air mixtures, another study was performed with the intention to quantify the smallest structure sizes in the flames. This study was placed in the Appendix B.2, as it adds limited additional information to the present discussion.

5.4.3.3. Hydrodynamic Instabilities

Hydrodynamic instabilities, also known as DL instabilities, are known to increase negative curvature, influence strain rate and vorticity patterns, and enhance the counter-gradient diffusion of turbulent scalar fluxes [81]. Although they seem to primarily affect flame front structures of thin flames at high pressures [4, 73], their potential contribution shall be ruled out for the present work, as well.

Linear stability analysis can be used to determine whether flames are inherently stable or unstable due to DL instabilities [73, 92]. Two of these analyses are performed here along with a small growth rate study and the consideration of the curvature PDF symmetry.

Firstly, the Markstein number Ma is calculated for all flame conditions and fuels using the Clavin/Williams [26] and Peters [111] methods. If Ma is larger than the critical Markstein number Ma_c, planar flames are stable against DL instabilities, even for laminar flames that are generally more susceptible to becoming unstable [92]. As visible in Table 5.4, this is the case for all mixtures in this study.

Secondly, according to Creta et al. and Matalon et al. [28, 92], the critical wavelength λ_c can be compared to the hydrodynamic length scale (here: nozzle diameter). As shown in Table 5.4, it is always larger than or equal to the hydrodynamic length scale, again indicating no substantial impact of DL instabilities.

Furthermore, a growth rate study according to Sivashinsky [128] is conducted. Although not shown at length here, the growth rate magnitude is more than ten times smaller than that of laminar hydrogen flames at $\phi=0.6$ [108], suggesting no substantial influence by DL instabilities.

Finally, the symmetric curvature distributions in the entire FOVs PDFs (Section 5.4.3.2) support the findings and indicate the suppression of DL instabilities [73].

Table 5.4.: Summary of parameters to assert whether DL instabilities play a major role. If the Markstein number Ma is greater than Ma_c, laminar flames are expected to be stable [92]. It is conservative to expect that for the turbulent flames in this study, this is the case, as well. As for the critical wavelength λ_c parameter, it is found that only flame segments with a wavenumber between the nozzle diameter and the critical wavelength λ_c could experience DL instabilities [28, 92]. In this case, nearly all critical wavelengths are larger than the nozzle diameter (D=0.0114 m), leaving no room for that criterion to be valid. Based on these indicators, in the present study, DL instabilities have a minor, if any, impact on flame topologies. Adopted from Trabold et al. [141].

Equiv. ratio	Parameter	Methane/air	Methanol/air	Ethanol/air	2-Propanol/air	2-Butanol/air
	Ma	2.056	2.935	3.996	4.978	5.851
ϕ=0.80	Ma_c	0.932	0.994	0.998	0.997	1.005
	λ_c [m]	0.0155	0.0177	0.0263	0.0330	0.0366
	Ma	2.064	2.936	3.997	4.962	5.842
ϕ=0.90	Ma_c	0.997	1.059	1.067	1.070	1.078
	λ_c [m]	0.0142	0.0149	0.0225	0.0292	0.0323
	Ma	2.071	2.932	3.989	4.951	5.837
ϕ=1.00	Ma_c	1.041	1.107	1.117	1.122	1.131
	λ_c [m]	0.0141	0.0127	0.0185	0.0238	0.0257
	Ma	2.080	2.927	3.980	4.951	5.843
ϕ=1.05	Ma_c	1.050	1.119	1.131	1.134	1.144
	λ_c [m]	0.0143	0.0115	0.0161	0.0203	0.0214
	Ma	2.088	2.928	3.975	4.956	5.835
ϕ=1.10	Ma_c	1.048	1.123	1.136	1.140	1.152
	λ_c [m]	0.0143	0.0106	0.0145	0.0171	0.0175
	Ma	2.096	2.926	3.961	4.936	5.825
ϕ=1.20	Ma_c	1.032	1.116	1.113	1.131	1.145
	λ_c [m]	0.0154	0.0096	0.0132	0.0150	0.0149
	Ma	2.104	2.922	3.951	4.907	5.787
ϕ=1.30	Ma_c	1.011	1.104	1.116	1.117	1.131
	λ_c [m]	0.0204	0.0094	0.0164	0.0153	0.0149
	Ma	2.113	2.919	3.942	4.856	5.728
ϕ=1.40	Ma_c	0.989	1.090	1.100	1.100	1.116
	λ_c [m]	0.0333	0.0097	0.0153	0.0178	0.0169
	Ma	2.122	2.916	3.927	4.754	5.589
ϕ=1.50	Ma_c	0.966	1.076	1.085	1.084	1.100
	λ_c [m]	0.0443	0.0108	0.0195	0.0228	0.0211

5.4.3.4. Flame Surface Density

As discussed in Section 5.4.2, the fuel type has an influence on the flame length, leading to variations in the mean reaction rates $\overline{w}$. In Section 5.3, it was demonstrated that the mean reaction rate is primarily influenced by the FSD. Thus, it is an important parameter to compare among different fuels.

The radial profiles of the Σ_{2D} field depicted in Figure 5.13 (left) are obtained from cross-sections in the data shown in Figure 5.4(f). The integrated FSD, $\Sigma^*_{2D,int}$, was then computed by integrating the Σ_{2D} cross section along the radial dimension, and the resulting graphs are displayed in Figure 5.13 (right).

It is important to note that all curves start at unity, indicating that flame curvature at the flame's base is initially zero. As the flame progresses downstream, the flame surface area doubles on average, with values up to approximately two being reached. Once the maximum has happened, the likelihood of reaction zones gradually decreases again and eventually converges to zero. This position also corresponds to where the mean reaction rate c ceases near the flame tip, as shown in Figure 5.4 (e) at $x/D=13$.

Notably, the height where $\Sigma^*_{2D,int}$ reaches zero coincides with the flame length derived from CH* CL, proving that the two independent measurements provide accurate results.

The following observations are made from the data displayed in Figure 5.13 (right):

1. The integrated FSD $\Sigma^*_{2D,int}$ growth rate upstream of the maximum clearly differs between the fuel/air mixtures. The difference is even bigger at the slightly rich condition than in the lean condition. Methane/air, methanol/air, and ethanol/air $\Sigma^*_{2D,int}$ growth rates increase substantially faster than those of 2-propanol/air and 2-butanol/air. This shows a more concentrated combustion due to faster wrinkling development and subsequently a faster increasing reaction rate.

2. With larger turbulence intensity, the integrated FSD maxima increases simultaneously for all fuel/air mixtures. This is expected, as the turbulence intensity is directly correlated with smaller vortices and therefore increased wrinkling. Furthermore, the profiles extend to larger heights, which can be explained by the larger bulk mass flows.

3. Going from lean to slightly rich, the alcohol/air flames show substantially shortened integrated FSD profiles, which means combustion occurs on smaller volumes. Methane/air on the other hand barely changes. This can be seen even better in Figure 5.14, which shows the same profiles, but for each fuel individually.

Concerning the aforementioned point, it is remarkable that a small change in equivalence ratio leads to such contrasting behaviors in methane/air and alcohol/air flames. No other parameter except the effective Lewis number could be found that can explain such a significant shift with such a minor alteration in equivalence ratio. As illustrated in Figure 3.4, effective Lewis numbers for methane/air slightly increase towards rich conditions, while those of alcohol/air flames declines notably. This variation in results in reactant transport and flame front wrinkling changes, as explained in Section 2.5.1, which in turn accounts for the behavior captured by the integrated FSD
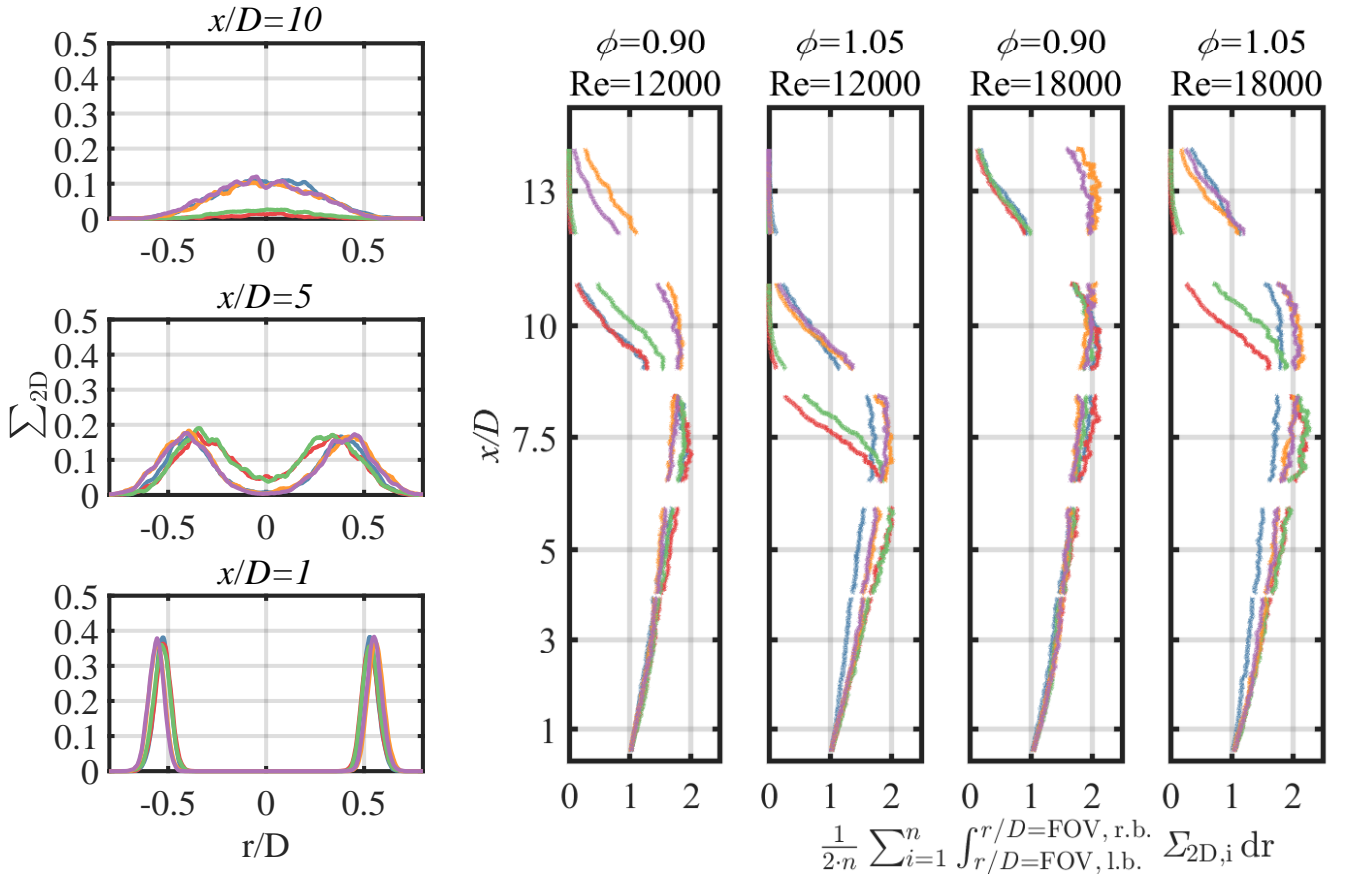
Figure 5.13.: Exemplary horizontal flame surface density field Σ_{2D} cross-sections at equivalence ratio $\phi=1.05$ and bulk Reynolds number $Re_{bulk}=12000$ (left). Radially integrated FSD $\Sigma_{2D,int}^*$ resulting from ensemble averaged radially integrated Σ_{2D} (right). ■ Methane/air; ■ Methanol/air; ■ Ethanol/air; ■ 2-Propanol/air; ■ 2-Butanol/air. Adopted from Trabold et al. [141] with minor changes.

graphs. These results also align with the hypothesis by Carbone et al. [23] that different Lewis numbers cause different fuel/air mixtures' flame lengths under lean conditions.

While the explanation is valid with regard to the general trend of effective Lewis numbers and flame lengths, the Lewis number magnitude does not correlate directly with wrinkling intensity. For example, the lean alcohol/air flames have substantially higher effective Lewis numbers and thus wrinkling dampening effects, but achieve similarly short flames. And even though in rich conditions, their effective Lewis numbers are still higher than that of methane/air, they have significantly shorter flames and larger wrinkling. Therefore, other influences besides the diffusional-thermal ones represented by the effective Lewis number may be present.

In order to find these influences, it is desirable to capture the flames' thermochemical states, which yield even more parameters, for example the flame thickness. This is done in the next chapter, where the first quantitative single-shot Raman and Rayleigh spectroscopy measurements on vaporized premixed fuels are performed with ethanol/air flames as a model fuel.
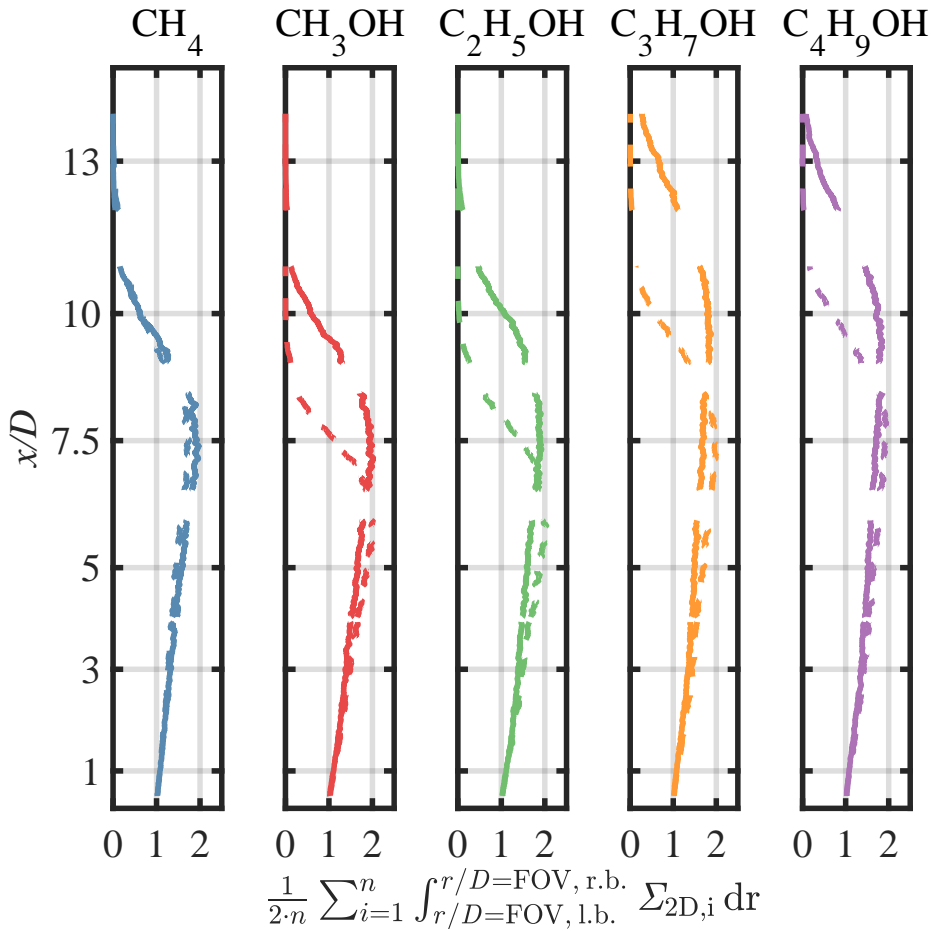
Figure 5.14.: Fuel-specific radially integrated FSD $\Sigma^*_{2D,int}$ at equivalence ratios $\phi=0.9$ (solid) and $\phi=1.05$ (dashed), both at bulk Reynolds number $Re_{bulk}=12000$. Adopted from Trabold et al. [141] with minor changes.

5.5. Summary and Conclusion

Premixed methanol/air, ethanol/air, 2-propanol/air, and 2-butanol/air were compared to methane/air flames under different turbulent conditions and over a wide range of equivalence ratios. Therefore, the novel TCJB burner system was commissioned, which incorporates well-defined flows and thermal boundary conditions and is therefore well-suited to isolate fuel-specific differences in turbulence-chemistry interaction.

In this chapter, the blow-off bulk velocities among a variety of fuels and equivalence ratios was described first. This resembles the operational envelope of the burner to the upside and the fuel-respective resistance against strain rate-induced extinction. Next, flame lengths of all fuel/air mixtures was obtained at a variety of equivalence ratios using a low-footprint CH*-chemiluminescence setup. Lastly, OH-PLIF was used to capture local flame contours at two selected equivalence ratios and turbulence intensities. This analysis resulted in information on the general flame appearance, curvature PDFs, and radially integrated FSD profiles. The potential influence by hydrodynamic instabilities (Darrieus-Landau instabilities) on the flame curvature was assessed without experi-

ments, but with a number of analytical criteria. No indication was found that hydrodynamic effects play a measurable role.

In summary, the alcohol/air flames behave in an opposed trend with regard to a rising equivalence ratio compared to methane/air. While alcohol/air flame lengths stay constant or decrease from lean to rich conditions, methane/air flame lengths increase. The reason is found in the microscopic flame topology, which shows that the wrinkling of alcohol/air flames stays constant or increases in rich conditions, while that of methane/air decreases. In consequence, methane/air requires a relatively larger volume for the combustion, thus increasing in flame lengths.

The increased wrinkling reason are most likely the different effective Lewis numbers. If larger than unity, as is the case for alcohol/air flames in lean conditions, wrinkling is dampened due to a stabilizing balance between mass and thermal diffusion. In rich conditions, however, alcohol/air effective Lewis numbers decrease towards unity or below, taking away the stabilizing effect. Rich methane/air flames, however, experience the opposite and have a wrinkling-dampening behavior in rich conditions.

Having reached all defined research goals, the parametric study presented in this chapter serves as a background for future fuel effect studies, particularly those of alcoholic fuels. An important next step are the quantitative thermochemical state investigations of ethanol/air flames compared to methane/air, which are obtained with the TUDa single-shot Raman setup. This experiment will be covered in the next chapter.

6. Thermochemical States in Laminar and Turbulent Methane- and Ethanol/air Flames

6.1. Introduction

This chapter describes single-shot Raman and Rayleigh spectroscopy experiments with the goal of measuring temperatures and main species quantities in premixed laminar and turbulent ethanol/air flames.

The research targets to achieve these novel measurements are:

1. To develop a Matrix inversion (MI) calibration method that is suitable for ethanol/air flames

2. To identify suitable binning regions in the main hydrocarbon region

3. To adjust the ethanol response curve and crosstalks

4. To verify the methods in laminar flames

5. To compare thermochemical states of turbulent methane/air and ethanol/air flames

The chapter is structured into the employed ethanol/air flame calibration methodology, the experimental apparatus and descriptions of the studied flames, and results.

6.2. Ethanol Calibration Methodology

6.2.1. Novel Calibration Method

Since several years, the common Raman calibration tools for methane/hydrogen/air flames are pure gases, *flat flame*, *Hencken burner*, and *v flame*. As the flat flame is inherently limited to gaseous fuels due to its sintered metal flame holder, a direct calibration method adaptation for ethanol/air flames is infeasible. Three options to resolve this challenge are presented in the following. Subsequently, the final concept is outlined, and implementation aspects are described.

6.2.1.1. Alternative Calibration Concepts

Utilizing the Flat Flame In this approach, the flat flame would still be used with methane as a fuel, regardless of the ethanol/air target flame. This may initially be deemed sufficient because the flat

flame's purpose as an equilibrium burner is to provide hot exhaust gases (mainly carbon dioxide and water). However, measuring the unignited mixture equivalence ratio over the flat flame is also an essential part of the calibration procedure. Thereby, parity between the detected unignited and ignited equivalence ratios of lean, stoichiometric, and rich conditions is realized. Without an unignited mixture equivalent, the calibration results are prone to significantly larger equivalence ratio uncertainty. Therefore, other possibilities are considered in the following.

Heat-flux Burner   Another equilibrium burner referred to as a *heat-flux burner* would be used in the next approach. With its water-circulating, temperature-controlled body and wider flow-guiding structures compared to the flat flame, it initially appears suitable for ethanol/air calibration. In addition, both cold and ignited mixture could be measured, thereby enabling the equivalence ratio parity calibration. However, the brass burner's ability to deal with hot exhaust gas temperatures is limited to lean or very rich conditions. Therefore, this concept is also ruled out.

New Burner Concepts   A new flat flame burner development is another option. It would look very similar to the heat-flux burner, but resolve the overheating issue near stoichiometric conditions. Solutions incorporating a different cooling media and an alternative to brass as surface material appear most promising. However, the sRS system also requires an approximately 80 mm dust-free diameter around the probe volume to avoid optical breakdowns of dust. This requirement is currently also not fulfilled by the heat-flux burner.

In consequence, this approach comes with an entirely new design and production task for a burner, accompanied by high costs for the design, materials, components, and production. Furthermore, a heating and mass flow controlling software would have to be built. Therefore, this approach is discarded for time and cost reasons.

6.2.1.2. Chosen Calibration Concept

In the ultimately chosen approach, the LTOJ developed in this work is used (Section 4.2.1). As will be shown, the only necessary hardware change to the existing system from Chapter 4 is a slight variation in flow guidance.

However, first, the line of thought on which this concept is based is given:

1. The flat flame Matrix inversion calibration procedure generally only utilizes three to four probe volume center pixels to increase processing speed. Furthermore, it is unnecessary to probe more, as the calibration quality does not increase by using more than three pixels, or about 350 μm.

2. These stationary known exhaust gas conditions do not demand the nearly constant conditions throughout the entire probe volume that the flat flame provides.

3. Therefore, such stationary conditions at the probe volume center can also be provided by another flame geometry than the flat flame, for example, by a *twin flame*. Twin flames are two identical flamelets in an opposed jet configuration.

4. In the twin flame's center, the velocity converges towards zero. Basic numerical 1D twin flame calculations show that when the strain rate is minimized, species and temperature are almost gradient-free around this point.

5. If the opposing premixed flows originate from the same mass flow controllers or coriflows, the equivalence ratios of the opposing nozzles are entirely the same.

6. These well-defined conditions are valid for both the unignited and ignited mixtures, facilitating the discussed necessary equivalence ratio parity requirement.

7. A significant benefit of an opposed jet flame setup is that the strain rate fitting of numerical 1D calculations onto the experimental data can be very accurate. With hot gas region width fitting, uncertainties of only about $\pm 5\,\mathrm{s}^{-1}$ are attainable, as shown in Section 3.4.1.

It needs to be noted that this process is the evolution from an attempt to calibrate the system using one-sided opposed jet flames, i.e., fuel/air vs. air. However, a much larger probe volume in the 5-6 mm range would need to be calibrated to match experiment and numerical calculation, rather than the typically used central 350 µm in flat and twin flames. This increases the processing duration on the order of 10 to 15, which is highly impractical even for automated parameter tuning in the MI. Nevertheless, while one-sided opposed flames will not be utilized as equilibrium condition calibrations, they will be used as a v flame calibration equivalent, with which the calibration results are validated in temperature space. This will be covered in Section 6.7.1.

6.2.2. Concept Implementation

6.2.2.1. Hardware

Both LTOJ burner sides need to be supplied with the same fuel/air mixture in order to generate twin flames. Therefore, a logical choice is to utilize the identical supplying mass flow controllers for gases and coriflows for the liquid fuel. This is especially advisable in the liquid fuel/air case, as cost and complexity are reduced to that of one vaporization apparatus instead of two.

In practice, only a heated Y-connection and a second heated hose need to be added after the vaporizer system (described in Section 4.2.2). However, due to different hose lengths, for example, the pressure drop in each direction is slightly different, which leads to the two flames not being centered between the nozzles. Therefore, an additional heated ball valve is required to throttle the flow in one direction and increase it towards the other. This enables to freely position the two flames between the nozzles.

After implementation, the described setup proved to be an effective way to produce and position twin flames in the probe volume. This setup's benefit is also that the set strain rate accuracy and the equivalence ratio depend only on the uncertainty of two mass flow controllers instead of four. A useful future modification would be an electrically controlled ball valve to control the system remotely.

6.2.2.2. Burner Control Software

After the Y-connection scheme installation, the control software modification requirement is limited to doubling the fuel/air supply from the mass flow controllers that previously supplied the premixed burner side while turning off the controllers that previously supplied the opposed nozzle with air.

6.2.2.3. Measurement Procedure

Typically, a broad main equivalence ratio range is desired for the main calibration flame, from as lean to as rich as possible. However, a conflict of interest appeared during the initial operational envelope investigation of LTOJ ethanol/air twin flames. On the one hand, the strain rates need to be as low as possible to have small gradients in the flames' centers (as discussed in Section 6.2.1.2). On the other hand, the twin flames' hot gas region widths need to be captured within the 6 mm probe volume lengths to enable the corresponding numerical setup's strain rate fitting.

The low strain rate requirement and the relatively large ethanol/air burning velocities around stoichiometry lead to particularly wide hot gas regions. Therefore, the commonly applied Raman and Rayleigh sensor cropping to ±3 mm in the axial direction needed to be switched off for the width measurement. Notably, this probe volume extension is usually avoided because the signal strength declines strongly farther out. However, an intensity fall-off correction in this stationary flame setup can readily be performed using concurrently recorded unignited mixture data (Section 6.2.2.6).

As a result, all flames between equivalence ratios ϕ=0.65 and 1.55 could be captured within the unbinned ±3.75 mm probe volume. With these measurements, the hot gas region width is calculated to fit numerical 1D flame calculations. To produce the actual calibration data, the same flames are recorded again with the ±3 mm standard probe volume length. A future improvement would be capturing the wide probe volume data only and cropping it in post-processing.

6.2.2.4. Raman Species Channel Normalization

An essential MI calibration process step are the Raman channel normalizations against vignetting effects (Section 2.6.3). This is usually done by capturing pure species mixtures or evenly distributed exhaust gas species along the probe volume. The water channel normalization typically happens in the rich flat flame exhaust gases. Using the LTOJ as the main calibration flame, this is not directly possible, as the twin flames do not produce constant edge-to-edge conditions.

One attempted alternative was to use Ulbricht sphere-illuminated slit images to measure intensity fall-off. These images are binned and cropped with the measurement region of interest (ROI) settings and then normalized to yield the desired intensity curves. However, the slit misalignment sensitivity turns out to be too high to capture the intensity fall-off accurately.

As a result, the normalization was performed using the same means as for the methane/air cases (Section 2.6.3).

6.2.2.5. Rayleigh Signal

For the Rayleigh signal, the process remains mostly the same. Besides changing the ROI to capture a wide probe volume series of the twin flames, the only change necessary is to adjust the fuel specie's Rayleigh cross-section. The value for ethanol is available from Fuest [53].

6.2.2.6. Fitting Experimental and Numerical Strain Rates

While twin flames reach similar absolute values in the center as the 0D reactor calculations typically used for the flat flame, an offset due to stretching effects remains. This can be seen in Figure 6.1, which shows the differences obtained by respective calculations for lean to rich ethanol/air calibration flames.

Therefore, the strain rate fitting from numerical calculations to experiment needs to be performed the same way as described in Section 4.4.1. Thereby, experimental and synthetic Rayleigh signals are fitted by aligning the maximum temperature gradients on each probe volume end. Notably, a necessary pre-processing step is to correct the Rayleigh signal for vignetting. Here, this is done by multiplying the ignited target flame Rayleigh signal with the normalized and inversed signal in the unignited mixture.
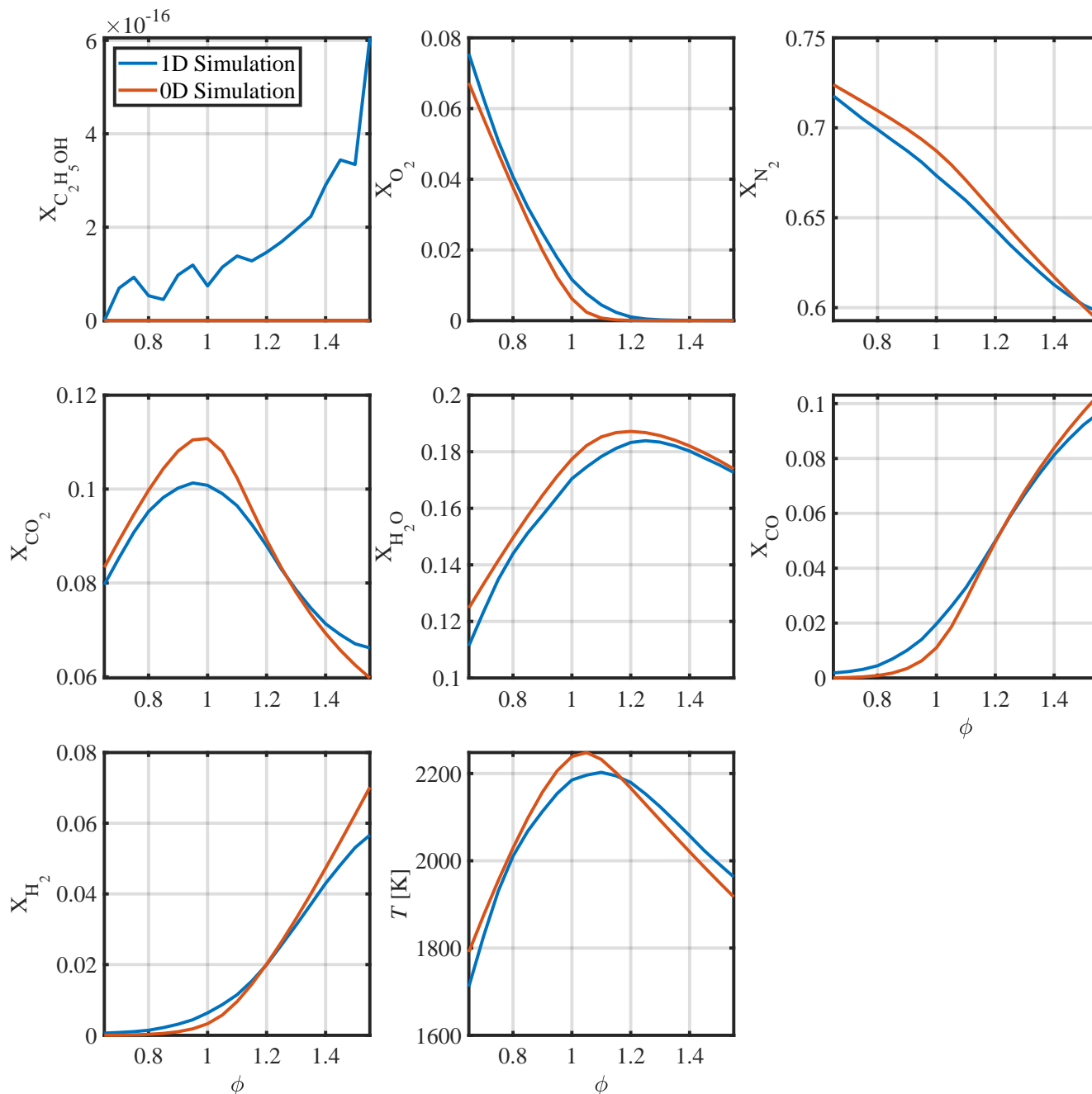
Figure 6.1.: Comparison of numerical 0D reactor and 1D strained flame calculation results.

6.2.3. Binning Regions

To attain a sufficient SNR in single-shot operation, hardware binning the Raman camera chip's wavenumber direction is a must. This section is concerned with the boundary placement of these channels during ethanol/air flame studies.

6.2.3.1. Requirements

The binning channel placement is conventionally realized with the following procedures:

1. The temperature-dependent stick spectra of all non-hydrocarbon main species are obtained from RAMSES simulations (Section 2.6.2). After convolution with the spectrometer's apparatus function, the expected answers on the sensor are known and those species' channel boundaries can be placed (Section 2.6.3).

2. For hydrocarbon fuel molecules, the boundaries are placed in consideration of heuristically derived experimental Raman answers, for example from gas heater measurements (Section 6.2.4).

Thereby, the following requirements are taken into account:

1. The channel boundaries should be placed conservatively to also capture the species' Raman signals at higher temperatures, which are generally broader.

2. Boundaries should not be placed too conservatively to avoid unnecessary crosstalk from other species, flame luminosity and C_2-LIF.

The requirements remain the same for all non-fuel species within this work. Therefore, these channels' binning regions are untouched and adopted from Butz [20].

Moving on from methane/air to ethanol/air flames, further requirements concerning hydrocarbon channels (CH-stretch region) appear:

3. The commonly made assumption for methane/air flames that claims that the intermediate species' influences on the CH-stretch region are negligible is not applicable anymore. Therefore, hydrocarbon channels should be strategically placed in consideration of intermediate species spectral answers. The works by Magnotti et al. [88, 90] and Dieter et al. [34], as well as student theses by Bok [16] and Koschnick [76] are therefore essential foundations.

4. Given the large ethanol Raman cross-section, a requirement is that the captured signal intensity in any hydrocarbons channel should not exceed the sensor's saturation limit. This is most likely in the unburned flame regions' high densities. To prohibit this, the CH-stretch signal is split into several pieces. For methane/air, for example, three binning channels are commonly used.

Note that intermediate species are not individually assessed in this work's post-processing. However, considering the intermediate species during channel placement now may enable to do so in the future using the same data sets.

6.2.3.2. Main Species Channels

Figure 6.2 shows the temperature-dependent spectra of all species captured in this work.

In order to ease the referencing to individual channels, the channel indexes at the figure's top are only connected to one specific species or species group, disregarding any crosstalks: (1) C_2 LIF, (2-3) CO_2, (4) O_2, (5) CO, (6) N_2, (7) C_2 LIF, (8-12) HCs, (13) H_2O, (14) H_2, (15) Background B3. The colors are arbitrary units of intensity.

While ethanol spectra are shown preemptively with their source being relatively new experiments (next section), the non-hydrocarbon species spectra are calculable using the RAMSES simulation tool (Section 2.6.2). Thereby, a database with each individual Raman transition's strength and wavenumber is generated for all relevant temperatures. This data type enables a straight-forward transfer to experimental spectrometer systems by convolution with the respective apparatus function. Within this work, the convolution is done with the Rayleigh image cross-section in dry air at room-temperature under consideration of the magnification.

As can be seen in Figure 6.2, the C_2 LIF, CO_2, O_2, and H_2O channels are subjected to substantial crosstalk by ethanol, which will be discussed in more detail in Section 6.2.4. Before, the hydrocarbon region's subdivision into smaller channels is discussed in the following.
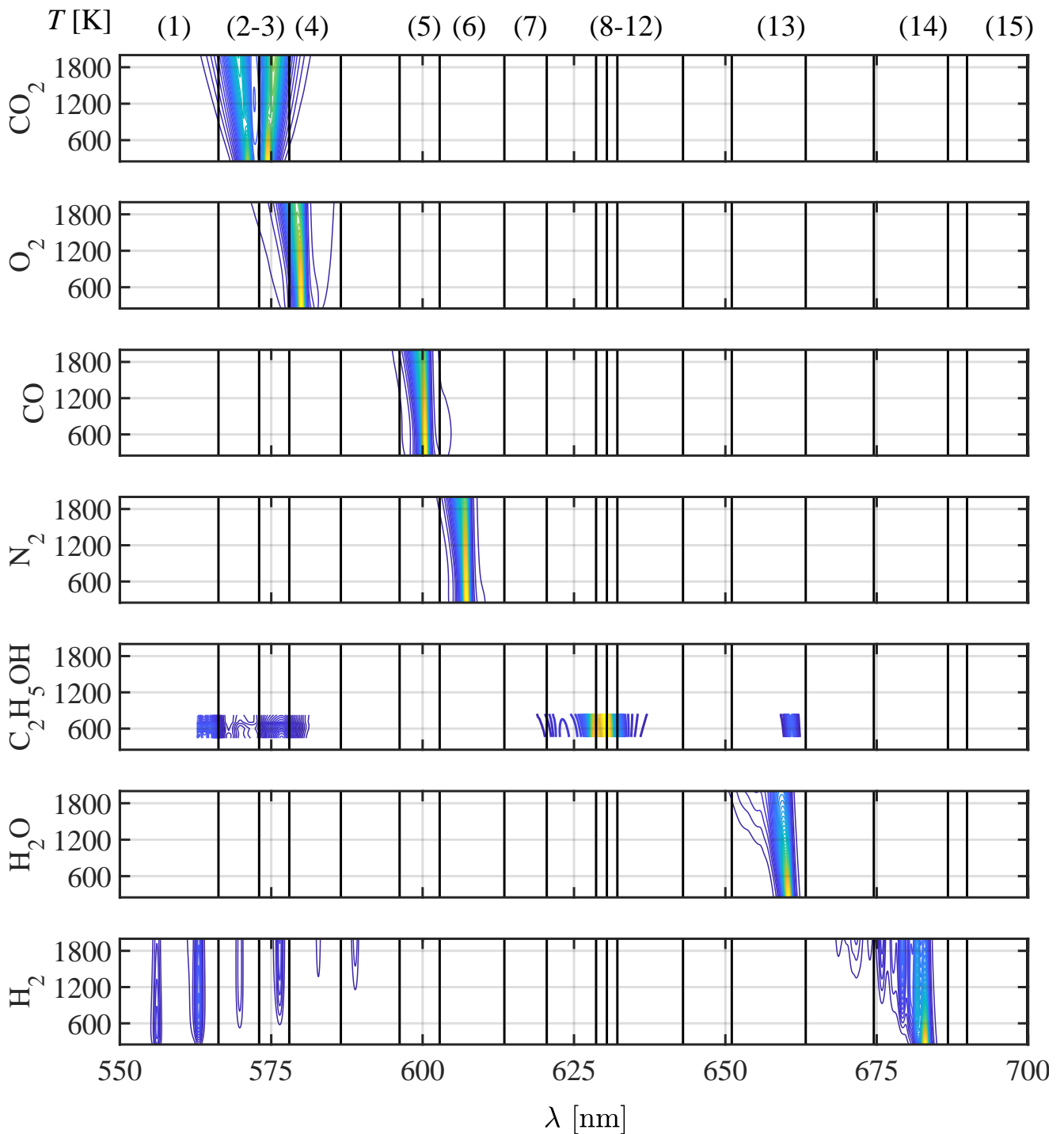
Figure 6.2.: Temperature-dependent individual species spectra from the RAMSES spectral simulation tool. The color resembles spectral intensity in arbitrary units. Graph concept adapted from Fuest [52] with some changes.

6.2.3.3. Hydrocarbon Spectra Sources and Transfer

The source of the relevant hydrocarbons' pure species spectra, which are essential for the boundary placement, is introduced first. Next, the transfer process between spectrometers is described. Lastly, the resulting intermediate species spectra are shown together with ethanol to define suitable channel boundary locations.

Source of Ethanol and Intermediate Species Spectra: All spectra shown in this section are obtained from measurements described by Dieter et al. [33, 34]. They captured time-averaged, but spectrally highly-resolved hydrocarbon spectra using a multipass-cell spectrometer setup. For easier reference, that test rig and spectrometer are in the following referred to as Spectrometer A at ODEE Institute, Hochschule Darmstadt (S.A.).

The target species were emitted from a well-defined apparatus, where the heating was provided through mixing with the heated carrier gases helium and nitrogen. In the case of ethanol, temperatures reached between 460 and 845 K and were measured either in-situ by spectral fitting the distinct nitrogen Raman peak (in the CH-stretch region images) or by a thermocouple measurement (in CH_2-bend region images).

The same setup was used to measure several intermediate species in Bok's [16] and Koschnick's [76] theses. Kevin Dieter provided all of this data via personal communication. The captured spectral intensities were thereby transformed into stick spectra using the *RESTIFI* process [33], which produces data resembling RAMSES results.

Spectra Transfer from S.A. to S.B.:   The first objective for why spectra are transferred from S.A. to Spectrometer B at RSM Institute, Technische Universität Darmstadt (S.B.) is to properly subdivide the hydrocarbon channels in S.B. in anticipation of possible intermediate species investigations in the future. The second objective is to attempt deriving a temperature-dependent ethanol response function and its crosstalks (Section 6.2.4).

The spectra are transferred using the following two steps:

1. First, both spectrometers' dispersion functions must be known to map the spectra's wavelengths/wavenumbers to the respective CCD pixels. Dieter et al. [33] recorded gas lamp targets and performed several procedures to exclude test rig-specific influences in the spectra, such as transmissivity and background. For this work's S.B., capturing the dispersion function using a Neon lamp is part of the daily calibration routine.

2. Secondly, the S.A. spectra were transformed into stick spectra by Kevin Dieter using RESTIFI and are convoluted with the apparatus function of S.B. to yield the equivalent spectral response. Like for the RAMSES spectra, the Rayleigh image cross-section in cold and dry air is taken as an apparatus function.

To validate the approach, transferred spectra are compared against ethanol spectra from S.B. in the following manner:

1. To correct S.B.'s spectras' vignetting and wavelength dependent transmission, an Ulbricht-sphere-illuminated slit image is recorded (process described in Section 4.3).

2. As mentioned, the temperature range for S.A.'s ethanol spectra is between approximately 460 and 840 K. In case of S.B., the pure ethanol spectra are recorded at 343 K. For comparison, S.A.'s spectra are therefore extrapolated to lower temperatures (Appendix B.3 for more details).

3. Due to the high dispersion utilized by Dieter et al. [33], the CH-stretch and CH_2-bend modes were captured with two separate gratings and in different measurements. Therefore, there is an unknown intensity relation between the two regions. For the purpose of the comparison, the S.A. CH_2-bend peaks are scaled in magnitude to the ones captured with S.B..

Transfer Result   Figure 6.3 shows the overlayed results for the CH_2-bend (left), the CH-stretch, and the OH-stretch regions (both right). As mentioned, the S.A. spectrum at 343 K is extrapolated from higher temperatures. In color, higher experimental temperatures are shown. Due to the varying temperatures captured in the bend and stretch regions, those are interpolated at the equidistant temperatures $T = 441$ K, 520 K, 599 K, 678 K, 758 K, 837 K. In the bottom, the different spectrometers' spectra are subtracted to derive a residuum.

The wavelength axes needed to be shifted 0.19 nm in the bend and 0.12 nm in the stretch region to align the largest peaks of both spectrometers. These shifts may be due to S.B.'s relatively coarse pixel resolution (approximately 2-3 pixels per peak). Deducing from the residuum between the signals, the maximum error in magnitude amounts to approximately 12 % in the CH_2-bend region and approximately 7.5 % in the CH-stretch and OH-stretch regions.

The reason for lower intensities of the CH_2-bend region's peaks towards the higher wavelength end is unknown. No systematic error of linear or cubic nature can be seen in the residuum. Nevertheless, the results look sufficient in light of the main goals of being able to define binning regions, response functions, and crosstalks of the binned channels.

Particularly the CH-stretch region, which will be subdivided into smaller channels in the following, appears very similar between convoluted S.A. and S.B. results. This is important because it increases the confidence in the correct transfer of the intermediate species in the CH-stretch region, which are subjected to the identical transfer procedure. They are shown in the next section in the context of the hydrocarbon channel's boundary placement.
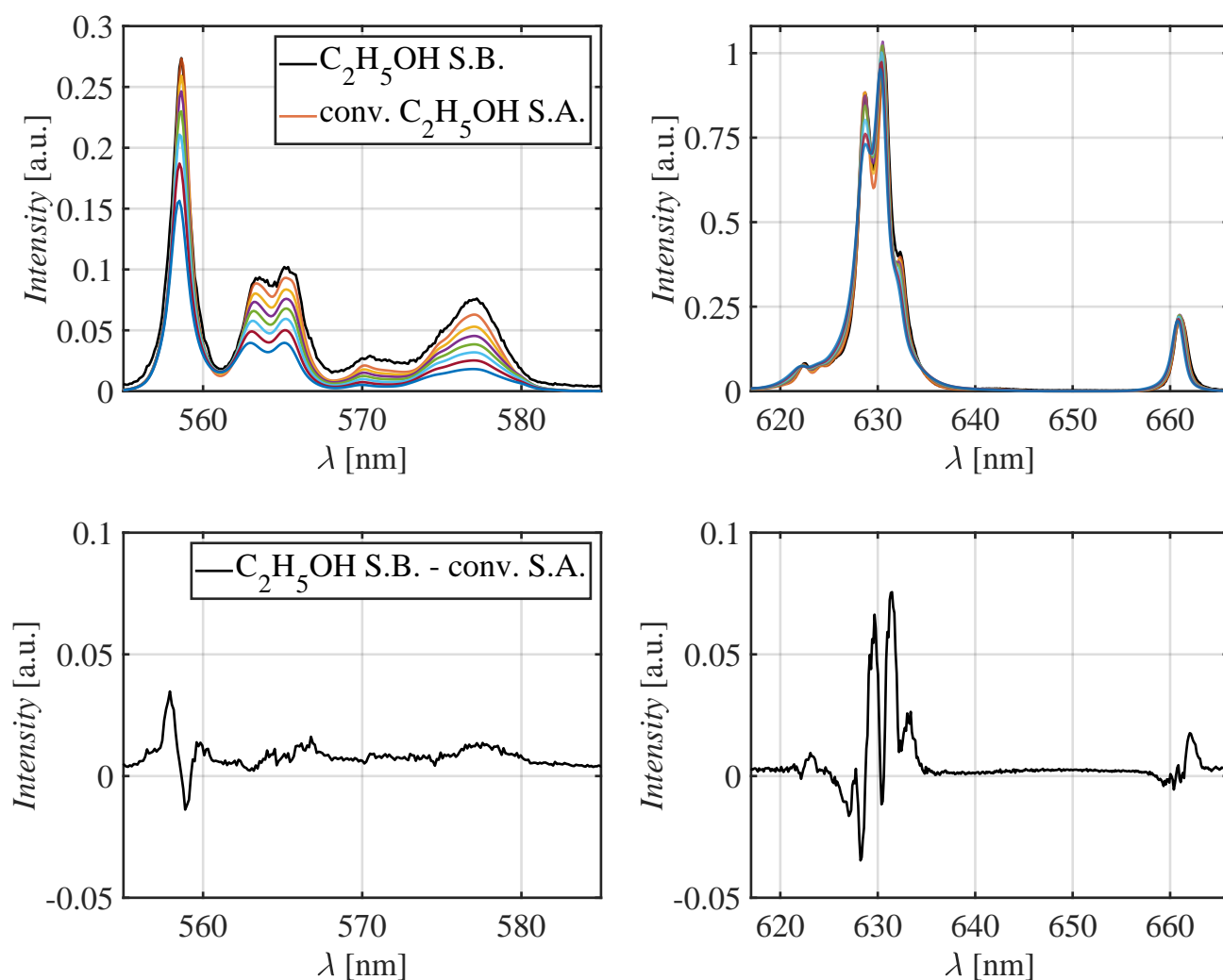
Figure 6.3.: Ethanol spectra transfer from the Dieter et al. [33] spectrometer (S.A.) to the present work's system (S.B.). Shown are the CH_2-bend (left), the CH-stretch, and OH-stetch regions at temperatures starting at 343 K (black, extrapolated in case of S.A.) and above (colored, inter- and extrapolated: T=441 K, 520 K, 599 K, 678 K, 758 K, 837 K). The residuum is the subtraction of S.B. spectra from the convoluted (transferred) S.A. spectra at 343 K.

6.2.3.4. Intermediate Species Spectra and Hydrocarbon Channels:

In Section 3.6, relevant intermediate species were defined as those with more than 0.1 mol % (refer to Figure 3.5). Because there is no suitable data source and because they are only present in very small amounts, methyl (CH_3), acetylene (C_2H_2), and ketene (CH_2CO) spectra are disregarded in this work. Figure 6.4 shows the other relevant intermediate species spectra which were captured by Dieter et al., Bok, and Koschnick [16, 33, 34, 76].

As visible, the CH-stretch region is densely populated. Therefore, making particular channels containing only one species is impossible with S.B.'s dispersion and apparatus function. The goal can thus only be to limit each channel's input to two or three species and ethanol at max. In the following, the rationale for each hydrocarbon species channel boundary placement is given:

Channel Seven: Channel seven is positioned considering that its blue-sided end (lower wavelength) is directly located at the conventional nitrogen channel's red side (larger wavelength). Furthermore, channel seven's red-sided end is positioned right behind the red-sided C_2-LIF end. That location was found heuristically in the luminous partially-premixed flames captured highly-resolved in Chapter 4.

Channel Eight: Channel eight starts directly at channel seven's end to capture as much ethanol signal as possible. Formaldehyde is almost entirely captured within this channel at the available temperatures. The red-sided end is located at the first ethanol peak for reasons which will be discussed next.

Channel Nine, Ten, Eleven: The three major ethanol peaks in the CH-stretch region are termed blue-sided, central, and red-sided peaks for the following discussion. At the available temperatures, methane and acetaldehyde peaks are located between the blue-sided and the central ethanol peak. Ethylene is located on the red-sided ethanol peak's red side. Therefore, a subdivision right at the ethanol's peak locations appears, by chance, as logical. Exemplary experiments using these boundaries also reveal a similar intensity distribution among the channels and no saturation limit breaching in low-temperature ethanol/air mixtures.

Another reason to place the boundaries right on the ethanol peaks is that during the measurement, it enables checking more quickly whether the channels are correctly positioned relative to the spectrum. This can be done by capturing a spectrally resolved image inbetween and checking whether the peak position is aligned with the set pixel binning boundary. During a measurement day, this can be done more often than capturing a neon lamp image and evaluating it.

Lastly, a good reason for this placement is to retain the most resilience against vertical laser-pointing movement (spectral direction). If the channel boundary locations were instead at the ethanol peaks' flanks, the intermediates' peak positions could jitter between neighboring binned pixels. This risk is due to the lower-dispersed spectrometer arm's limited pixel resolution in the spectral direction. As a reference, the central ethanol peak already has only about ten pixels in its FWHM.
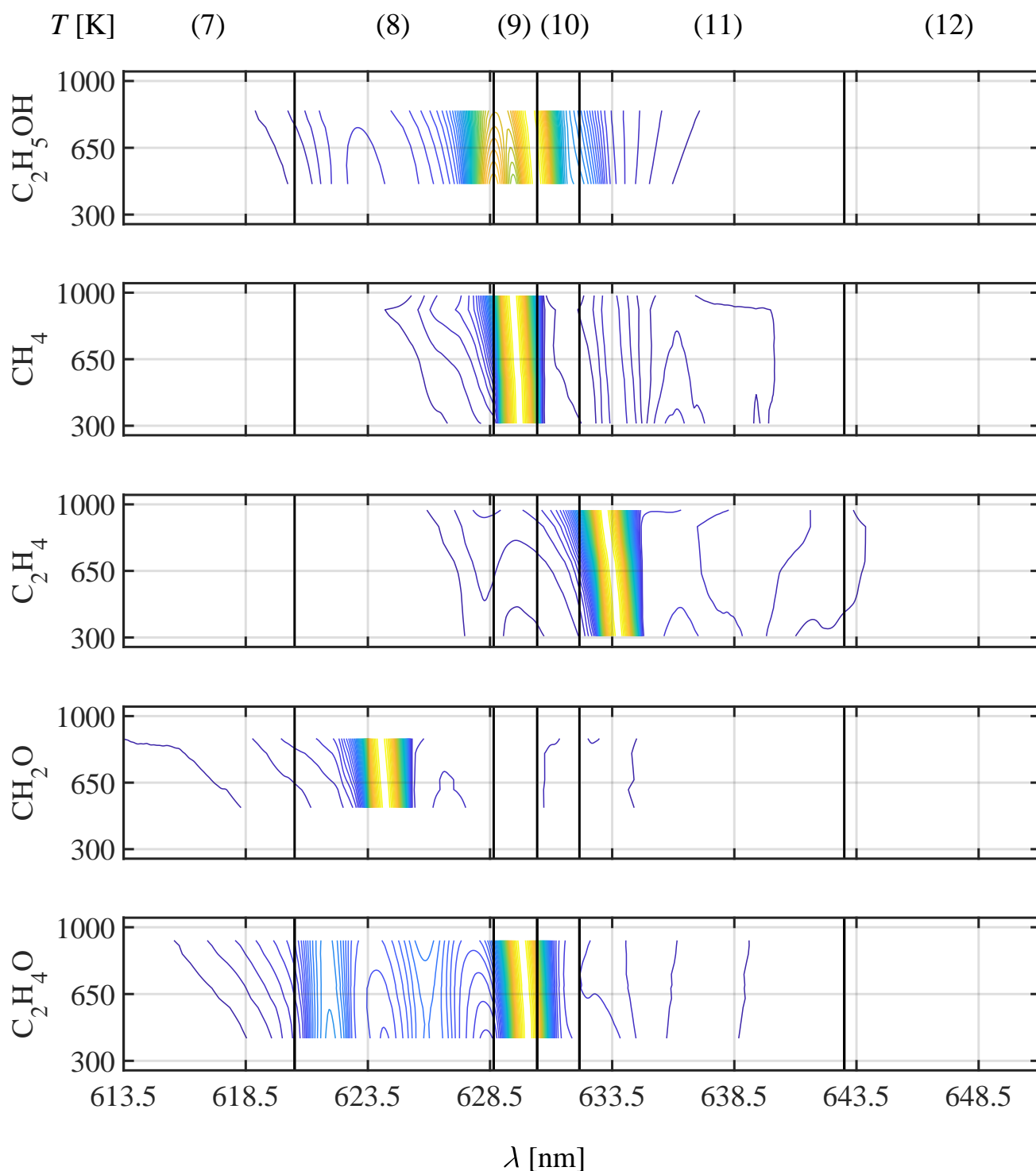
Figure 6.4.: Temperature-dependent hydrocarbon spectra stemming from convoluted RESTIFI stick spectra provided by Kevin Dieter via personal communication. The color resembles spectral intensity in arbitrary units. The graph concept was adapted from Fuest [52] with some changes.

At this point, it is noted that using the higher-dispersed spectrometer arm would give some more room in this aspect. However, in the single-shot application, it may only become viable if a custom-

designed beam splitter, which entirely reflects the CH-stretch region, is used. Otherwise, due to the low efficiency of the high-dispersion grating prism, the SNR is too low for the already low intermediate species mole fractions. Such a beam splitter was not purchased during this work.

Channel Twelve: Channel twelve could have been integrated with Channel eleven, but was not to limit the noise input.

Table 6.1 finally summarizes the channel boundaries information, including wavelengths, pixel widths, and the species with substantial contributions.

Table 6.1.: Channel distribution in the CH-stretch region.

Channel	Wavelength region [nm]	Pixel width	Substantially contributing species
7	613.5-620.5	59	C_2
8	620.5-628.65	68	$C_2H_5OH+CH_2O$
9	628.65-630.43	15	$C_2H_5OH+CH_4+C_2H_4O$
10	630.43-632.16	14	$C_2H_5OH+C_2H_4O+C_2H_4$
11	632.16-643	91	$C_2H_5OH+C_2H_4$
12	643-651.06	68	empty

6.2.4. Ethanol Response Curves and Cross Talks

In the hybrid MI evaluation method, polynomials (usually fifth-order) describe a specie's temperature-dependent Raman signal produced in a specific spectrally binned region. This can either regard the temperature-dependent signal within its own channel, referred to as *response curve*, or those onto other channels, referred to as *crosstalks*. Polynomials are typically normalized to 290 K and carry a *multiplier* to quantify the signal's relative strength.

As mentioned before, response functions and crosstalks for hydrocarbon fuel molecules still have to be heuristically determined from electric heater measurement data. As these are limited to 800 to 1000 °C, they then need to be extrapolated towards adiabatic flame temperatures [104].

In this work, the polynomials are initially generated from such electrically heated ethanol spectra provided by Dieter et al. [33]. The procedure is thoroughly described in Appendix B.3. However, with the complex resulting polynomials described there, no useful MI calibration result could be obtained. If the process described in Appendix B.3 is not to blame, the difficult-to-combat uncertainties described in the following are potentially the problem:

1. The multi-pass cell jitter inherently produces a spatially undefined structure. This diminishes the comparability between different exposures.

2. The probed hot gases lead to substantial beam steering, which, under long-exposure environments, results in random smearing of gradients. Comparability among different exposures is again not given.

3. The CH_2-bend region exposures do not contain a nitrogen peak to which a temperature fit or intensity relation can be performed, again prohibiting a comparison between exposures.

4. The electrical heater temperature range is too limited to make trust-worthy claims on the extension towards flame-high temperatures.

While the first three could be solved by probing the spectra with a strong pulsed laser in single-shot mode and by using a concurrent Rayleigh image, the last one will remain until more suitable heating methods have materialized (e.g. plasma heating).

To still deal with the challenge of evaluating ethanol/air flame data, the following alternative approach for the polynomials was tried. By setting all polynomial coefficients to ones, a temperature-independent spectral shape of the ethanol response curve and crosstalk is assumed. Their strengths, which are represented by the multipliers, are first heuristically derived from in-situ S.B. measurements in a mixture with the Raman-inactive Helium. Subsequently, it is refined in the unburned twin flame mixtures, where the signals of all channels beside ethanol, nitrogen and oxygen are calibrated to be zero.

The accuracy of this simplification can best be judged in the temperature space of flame fronts, which are given in Section 6.5.4. As will be discussed there, the approach appears to be sufficient for the MI calibration.

6.3. Experimental Apparatus

The experimental apparatus consists of several devices already introduced in previous chapters. One is the Raman and Rayleigh system introduced in Section 4.2.4. In the present experiment, the 50/50 beam splitter that divides the spectrometer arms is removed. This increases the lower-dispersed spectrometer arm's SNR to attain sufficient levels in single-shot mode.

In the probe volume, the flat flame, the Hencken flame, the LTOJ, and a custom designed nozzle for pure gases are used for methane/air and calibration purposes (Section 2.1.3). The first two burners are described in detail by Schneider [123] and Butz [20], and are therefore not covered in more detail here. The LTOJ, which replaces the flat flame in the ethanol/air calibration, was introduced in Section 4.2.1. The only difference is that in the present experiment, a Y connector and throttle will be utilized after the vaporizer to feed both nozzles with fuel/air mixtures and thereby produce twin flames (Section 6.2.2.1).

As a target flame burner, the TCJB introduced in Section 5.2.1 is used without any modifications.

6.4. Flame Operating Conditions

6.4.1. Conventional Calibration Flames

The flat flame was operated unignited with equivalence ratios from $\phi=0.65$ to 1.3 in 0.05 steps and subsequently ignited in the opposite direction. Measurements were taken approximately 10 mm above the burner's surface. The Hencken flame was used only for the methane/air flame calibration, with equivalence ratios running from $\phi=0.1$ to 1.5 in 0.1 steps. The height above the burner was also 10 mm. The v flame, which is commonly used to validate the correct alignment of Rayleigh and Raman cameras, is neglected, since the same functionality can be provided with even more equivalence ratios by the laminar opposed jet burner introduced in the next section.

## 6.4.2. Temperature-controlled Laminar Opposed Jet Burner (LTOJ)

The LTOJ serves as a calibration and target burner in this experiment. First, twin flames from as far lean to as far rich as possible are run for the ethanol/air MI calibration (Section 6.2.2.3). Secondly, laminar opposed fuel/air against air flames from lean to partially-premixed conditions validate the twin flame calibration in the temperature domain. Furthermore they serve to compare laminar methane/air and ethanol/air flames.

6.4.2.1. Twin Flames

Figure 6.5 displays photographic images of those setpoints. Two vertical lines indicate the nozzle opening, and a dashed line is the burner's axis.

As mentioned before, the twin flames' strain rates must be minimized during the calibration process (Section 6.2.1.2). This is generally not an issue for rich flames, where a secondary diffusion-type flame leads to increased stability. However, the leanest conditions (equivalence ratios $\phi=0.6$, 0.65, and 0.7) are challenging, as with the LTOJ's geometry, they are very small flames that are influenced by the laboratory's slightest air movements. While the coflow inhibits these influences to some extent, it impedes the manual ignition by the typical lighter device. Conversely, a larger device that is not quenched by the nitrogen coflow is too large for the small lean target flames. As a result, a more rich condition needs to be set first, from which the equivalence ratio can slowly be decreased to the leanest target ratios.
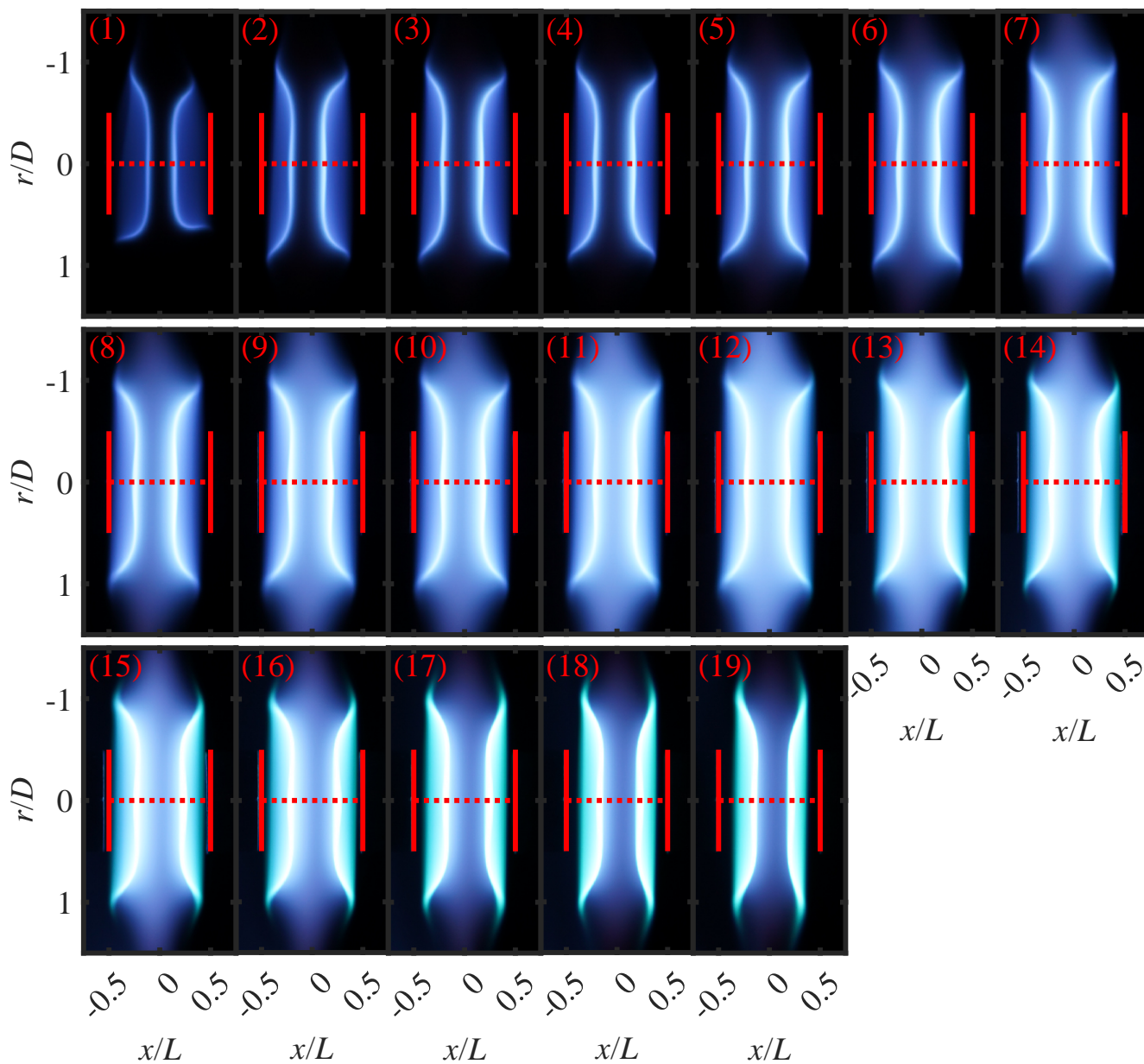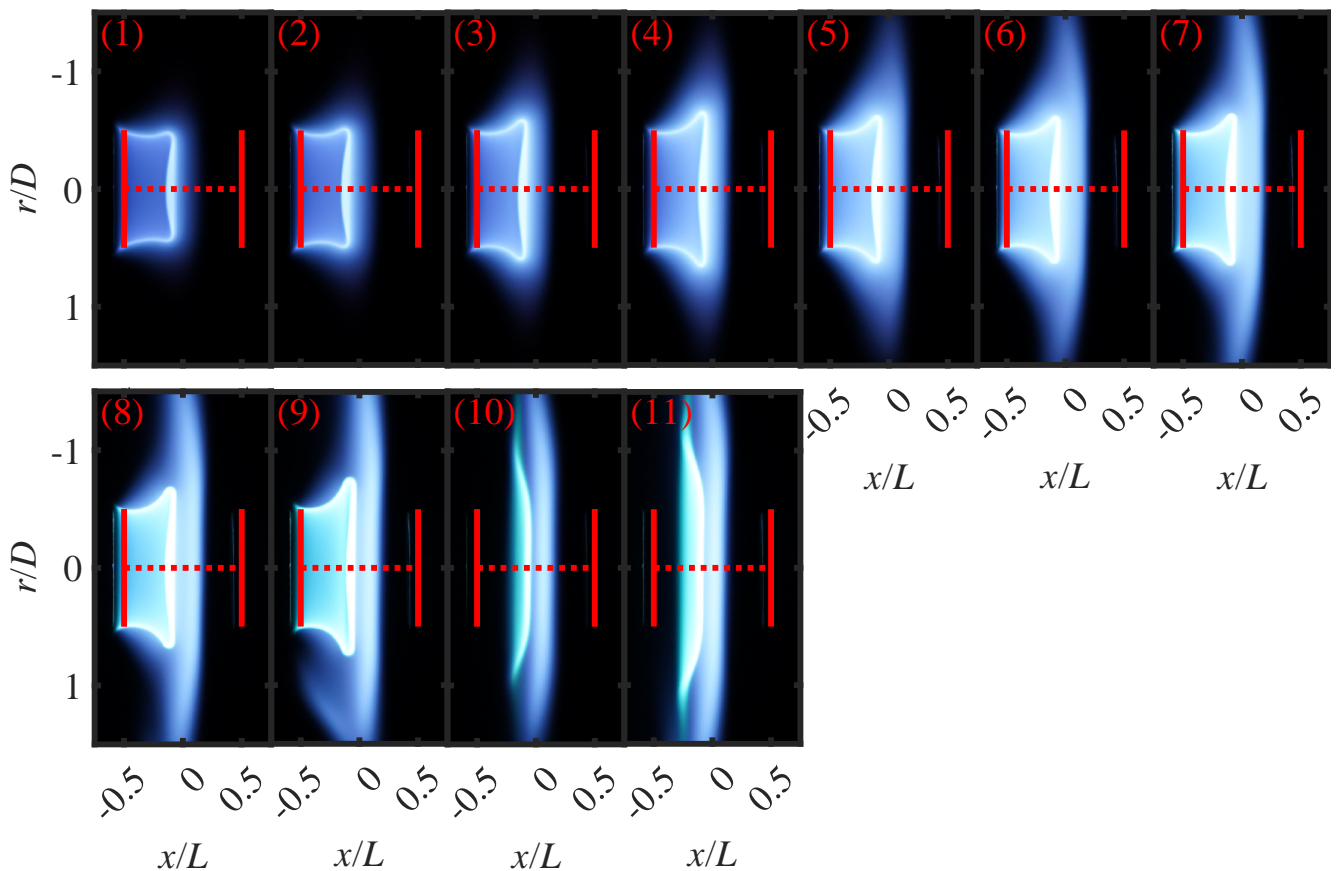
Figure 6.5.: Photographic images of LTOJ twin flames in scale. (1)-(19) are all equivalence ratios between ϕ=0.6 and 1.45 in 0.05 steps.

6.4.2.2. Laminar Opposed Jet Flames

Figure 6.6 shows photographs of opposed ethanol/air jet flames at equivalence ratios ϕ=0.75, 0.8, 0.85, 0.9, 1, 1.1, 1.2, 1.3, 1.4, 1.5, and 1.75 with a 343 K premixed mixture temperature. Two vertical lines indicate the nozzle position and size, and a horizontal line the burner's axis. The strain rate is set as low as possible so that even the weakest flames on the lean equivalence ratio side are burning stable.

Methane/air opposed jet flames are run with a 293 K premixed mixture temperature, and in equivalence ratio steps of 0.1 between ϕ=0.7 and 1.6, plus at ϕ=1.9. Because of their visual similarity to ethanol/air flames, they are not shown here.


Figure 6.6.: Photographic images of laminar opposed ethanol flames. (1)-(10) are all equivalence ratios between ϕ=0.75 and 0.9 in 0.5 steps, ϕ=1 to 1.5 in 0.1 steps, and ϕ=1.75.

125

6.4.3. Temperature-controlled Piloted Jet Burner (TCJB)

In this section, the equivalence ratio and Reynolds number selections for the turbulent flames are explained.

6.4.3.1. Flow and Mixture Variables

During the selection of operating conditions for turbulent flames, the objective is to induce a significant effective Lewis number change (as explained in Section 3.5.3), while keeping the laminar burning velocity constant. This allows the thermo-diffusive effects to be mostly isolated from individual fuel kinetics. To maintain a constant laminar burning velocity, the mixture can either be heated to a different temperature or the equivalence ratio can be adjusted. Figure 6.7 shows the premixed mixture temperatures of four laminar burning velocities (colored curves) for methane/air and ethanol/air mixtures in the equivalence ratio space.
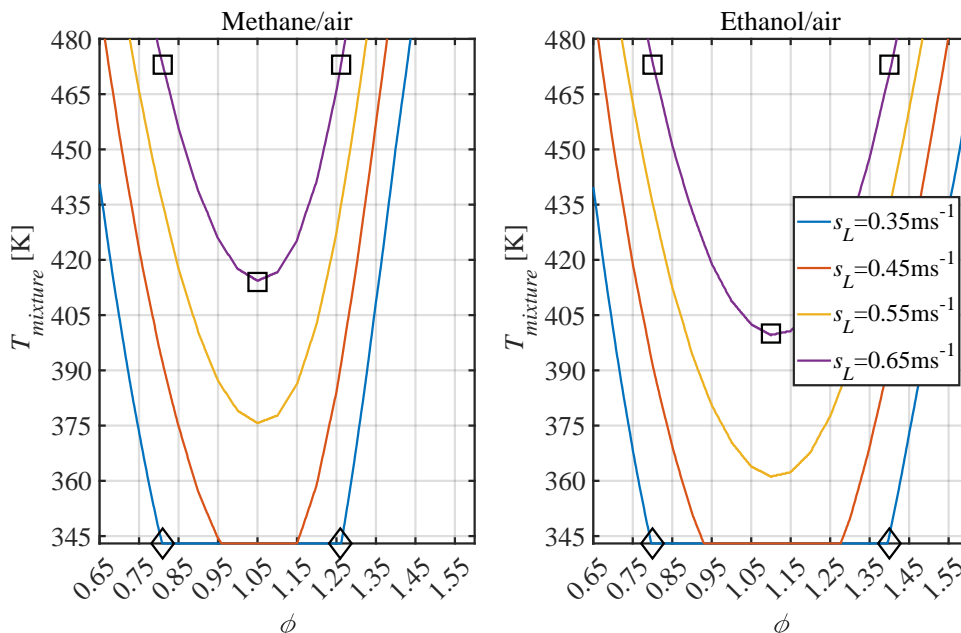
Figure 6.7.: Laminar burning velocities in the equivalence ratio and temperature space. Two potential setpoint choices with constant laminar burning velocities are indicated. The squares' locations include a point around stoichiometry, but require temperature elevation and variation between the setpoints. The diamonds' locations mark the finally chosen set of lean and rich setpoints at constant temperature. It is referred to the text for the rationale behind this decision.

The figure also illustrates two potential setpoint pairs with a constant laminar burning velocities, represented by diamonds and squares. These are discussed in the following:

1. As seen in the figure, if the lean and rich mixtures are heated to 473 K, three setpoints with the same equivalence ratio per fuel can be obtained. This was also tested during the setpoint definition process. However, increasing the premixed mixture temperature leads to a drastic increase in the necessary mass flows, if the higher Karlovitz areas in the Borghi-Peters diagram are desired to be reached. This is because the burning velocity, which increases

with premixed mixture temperature, is in the denominator. Additionally, at higher bulk velocities, stabilization at the nozzle becomes increasingly challenging. Since the pilot flame approaches its limits (glowing) and the available mass flow controlling gear options are already exhausted, heating to such an extent is not pursued.

2. If the central equivalence ratio is removed, lower laminar burning velocity curves can be taken without risking to go below ethanol's due point. The logical choice is then to decrease the temperature as much as possible in order to reach as high Karlovitz numbers as possible with the availabe flow controlling equipment. It's worth noting that maintaining a constant temperature between only the lean and the rich setpoint has the practical advantage that the burner does not have to find a new equilibrium heating state when transitioning between them. Additionally, exploring thermo-diffusive effects does not necessitate a near stoichiometric point. Thus, a fixed premixture temperature of 343 K combined with varying the equivalence ratio to maintain a constant laminar burning velocity is considered the best and thus final solution.

Regarding bulk Reynolds numbers, three points are selected. The first setting, Re_{bulk}=12000, is chosen because flame topology experiments are available at the same setting from the OH-PLIF study (Chapter 5). Additionally, a lower and higher turbulence level are desired.

At the lower end, Re_{bulk}=6000 is selected. An even lower Reynolds number is not chosen because observations in the laboratory and numerical calculation (as described in Appendix B.1.1) indicate that the pilot flame's impact on the jet would become too significant. It's worth noting that turning off the pilot quickly leads to the turbulent flame's extinction and is therefore not a feasible option.

At the higher Reynolds number end, ethanol/air was increasingly difficult to stabilize in lean conditions. This difficulty was already observed and discussed in the blow-off limit experiments context (as explained in Section 5.4.1). As the reachable turbulence level of about Re_{bulk}=23000 with the commonly used pilot condition was deemed too small, the pilot's bulk velocity and equivalence ratio were ultimately increased to achieve a Re_{bulk}=28500 bulk Reynolds number.

Table 6.2 summarizes the selected operating conditions for the jet and pilot flames.

Table 6.2.: Turbulent single-shot experiment operating conditions.

Fuel	Equivalence ratio	Bulk Reynolds number	Pilot conditions
Methane/air	0.81/1.26	6000	ϕ =0.7/u_{bulk}=0.7
	0.81/1.26	12000	ϕ =0.7/u_{bulk}=0.7
	0.80	28500	ϕ =0.8/u_{bulk}=2.65
	1.40	28500	ϕ =0.7/u_{bulk}=0.7
Ethanol/air	0.80/1.40	6000	ϕ =0.7/u_{bulk}=0.7
	0.80/1.40	12000	ϕ =0.7/u_{bulk}=0.7
	0.80	28500	ϕ =0.8/u_{bulk}=2.65
	1.40	28500	ϕ =0.7/u_{bulk}=0.7

The axial measurement planes through which the burner is traversed are x/D=0.5, 1, 2, 3.5, 5.5, 8, 11, and 14.5. At these heights, it is traversed radially in 3 mm steps. First, negative locations

until the minus 6 mm mark are measured, so that both flame branches in the radial profile can be checked for symmetry. Next, the burner is traversed in the positive direction to as far as flame features are present in the live Rayleigh images. At rich conditions and large axial heights, the maximum distance is about plus 39 mm outside the burner axis.

The laser shots captured per location are 300 at the first two heights, 400 on the third, and 500 from there on upwards. At particular locations of interest, 6000 extra images were captured in the flame front region to generate a larger statistical foundation. Those were at $x/D=3.5$ for the $Re_{bulk}=6000$ cases, $x/D=3.5$ and 8 for the $Re_{bulk}=12000$ cases, and $x/D=3.5$, 8, and 14.5 at the $Re_{bulk}=28500$ cases.

A characterization into the Borghi-Peters diagram was attempted using a LES study. Because of the small depth of this simulation project and the minor importance on the following discussions, it was decided not to show it here, but place it in Appendix B.1.2.2.
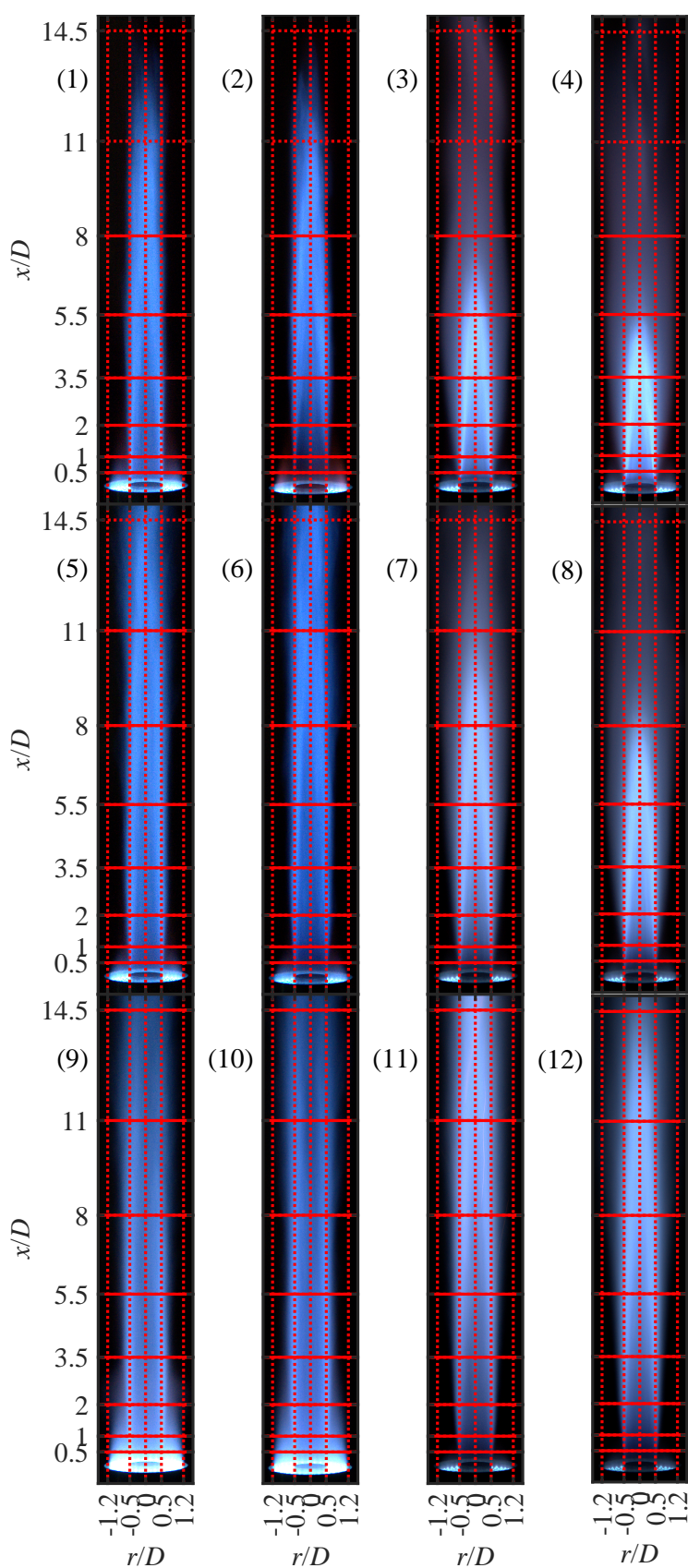

6.4.3.2. Photographic Flame Images

Photographic flame images including scaled axes are shown in Figure 6.8.

The flame images are captured using a Nikon Z6 CMOS camera recording for 5 s with an ISO 200 setting and at the full 4024x6048 pixels resolution. The lens is a Nikon 50 mm F1.2, which had sufficient depth of field at the utilized widest aperture. As no filter was used, the images captured the entire visible chemiluminescence spectrum of CH*, OH*, and C_2* (Section 2.7.2).

An Abel inversion was attempted to make the flame cone more distinguishable. However, the signal intensity captured was too small in the lean flame cases. Therefore, the images shown are raw, and no further adjustments have been made.

With respect to the flames' visual appearances, the $Re_{bulk}=6000$ cases look rather similar to the $Re_{bulk}=12000$ case, but are smaller in axial height. It is noted again that the local flame structures for the $Re_{bulk}=12000$ cases can be viewed in detail in Chapter 5's study, with the limitation that the equivalence ratio is slightly different.

For the lean $Re_{bulk}=28500$ cases, the larger pilot flames visibly extend up to approximately $x/D=3.5$. Above, local extinction due to turbulence can be seen starting around $x/D=8$. The rich cases show a comparatively larger extent of the primary reaction zone, even exceeding the $x/D=14.5$ axial location.

Figure 6.8.: Photographic flame images with constant 5 s exposure times and settings of the turbulent jet flames stabilized on the TCJB. (1) Equivalence ratio ϕ=0.81 methane/air, (2) ϕ=0.8 ethanol/air, (3) ϕ=1.26 methane/air, (4) ϕ=1.4 ethanol/air. The three rows are the respective Re$_{bulk}$=6000, 12000, and 28500 cases. The pilot flames in (9) and (10) show a significantly brighter luminosity, as those lean cases needed larger pilot flame enthalpies for stabilization.

6.5. Calibration and Uncertainty

This section describes two quantitative single-shot experiment calibrations, which were recorded at identical flame conditions but with different spatial binning intervals of the Raman camera. The first set, using a four-pixel binning interval, is used to verify the accurate resolution of gradients within different ethanol/air flame reaction zones. The second set, with a ten-pixel binning interval, serves as the calibration for the turbulent TCJB target flames, which are solely recorded with a ten-pixel binning interval to achieve a higher SNR.

To provide a basis for comparison, the same flame setups and binnings are also used for methane/air flames. Both data sets are augmented with pure gas calibrations, which will be covered first in the following.

6.5.1. Pure Calibration Gases

The pure gas calibration serves two purposes. As discussed in Section 2.6.3, it enables the vignetting correction of the individual channels. Furthermore, important multipliers and gains are tuned using the respective pure gases. Accordingly, the following pure gases were used.

Dry Air (78.08% nitrogen / 20.95% oxygen/ 0.93% argon / 0.04% carbon dioxide):   Dry air is used to perform the vignetting correction on nitrogen and oxygen, tuning their multipliers, as well as tuning the oxygen onto carbon dioxide crosstalk multiplier. Furthermore, the Rayleigh and YAG gains can be calibrated, which serve to find the correct Rayleigh and perfect gas temperature, respectively. Therefore, a thermocouple measurement is installed and monitors the temperature 5 mm downstream of the pure gas nozzle.

Methane (specified >99.5%):   Besides being used to perform vignetting correction on the methane channels, pure methane is also used to generate an initial guess for its own multiplier, as well as providing final values for methane crosstalk strengths onto other channels. In order to inhibit plasma generation during this pure gas measurement, the laser energy needs to be reduced to approximately one fourth of the maximum value.

Ethanol (in a 15% / 85% mixture with helium):   Vaporized ethanol at 343 K in helium carrier gas is used, equivalent to the methane calibration described above, for an initial guess of ethanol fuel's multiplier and crosstalk strengths onto other channels.

Hydrogen (specified >99.9%):   Pure hydrogen serves as a vignetting correction and is used for an initial guess of its multiplier and crosstalks.

Defined Gas Mixture #1 (1.99% carbon monoxide / 35% hydrogen / 63% nitrogen):   The defined gas mixture with carbon monoxide is necessary to obtain a strong signal for the carbon monoxide channel vignetting correction.

Defined Gas Mixture #2 (20% carbon dioxide / 80% nitrogen):   The defined gas mixture with carbon dioxide is necessary to obtain a strong signal for the vignetting correction of the carbon dioxide channel.

Notably, no vignetting correction data sources have been mentioned above yet for water, the background (B3), and the C_2 channels. In the case of water, this is achieved using the richest flat flame setpoint. As they are in close proximity, the hydrogen vignetting correction is used for B3. Lastly, the carbon dioxide vignetting correction is used for the C_2 channel.

6.5.2. Flat Flame Exhaust Gases

As discussed in Section 2.1.3, the flat flame burner is an essential piece to calibrate methane/air flames in sRS systems, with most multipliers being calibrated in its exhaust gas cone.

One hundred samples are acquired in the exhaust gas cone above the flat flame for each equivalence ratio in both the unburned and the burned mixtures. Thereby, the unburned mixtures are used to measure the equivalence ratio, so that the mass flow controller uncertainty is not of importance. Based on these equivalence ratios, the adiabatic state of the mixtures is derived in a concurrent 0D reactor calculation. Notably, heat losses due to radiation of approximately 20 K (private communication with PhD. Robert Barlow, April 2022) are accounted for.

The mole fraction and temperature results of these numerical calculations are then used to tune the MI multipliers, utilizing the simplex search method of Lagarias et al. [80]. Specifically, the following multipliers were tuned using the flat flame:

1. Carbon dioxide and water multipliers are tuned across the whole equivalence ratio range, and carbon monoxide and hydrogen are tuned under rich conditions.

2. Furthermore, the nitrogen onto carbon dioxide carbon dioxide onto oxygen crosstalks are tuned in the lean and rich conditions, respectively.

3. After the initial methane multiplier calibration in pure gas, it is manually finalized by minimizing the oxygen mole fraction in the flat flame. This is a notable difference to how it was commonly done, which was adjusting the Rayleigh temperature peak location to approximately equivalence ratio $\phi = 1.05$ However, the resulting small temperature inaccuracy of 2 to 3 % was preferred over the substantial overestimation of oxygen, which commonly happened using the Rayleigh temperature peak location procedure.

6.5.2.1. Methane/air with Higher Spatial Resolution Binning

The methane/air flame calibration result for the higher resolution cases is given in Figure 6.9. Depicted in blue, with errorbars measuring two standard deviations, are the measured mean mole fractions of 100 single shots. A concurrent 0D reactor calculation's result, to which the MI was tuned, is shown in red.
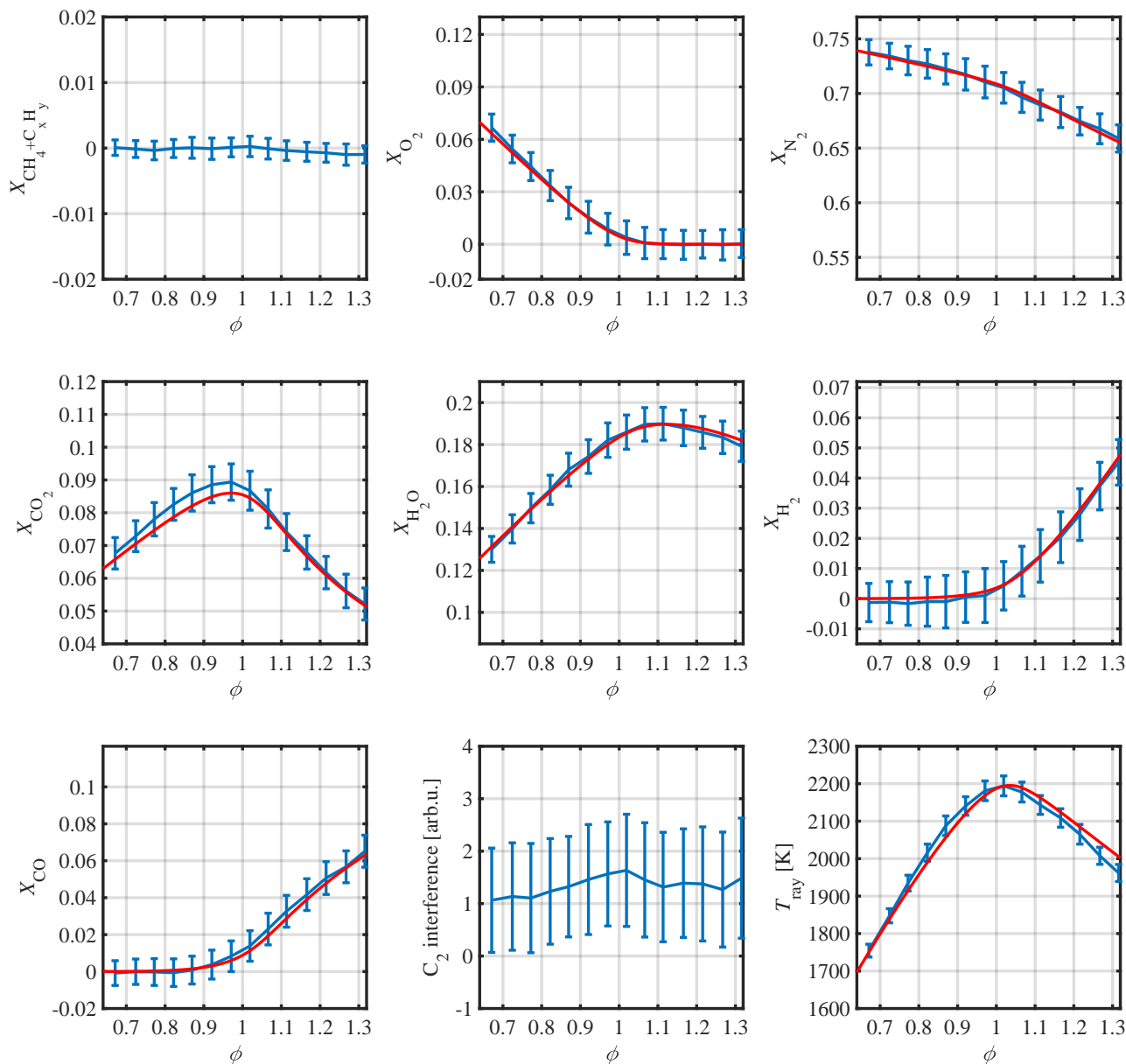

Figure 6.9.: Methane/air flat flame data at higher resolution (pixel binning of four).

The following observations are made given these results:

1. While the major species nitrogen and water are completely aligned with the numerical calculation results, carbon dioxide is slightly overestimated in lean conditions. The deviation is acceptable, as they remain within the standard deviation error envelope.

2. Unphysical slightly negative values can be seen for hydrogen in lean conditions and for methane in rich conditions. However, with less than $-0.3\,\%$, they are treated as insignificant in the grand scheme.

3. For comparison with values in ethanol/air, C_2 fluorescence is shown, as well. The general appearance with a peak near stoichiometry is expected due to the high temperatures.

4. Lastly, the temperature is slightly overestimated in lean and underestimated in the richest three equivalence ratios. While the cause in lean conditions is likely the carbon dioxide offset, the rich condition deviation is not clarified.

6.5.2.2. Methane/air with Higher SNR Binning

Figure 6.10 shows the flat flame calibration results that serve as a base for the turbulent flame cases. To shed a light on the high stability of the sRS system, these results were measured first and preceded the smaller binning experiment by about four weeks. Despite this and the fact that turbulent flames with high thermal loads were captured inbetween the measurements, the results are almost identical and all notes that were given before have validity for the larger binning case, as well.
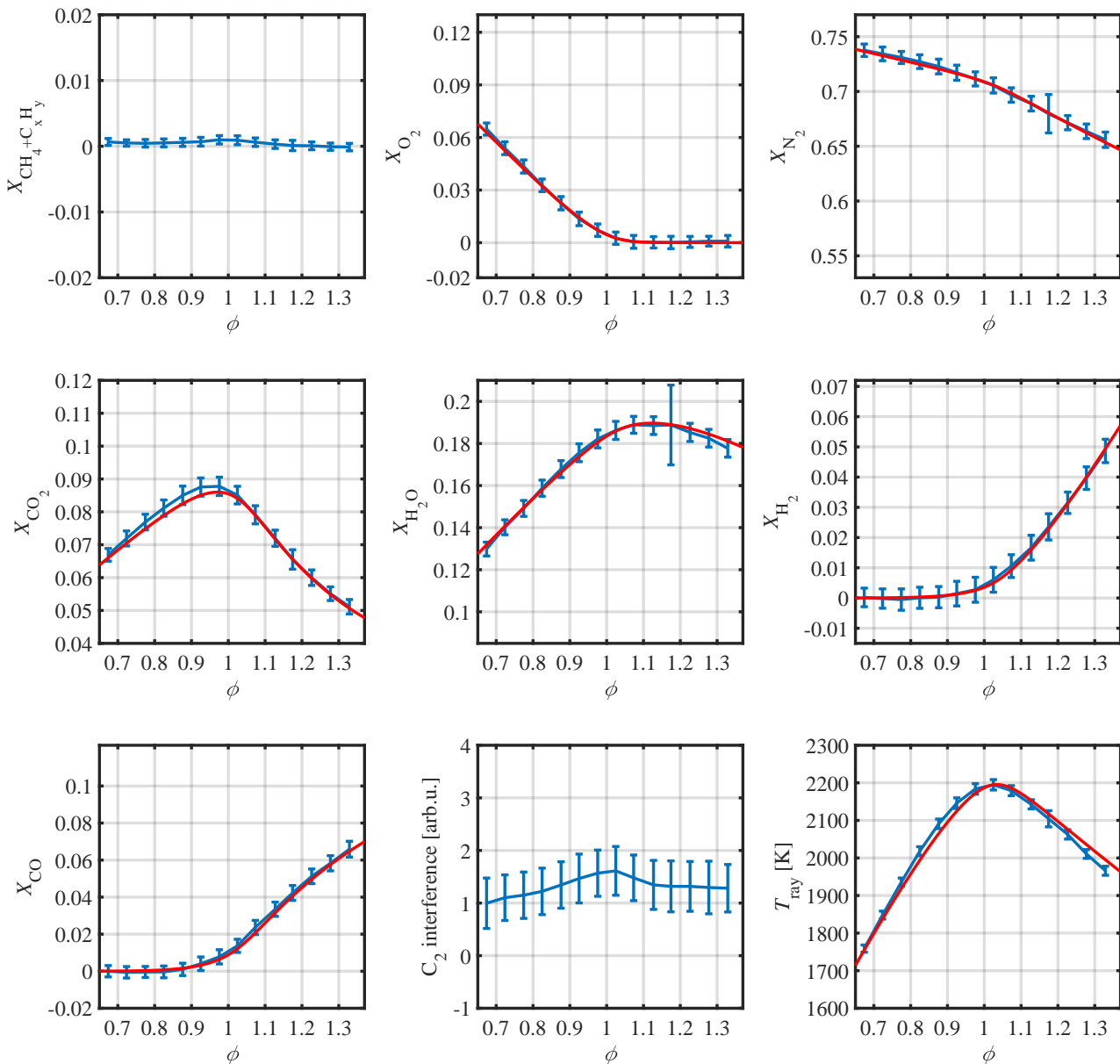

Figure 6.10.: Methane/air flat flame data at lower resolution (pixel binning of ten).

6.5.3. Hencken Burner Exhaust Gases

The Hencken burner stabilizes hydrogen/air flames over a wide range of equivalence ratios, making it particularly suitable to tune all water and hydrogen multipliers and crosstalks due to the lack of carbon species. For each equivalence ratio one hundred samples are measured. In the Hencken burner, the cold mixture is not captured concurrently, as the equivalence ratio derivation in the ignited mixture is more reliable than that of the flat flame.

6.5.3.1. Hydrogen/air with Higher Spatial Resolution Binning

Figure 6.11 shows the Hencken burner results recorded with a smaller binning of four pixels. The blue lines with two standard deviation long errorbars are mean mole fractions, the C_2 LIF, and the temperature. In red, the results of a concurrent numerical reactor calculations are shown. Generally, all species are well captured by the calibration. This is despite the fact that the flat flame and Hencken burner results share the identical multipliers.
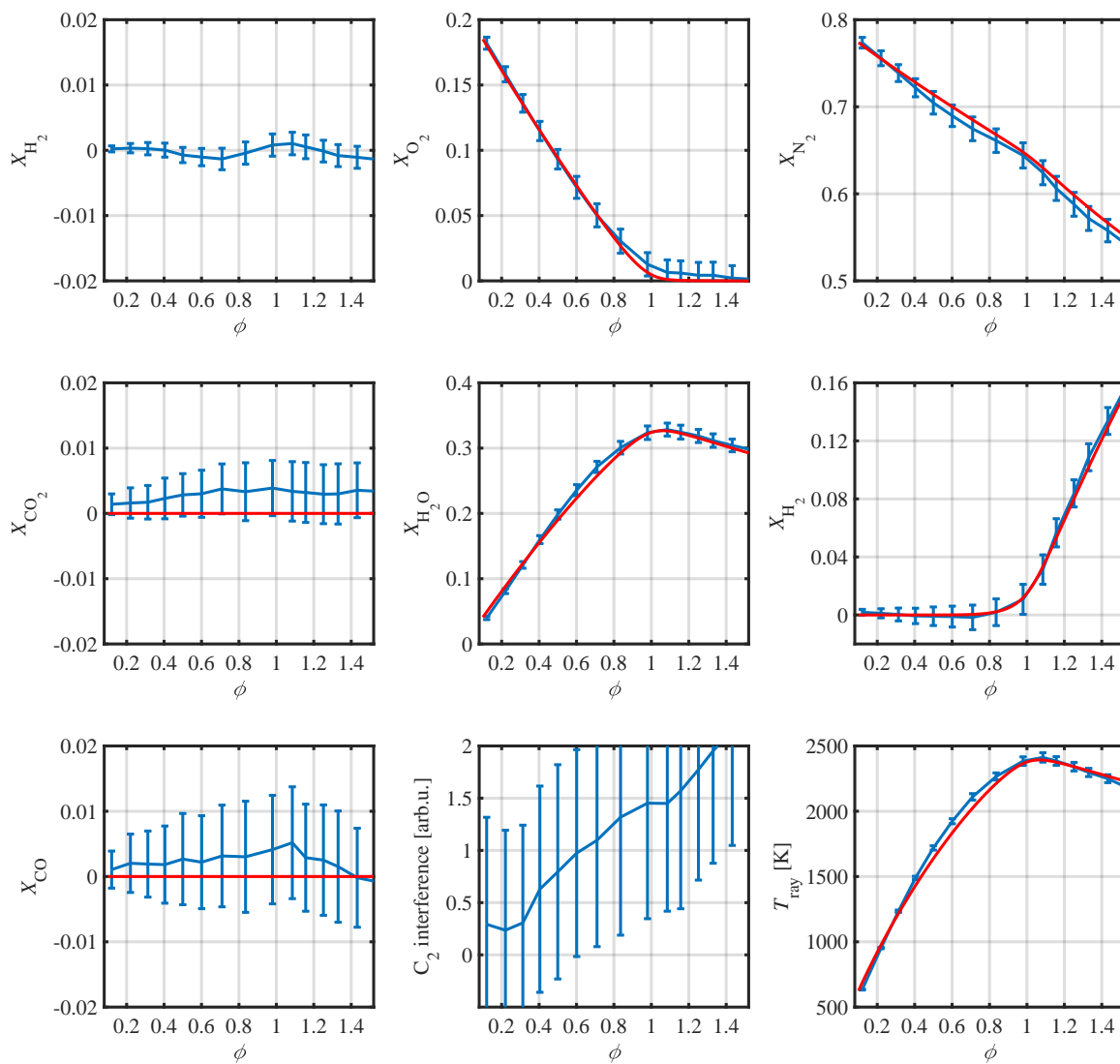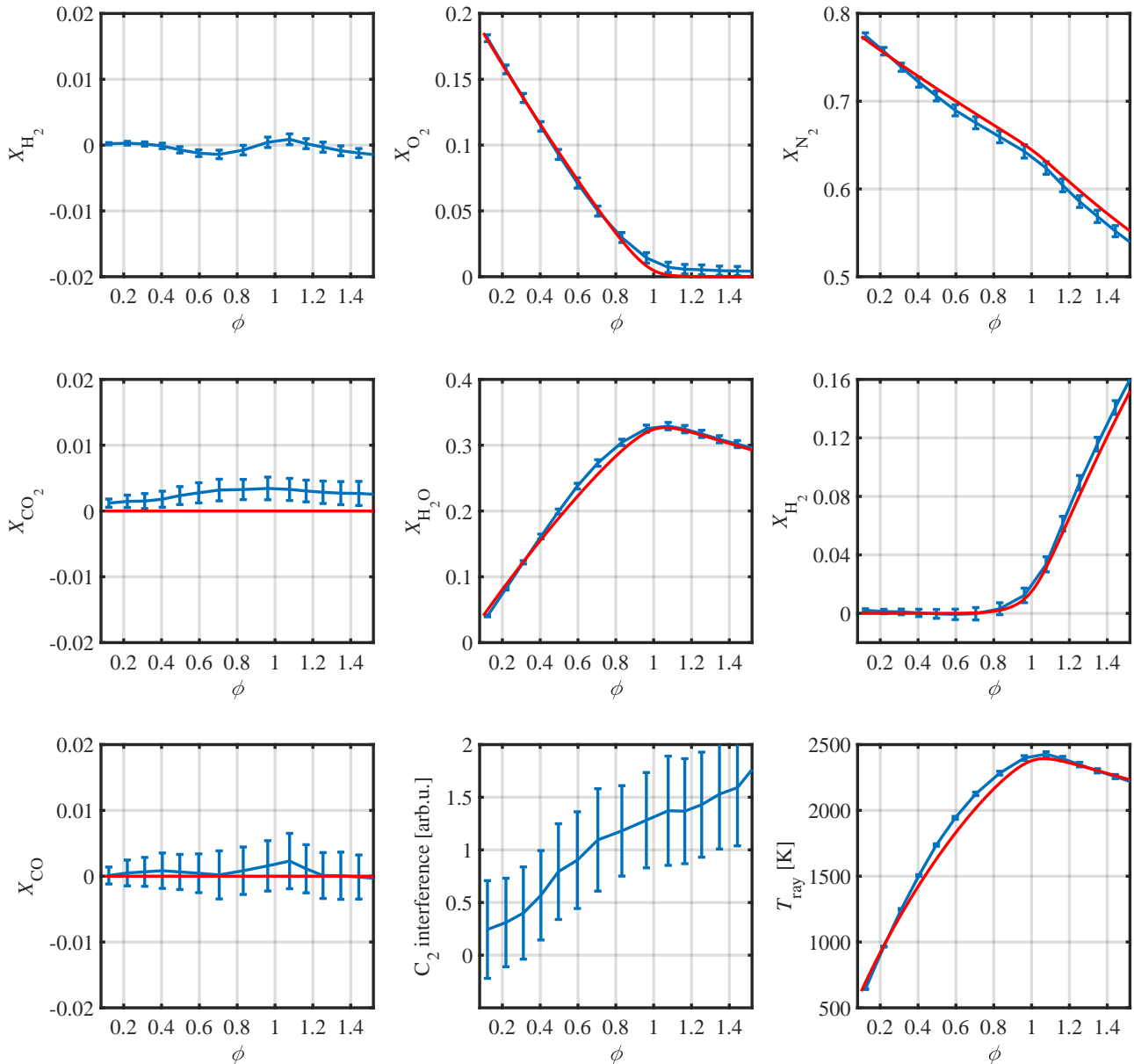
Figure 6.11.: Hydrogen/air Hencken flame data at higher resolution (pixel binning of four).

6.5.3.2. Hydrogen/air with Higher SNR Binning

Figure 6.11 shows the Hencken burner results with a larger binning of ten pixels, which is used together with the flat flame as a calibration source for methane/air TCJB flames. Besides smaller errorbars, the results appear almost identical to the four-binned pixels set, again highlighting the system's stability between measurement days.

Figure 6.12.: Hydrogen/air Hencken flame data at lower resolution (pixel binning of ten).

6.5.4. Twin Flames Exhaust Gases

The concept of using twin flames for the ethanol/air calibration was broadly discussed in Section 6.2.1.2. In brief, the ethanol/air flame exhaust gases at the central point between two identical twin flames offer a possibility to tune the MI multipliers at flame-relevant temperatures, similar to what is done in the flat flame exhaust gases for methane/air.

Thereby, twin flames at each equivalence ratio are first centered in the Rayleigh camera FOV, which is possible with an uncertainty in accuracy of approximately $\pm 60\,\mu m$. Next, the hot gas region width is measured so that the strain rate of a concurrent numerical 1D flame calculation can be fitted to the experiment (Section 3.4). In the next step, the flame is turned off so that the unignited mixtures can be measured. As for the flat flame, this can yield a better equivalence ratio estimation than relying on the mass flow controllers' accuracy. After one hundred samples, the mixture is ignited, and the hot gases are probed with one hundred samples.

Ideally, as the twin flame hot gas region does not technically provide gradient-free conditions, only the twin flames' center would be used to tune the multipliers. However, for a sufficient compromise between noise and spatial integration, the central four pixels' mean is taken instead ($120\,\mu m$).

One advantage of this method is that the twin flame equivalence ratios span even wider than those of the flat flame, which can increase the confidence of a successful calibration at the equivalence ratio boundaries.

Another difference to the methane/air calibration is that the ethanol/air calibration is solely based on the twin flames and its unignited mixtures. This is because incorporating the Hencken burner results did not increase, but decrease the result quality. The reason therefore could be that unlike in the methane/air flat flame and Hencken burner calibration, the laminar opposed jet burner producing the twin flames might have a slightly altered vignetting behavior. The vignetting is thereby stronger because any slight misalignment of the burner towards the first achromatic lens of the Raman detection system will put the optical signal cone at risk of being geometrically cut.

The best results were thus reached by tuning the water crosstalks across the whole equivalence ratio range, while calibrating hydrogen crosstalks within the rich twin flames. Other than that, the multiplier calibration occurred identical to the flat flame case.
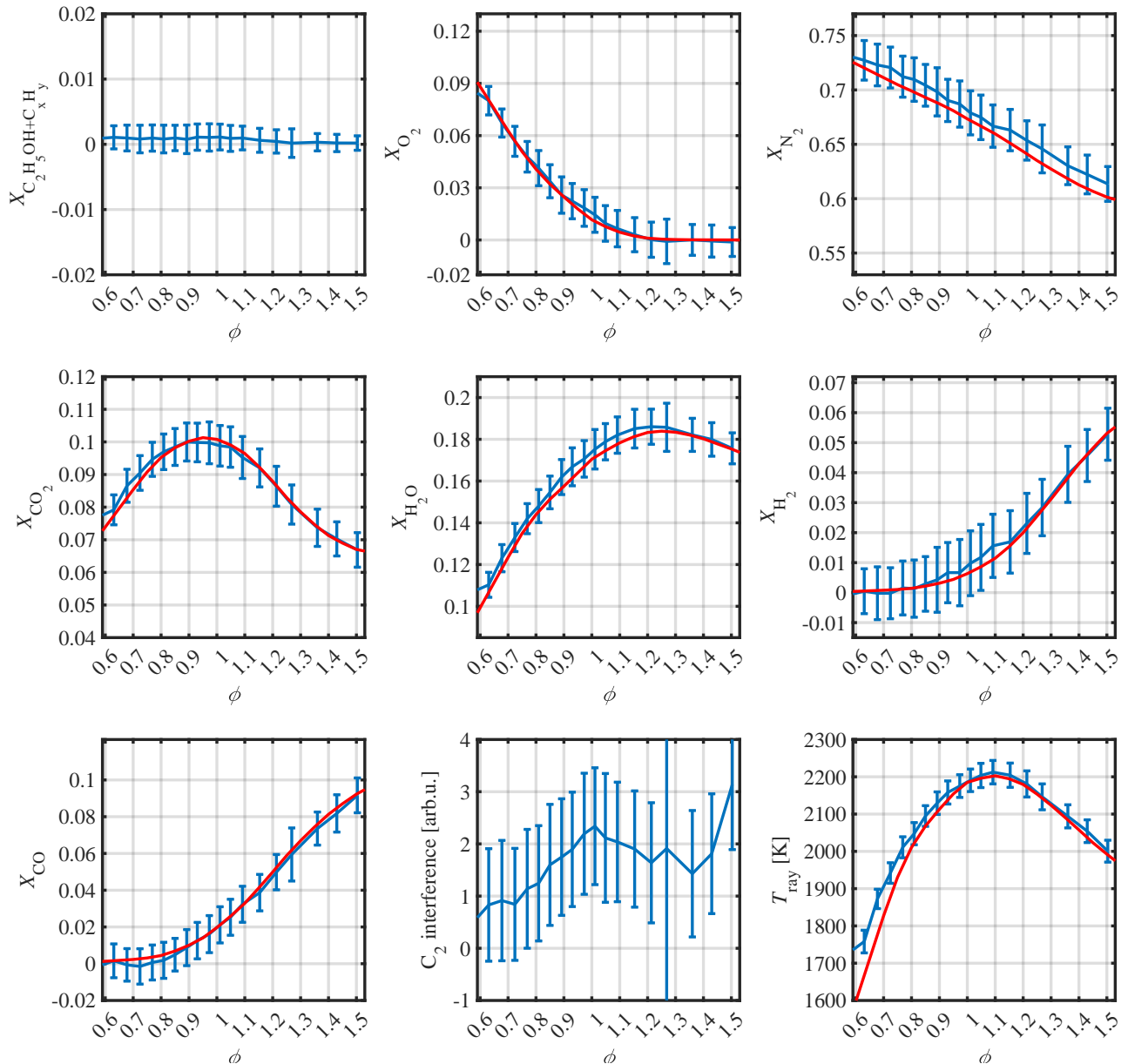
6.5.4.1. Ethanol/air with Higher Resolution Binning

The results of the ethanol/air calibration with the smaller binning of four pixels is shown in Figure 6.13.

The following observations are made when looking at the calibration results:

1. The biggest inaccuracy is found in the water mole fraction below equivalence ratio $\phi = 1.2$, where the experimental and numerically calculated values diverge by approximately 10 %.

2. For nitrogen in very rich conditions, the values are 3 % off from one another.

3. Hydrogen is overestimated near the central equivalence ratio and is slightly underestimated at ϕ=1.5.

4. Although the maximum flame temperature location is well captured at about equivalence ratio ϕ=1.1, the temperatures under lean conditions are increasingly overestimated below ϕ=0.8. Disregarding the lowest equivalence ratio setpoint, the highest deviation from the numerical calculation is approximately 5 %, which is considered acceptable.
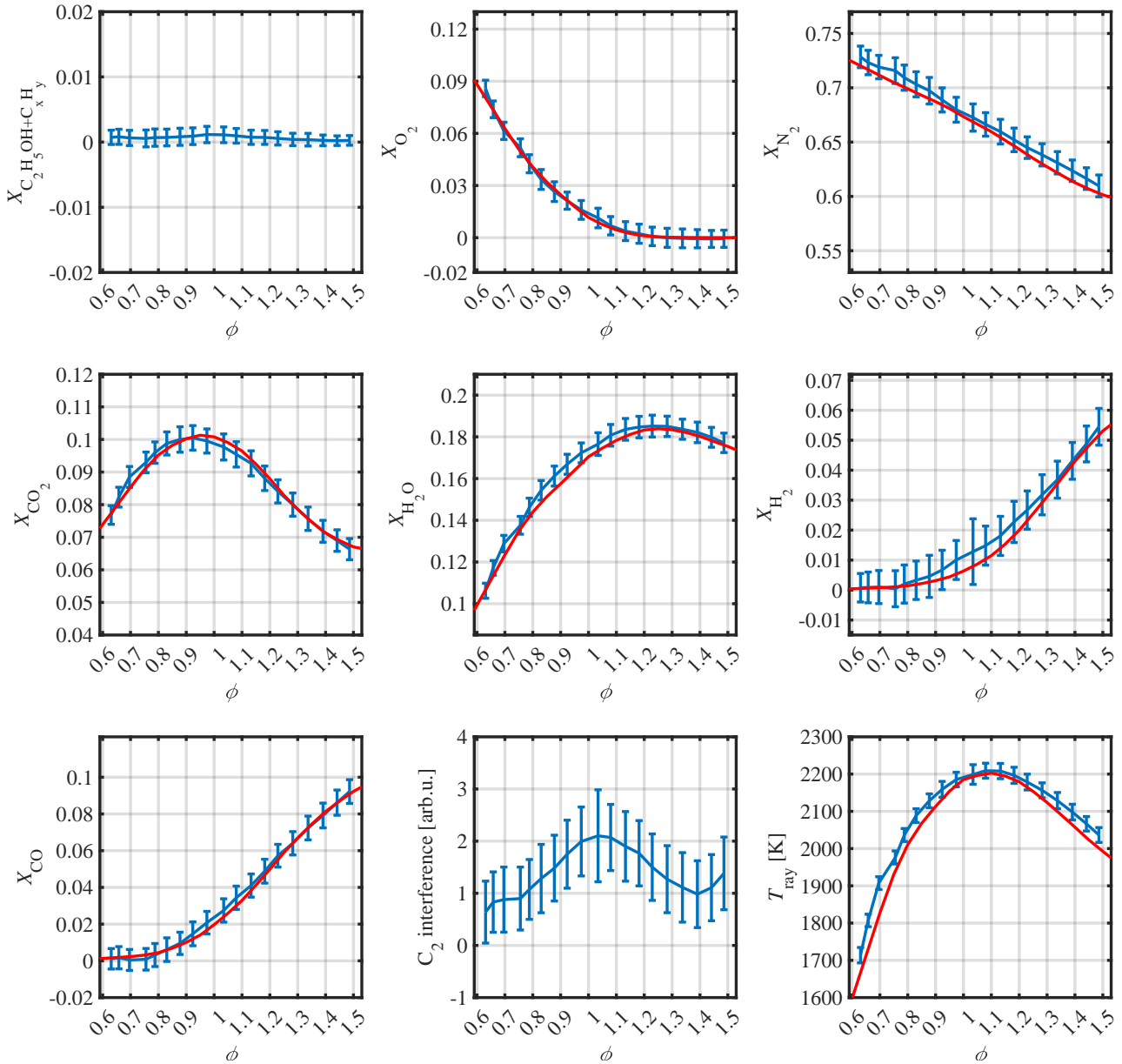

Figure 6.13.: Center of premixed ethanol/air twin flames as an alternative to the exhaust gas calibration in the flat flame. Data recorded with a higher resolution.

6.5.4.2. Ethanol/air with Higher SNR Binning

The calibration results for ethanol/air twin flames with the larger binning are shown in Figure 6.14.

Figure 6.14.: Center of premixed ethanol/air twin flames as an alternative to the exhaust gas calibration in the flat flame. Data recorded with a lower resolution.

The results show some deviations compared to the previous calibration using the higher resolution binning:

1. Nitrogen is now slightly overestimated even in the lean conditions.

2. Carbon dioxide, with an offset of up to 5 % at equivalence ratios larger than $\phi = 1.3$, is not as accurate as before.

3. Furthermore, the temperature became inaccurate towards the rich side.

The reasons for these deviations from the first calibration set are not clear. Due to the large system stability demonstrated with the methane/air calibrations, the influence by excitation and detection system drifts is not the primary suspect.

Instead, the following two random uncertainty sources are suspected, which are introduced with the twin flame calibration:

1. The twin flames need to be accurately probed in their center to avoid obtaining false data points. Aligning them, which is so far a manual procedure, could be done by finding the symmetry in the data. However, the required amount of time to realize this within the post-processing code could not be invested within this work.

2. The added fuel/air mixture preparation devices come with additional uncertainties. Besides only relying on mass flow controllers, the vaporizer, heating hoses and burner heating elements all need to operate correctly.

Despite all the mentioned inaccuracies, the result's uncertainties are not excessive. Rather, they are not too far from the previously shown methane/air flat flame results. Thus, it is appropriate to continue with these tuned multipliers and crosstalks towards target flames.

## 6.6. Ethanol/air Flame Intermediate Species Estimation

As shown in Section 3.6, methane/air flames contain a negligible amount of intermediate hydrocarbons smaller than 1 %, whereas those in ethanol/air can reach between 3.3 and 4.4 % in rich and partially-premixed conditions. At such amounts, the intermediates make up a substantial part of the thermochemical state in the primary reaction zone. Thus, it is essential to account for them in some way. This process is described in the following.

6.6.1. Observed Intermediate Species Influence

Quantifying intermediate species amounts using sRS is challenging. First, their temperature-dependent spectral shapes are unknown at flame level temperatures. Second, they are clustered within the CH-stretch region and submerged under the relatively wide ethanol spectrum (Chapter 4).

To overcome these obstacles at the current state of research, the engineering approach described below is utilized. Therefore, after successfully calibrating the unburned and burned gases using twin flames (previous sections), the intermediate species' influences on other species within the primary reaction zone of opposed jet flames is investigated in the temperature space.

Figure 6.15 shows an example at $\phi=1.1$.
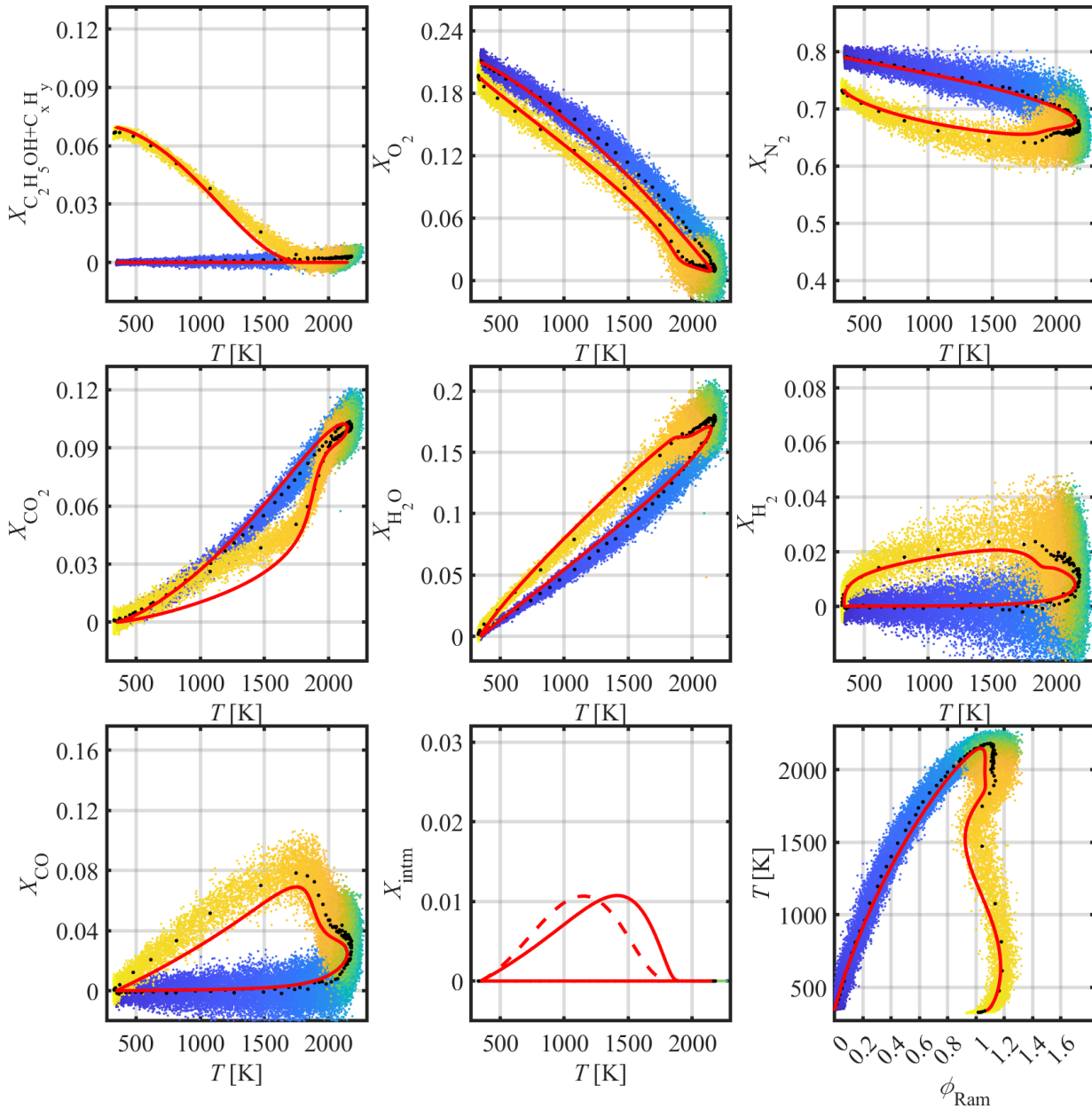
Figure 6.15.: Thermochemical states of ethanol/air opposed jet flame at equivalence ratio $\phi=1.1$ in temperature space. The scattered data color indicates the spatial dimension from the cold ethanol/air mixture (blue) to the opposing nozzle's cold air (yellow). The scattered data results are inconsiderate of any intermediate species solution, which will follow below. On the lower central graph, the actual sum of intermediates (solid line) obtained from the numerical calculation is plotted next to the surrogate intermediate signal (dashed line), which is an engineering approach of measuring intermediate species that will be introduced in this section.

The following observations are made regarding the intermediate species' influence at medium temperatures:

1. The top left graph shows the numerically derived mole fractions for ethanol alone. The scattered data points clearly overestimate the ethanol line. This is because the intermediates lead to an excess amount of signal in the ethanol and CH-stretch region.

2. The carbon dioxide channel is subject of crosstalk by a number of intermediate species, namely by ethylene, acetaldehyde and formadehyde (Kevin Dieter, personal communication February 2023). This also becomes evident by looking at the scatter deviation from the numerical solution in the yellow scattered region.

3. Carbon monoxide and oxygen are also overestimated, likely by proxy crosstalk via other species.

4. The overestimation of the species described above leads to the underestimation of nitrogen and water, as the matrix inversion is set out to balance all species.

6.6.2. Engineering Approach

As mentioned, an engineering approach is used to estimate the summed intermediate species' quantity and control the resulting bias. From the red solid line in Figure 6.15's lower central graph, it is visible that the intermediates species are zero initially, rise linearly with temperature, peak at approximately 1400 K and then drop to zero again.

This behavior can be mimicked by multiplying the ethanol and carbon monoxide mole fractions with the temperature and a heuristically derived constant:

$$X_{\text{intm,surr}} = K_{\text{heur}} \cdot X_{\text{C}_2\text{H}_5\text{OH}} \cdot X_{\text{CO}} \cdot T_{\text{Ray}} \tag{6.1}$$

In this surrogate intermediate species calculation, the individual values each serve a certain purpose:

1. Carbon monoxide, which itself is an intermediate species, serves as a base parameter. It is required because relying singularly on the ethanol mole fraction would not pull down the intermediate species mole fraction to zero before the temperature rises.

2. As mentioned, the intermediate species then rise approximately linear with temperature. Therefore, the temperature is included.

3. In the flame's very hot regions, the intermediates again need to decrease. Therefore, the ethanol mole fraction is included, which should converge towards zero there.

4. Lastly, the intermediate species peak's height is adjusted using the heuristically determined constant K_{heur}. For the ethanol/air flames in this study, it is tuned to $0.0055\,\text{K}^{-1}$.

The resulting intermediate species mole fraction is comparatively displayed as a dashed line with the actual intermediate mole fraction (solid line) in Figure 6.15's lower central graph.

While the magnitude of the surrogate signal is capturing the actual summed intermediate mole fraction rather accurately, the resulting curve's approximately symmetric shape in temperature

space is not skewed towards the hot side in comparison to the numerical data. Thus, the surrogate peak precedes the summed intermediate mole fraction's peak by about 200 to 300 K. To put the deviation into perspective, it is equivalent to roughly the size of one binned pixel in the target flame experiment (using a binning of ten). Because this error is limited and because no better definition of the surrogate was found, this shortcoming in temperature space is acknowledged, but accepted from here on.

Using the derived surrogate intermediate signal, it is now possible to reduce the before mentioned biases in the primary reaction zone in two steps. While the two steps could be combined, they are calculated individually for easier comprehension:

1. First, to ensure that the integrated mole sum of major species and surrogate intermediate species is equal to one, all major species are reduced by fractions of the intermediate species:

$$X_{\mathrm{i,corr}} = X_{\mathrm{i}} \cdot (1 - X_{intm,surr}) \tag{6.2}$$

2. Next, to fix the biases resulting from intermediates species' crosstalks and proxy crosstalks described in the previous section, the intermediate species surrogate is added or subtracted from the channels in a heuristic fashion as necessary:

$$X_{\mathrm{i,corr}} = X_{\mathrm{i}} + kk_{\mathrm{heur,i}} \cdot X_{intm,surr} \tag{6.3}$$

The $kk_{\mathrm{heur,i}}$ factors are thereby like Raman calibration factors m_{ij} in the matrix inversion, which are also, at times, heuristically tuned under well-defined boundary conditions (Section 2.6.3). The goal is to account for the combined crosstalk that the intermediate species exert on all channels. Notably, these factors can either have a positive or negative sign. This is due to the fact that a intermediate species crosstalk onto one species will lead proxy crosstalks by this channel onto other channels via its previously defined non-intermediate species crosstalks.

As an example, since water and nitrogen are underestimated, their calibration factor $kk_{\mathrm{heur,i}}$ values need to be positive. As a result of the heuristic tuning, 12/7 and 5/7 times the surrogate intermediate species are added to their respective mole fractions. Ethanol, oxygen, carbon dioxide, hydrogen, and carbon monoxide, on the other hand, are overestimated and the $kk_{\mathrm{heur,i}}$ values need to be negative as a result. The respective factors are -3/7, -1/7, -5/7, -2/7, and -6/7. In the end, the sum of all factors needs to be zero in order to retain the combined mole fraction of one at all locations.

The described procedure removes as much of the biases as possible when compared to the numerical calculation benchmark. The processes results for the central $\phi=1.1$ equivalence ratio can be seen in Figure 6.27, where the remaining offsets will be discussed. A lean and a rich setpoint with identical surrogate correction terms are shown in Figures 6.26 and 6.28, respectively.

6.6.3. Limitations

There are limitations as to how trustworthy the surrogate intermediate species mole fraction is. For one, the relation between ethanol, carbon monoxide, and temperature is dependent on both the

equivalence ratio, and the given strain within the flame. The dependence on equivalence ratio can be observed by comparing the lower middle graphs of the mentioned result Figures 6.26, 6.27, and 6.28. While there is a considerable discrepancy to the numerically calculated intermediate sums at the very lean and rich setpoints, the results are still improved by the engineering approach and thus accepted.

Regarding the limitation with regard to flame stretch, Figure 6.16 compares the maximum of the surrogate signal mole fraction (red lines) with the numerically calculated maximum intermediate species mole fraction (black) for laminar opposed jet ethanol/air flames (equivalence ratio $\phi=1.1$). Two different situations are shown. On the left, the ethanol/air stream is opposed with an air stream. On the right, it is opposed against lean ethanol/air exhaust gases ($\phi=0.8$). Based on the numerical calculation displayed on the right, intermediate species are underestimated by up to 30 % at extremely high strain rates of $2500\,\text{s}^{-1}$. Because the actual strain rate within the experiment is not measured concurrently, this bias can also not be accounted for and needs to be accepted.
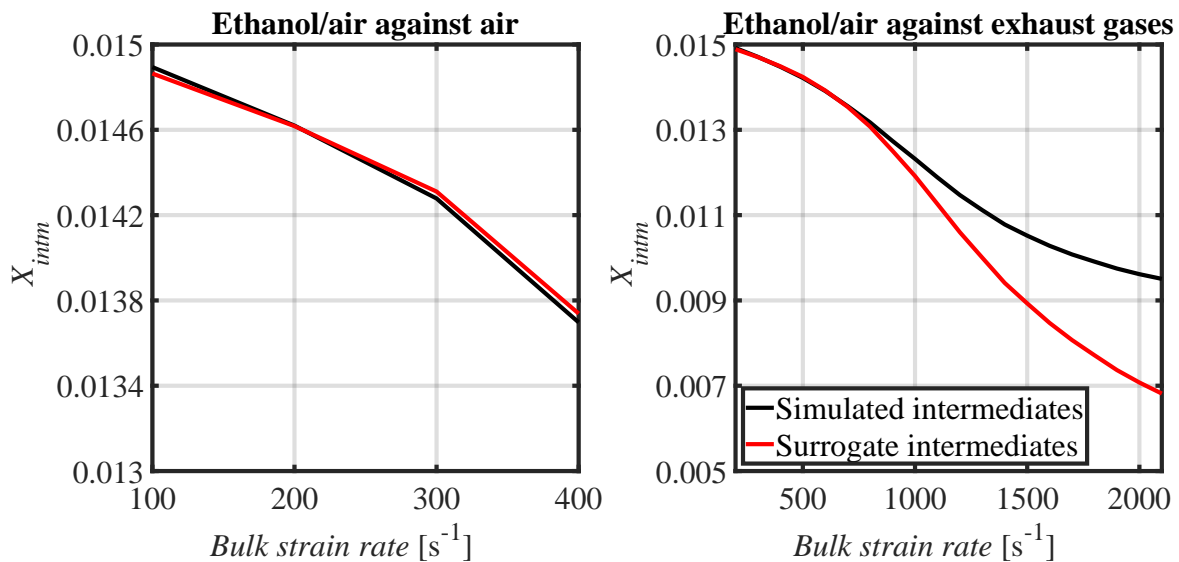
Figure 6.16.: Strain rate sensitivity of surrogate intermediate species mole fractions against numerically calculated intermediate species mole fractions at equivalence ratio $\phi=1.1$.

Lastly, the procedure relies on the correct measurements of the ethanol and carbon monoxide mole fractions used to generate this signal. These species are measured at very low amounts within the medium to hot regions of the flame front. Nevertheless, this would also be the case if the intermediate species would be measured directly and, even more so, individually.

Regardless of its imperfections, the approach is still considered to be the best option to account for intermediate species in single-shot measurements. Therefore it will be used while post-processing all target flames, including the turbulent ones. More discussions regarding the remaining offsets will follow for the laminar flames in Section 6.7.1.2.

6.6.4. Intermediate Species Influence on Equivalence Ratio

In Figure 6.15's lower right graph, the temperature is plotted in equivalence ratio space. Within the reaction zone (yellow scatter), the mean data shows a clearly visible s-shape in both numerical calculation and experiment.

Fuest et al. [54] studied a similar situation of the temperature in mixture fraction space of DME/air flames. They described in detail how differential diffusion and the subsequent local lack of species can lead to the visible mixture fraction under or overestimation. This happens when only the largest seven to twelve species are considered in the mixture fraction's calculation, rather than all 55 species that the DME mechanisms contains.

They found this using numerical flame calculations and incrementally including or excluding the different intermediate species. While using only the major seven species accurately captures mixture fractions for the methane/air flames, the larger amount of ethanol/air flame intermediate species results in an incomplete picture and the subsequent s-shape behavior.

In this work's experiments, the inclusion of strain rate and temperature dependent correction terms from numerical calculations, as done by Fuest et al.,[54], is not intended. The equivalence ratio is instead only calculated using the seven main species available from the Raman and Rayleigh measurements. Notably, a valid comparison with the numerical calculation is still possible by calculating the equivalence ratio there from only the seven major species only, as well.

6.7. Results and Discussion

In this section, the quantitative single-shot Raman results of laminar and turbulent methane/air and ethanol/air flames are presented and discussed.

First, the laminar opposed jet flames are shown of which the results can be compared one-to-one with concurrent numerical calculations. As these flames are stationary, the hardware binning can confidently be reduced to four pixels (approximately 50 µm) to increase the spatial resolution in the reaction zone. The data of the comparison fuel methane/air will be presented before the ethanol/air flame data, so that the new calibration methodology can be validated against the old one (Section 6.2).

Second, building upon the confidence established with the laminar flames, lean and rich methane/air and ethanol/air TCJB flames at three turbulence levels are evaluated using the same post-processing procedure. A notable difference is that compared to the laminar flames, the spatial binning is now increased to ten (approximately 130 µm) for the best trade-off between SNR and resolution.

6.7.1. Laminar Flames

The laminar flame investigation's main focus is to judge whether the magnitudes and gradients of main species, temperature, and surrogate intermediate species are accurately captured in the spatial dimension and in temperature space. The particular challenge in the ethanol/air flame cases is the effective treatment of C_2 LIF interference, as well as handling the presence of intermediate species in the primary reaction zone (Section 6.6).

Furthermore, another focus in this undertaking is to gather experience with the LTOJ as a calibration burner. Even for methane/air, its wide operational envelope adds significant value to the previous flame front calibration via a singular equivalence ratio point of the v flame. This includes operating the opposed jet flames in lean to partially-premixed conditions, as well as at different strain rates.

6.7.1.1. Premixed Laminar-opposed Methane/air Jet Flames

In the methane/air laminar opposed jet flame setup, methane/air mixtures at room temperature enter from the left (negative spatial direction) and oppose air flows at the same temperature entering the reaction space from the right. The mixtures are externally ignited and burn slightly left of the nozzles' center in a stable fashion. Concentric to the jets, nitrogen coflows at a common $0.3\,\mathrm{m\,s^{-1}}$ bulk velocity shield the streams against ambient fluid motions.

Several flames with equivalence ratios between $\phi=0.7$ and 1.6 in steps of 0.1 are recorded and evaluated. In the following, the lean setpoint at $\phi=0.7$, the rich setpoint at $\phi=1.5$, and a central equivalence ratio at $\phi=1.1$ will be discussed to showcase the accuracy and precision throughout the entire equivalence ratio range.

Figures 6.17, 6.18, and 6.19 show the main species mole fractions in the spatial dimension. Furthermore, the Rayleigh-derived temperature and the C_2 LIF interference are displayed. Note that although the data was captured with a binning of four, only half the increments are plotted to avoid overloading the graph.

The following observations are made from these figures:

1. Compared to the numerical laminar flame calculation, carbon monoxide is overestimated by about 10 % at its peak ($x=$-1 mm). Concurrently, nitrogen is underestimated by about 3 %. These inaccuracies likely result from their crosstalk interrelation. Looking at the lean equivalence ratio $\phi=0.8$ setpoint in Figure 6.17, the described inaccuracies appear non-existent, while for the rich $\phi=1.5$ equivalence ratio (Figure 6.19), they are magnified.

2. Hydrogen is underestimated at its peak by about the same amount as carbon monoxide. Additionally, hydrogen is underestimated at the rich setpoint throughout the whole fuel/air side of the flame. This might be due to its small mole fraction, which leads to it being the *weakest* species of all. This means that it is also the least productive to be optimized for by the solving algorithm in terms of overall error.

3. Carbon dioxide on the other hand is overestimated in the preheating region (minus 1 mm) at the central and the leaner equivalence ratio, but that inaccuracy diminishes for the $\phi=1.5$ equivalence ratio flame.

4. With the exception of hydrogen, all species are still within a $1\,\sigma$ precision band, indicating sufficient accuracy.

5. The temperature is also accurately captured throughout all equivalence ratios.
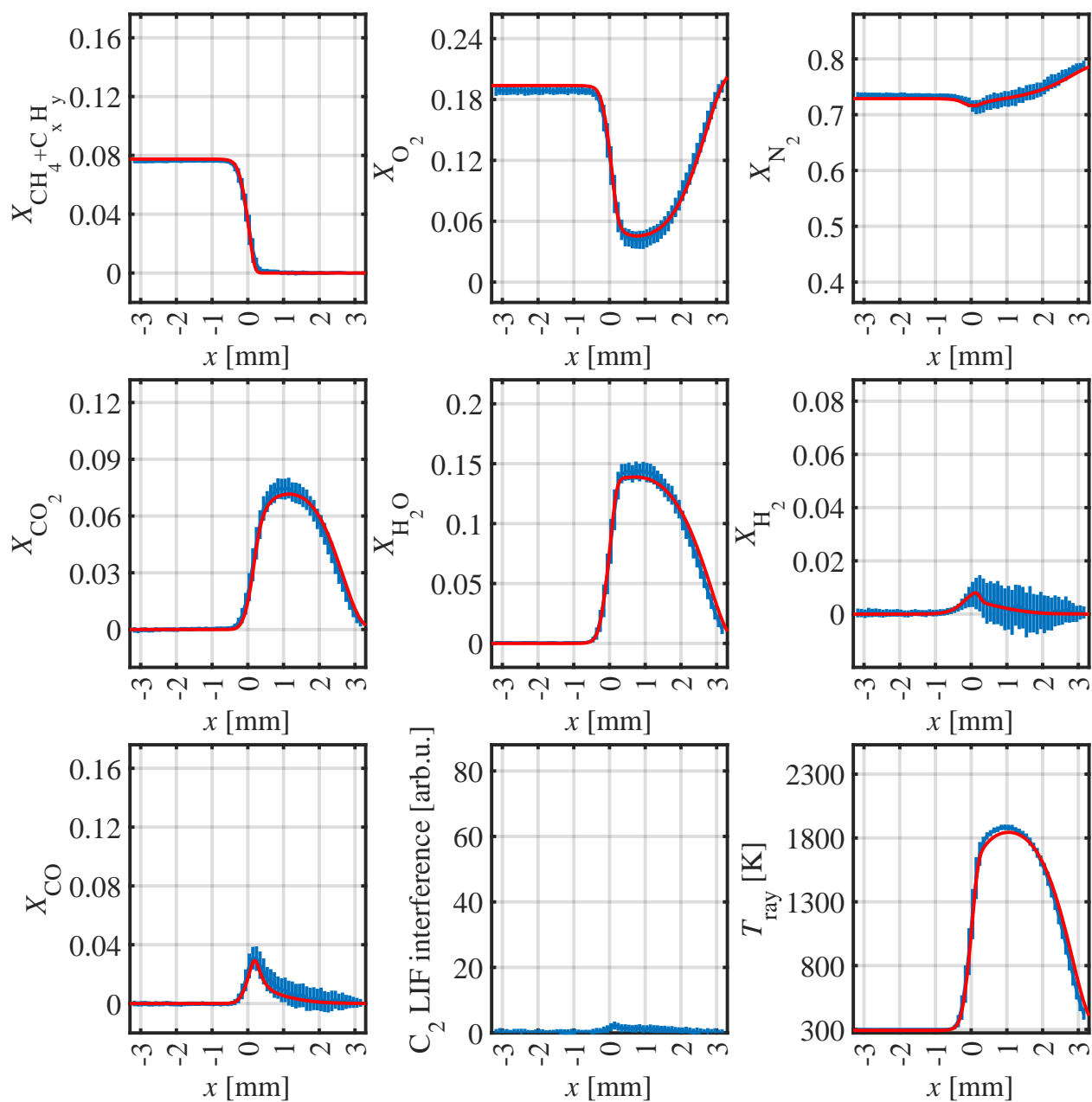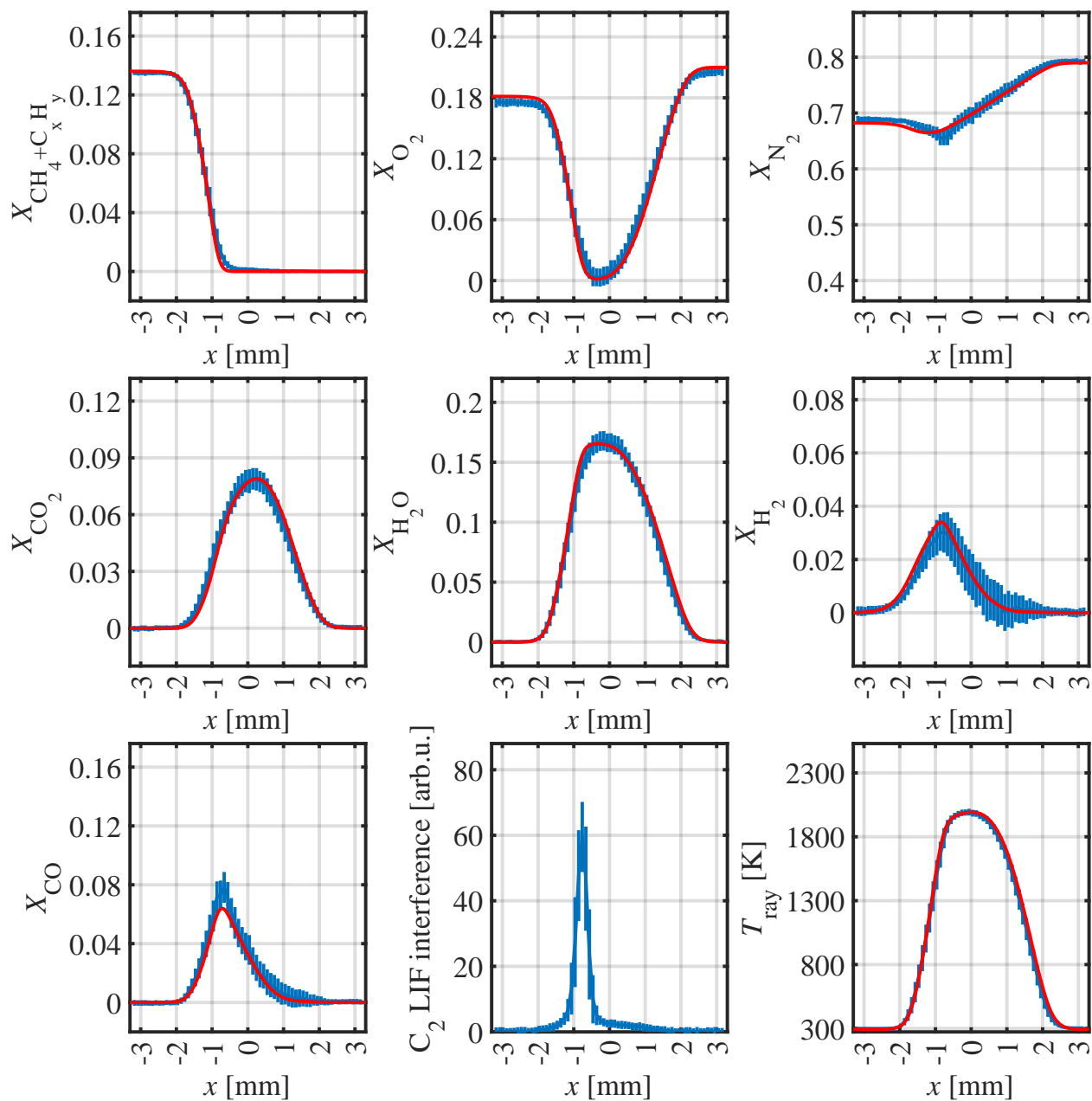
Figure 6.17.: Thermochemical states in spatial dimension of methane/air opposed jet flame at equivalence ratio $\phi = 0.8$ and strain rate $\alpha = 180\,\mathrm{s}^{-1}$.
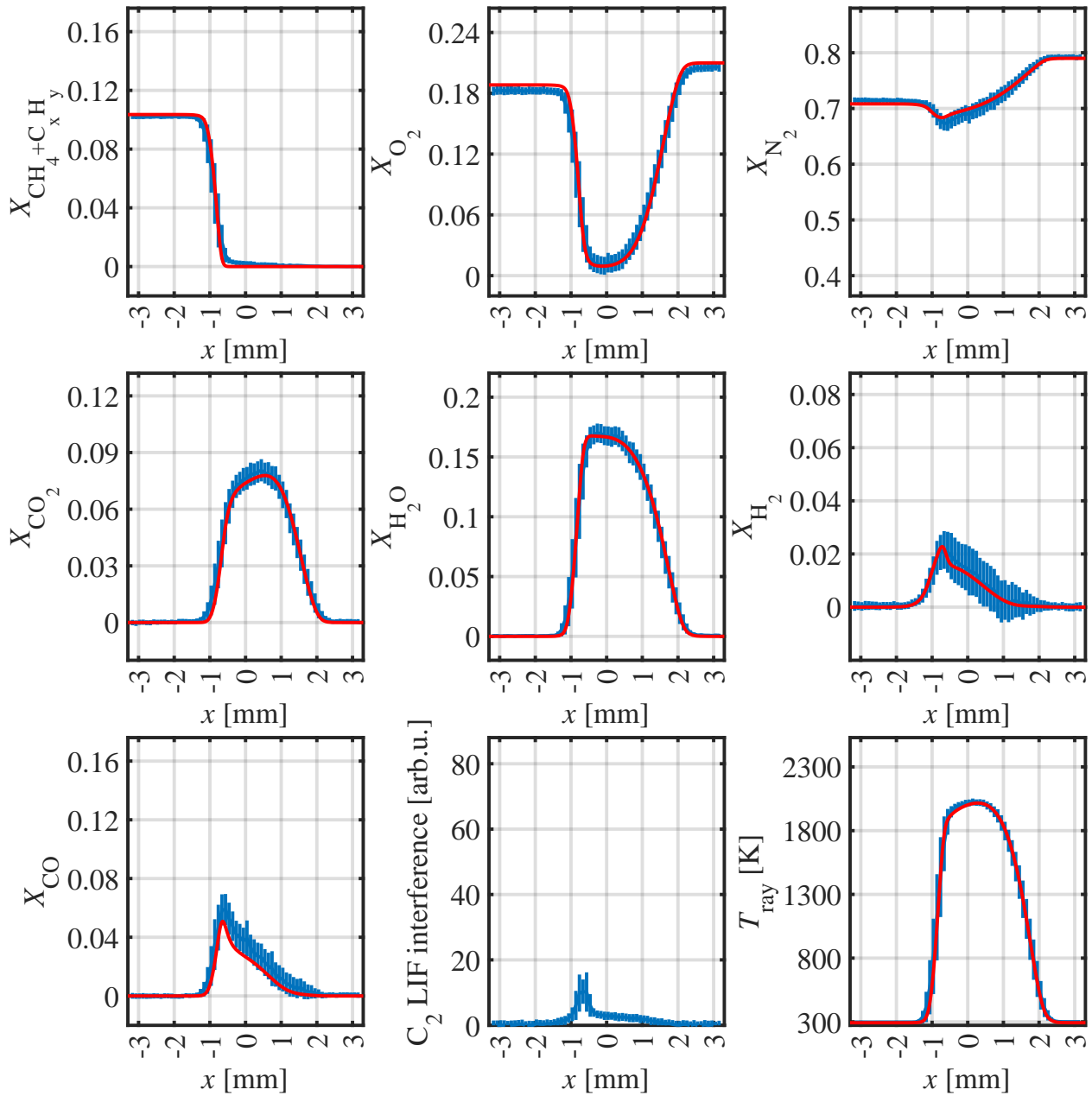
Figure 6.18.: Thermochemical states in spatial dimension of methane/air opposed jet flame at equivalence ratio $\phi=1.1$ and strain rate $\alpha=270\,\mathrm{s}^{-1}$.
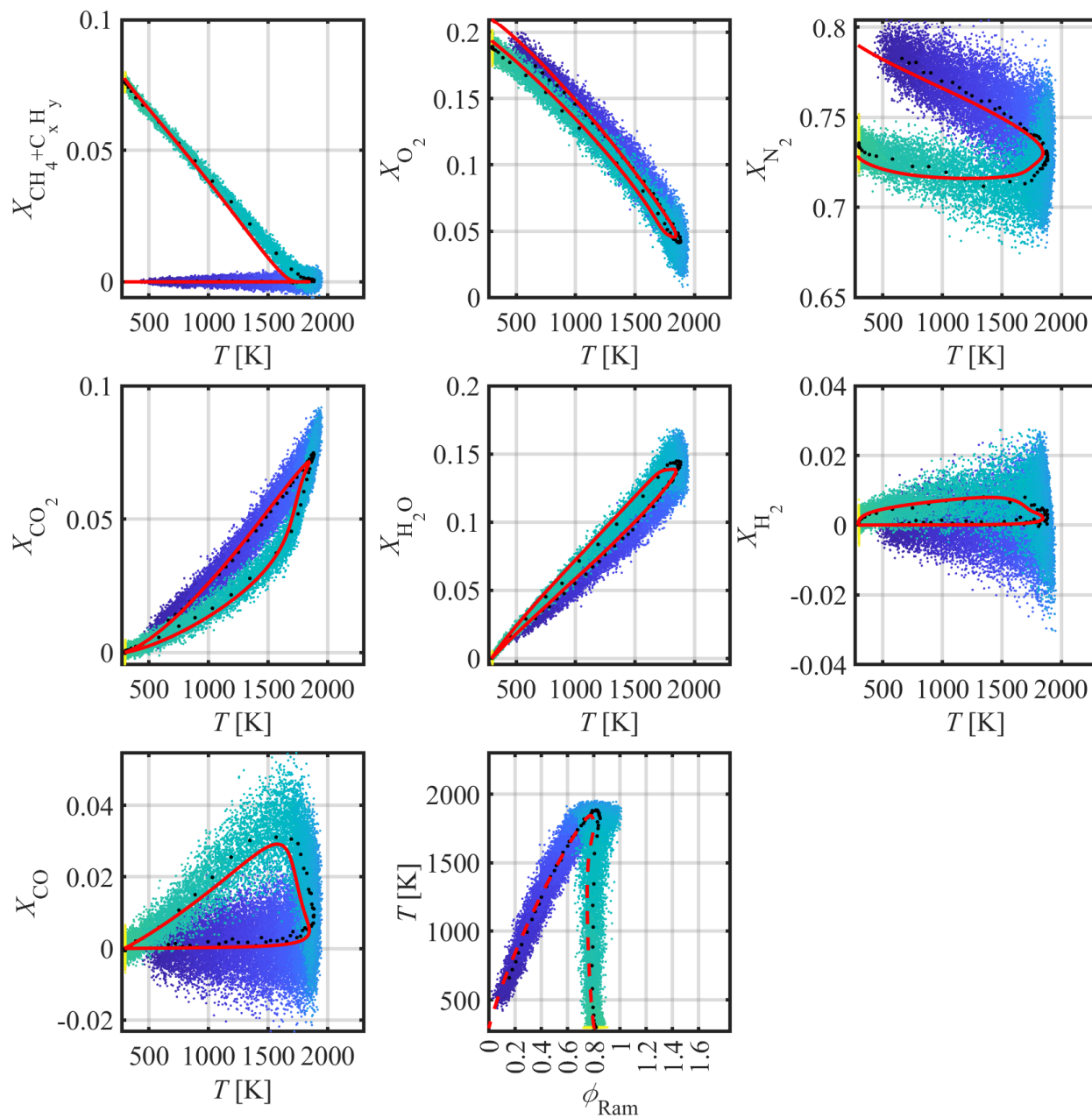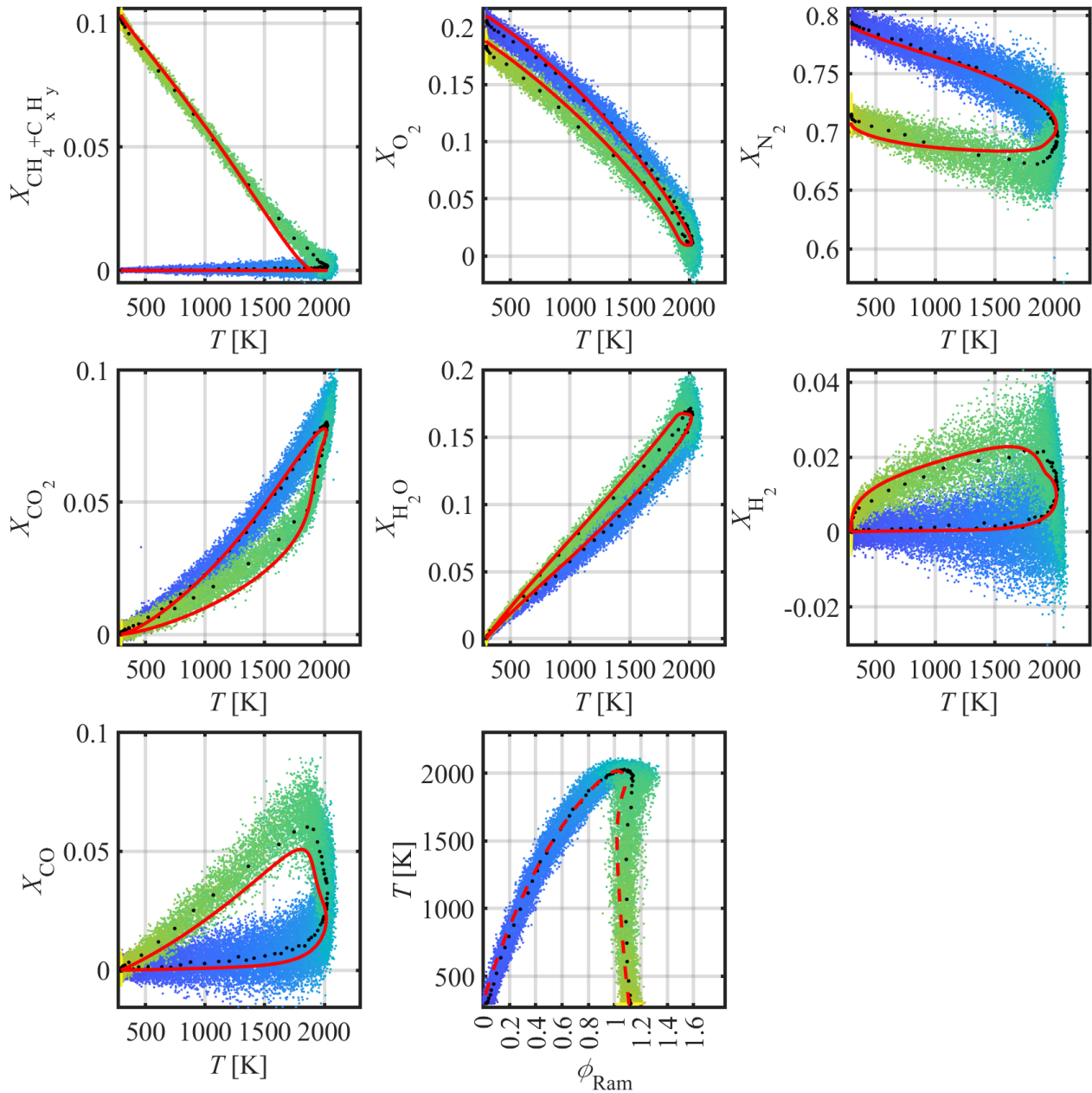
Figure 6.19.: Thermochemical states in spatial dimension of methane/air opposed jet flame at equivalence ratio $\phi=1.5$ and strain rate $\alpha=100\,\mathrm{s}^{-1}$.

Figures 6.20, 6.21, and 6.22 show the identical data, but in temperature space. Thereby, the primary reaction zone behavior can be inspected in more detail. The scattered data color spectrum represents the spatial information, with yellow dots being data points from near the methane/air nozzle, blue from the air nozzle and green from in between.

No new inaccuracies, in addition to the ones described above, have appeared. It is worth noting that while the multipliers and polynomials remained the same compared to the flat flame and Hencken burner calibration, their determination was an iterative procedure between those flames and the laminar opposed flames presented here. Finding these multipliers and polynomials is challenging due to the increasing amount of C_2 in rich flames. Furthermore, the fact that multipliers are not only a function of temperature, but also behave interdependently with those of other species and crosstalks, adds to the complexity level. In light of these factors, the data accuracy and precision presented here, and the fact that it could be mostly preserved under both lean and rich conditions, indicates a successful tuning process for methane/air flames.

Figure 6.20.: Thermochemical states in temperature space of methane/air opposed jet flame at equivalence ratio $\phi=0.8$ and strain rate $\alpha=180\,\mathrm{s}^{-1}$. The scatter data color indicates the spatial dimension from the cold methane/air mixture (yellow) to the opposing nozzle's cold air (blue).

Figure 6.21.: Thermochemical states in temperature space of methane/air opposed jet flame at equivalence ratio $\phi=1.1$ and strain rate $\alpha=270\,\mathrm{s}^{-1}$ The scatter data color indicates the spatial dimension from the cold methane/air mixture (yellow) to the opposing nozzle's cold air (blue).
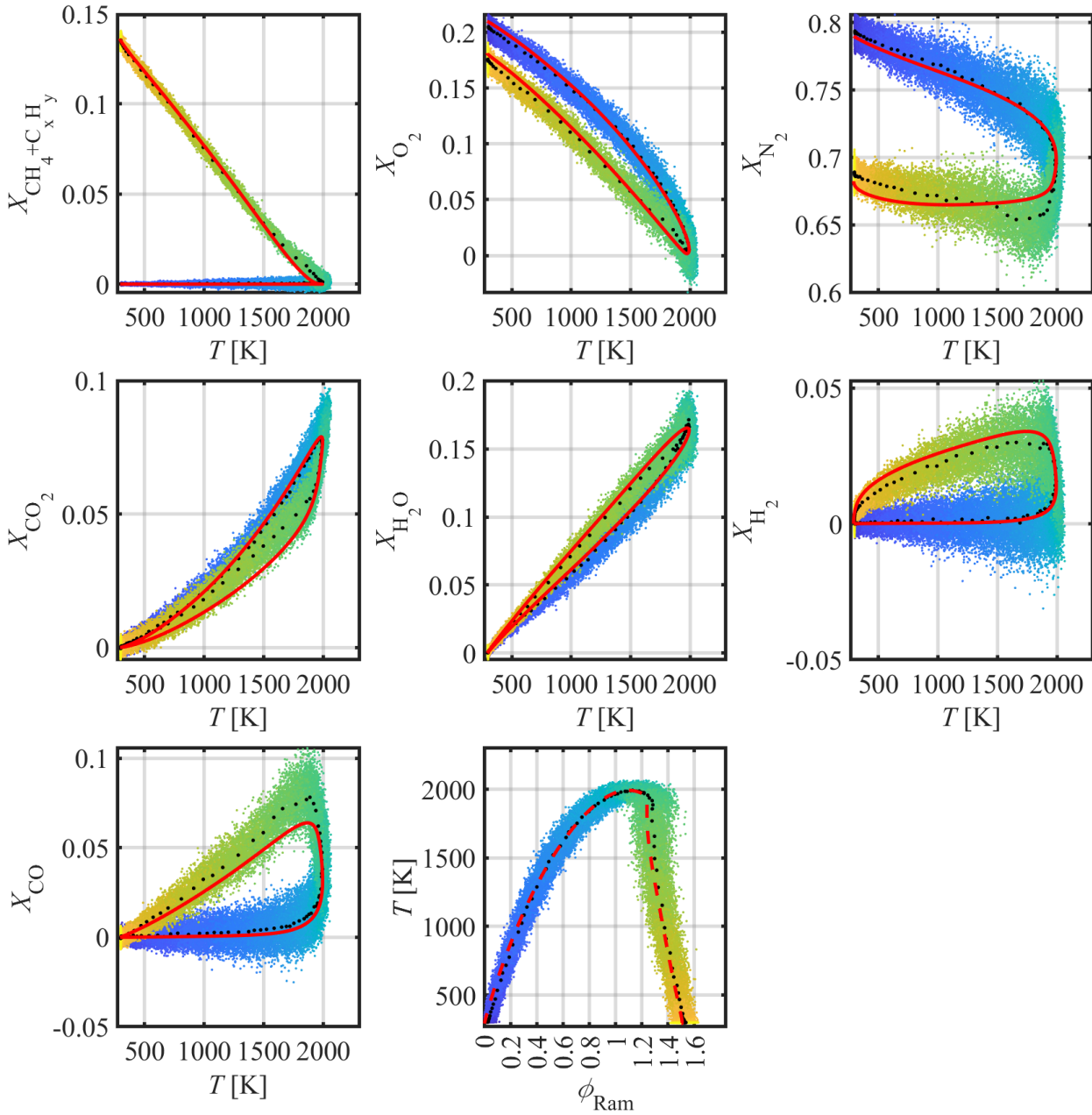
Figure 6.22.: Thermochemical states in temperature space of methane/air opposed jet flame at equivalence ratio $\phi=1.5$ and strain rate $\alpha=100\,\mathrm{s}^{-1}$. The scatter data color indicates the spatial dimension from the cold methane/air mixture (yellow) to the opposing nozzle's cold air (blue).

6.7.1.2. Premixed Laminar-opposed Ethanol/air Jet Flames

In this laminar opposed ethanol/air jet flame setup, vaporized ethanol/air mixtures at 343 K are introduced into the reaction space from the left (negative spatial direction), while air flows at the same temperature oppose from the right. The mixtures are ignited externally and burn slightly left of the nozzle center in a stable fashion. Nitrogen coflows with a common $0.3\,\mathrm{m\,s^{-1}}$ bulk velocity shield the streams against ambient fluid motion.

It is important to note that the ethanol/air opposed jet flames did not burn steadily in equivalence ratios below ϕ=0.75, regardless of the chosen strain rate. The range finally recorded and evaluated spans from ϕ=0.75 to 0.9 in 0.05-steps and continues until ϕ =1.5 in 0.1-steps.

While Figures 6.23 and 6.25 show the lean and rich setpoints with equivalence ratios ϕ =0.8 and 1.5, respectively, Figure 6.18 shows the central ϕ=1.1 equivalence ratio. Again, main species' mole fractions in spatial dimension are plotted and additionally, the Rayleigh-derived temperature and the C_2 LIF interference are displayed.

The following observations are made regarding the matching of experiment and numerical calculation:

1. The carbon monoxide mole fraction is overestimated by about 25 % throughout the hot gas region. At the same time, the nitrogen mole fraction is underestimated, with the offset being approximately 3.5 %. Like in the methane/air case, this is the result of sensitive bidirectional carbon monoxide and nitrogen crosstalks. Notably, that balance could be optimized for the presented target flame. However, using the optimized multipliers would lead to a worsened twin flame calibration result. In the end, the twin flame-optimized multipliers are taken.

2. Carbon dioxide is slightly overestimated behind the primary reaction zone. In lean conditions, the overestimation shifts to the complete hot gas region. At rich conditions, the carbon dioxide estimate is flawless, also thanks to the treatment of intermediate species (Section 6.6).

3. Water is overestimated in the hot gas region by about 3 %. This inaccuracy is the same at lean conditions, but vanishes at rich conditions.

4. Hydrogen is overestimated in the hot gas region by about 25 %. At lean conditions, the amount of hydrogen is minuscule, but it seems to be accurately captured. At rich conditions, the result is even more accurate.

5. The C_2 LIF interference is almost twice as high as for the methane/air flames. However, looking at the presented graphs, the correction thereof is considered a success.

6. The Rayleigh-estimated temperature is overestimated at lean conditions and accurately captured at equivalence ratios ϕ = 1.1 and 1.6.
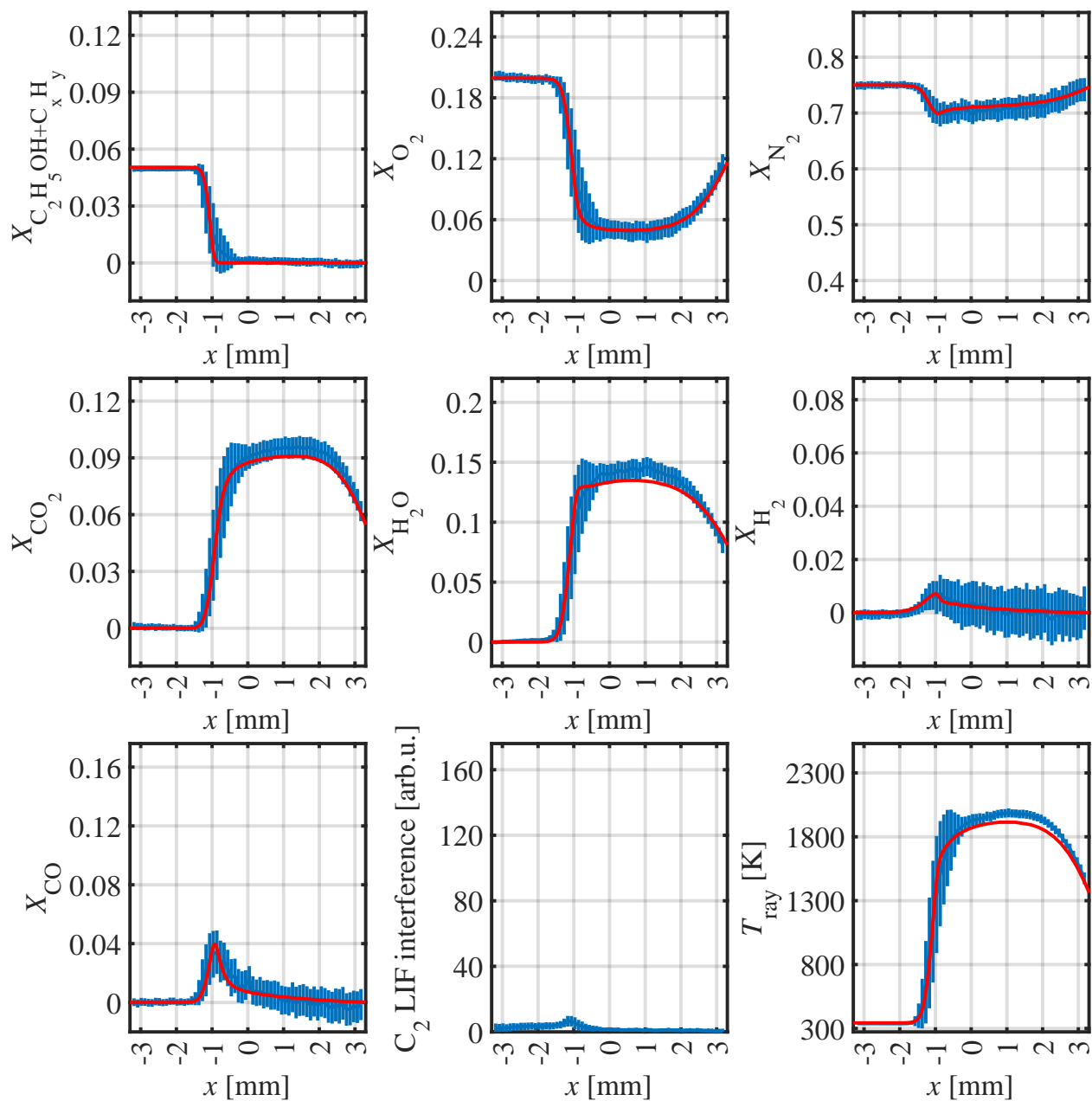
Figure 6.23.: Thermochemical states in spatial dimension of ethanol/air opposed jet flame at equivalence ratio $\phi = 0.8$ and strain rate $\alpha = 120\,\mathrm{s}^{-1}$.
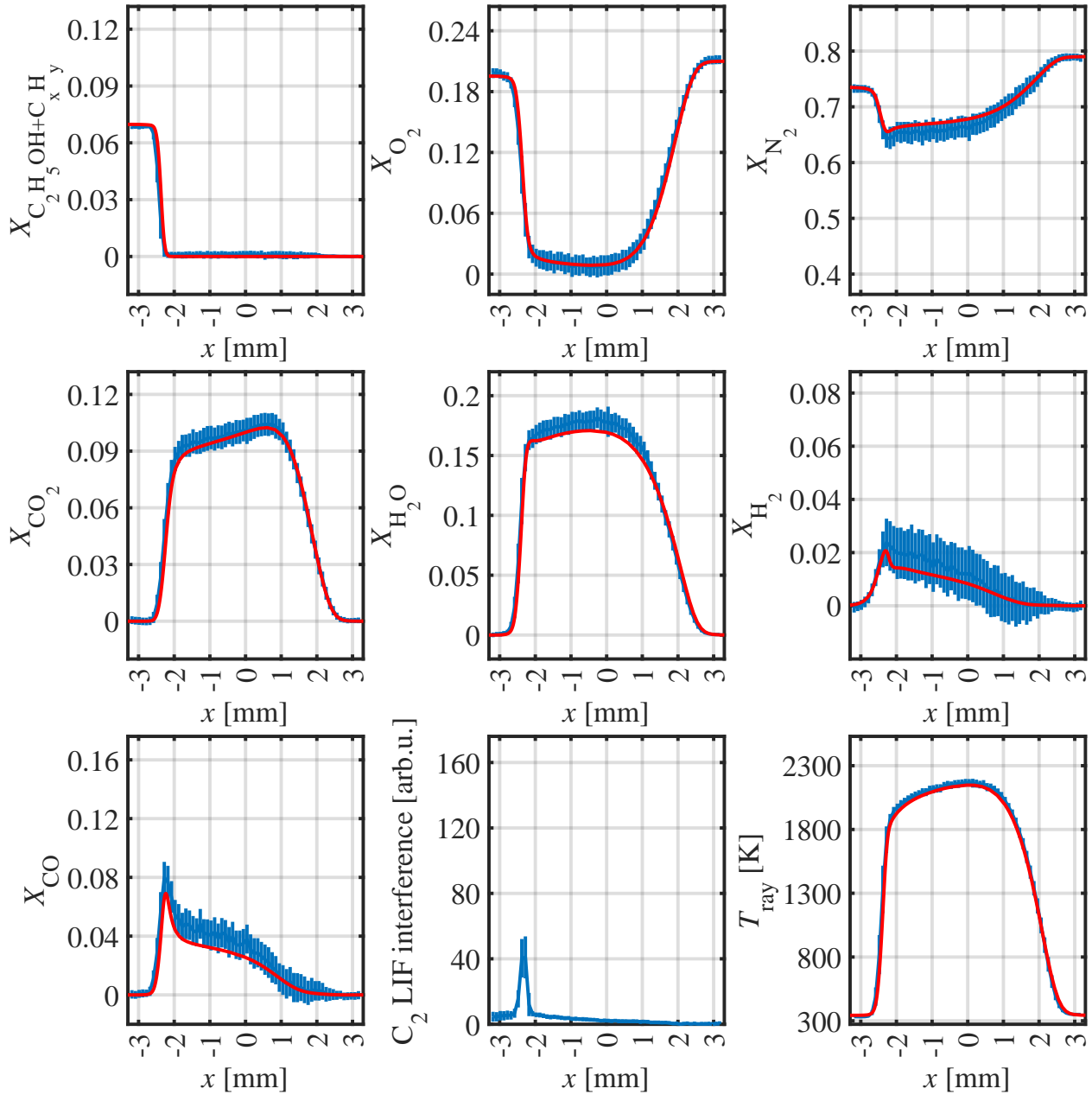
Figure 6.24.: Thermochemical states in spatial dimension of ethanol/air opposed jet flame at equivalence ratio ϕ=1.1 and strain rate α=250 s^{-1}.
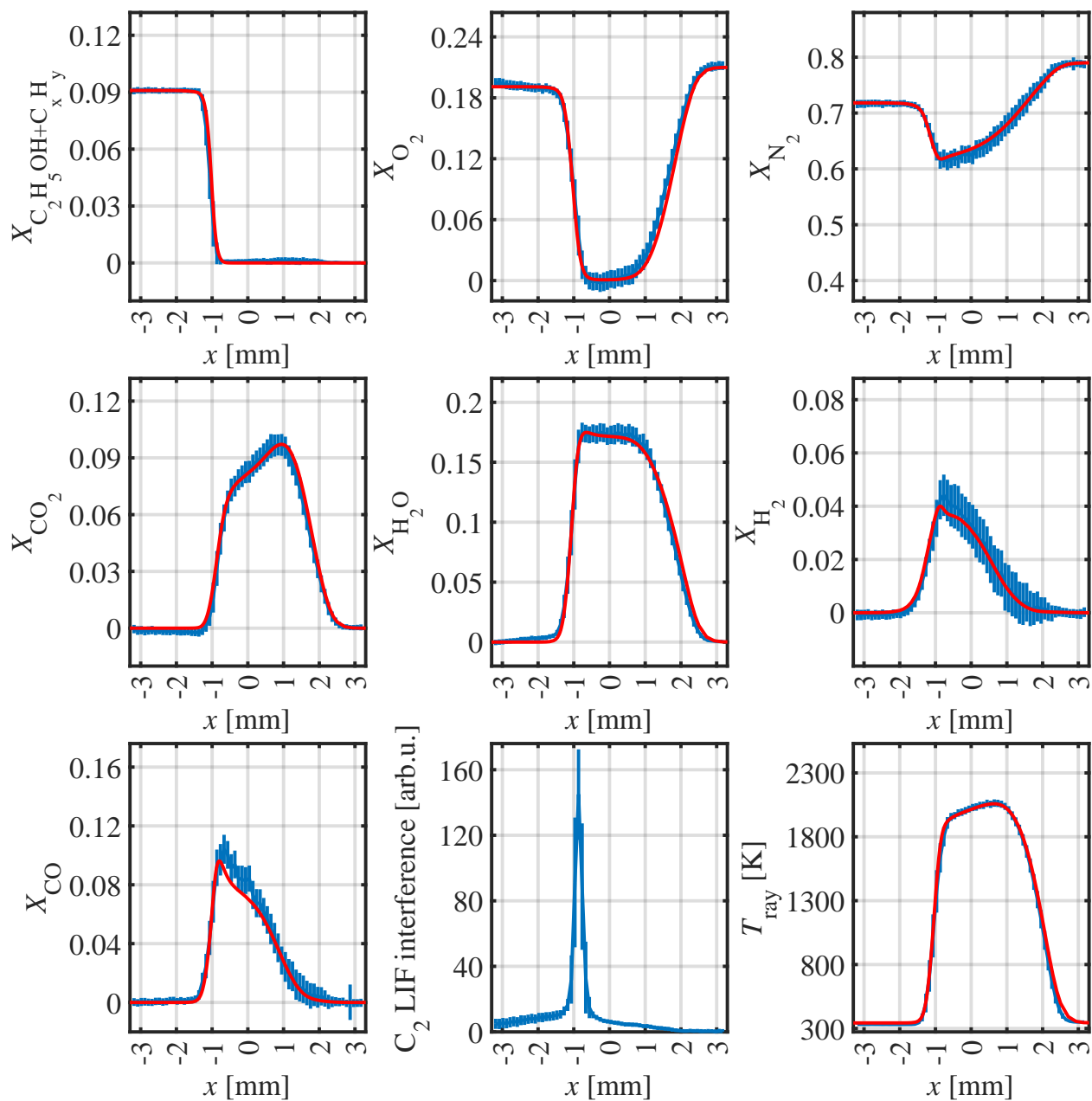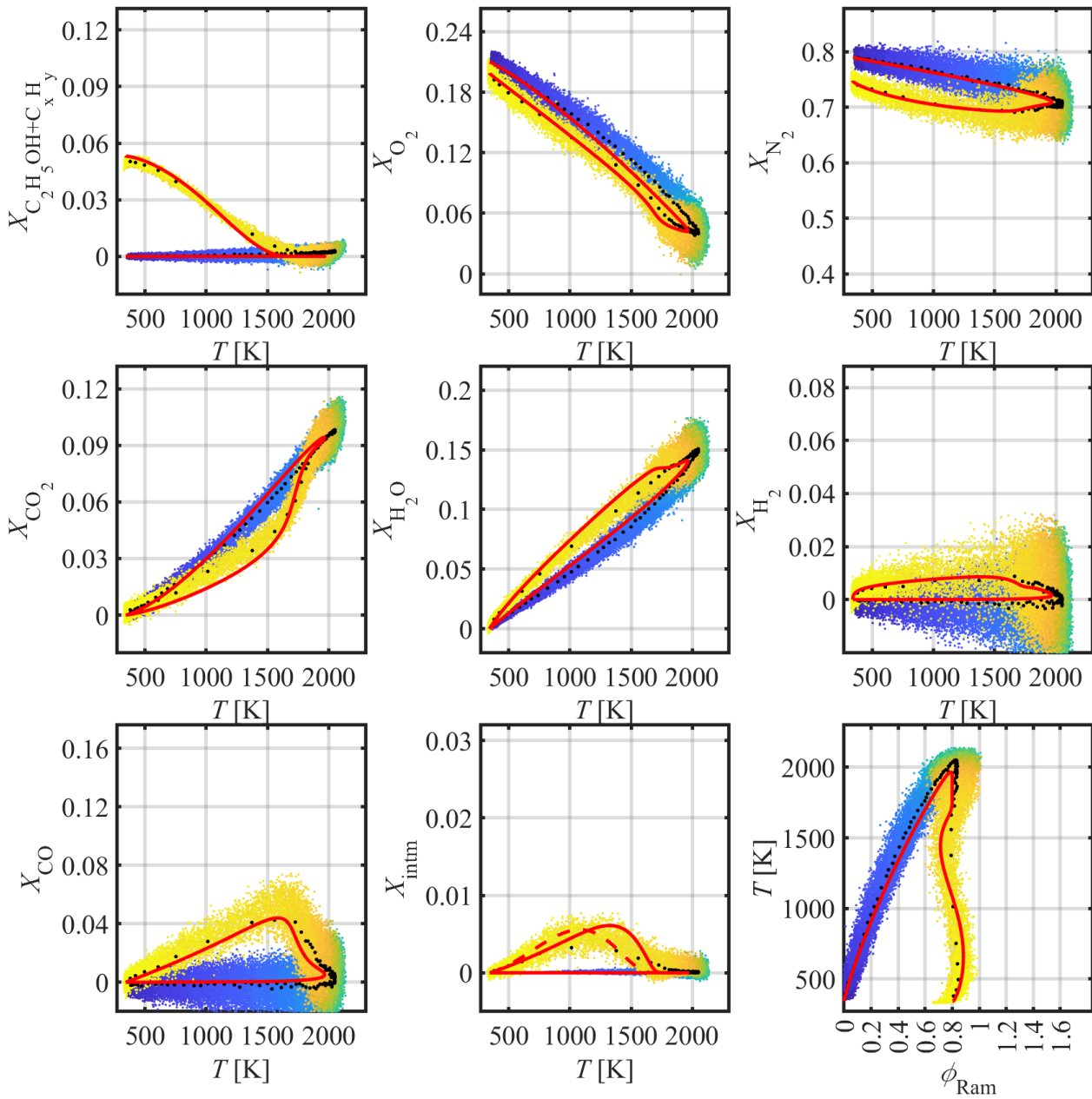
Figure 6.25.: Thermochemical states in spatial dimension of ethanol/air opposed jet flame at equivalence ratio $\phi=1.5$ and strain rate $\alpha=250\,\text{s}^{-1}$.

By switching the data display into temperature space, the primary reaction zone can be investigated in more detail. Figures 6.26, 6.27, and 6.28 show that data.

The following observations are made regarding these graphs:

1. Within the primary reaction zone, carbon dioxide is overestimated up to about 1700 K. At lean conditions the offset is about the same, while at rich conditions it reduces.

2. Carbon monoxide is overestimated by about the same amount and clearly also at the highest temperatures. Again, the inaccuracy is the same in lean conditions and reduced in rich conditions.

3. Ethanol is slightly overestimated starting at around 1000 K. The inaccuracy increases in lean conditions while it decreases towards rich conditions.

In comparison to the graphs in Figure 6.15 in Section 6.6, the described inaccuracies in the medium temperature range have decreased significantly. The chosen approach of using a surrogate intermediate species signal is thereby validated. Overall, the inaccuracies with respect to the numerical calculation are kept at a reasonable level, similar to what can be reached for methane/air.

Figure 6.26.: Thermochemical states in the temperature space of ethanol/air opposed jet flame at equivalence ratio ϕ=0.8 and strain rate α=120 s^{-1}. The scatter data color indicates the spatial dimension from the cold ethanol/air mixture (yellow) to the opposing nozzle's cold air (blue).
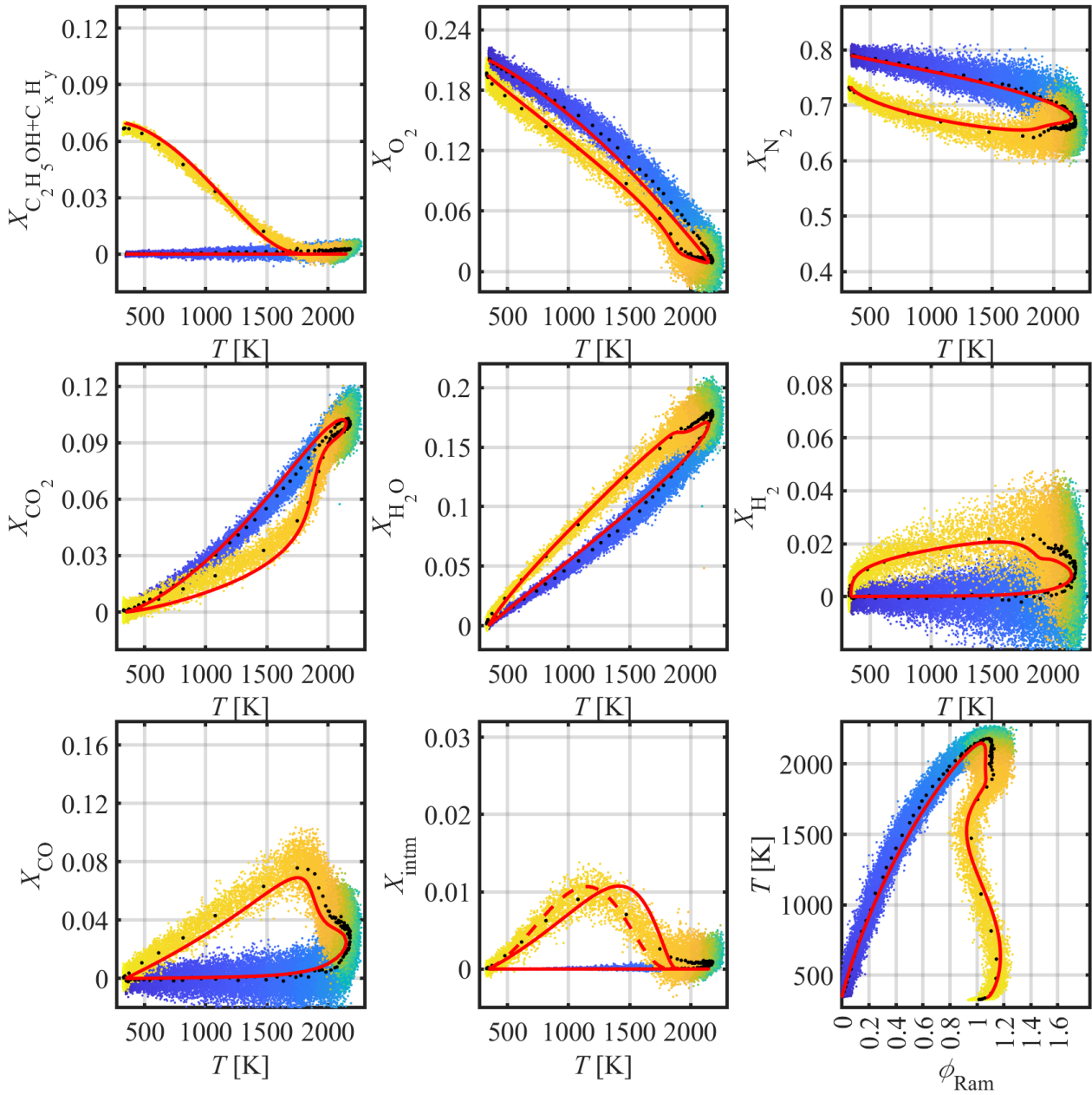
Figure 6.27.: Thermochemical states in the temperature space of ethanol/air opposed jet flame equivalence ratio $\phi=1.1$ and strain rate $\alpha=250\,\mathrm{s}^{-1}$. The scatter data color indicates the spatial dimension from the cold ethanol/air mixture (yellow) to the opposing nozzle's cold air (blue).
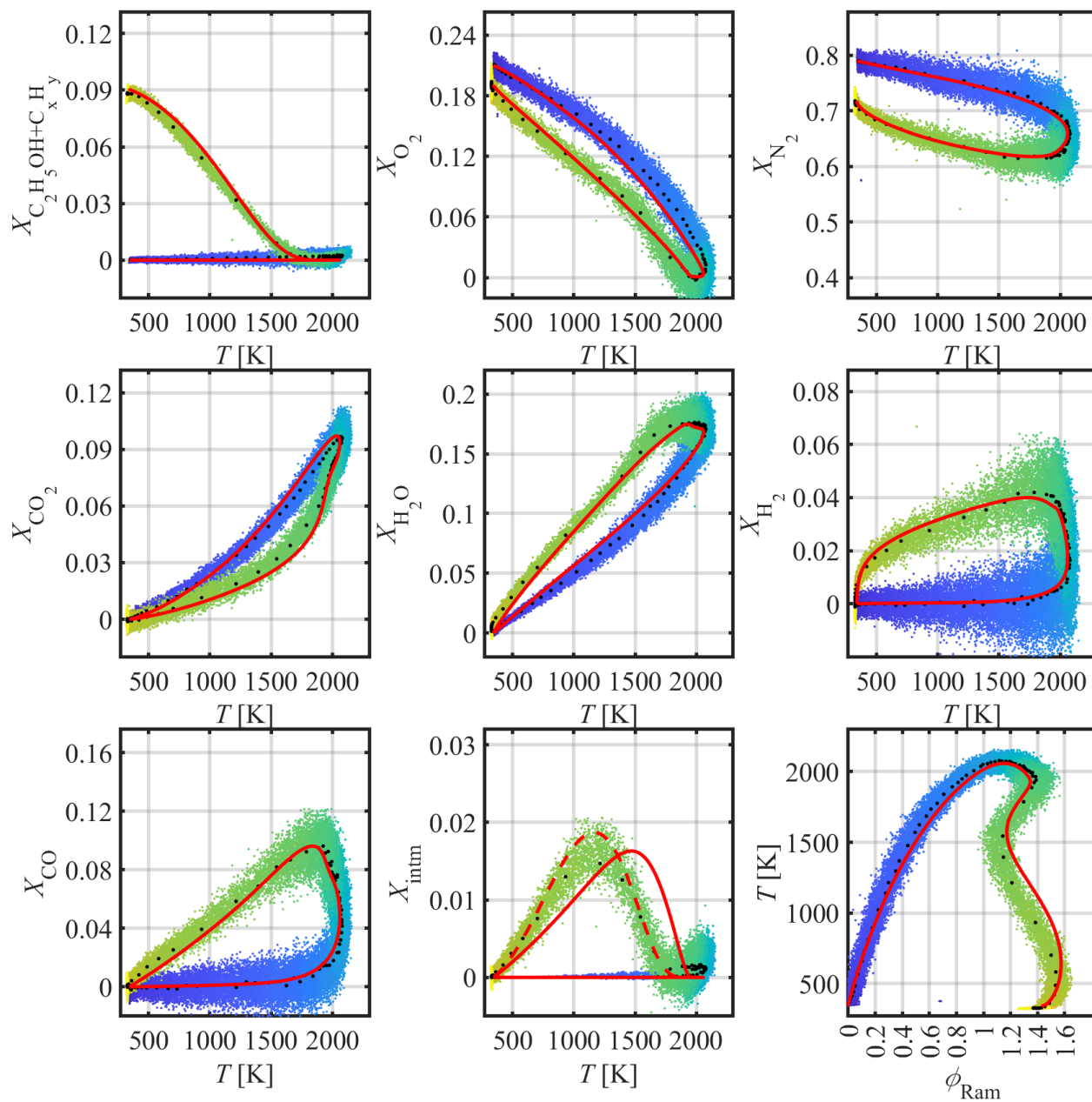
Figure 6.28.: Thermochemical states in the temperature space of ethanol/air opposed jet flame equivalence ratio $\phi=1.5$ and strain rate $\alpha=250\,\mathrm{s}^{-1}$. The scatter data color indicates the spatial dimension from the cold ethanol/air mixture (yellow) to the opposing nozzle's cold air (blue).

6.7.2. Turbulent Flames

The main objective during the turbulent flame investigation is understanding trends that occur at increased turbulence or equivalence ratio variations, as well as whether fuel differences between methane/air and ethanol/air flames can be observed. Furthermore, it is intended to use the obtained data to validate numerical ethanol flame calculations.

The discussion starts with an important disclaimer about the turbulence and mixture conditions in the experiments. Next, radial temperature and equivalence ratio profiles are shown in spatial domain to establish a discussion baseline. Furthermore, individual species are looked at to showcase the data quality for validation purposes. Lastly, the lean and rich methane/air and ethanol/air flames are shown in the equivalence ratio domain at three exemplary heights, enabling an insight into the respective flame structures.

6.7.2.1. Turbulence and Mixture Settings Discussion

The rationale for the chosen flame parameters is given in Section 6.4.3. In summary, for this experiment, bulk Reynolds number of Re_{bulk}=6000, 12000, and 28500 at both a lean and a rich condition are selected to vary turbulence intensity. The Re_{bulk}=28500 thereby equals the maximum at which the lean ethanol/air mixture still burns in a completely extended flame. Notably, the lean pilot flame of the two lower Reynolds numbers (equivalence ratio ϕ=0.7 and bulk mixture velocity $1\,\mathrm{ms}^{-1}$) needs to be increased at Re_{bulk}=28500 in order to maintain a burning ethanol/air flame (ϕ=0.8 and bulk mixture velocity $2.65\,\mathrm{ms}^{-1}$). For methane/air, the bulk Reynolds number setting and pilot settings are always identical to ethanol/air.

As for the equivalence ratios, it was intended to have constant laminar flame speeds across all investigated flames and thereby minimize the chemistry influence. As could only be realized a posteriori, the equivalence ratio settings for ethanol/air flames did miss their intended equivalence ratios ϕ=0.80 and 1.4 settings by about 12-13 % to the downside (0.7/1.25). This is significant when it comes to the laminar flame speed and could explain why the lean flames at the largest turbulence level were difficult to fully ignite. Unfortunately, at the time of the experiment, the post-processing method described in Section 6.2 had not been established. Only with this method, realizing the missed equivalence ratio and subsequently correcting it would have been possible.

Nevertheless, the equivalence ratios were off by a consistent margin. This means that the following results still give material insights into the above mentioned investigation focus. Albeit the incomparability due to different laminar burning velocities, the rich flames now have almost the same equivalence ratio due to the ethanol side not being as rich as intended. Furthermore, the lean and rich flames can be compared individually for each fuel with regard to the increased turbulence influence.

6.7.2.2. Radial Temperature and Equivalence Ratio Profiles

Figures 6.29 to 6.31 display the temperature (two columns on the left) and equivalence ratios (two columns on the right) along the four heights (bottom to top). Additionally, their fluctuations are

given as one standard deviation (red lines). The dashed lines are the ethanol/air and the solid lines the methane/air mixtures.

The data source are overlapping FOVs, which measured 51 super pixels each. As the optical quality is best in the FOV center, only the central 30 super pixels are utilized. Subsequently, in post-processing, every 60 μm are radially binned to reduce noise. This value is equivalent to the spectrometer optics' spatial resolution.

The following aspects are observed:

1. The burner's symmetric alignment relative to gravity and the vertical translation stage is verified by the mirrored appearance of the temperature gradients in the left and right flame brushes. This is the case throughout all investigated flames. Furthermore, there are almost no visible spikes in the curves, indicating a sufficient number of samples captured at each location.

2. As visible in the temperature graphs, both fuels have a common evolution, in which the two individual temperature peaks merge in the center and eventually culminate to form a mutual top hat profile. This evolution is a result of the flame length being completely captured. At closer inspection, it can clearly be seen that the fuels have opposing trends when switching from lean to rich conditions. While methane/air culminates later in rich conditions, ethanol does so earlier. This is in line with observations made in Sections 5.4.2 and 5.4.3, where it was connected to the effective Lewis number. In summary, a reduced flame size is likely induced by increased wrinkling and thus higher flame surface densities.

3. The previously described aspect is less pronounced in the most turbulent flame. To show case this, the lean mixtures' two lower turbulence levels are compared to the higher one at $x/D=11$, as all of these cases have their lowest temperatures near the burner's axis within a comparable range of 500 and 1000 K. In the rich counterpart, the temperature delta of the lowest point towards larger (ethanol/air) and lower (methane/air) heights is larger for the two lower turbulence levels. This indicates that the Lewis number induced fuel effect reduces with increased turbulence.

4. When the turbulence level is increased from $Re_{bulk}=6000$ to 12000, there are barely any temperature and equivalence ratio changes, and the same goes for their gradients. One thing to note is that the high-temperature region widths marginally reduce, indicating a thinner flame brush. However, due to the different lengths of the flames, this can be expected to vary if the same height is looked at. Furthermore, for the lean ethanol flame, the equivalence ratio top hat is slightly more curved. This might be due to a relatively lower pilot flame influence, which has not changed between these setpoints.

5. Going from bulk Reynolds number $Re_{bulk}=12000$ to 28500, differences become more visible. Above $z=5.5x/D$, the fluctuation magnitudes and temperature peak widths increase substantially, and accordingly, the temperature peaks of the flames of both fuels have a much wider base. All this indicates a substantially altered mixing structure starting at low heights, for which the following two explanations come to mind.

First, the pilot flame output of the lean flame is significantly increased for the bulk Reynolds number $\text{Re}_{bulk}=28500$ case, which leads to an approximately four times larger heat source in that region ($r=6$ to $15\,\text{mm}$). Secondly, the much larger jet bulk flow will produce large vortices at the jet exit, leading to strong in-mixing of the pilot exhaust gases and also ambient co-flow air into the jet flow.

Figure 6.29.: Radial temperature and equivalence ratio profiles of TCJB flames with a $Re_{bulk}=6000$ bulk Reynolds number. Bulk flow equivalence ratios are given at the top, fluctuations are included in red.

Figure 6.30.: Radial temperature and equivalence ratio profiles of TCJB flames with a $Re_{bulk}=12000$ bulk Reynolds number. Bulk flow equivalence ratios are given at the top, fluctuations are included in red.
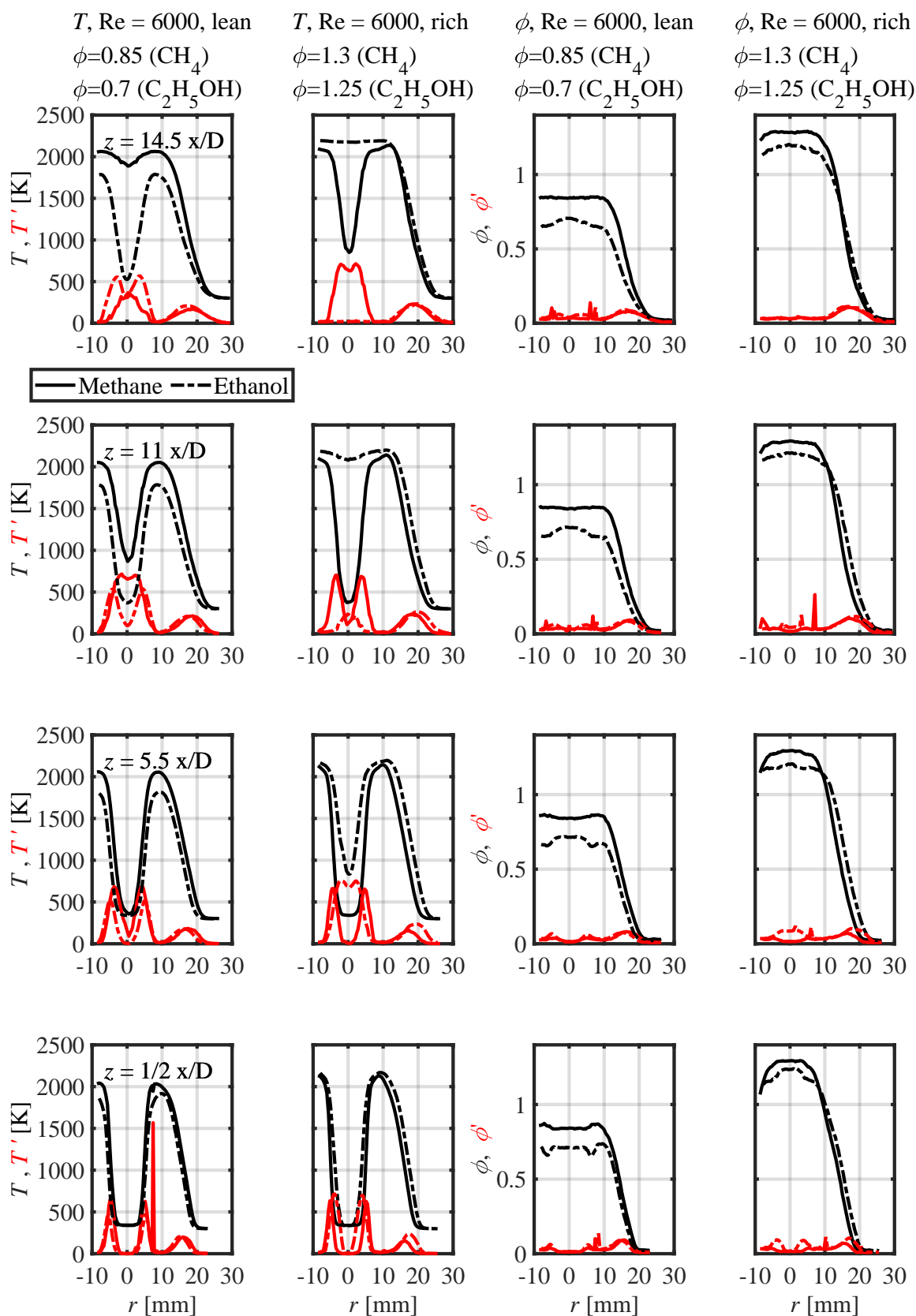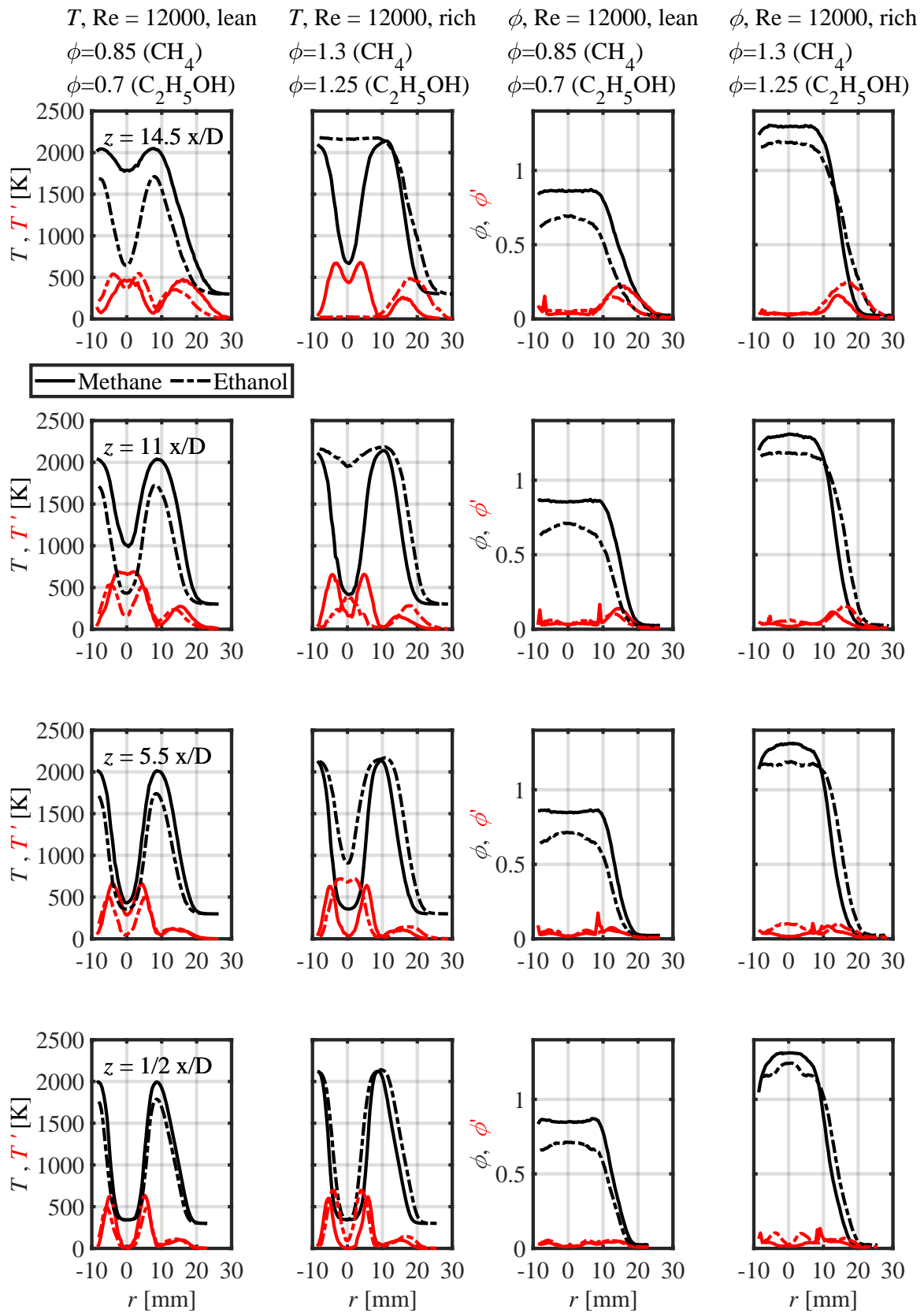
Figure 6.31.: Radial temperature and equivalence ratio profiles of TCJB flames with a $Re_{bulk} = 28500$ bulk Reynolds number. Bulk flow equivalence ratios are given at the top, fluctuations are included in red.
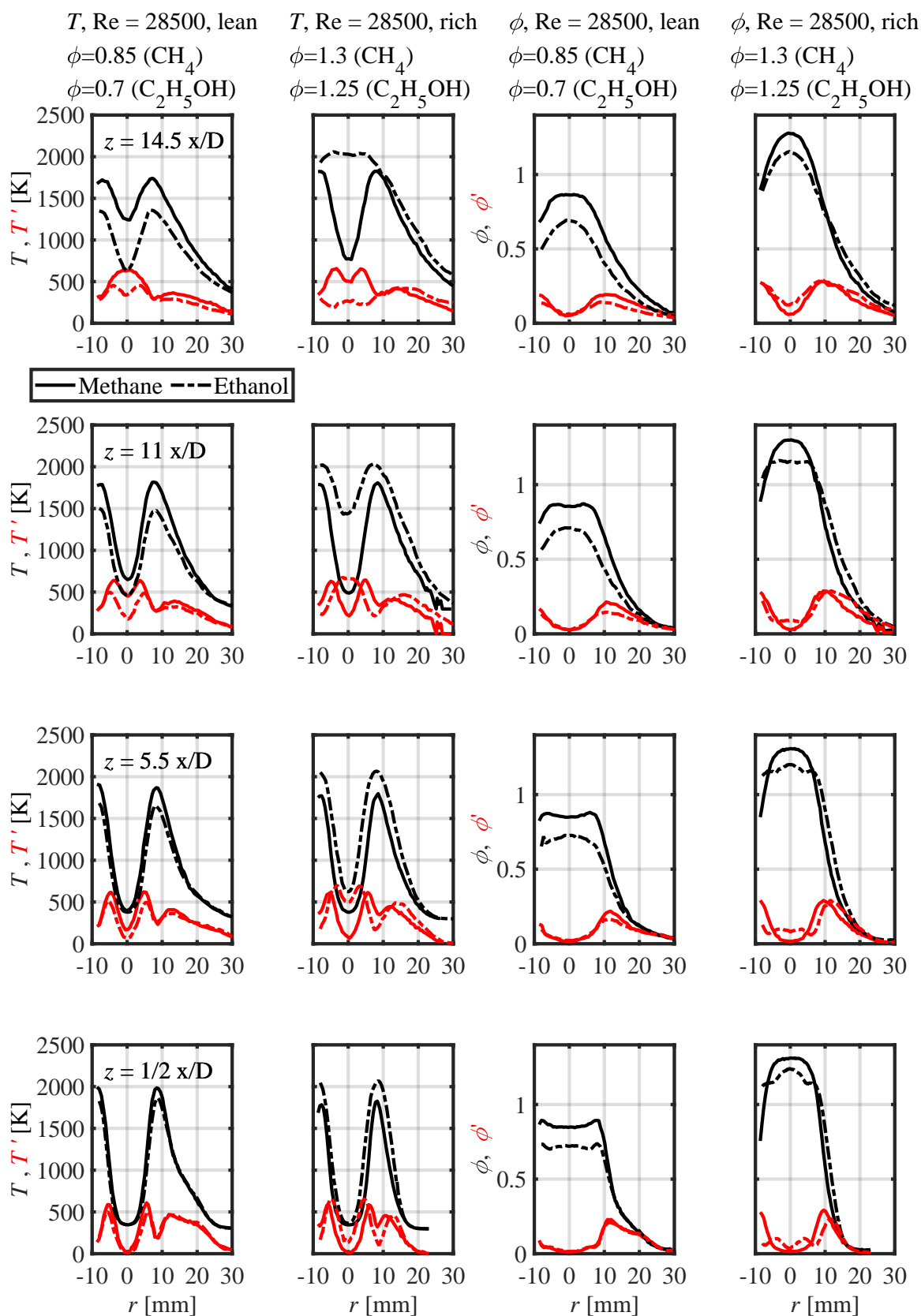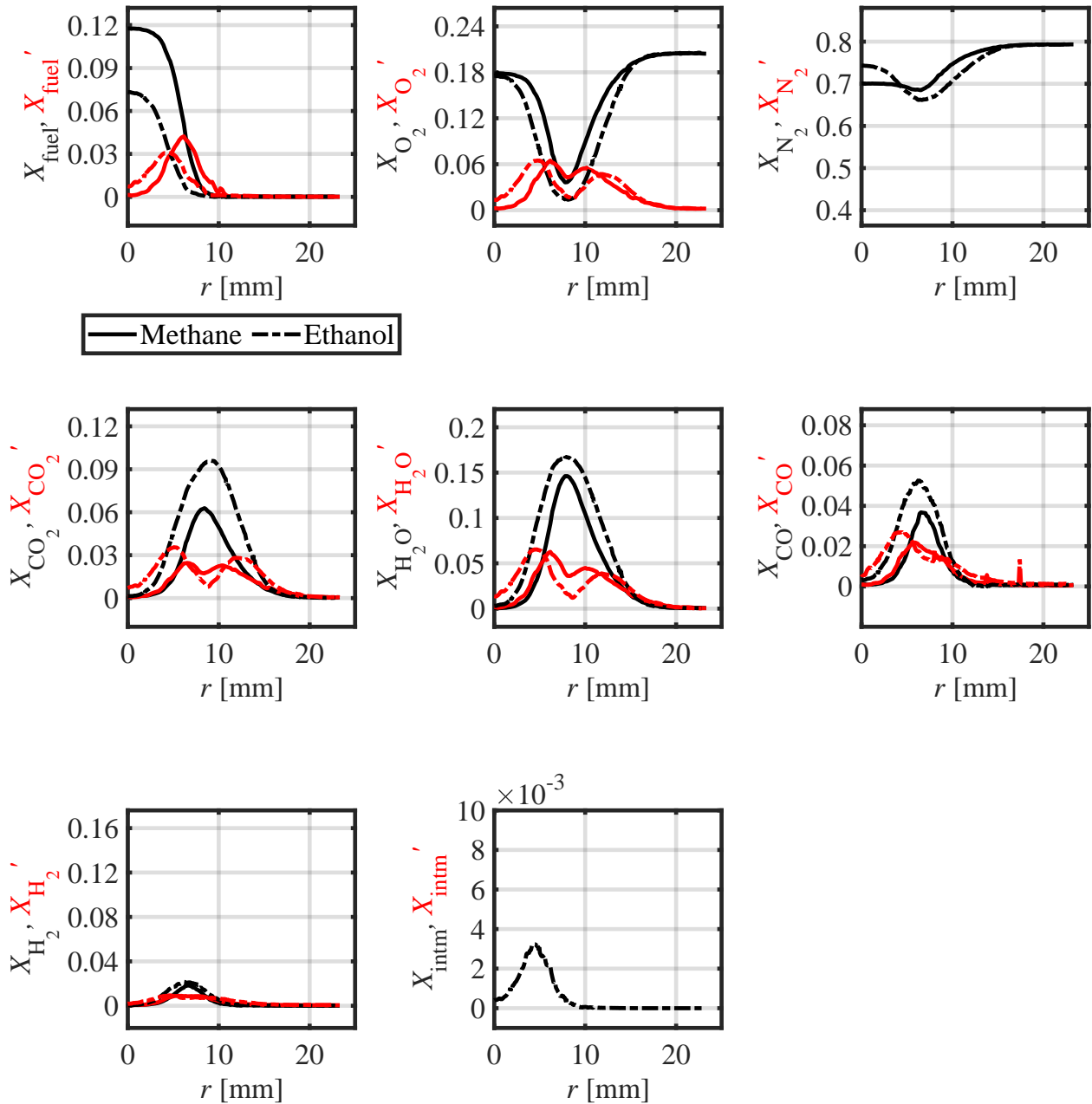
6.7.2.3. Radial Species Profiles

Figures 6.32 to 6.35 show radial species mole fractions in the most turbulent flame cases, each at a selected height. As discussed above, the different fuels' flames vary in length and a direct comparison at specific heights is thus not advised. However, it can be noted that at all heights, the individual data seems to be of sufficient quality to be used for validation purposes, which was one of the two main objectives of this measurement series.

When comparing this turbulent ethanol/air case with the laminar one presented in the previous section, the estimated maximum intermediate species mole fraction remains about 1/2-1/3 of the equivalent laminar opposed flame case with a similar equivalence ratio. This is likely due to its estimation directly from the carbon monoxide mole fraction, which itself is also roughly halved in the turbulent case. However, this finding is to be taken with caution. As shown in Section 6.6.3, the intermediates will be underestimated at strain rates above $1000 \, s^{-1}$, which might be the case in the bulk Reynolds number $Re_{bulk} = 28500$ flame. Therefore, to verify with confidence that the intermediates indeed behave as such, they would have to be individually measured, which was not possible at the time of the measurement due to missing individual high temperatures spectra.

Results of the less turbulent flames at bulk Reynolds numbers $Re_{bulk} = 6000$ and 12000, as well as the lean $Re_{bulk} = 28500$ flame are provided in Appendix A.
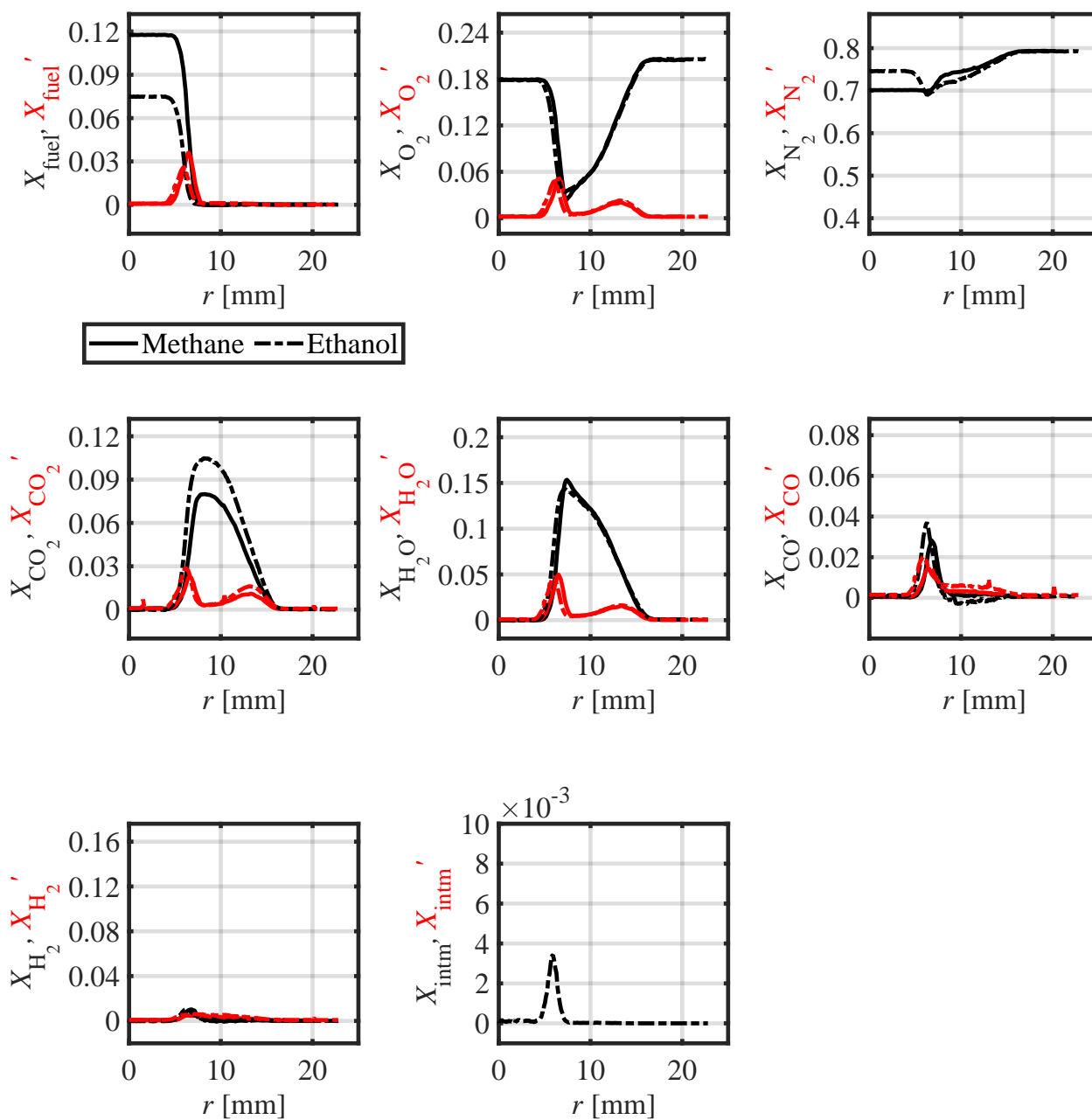
Figure 6.32.: Species mole fraction profiles of methane/air and ethanol/air TCJB flames at rich conditions (methane/air: ϕ=1.3, ethanol/air: ϕ=1.25) with a bulk Reynolds number of Re_{bulk}=28500 and at x/D=1.

Figure 6.33.: Species mole fraction profiles of methane/air and ethanol/air TCJB flames at rich conditions (methane/air: $\phi=1.3$, ethanol/air: $\phi=1.25$) with a bulk Reynolds number of $Re_{bulk}=28500$ and at x/D=5.5.

Figure 6.34.: Species mole fraction profiles of methane/air and ethanol/air TCJB flamesat rich conditions (methane/air: ϕ=1.3, ethanol/air: ϕ=1.25) with a bulk Reynolds number of Re_{bulk}=28500 and at x/D=11.
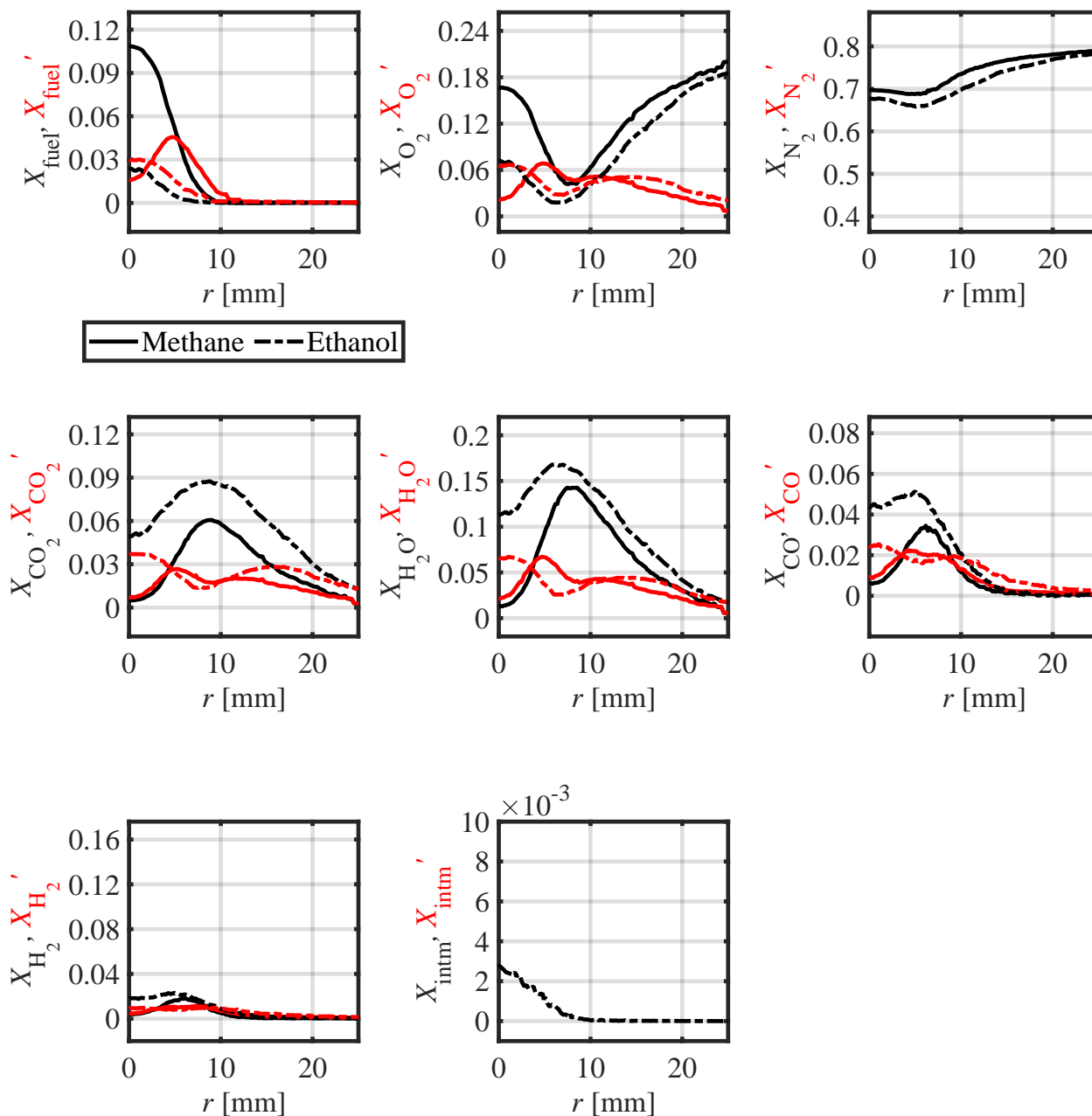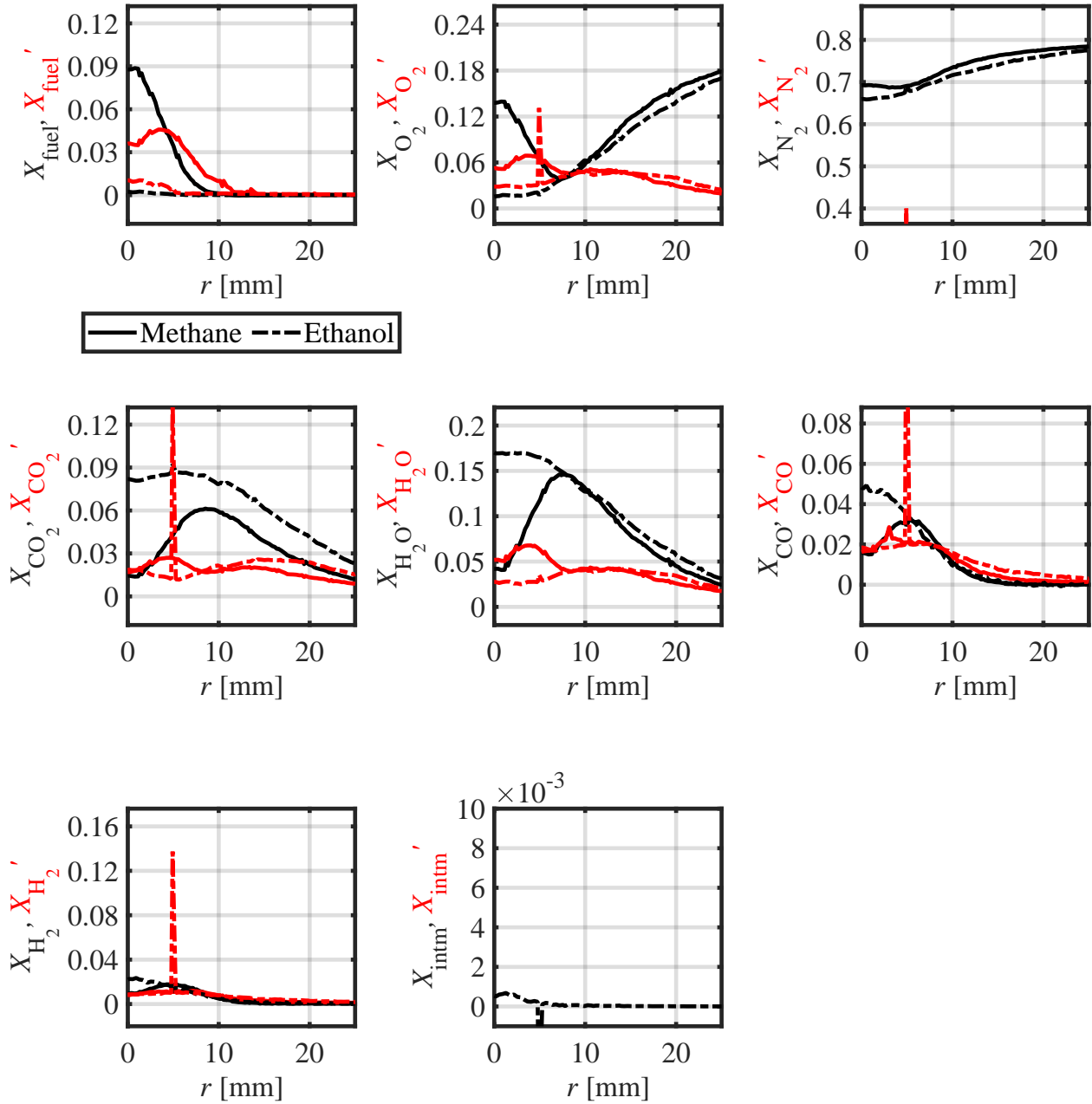
Figure 6.35.: Species mole fraction profiles of methane/air and ethanol/air TCJB flamesat rich conditions (methane/air: ϕ=1.3, ethanol/air: ϕ=1.25) with a bulk Reynolds number of Re_{bulk}=28500 and at x/D=14.5.

6.7.2.4. Scatter Data of Temperature in Equivalence Ratio Space

Lastly, the flames are examined in the equivalence ratio domain to develop a better flame structure understanding. Figure 6.36 compares the lean methane/air and ethanol/air flames at three respective turbulence intensities (left two, center two and right two) and several heights (bottom to top).

Added to the graphs are the adiabatic mixture temperature T_{ad} (red solid line) and the temperatures of stretched numerical 1D flame calculations with varying strain rates (red intermittent lines). It is mentioned that the varying strain rates mostly overlap in the lean cases and are hard to differentiate.

In order keep the calculations as close as possible to the actual experiment, two different flamelet types are plotted depending on the height above the burner. At flame's base, the flamelets are made up by the respective jet mixture opposing a stream with the pilot flame's exhaust gas conditions. At medium and large heights, the jet mixtures oppose an air stream at ambient temperature.

Notably, the exhaust gas flamelets can withstand strain rates as high as those expected in such turbulent flames (displayed are strain rates up to $1500\,s^{-1}$), but the air-opposed lean flamelets are rather limited in this regard (displayed only up to $200\,s^{-1}$ in lean and $200\,s^{-1}$ in rich conditions). In these cases, it is acknowledged that while in reality, some of the flames experience much higher strain rates, the curves are included nonetheless to compare the general shape with the measured data.

The following observations can be made from the lean flames' graphs:

1. At the lowest turbulence intensity, the temperature and equivalence ratio for both methane/air and ethanol/air flames is reproduced well by the calculated flamelets and adiabatic temperature curves. An exception to that observation is that the scattered methane/air flame data at $x/D=2$ exceeds the calculated maximum temperature. One explanation is that the pilot slightly exceeds its intended $\phi=0.7$ equivalence ratio.

2. Both methane/air and ethanol/air flames show the c-shaped or s-shaped temperature over equivalence ratio structure that their respective flamelets do, as well. However, going from the base to the tip of the flame, this structure is altered for ethanol/air. From the cold premixed mixture temperature, the curve is starting straight up at $x/D=5.5$ and 11, rather than being inclined with a small gradient like at $x/D=2$.

3. Besides the fact that the deviation described in the previous point has increased to a small degree, the medium turbulence intensity $Re_{bulk}=12000$ shows almost the same features as the lowest at $Re_{bulk}=6000$.

4. At the highest turbulence intensity and $x/D=2$, the scattered data follows the adiabatic mixture temperature until slightly below stoichiometry, although it should only reach the pilot flame's $\phi=0.8$ equivalence ratio. This offset vanishes at larger heights. One explanation is that the pilot flame exceeded the intended equivalence ratio. However, the pilot flame mass flows were verified to have reached their intended points and the error would have been be-

yond them. Another explanation is that the strong pilot flame luminosity at this low height acted as a bias to the data.

5. Outside the pilot flame's vicinity, the Re_{bulk}=28500 methane/air flames' primary reaction zones are still well approximated by the premixed mixture against air flamelet. However, compared to the lower two turbulence intensities, one deviation is that the c-shape is slightly tilted clockwise compared to the flamelet curve. While this can be caused by the overly rich pilot flame described above, it is noteworthy that although on a very small level, the tilting already started from Re_{bulk}=6000 to 12000, where the pilot flame was nominal and not overly rich.

6. At Re_{bulk}=28500, there is scatter located between the right primary reaction zone branch and the left outburning branch. This is typically a sign for turbulent mixing and becomes stronger with turbulence intensity. Here, it can be said that ethanol/air shows a slightly more dense scattered points cloud in this region compared to methane/air. This also leads to a larger deviance from the strained flamelets. Thus, the turbulence influence appears stronger for ethanol/air in this lean condition. Notably, as can be seen in Appendix B.1.2.2, this is mirrored by the fact that the lean ethanol/air flame condition is located higher in the Borghi-Peters diagram after accounting for the missed equivalence ratio. This can explain the larger turbulence influence. Notably, the flame lengths between the two lean flames are similar and can therefore not be the primary reason for this deviance.
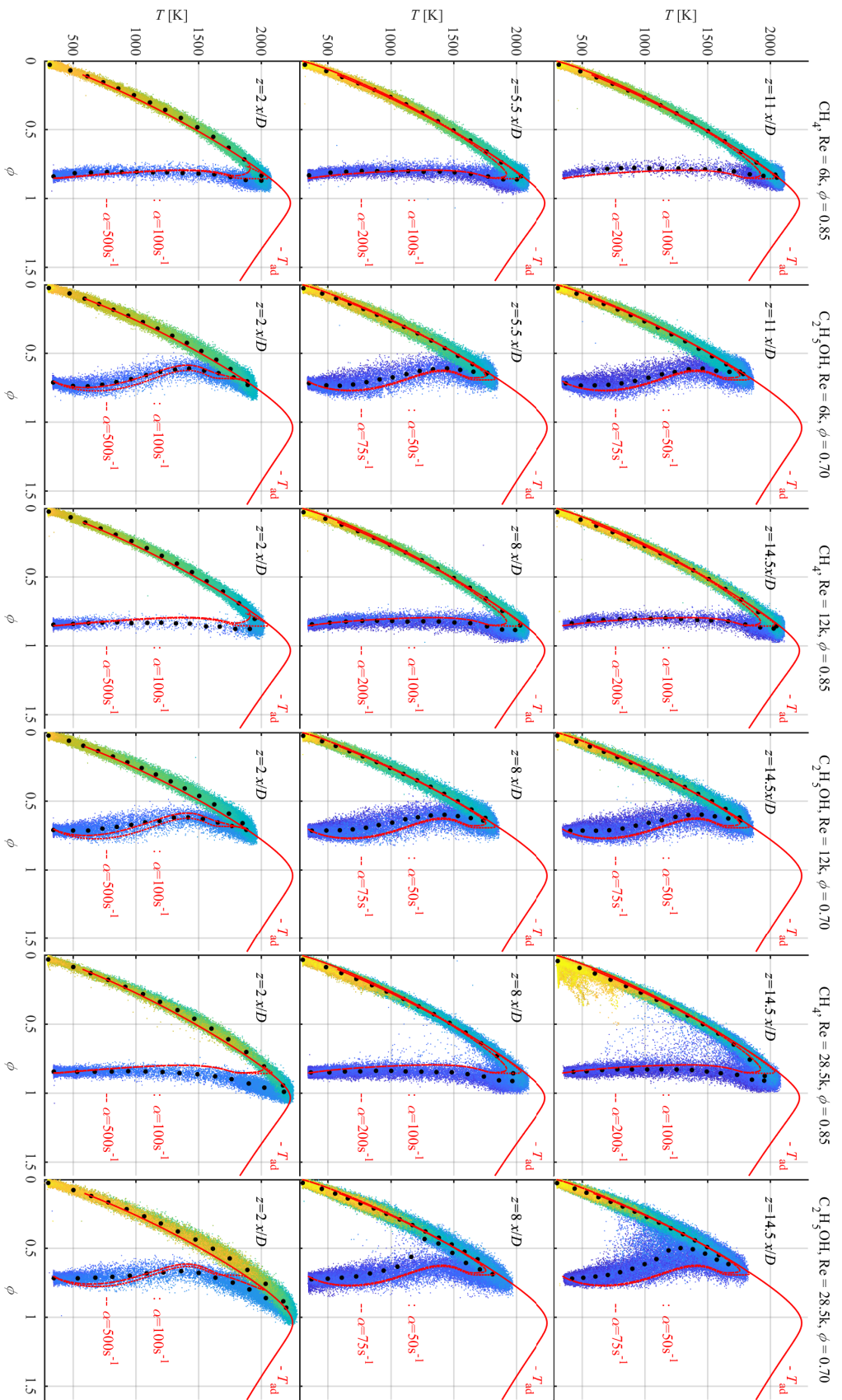
Figure 6.36.: Scattered data of temperature in equivalence ratio space for all lean flames at varying heights from bottom to top (methane/air: ϕ=0.85, ethanol/air: ϕ=0.7). While black dots equal mean values of the scattered data points, the color is the radial dimension from the burner axis (blue) until the coflow area (yellow). Additional numerical calculation data is given in red. The adiabatic mixture temperature T_{ad} is drawn at all heights as a solid line. The dotted and dashed lines are flamelets, which are either calculated from fuel/air mixture against pilot flame exhaust conditions (lowest height at x/D=2), or fuel/air mixture against air (two upper heights).

Figure 6.37 shows the rich flames' temperatures in the equivalence ratio space.

As in the lean flame graph previously discussed, the lowest height has flamelets of the jet mixture against pilot exhaust gases, the two larger heights have jet mixtures against air flamelets, and the adiabatic mixture temperature is plotted at all heights. The following observations are made:

1. Rich methane/air flames at Re_{bulk}=6000 and 12000 are well reproduced by the numerically calculated lowest strain rate flamelets. At the highest turbulence intensity, it can be reproduced by the medium strain rate flamelets.

2. Ethanol/air flames generally have a similar s-shape compared to the numerically calculated flamelets. However, there is a noticeable offset in the region until about 1500 K, where the equivalence ratio is smaller compared to the flamelets. In comparison with a similar equivalence ratio laminar flame at equivalence ratio ϕ=1.2 (not displayed here), this behavior is visible to roughly the same extent as in the least turbulent flame. While it can therefore not be ruled out that it is a calibration issue, it shall be noted that the effect seems to reduce along the height and increase towards flames with higher bulk Reynolds numbers, indicating that it is not independent to those factors.

3. At the largest turbulence intensity, the rich methane/air flame shows scattering points that indicate turbulent mixing phenomena, while the ethanol/air flame is almost free of them. The likely reason therefore is that the turbulence intensity was too low, as can be seen from the graph in Appendix B.1.2.2 that accounts for the missed equivalence ratio.
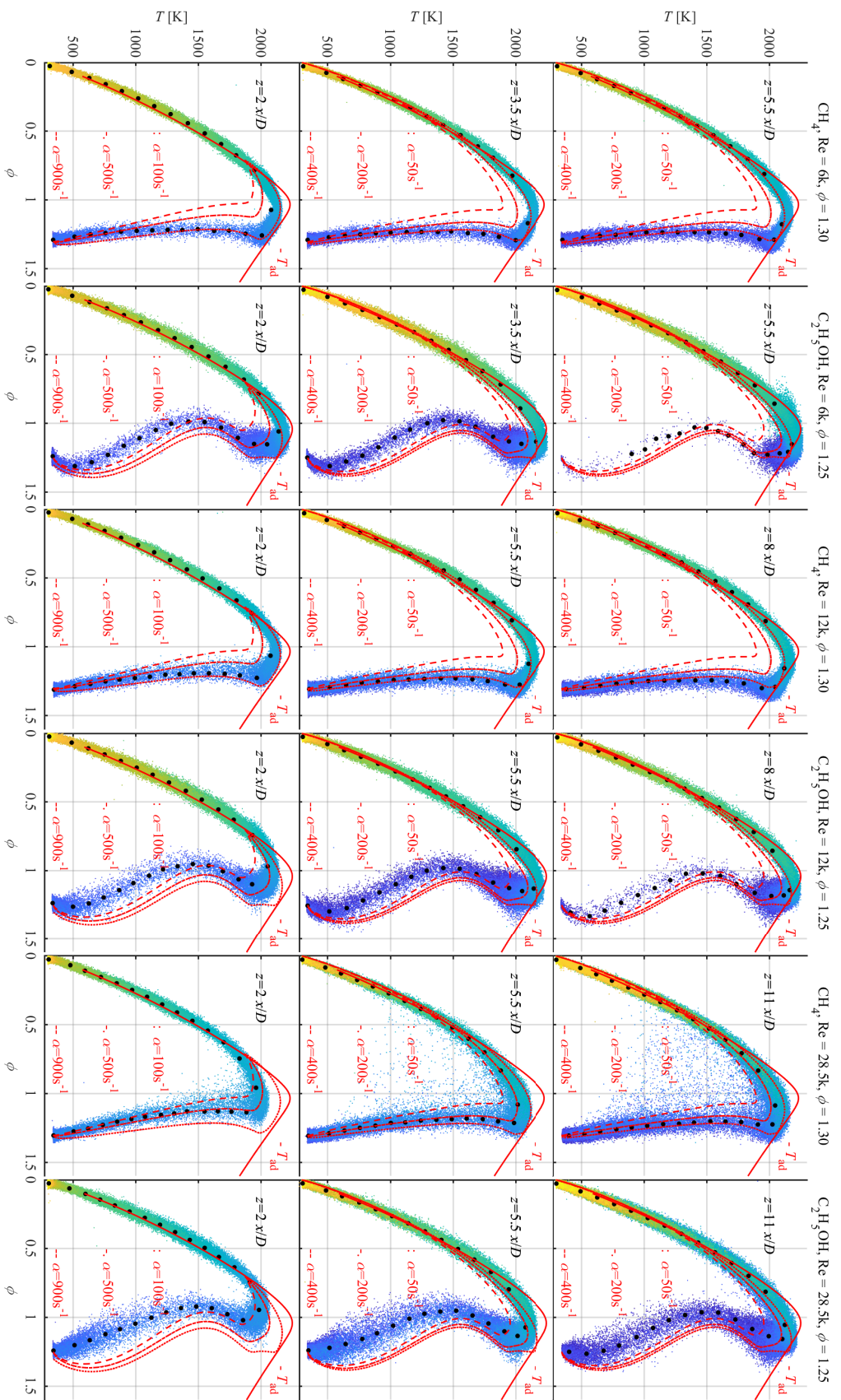
Figure 6.37.: Scattered data of the temperature in equivalence ratio space for all rich flames at varying heights from bottom to top (methane/air: $\phi = 1.3$, ethanol/air: $\phi = 1.25$). While black dots equal mean values of the scattered data points, the color is radial dimension from the burner axis (blue) until the coflow area (yellow). Additional numerical calculation data is given in red. The adiabatic mixture temperature T_{ad} is drawn at all heights as a solid line. The dotted, dashed and point-dash lines are flamelets, which are either calculated from fuel/air mixture against air (two upper heights), conditions (lowest height at $x/D = 2$), or fuel/air mixture against pilot flame exhaust conditions (lowest height at $x/D = 2$), or fuel/air mixture against air (two upper heights).

6.8. Summary and Conclusion

This chapter covered the planning, execution, and evaluation of the first quantitative Raman and Rayleigh spectroscopy measurements of a vaporized liquid ethanol flame. To investigate these laminar and turbulent ethanol/air flames, a number of challenges needed to be overcome, which are summarized below.

The main challenge was to invent a calibration method that does not rely on the commonly used flat flame, which is unsuitable for liquid fuels. A solution was found by probing ethanol/air twin flame exhaust gases, which were produced over a wide equivalence ratio range using the novel Laminar Temperature-controlled Opposed Jet burner (LTOJ, introduced in Chapter 4).

Furthermore, a detailed description of an attempt to transfer temperature-dependent intermediate species spectra from a partnering test rig to the present one was described, including an extrapolation method of multiplier and cross-talk polynomials towards high temperatures (Appendix B.3). However, that approach was unsuccessful, as it resulted in nonphysical high-temperature spectra and a failed matrix inversion calibrations. Instead, simplified temperature-independent polynomials were used, which yielded a successful calibration.

With the calibration methodology in place and the experimental apparatus and target flame conditions introduced, the calibration results for methane/air and ethanol/air flames were discussed in more detail. As significant offsets in species mole fractions from concurrent numerical calculations were discovered, a solution regarding the apparent influence by immeasurable intermediate species was invented and implemented. Subsequently, the ethanol/air data proved to be of similar quality to the established methane/air reference cases, which was displayed in both the spatial and temperature domains.

Finally, the turbulent target flame results produced using the Temparture-controlled Piloted Jet burner (TCJB, introduced in Chapter 5) were shown. With three different turbulence levels (Re_{bulk}=6000, 12000, 28500) and two lean and rich equivalence ratios each, a variety of interesting conditions were investigated in the spatial and equivalence ratio domains. However, as the originally selected equivalence ratios of ethanol/air flames were missed during the one-time measurement, a direct comparison between methane/air and ethanol/air flames with regard to turbulence-chemistry interaction lacks an identical laminar burning velocity. Nevertheless, the data sets serve as validation objects for numerical flame-solver mechanisms.

To conclude, the research targets given at the chapter's beginning were fulfilled with all but the one exception, which was the turbulence-chemistry interaction based on identical laminar burning velocities. It is stressed that the campaign still provides very important grounds for further studies on the subject of intermediate species and complex fuel flames.

Optimization potentials exist in the more accurate knowledge of temperature-dependent ethanol and intermediate species spectra, as well as the detailed inclusion of the latter as independent species within the matrix inversion. Furthermore, with the now established post-processing methodology, the equivalence ratio issue on the TCJB can be targeted more effectively in order to study the turbulence chemistry interaction differences in detail. Finally, the established tools should be applied to other liquid fuels and in the long run to different burner types.

7. Conclusion and Outlook

While individual summaries and conclusions were given at each experimental chapter's end, this final chapter provides conclusions for the complete work. Furthermore, an outlook on potential future studies or improvements is given.

7.1. Conclusion

A set of experiments was presented with which fuel-respective differences in laminar and turbulent flames were studied. The four lightest alcohols provided the main research ground, on which new equipment and methods could be developed and new phenomenological insights be gained.

On the apparatus side, this included the liquid fuel-ready Laminar Temperature-controlled Opposed Jet burner (LTOJ), with which a large calibration and target flame variety can be generated. Furthermore, the Temperature-controlled Piloted Jet burner (TCJB) was introduced, offering the possibility to stabilize vaporized liquid-fuel flames at high turbulence levels and varying inflow temperatures. On the detection side, the Raman spectrometer at TUDa was re-engineered to incorporate a second Raman spectrometer arm. This arm may be used to resolve intermediate hydrocarbon species with a higher dispersion simultaneously to all main species, or to apply the Raman depolarization technique. Furthermore, a new rotating shutter wheel facilitates capturing a high sample numbers without substantial wear to the system, and a new spectrometer housing increases stray light-tightness. All the while, some more material novelties were established during this work, including an improved flat flame burner, a pure gas nozzle, and some optical targets decisively combating weaknesses of the TUDa Raman spectrometer test bench.

On the methodology side, a long exposure procedure was established. Thereby, the Raman signals of several thousand laser shots are accumulated on the sensor and then read out only once after up to 70 minutes. This appears to be the only way to reach a high-enough SNR to detect intermediate hydrocarbon species. In the flames' primary reaction zones, these intermediates appear in such low quantities that they otherwise would remain below the read-out noise, even for the rather sensitive Raman cameras used. This approach benefits greatly from the LTOJs flame stability, as well as the possibility to adjust the laser and delaylines in real time through the Rayleigh camera image.

The presented experimental results benefited greatly from incorporating numerically calculated flames and mixture parameters. This included the general information on approximate intermediate species quantities, diffusion coefficients, and other mixture parameters, which were for example used to derive a variety of different dimensionless numbers (e.g. Markstein, Lewis, and Schmidt number). Furthermore, flame parameters like the laminar flame velocity and thickness could be

estimated. A major use was also generating numerical twins of the experiment, particularly twin and opposed jet flames.

In summary, both material and methodological advances were reached in the field of liquid fuel combustion. To be highlighted are the first non-intrusive intermediate species detections in laminar ethanol/air and OME-3/air flames, a comprehensive turbulent alcohol/air and methane/air flame topology study, and the first thermochemical state determination in laminar and turbulent ethanol/air flames.

7.2. Outlook

Several further research paths have opened up during this work, which shall be touched upon in the following.

The new higher-dispersed spectrometer arm may be used in a quantitative fashion by applying a spectral fitting approach similar to Geyer [57]. This is especially applicable in stationary flames, where the SNR can be almost limitless using the long exposure mode, and where the hybrid matrix inversion method is not the only viable choice. The acquired data could then be used to validate numerical mechanisms of complex fuels, such as OME-3. Notably, a custom-designed beam splitter that splits reflection and transmission at approximately 85/15 %, rather than 50/50 %, is recommended. For the single-shot operation, the new spectrometer arm may be used in very luminous flames, such as hydrocarbon diffusion flames or ammonia/methane flames, by installing polarization separation optics.

The two new burners developed and presented offer many possibilities to further study fuel effects phenomena. Although not executed to the complete thermochemical state detail as of yet, this work's ethanol/air single shot study offers a blueprint on how quantitative measurements, including those with large intermediate species amounts, could be performed. However, increasing the detail towards individual intermediate species quantification will remain challenging. This is due to the very limited signal in the reaction zone in combination with substantial local overlap of CH-stretch bands by up to four species (ethanol/air flames). In that case, attempting the described procedures with the smaller and less complex fuel methanol as an intermediary step might be a reasonable choice.

Lastly, as some of the captured flames are in the reaction sheet regime, the combined Raman and Rayleigh as well as OH-PLIF measurements offer themselves as interesting validation cases for numerical model development of complex fuels. Although the equivalence ratios were not set out as planned in the ethanol/air flames and thus comparisons with methane/air lack an assimilating laminar burning velocity, the turbulence-chemistry studies could be continued and expanded in simulations once the respective models have been validated with the presently determined thermochemical states. The highly-detailed flame surface density data gathered within this work completes the valuable validation data set for turbulent ethanol/air and methane/air flames.

A. Additional Thermochemical State Results

This appendix chapter provides additional thermochemical state graphs relevant to the turbulent jet flame discussion in Section 6.7.2.
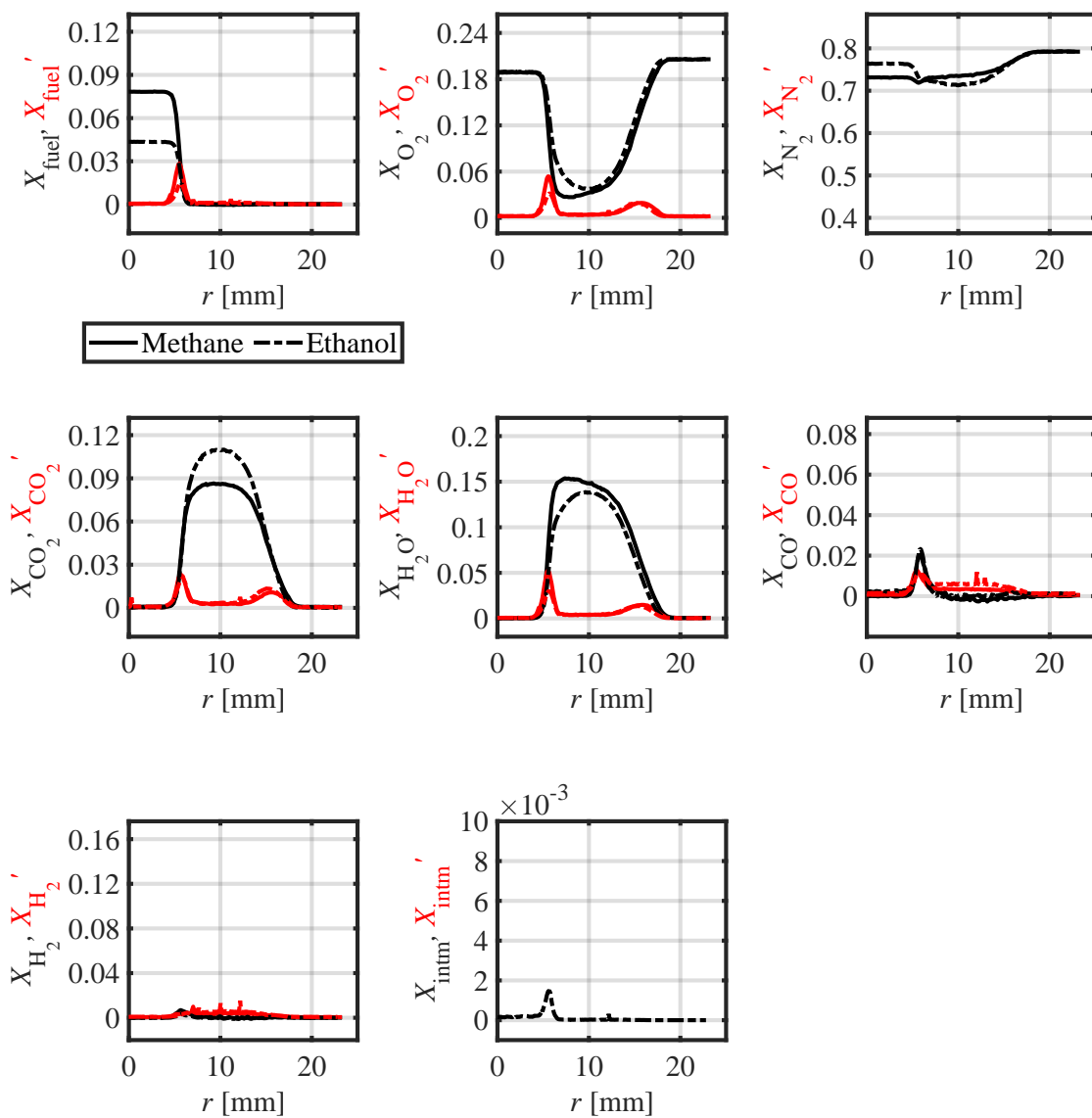
Figure A.1.: Species mole fraction profiles of methane/air and ethanol/air TCJB flames at lean conditions (CH_4: $\phi=0.85$, C_2H_5OH: $\phi=0.7$) with a Reynolds number of 6000 and at x/D=1.
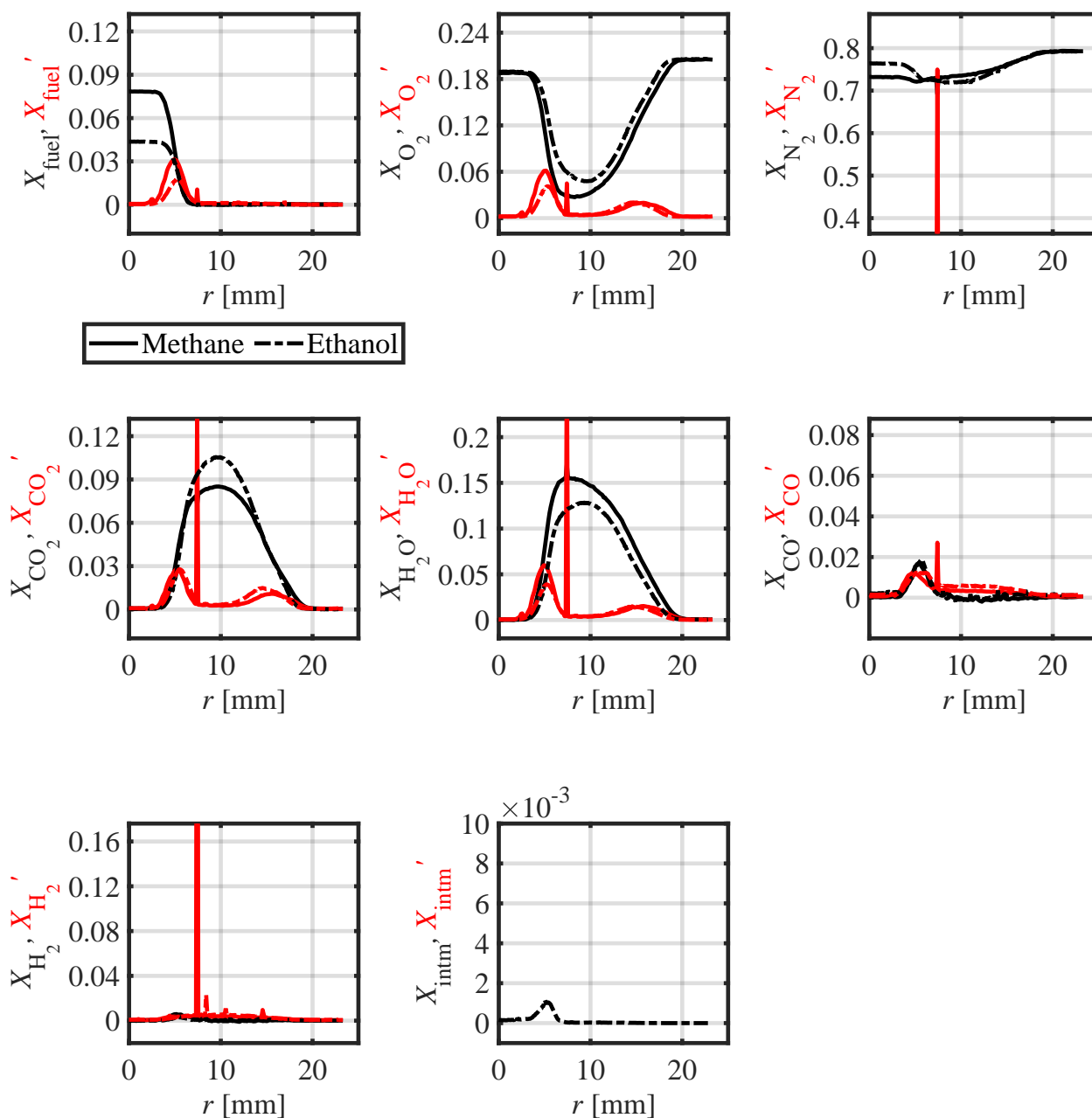
Figure A.2.: Species mole fraction profiles of methane/air and ethanol/air TCJB flames at lean conditions (CH$_4$: ϕ=0.85, C$_2$H$_5$OH: ϕ=0.7) with a Reynolds number of 6000 and at x/D=2.
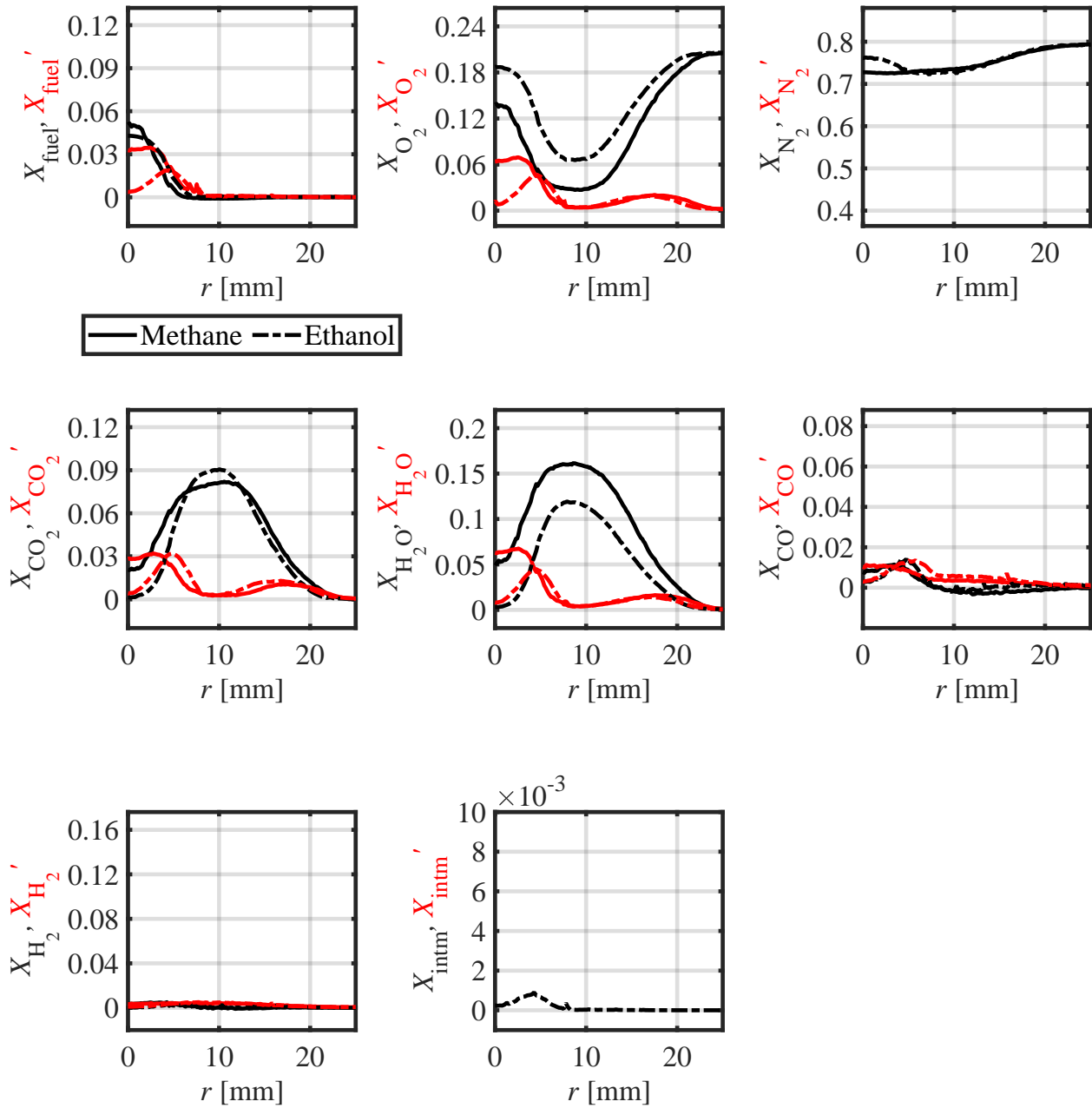
Figure A.3.: Species mole fraction profiles of methane/air and ethanol/air TCJB flames at lean conditions (CH$_4$: ϕ=0.85, C$_2$H$_5$OH: ϕ=0.7) with a Reynolds number of 6000 and at x/D=5.5.

Figure A.4.: Species mole fraction profiles of methane/air and ethanol/air TCJB flames at rich conditions (CH_4: ϕ=1.3, C_2H_5OH: ϕ=1.25) with a Reynolds number of 6000 and at x/D=1.

Figure A.5.: Species mole fraction profiles of methane/air and ethanol/air TCJB flames at rich conditions (CH$_4$: ϕ=1.3, C$_2$H$_5$OH: ϕ=1.25) with a Reynolds number of 6000 and at x/D=2.

Figure A.6.: Species mole fraction profiles of methane/air and ethanol/air TCJB flames at rich conditions (CH$_4$: ϕ=1.3, C$_2$H$_5$OH: ϕ=1.25) with a Reynolds number of 6000 and at x/D=5.5.

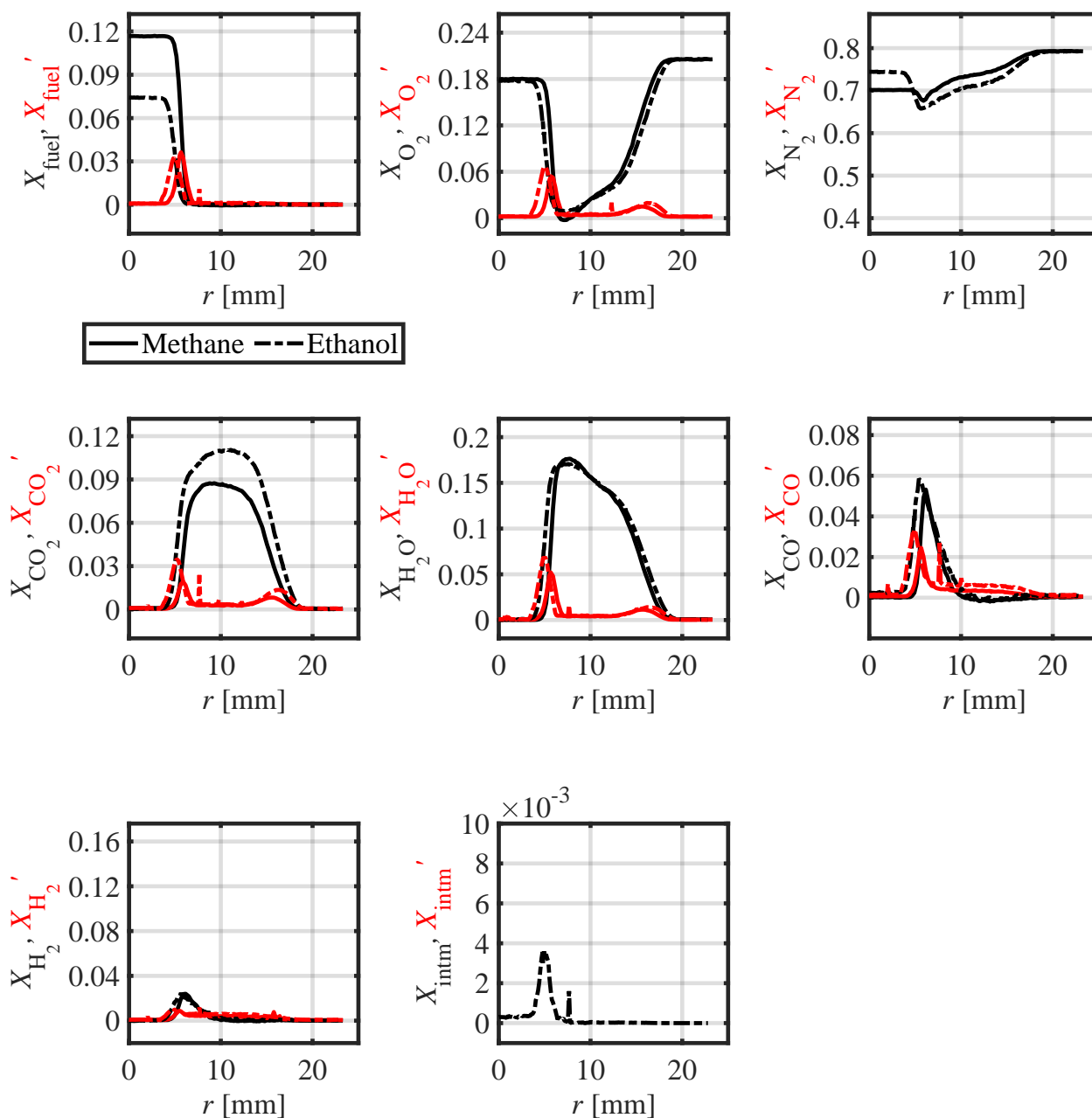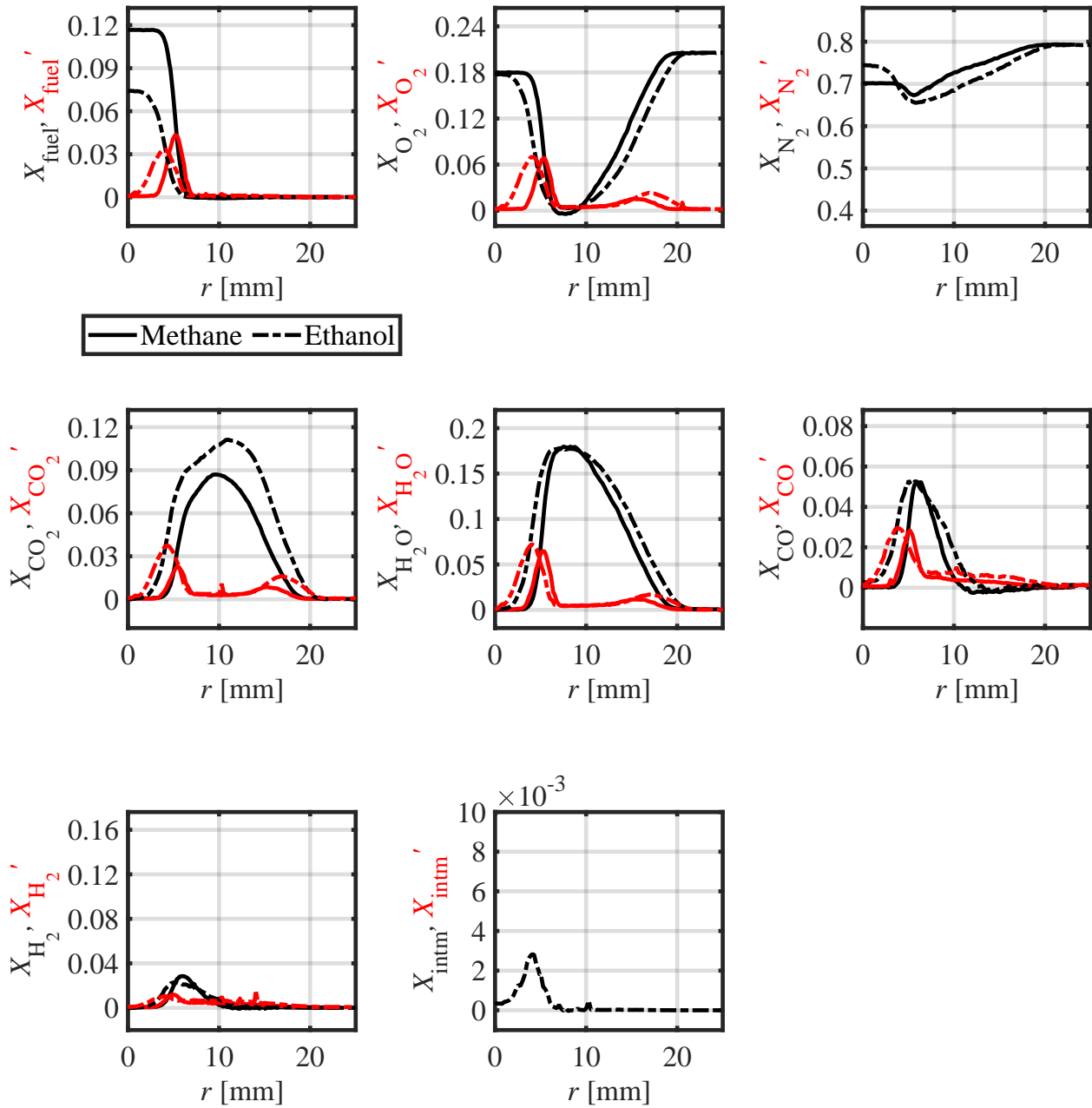**Figure A.7.:** Species mole fraction profiles of methane/air and ethanol/air TCJB flames at lean conditions (CH$_4$: ϕ=0.85, C$_2$H$_5$OH: ϕ=0.7) with a Reynolds number of 12000 and at x/D=1.

Figure A.8.: Species mole fraction profiles of methane/air and ethanol/air TCJB flames at lean conditions (CH$_4$: ϕ=0.85, C$_2$H$_5$OH: ϕ=0.7) with a Reynolds number of 12000 and at x/D=2.

Figure A.9.: Species mole fraction profiles of methane/air and ethanol/air TCJB flames at lean conditions (CH$_4$: ϕ=0.85, C$_2$H$_5$OH: ϕ=0.7) with a Reynolds number of 12000 and at x/D=5.5.
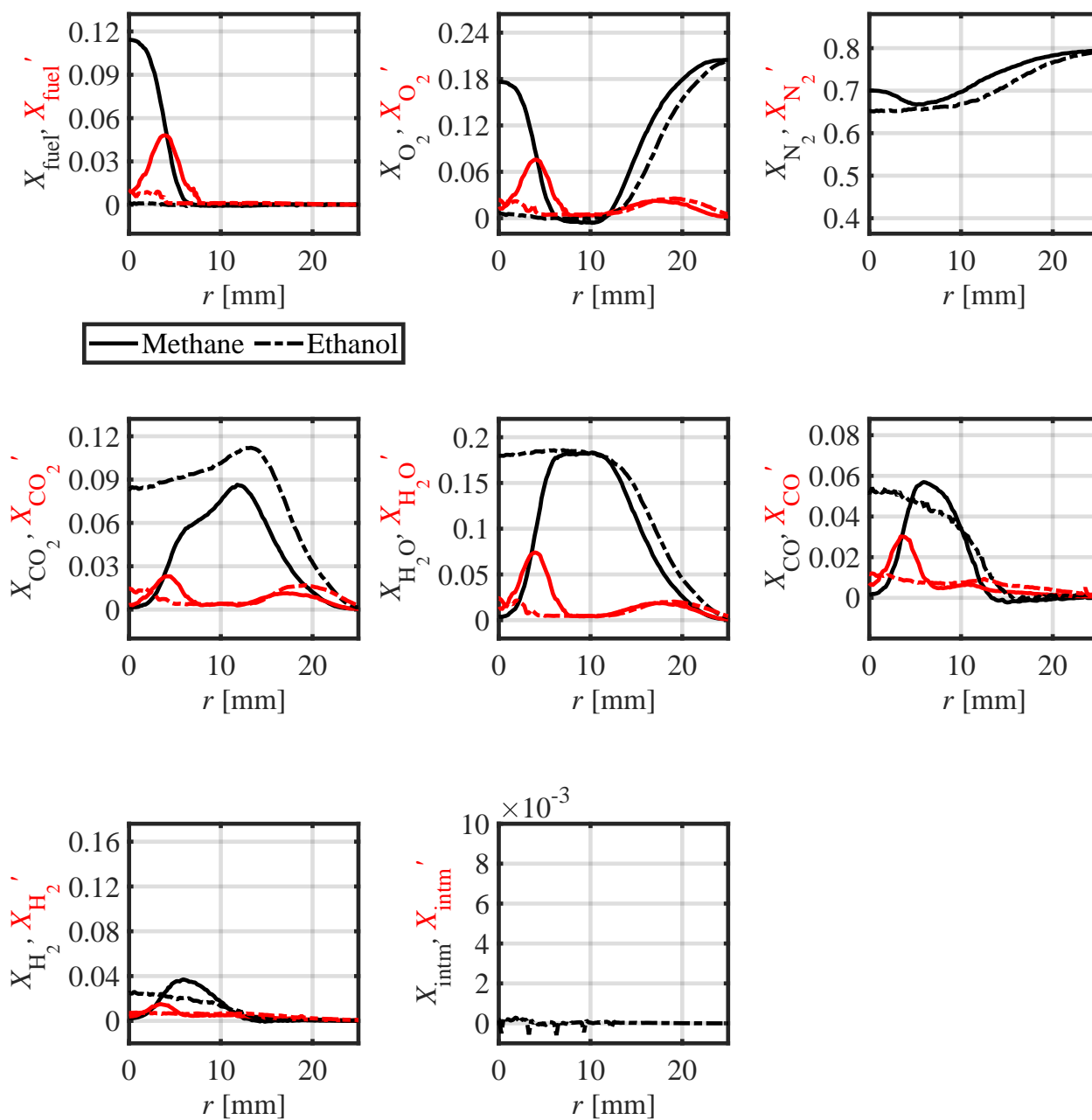
Figure A.10.: Species mole fraction profiles of methane/air and ethanol/air TCJB flames at rich conditions (CH$_4$: ϕ=1.3, C$_2$H$_5$OH: ϕ=1.25) with a Reynolds number of 12000 and at x/D=1.

Figure A.11.: Species mole fraction profiles of methane/air and ethanol/air TCJB flames at rich conditions (CH$_4$: ϕ=1.3, C$_2$H$_5$OH: ϕ=1.25) with a Reynolds number of 12000 and at x/D=2.
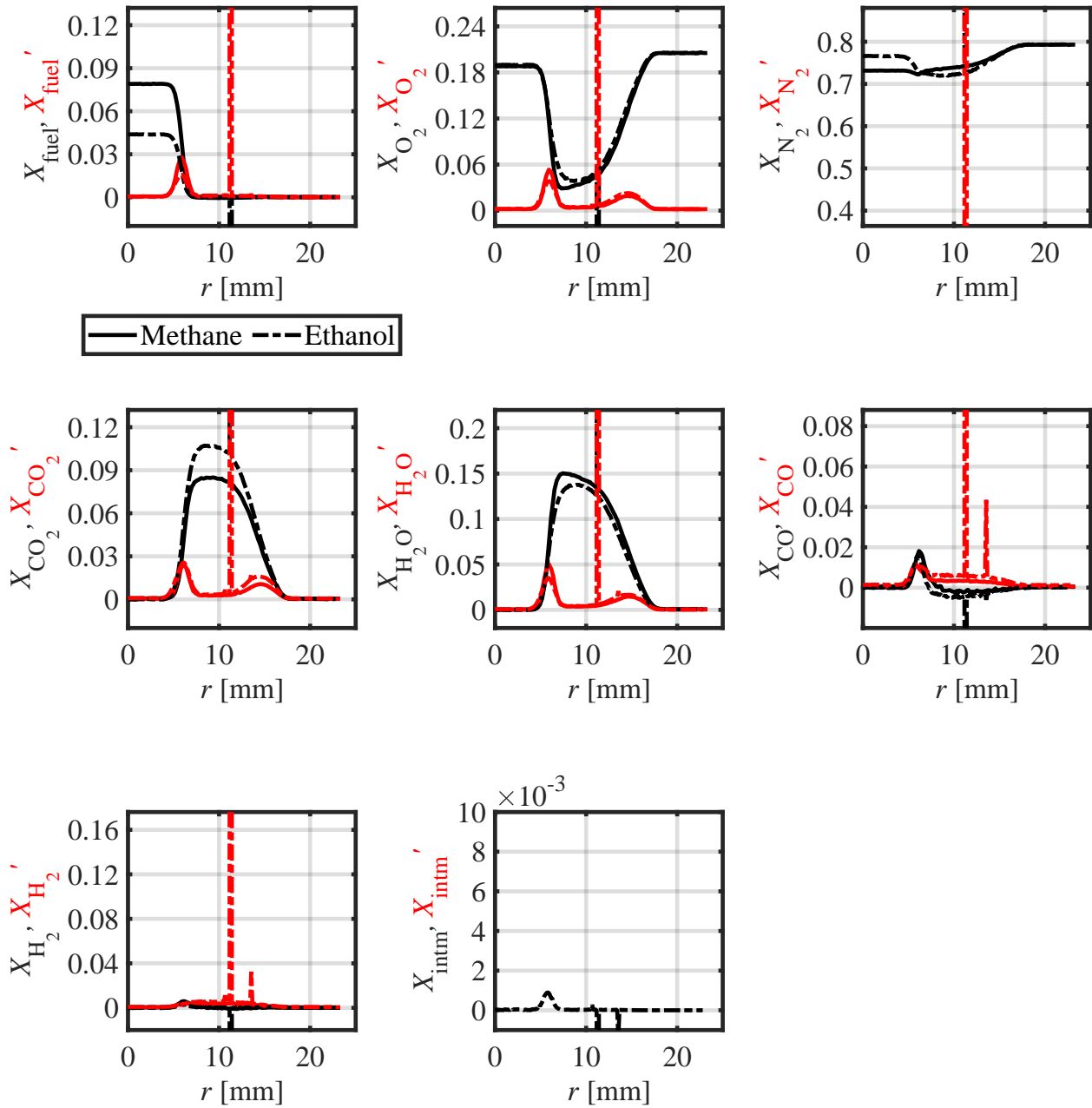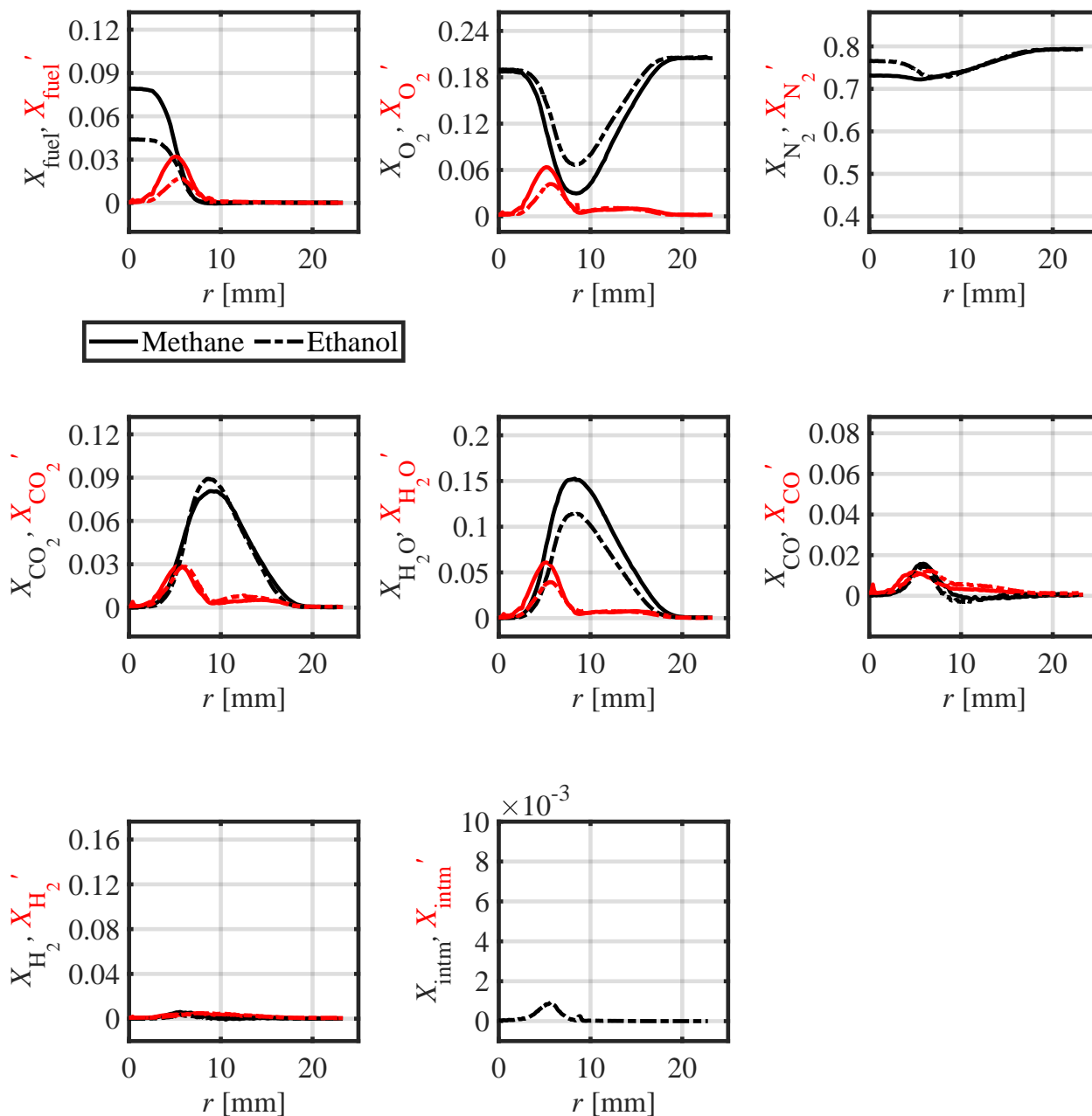
Figure A.12.: Species mole fraction profiles of methane/air and ethanol/air TCJB flames at rich conditions (CH$_4$: ϕ=1.3, C$_2$H$_5$OH: ϕ=1.25) with a Reynolds number of 12000 and at x/D=5.5.

Figure A.13.: Species mole fraction profiles of methane/air and ethanol/air TCJB flames at lean conditions (CH$_4$: ϕ=0.85, C$_2$H$_5$OH: ϕ=0.7) with a Reynolds number of 28500 and at x/D=1.

Figure A.14.: Species mole fraction profiles of methane/air and ethanol/air TCJB flames at lean conditions (CH$_4$: ϕ=0.85, C$_2$H$_5$OH: ϕ=0.7) with a Reynolds number of 28500 and at x/D=5.5.
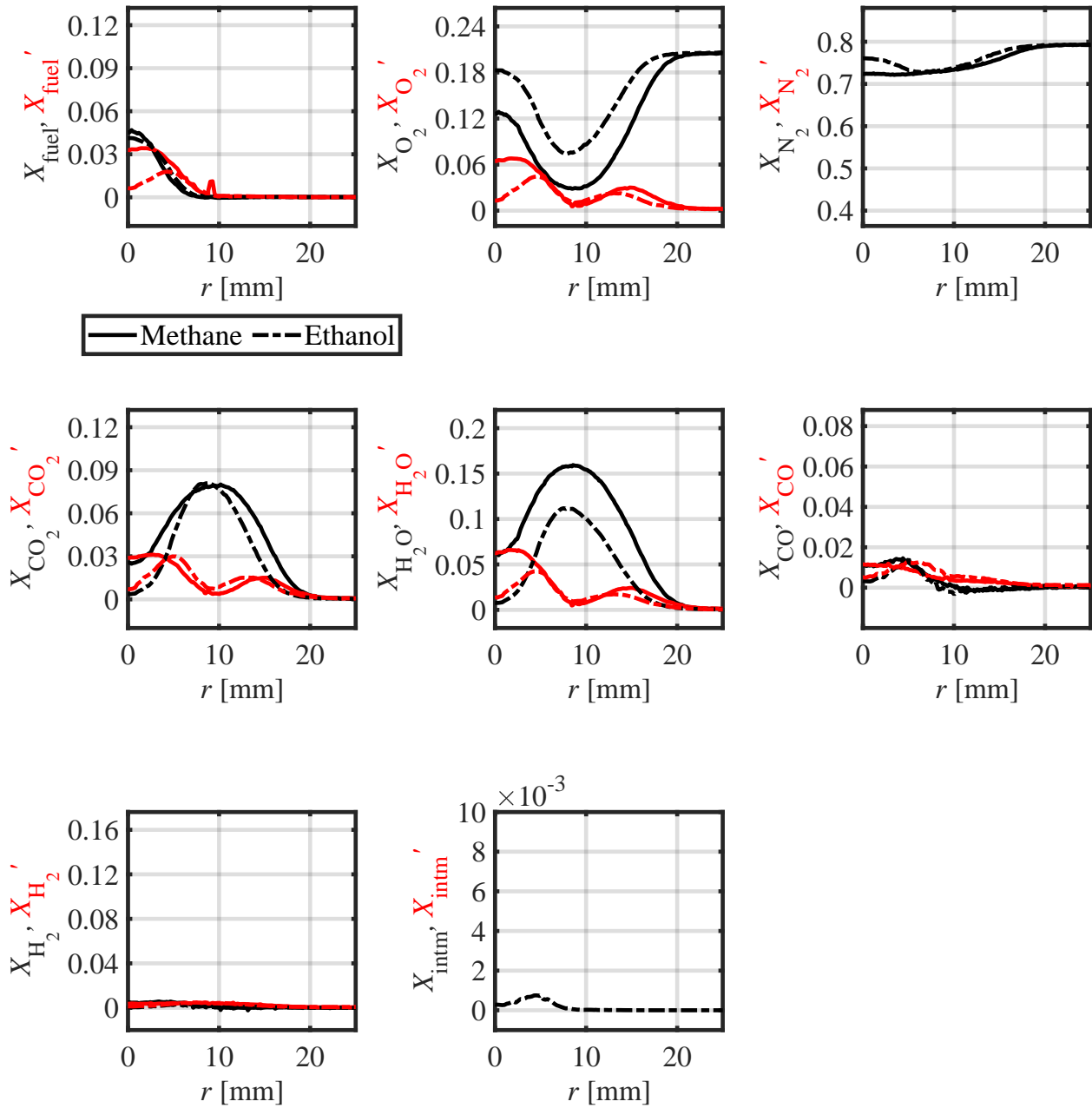
Figure A.15.: Species mole fraction profiles of methane/air and ethanol/air TCJB flames at lean conditions (CH$_4$: ϕ=0.85, C$_2$H$_5$OH: ϕ=0.7) with a Reynolds number of 28500 and at x/D=11.
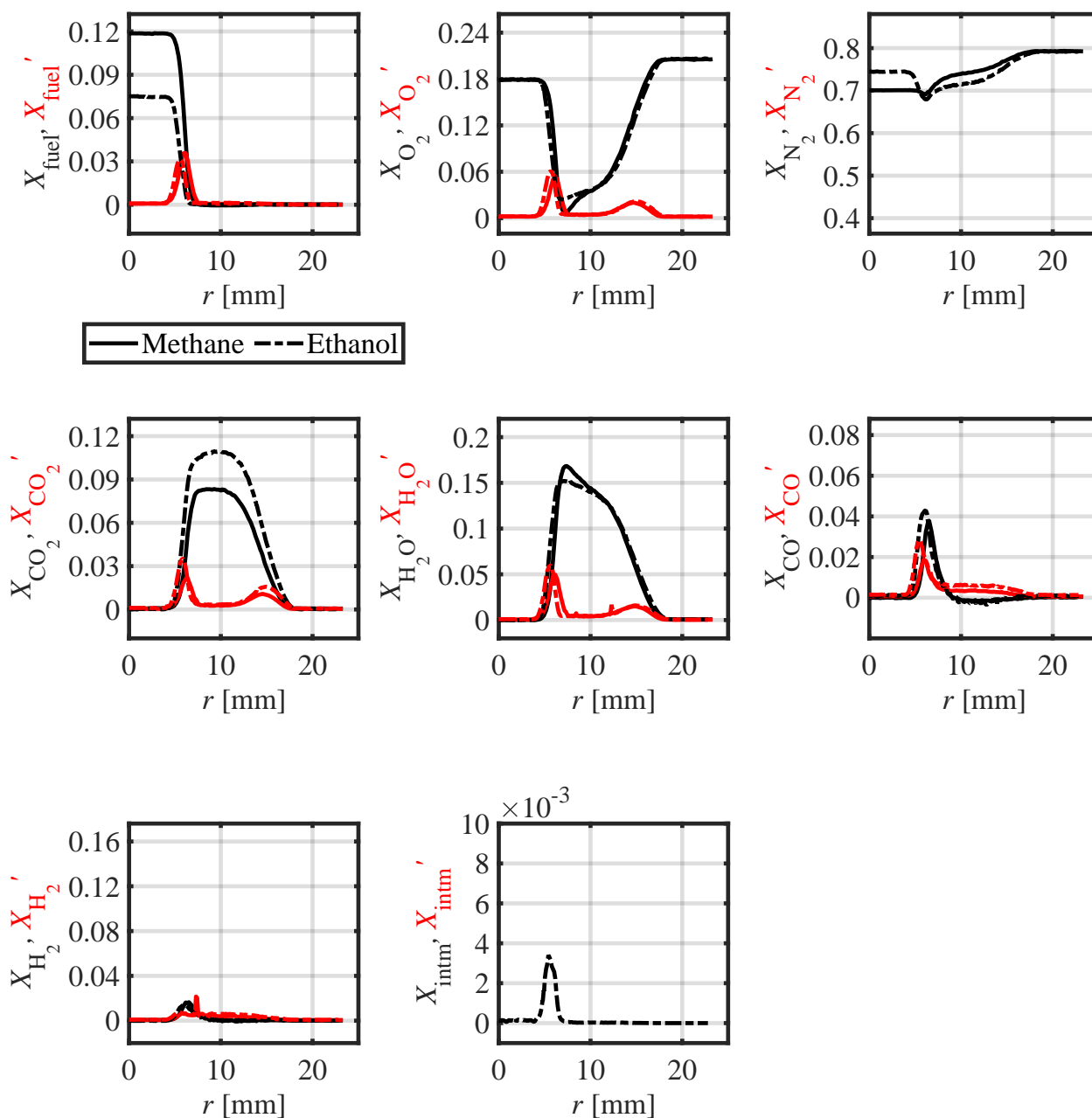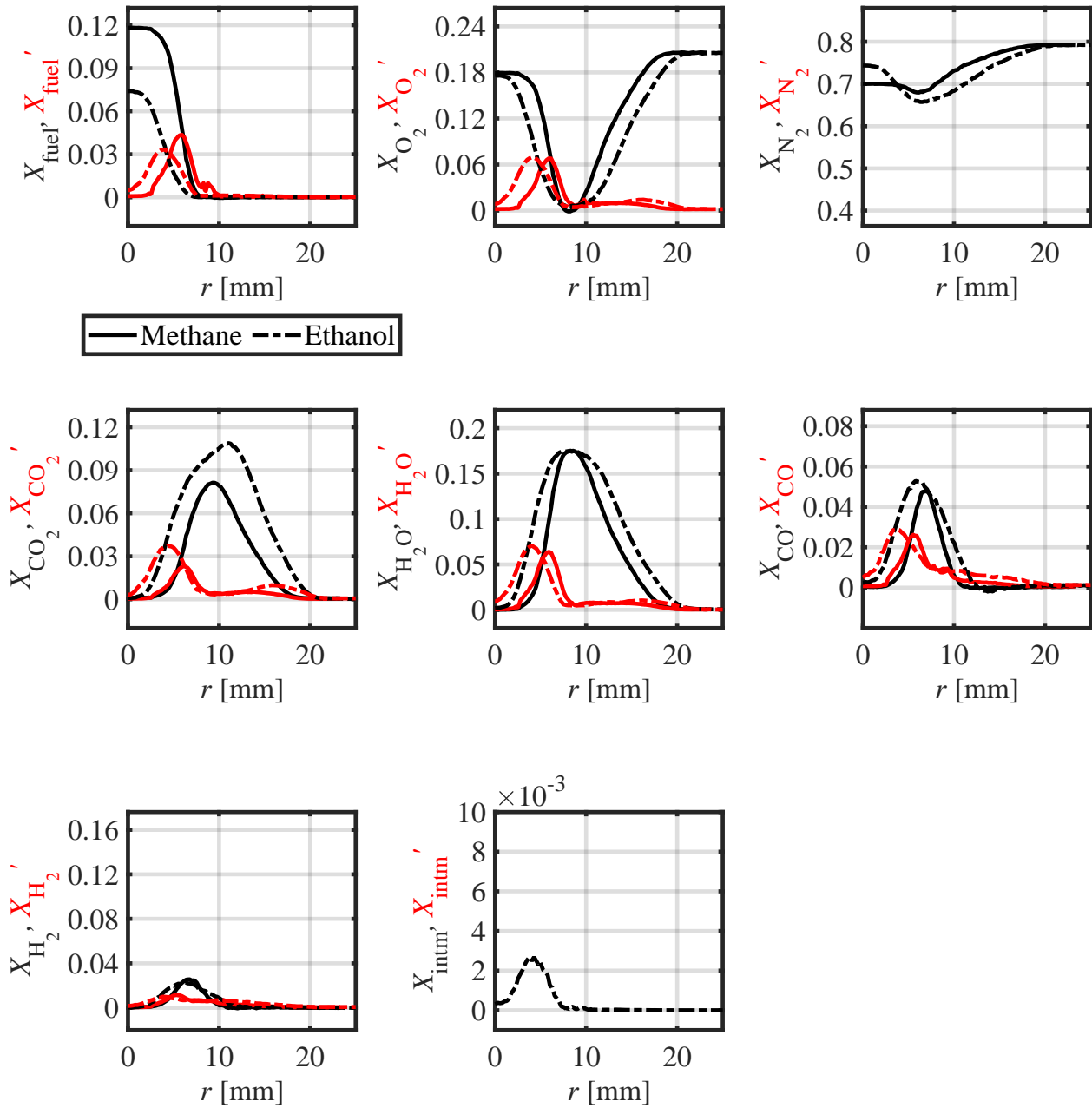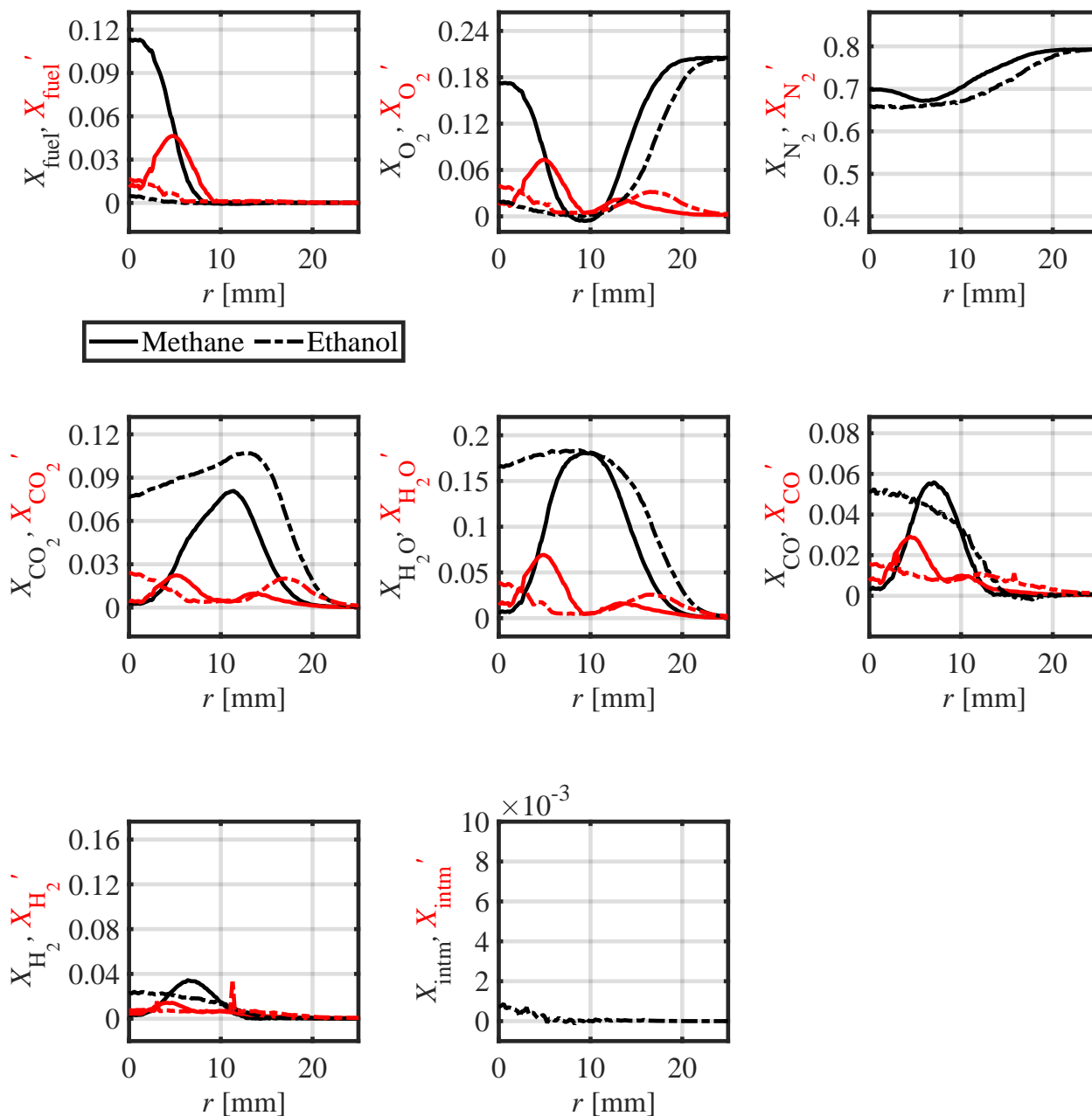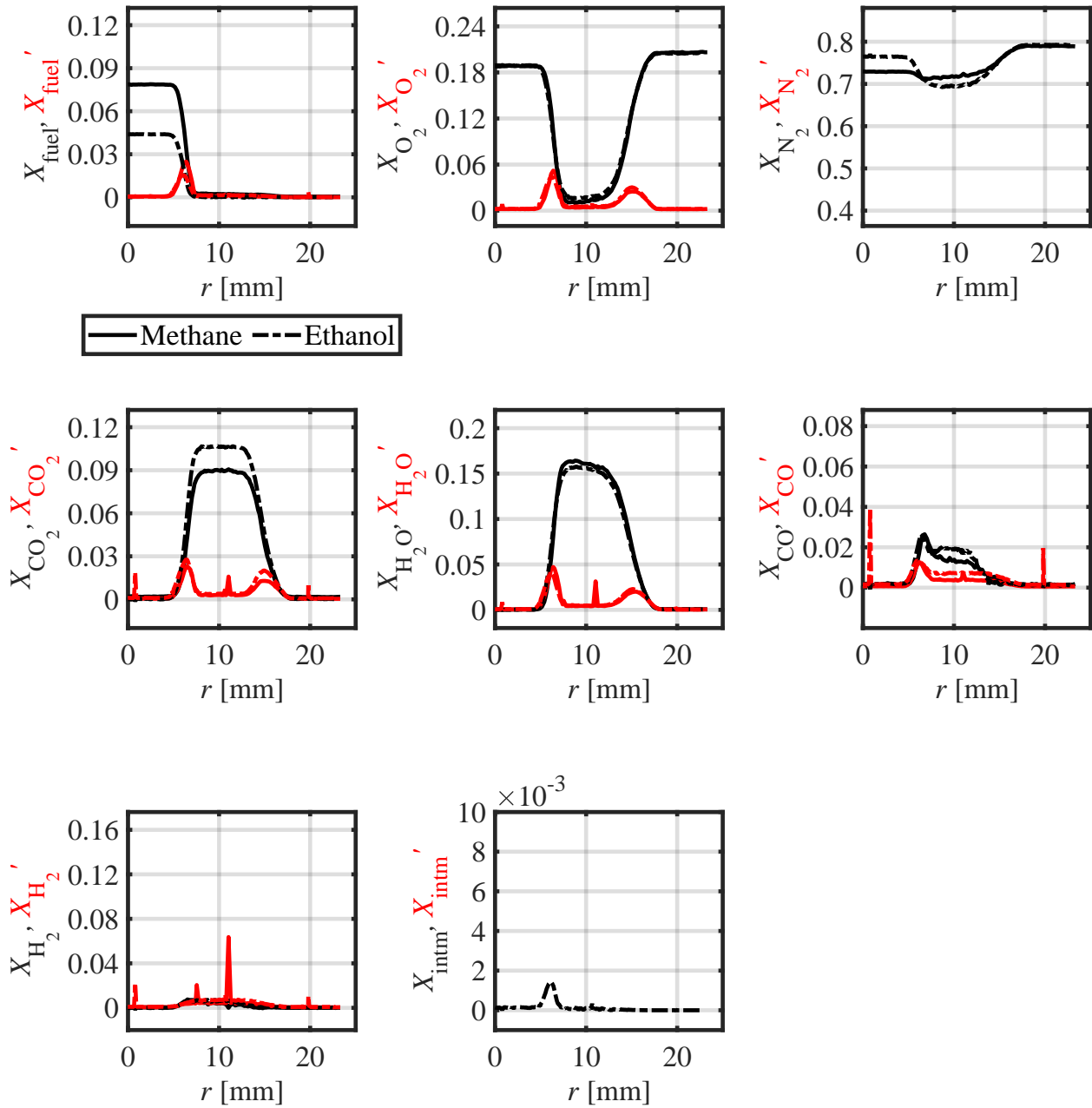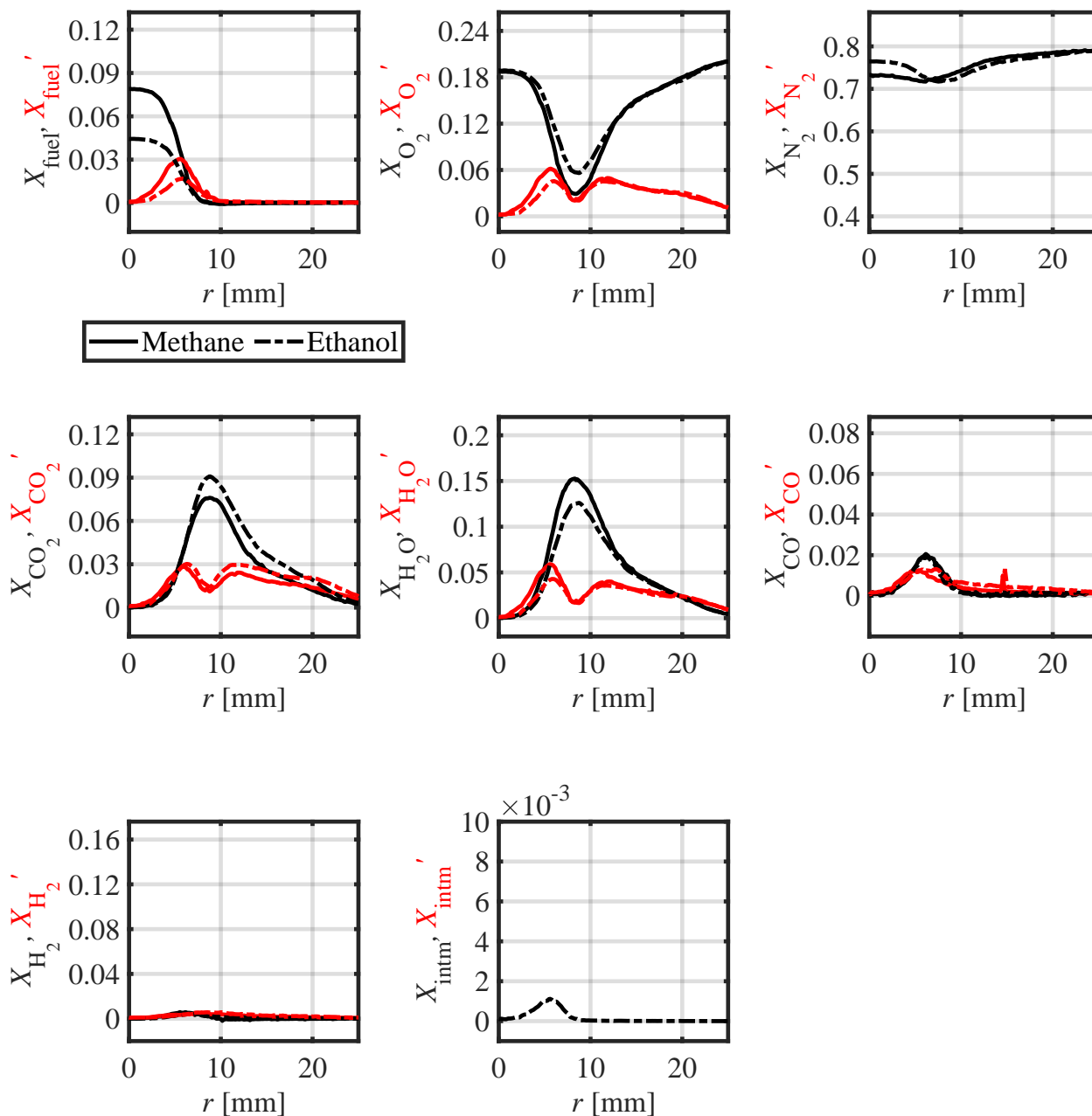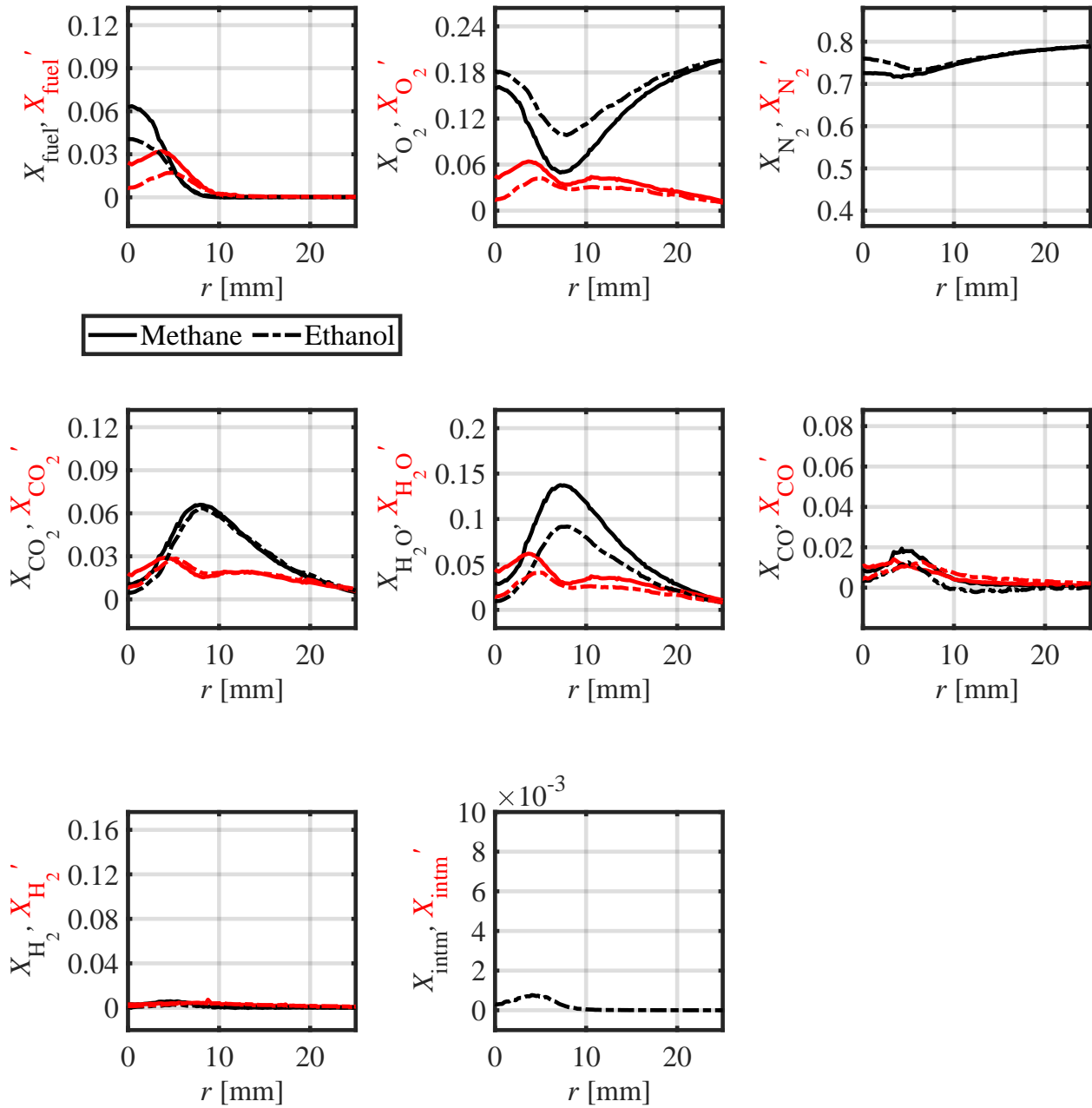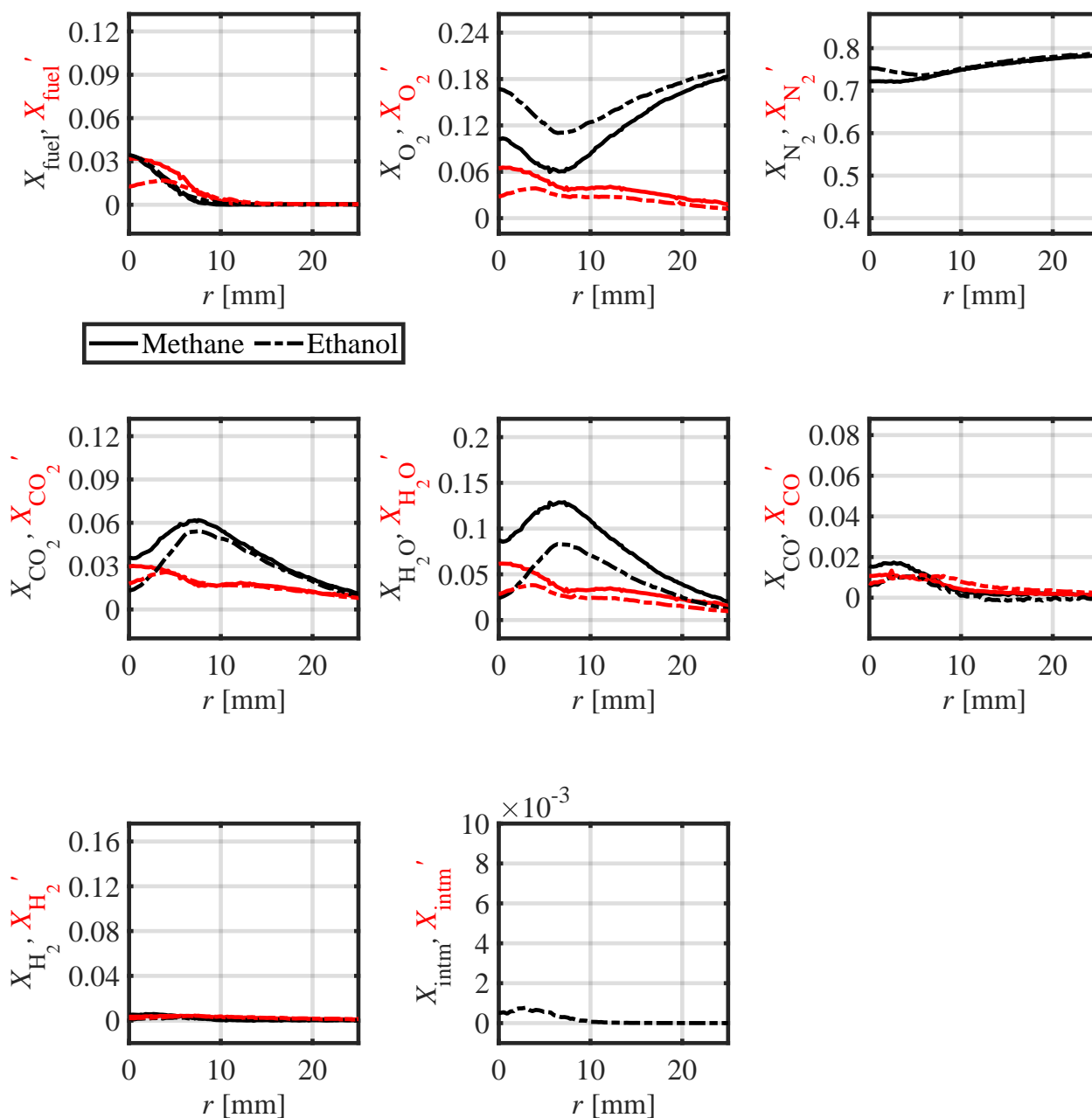
Figure A.16.: Species mole fraction profiles of methane/air and ethanol/air TCJB flames at lean conditions (CH$_4$: ϕ=0.85, C$_2$H$_5$OH: ϕ=0.7) with a Reynolds number of 28500 and at x/D=14.5.

B. Additional Research

This appendix chapter describes three studies that were not of importance for the discussions in the main body, but shall be documented nevertheless. First, a small experimental LES study with which Borghi-Peters diagrams are derived is shown. Secondly, a study on the smallest structures in turbulent flames is presented. Thirdly, the experimental derivation of temperature-dependent matrix inversion polynomials for the ethanol response function and crosstalks is demonstrated.

B.1. Characterization of Turbulent Flames in Borghi-Peters Diagram

For the current lack of particle tracking velocimetry (PTV), PIV, or LDV measurements on the novel TCJB (Section 5.2.1), the turbulent flow field is simulated using a LES (provided by Dr.-Ing. Louis Dressler via personal communication in April 2022). The goal is to estimate the turbulent flow parameters' magnitudes, mainly the velocity fluctuation (r.m.s.), axial velocity profiles, and the integral length scale.

B.1.1. LES Study

The TCJB's relatively simple jet pipe geometry is adopted from the CAD model, and the pilot's exhaust gas emissions and the air coflow are considered. Four exemplary turbulence levels are simulated, with Re_{bulk}=3000, 12000, 18000, and 48000 bulk Reynolds numbers.

Notably, the mixture is not ignited for simplicity reasons. Furthermore, assuming that the parameters will not drastically vary with fuel, only ethanol/air is simulated. This seems reasonable, as the mixtures' main ingredient is air for all fuels studied. The premixed mixture temperature is 343 K as that was the temperature chosen most often.

Figure B.1 shows the axial velocity at the nozzle exit for all bulk Reynolds numbers normalized to their respective maximum on the upper left. The same figure is given for x/D=10 on the upper right. The lower row shows the same heights but with the velocities' r.m.s. instead.

Figure B.2 shows the progression along the axial dimension on the burner's axis. To the left are the characteristic length scales L_t/D, to the right the velocities' r.m.s..

The results are incorporated into the following Appendix section on the present work's turbulent flames' Borghi-Peters diagram categorizations. Notably, since a broad range of turbulence intensities will be inspected there, the velocities' r.m.s. need to be interpolated. This is done by using
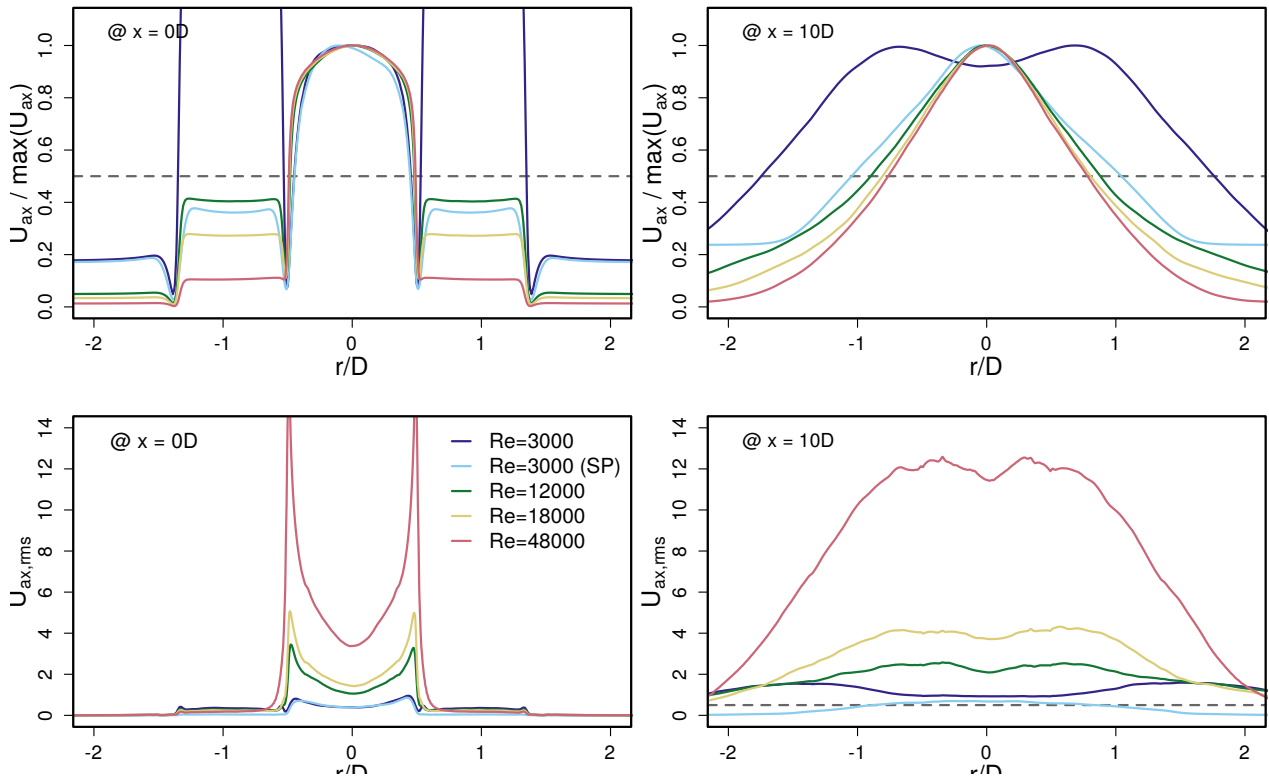
Figure B.1.: Cold mixture LES velocity and r.m.s. results in radial dimension. Simulated and provided by Dr.-Ing. Louis Dressler via personal communication in April 2022.
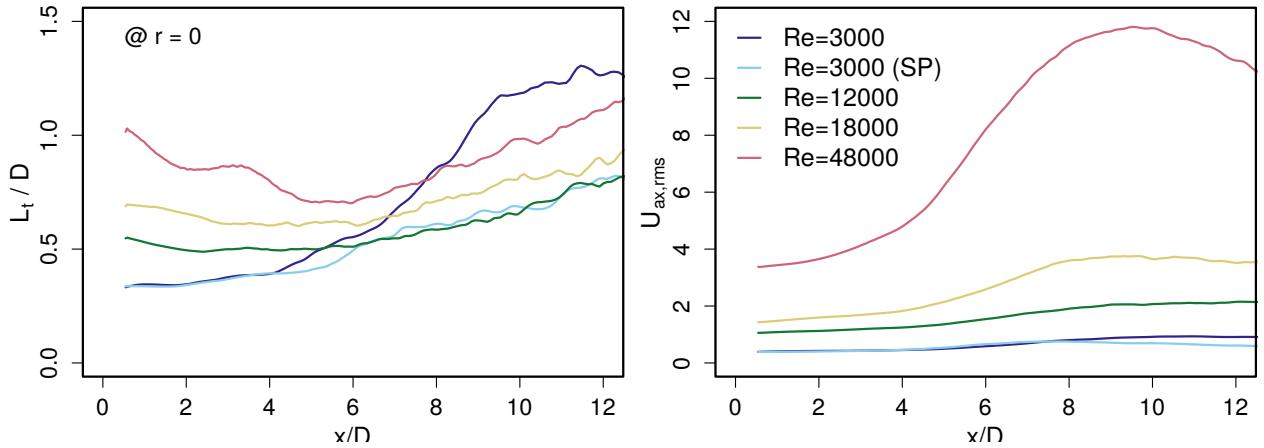
Figure B.2.: Cold mixture LES characteristic length scales and velocities in axial dimension. Simulated and provided by Dr.-Ing. Louis Dressler via personal communication in April 2022.

shape-preserving piece-wise cubic interpolation (Matlab's 'pchip' interpolation function) between the anker points at bulk Reynolds numbers Re_{bulk}=12000, 18000, 48000, and with their maximum velocity r.m.s. values of $\approx 2\,\mathrm{m\,s^{-1}}$, $3.8\,\mathrm{m\,s^{-1}}$ and $11.8\,\mathrm{m\,s^{-1}}$. Larger than Re_{bulk}=48000 values were extrapolated.

B.1.2. Borghi-Peters Diagrams

B.1.2.1. Blow-off, Flamelength, and Flame Topology Experiments

In the following, the blow-off, flamelength, and flame topology experiment flames are categorized into the Borghi-Peters regime diagram (theory in Section 2.4.2). It is emphasized that the velocity r.m.s., laminar burning velocity, and laminar flame thickness are all derived numerically and sometimes need to be interpolated or extrapolated. Furthermore, although flames have a turbulence level spectrum, only the highest turbulence intensities in the flames are marked (highest velocity r.m.s. along the axial dimension). More details regarding the parameters' derivations can be found in Sections B.1.1, 3.5.1 and 3.5.4, respectively.

Figure B.3 displays the blow-off experiment's flames in the Borghi-Peters diagram. Intense turbulence chemistry interaction can be expected, as all flames are located in the reaction sheet regime or above. This means that the smallest eddies are penetrating the preheating zone of the flame, leading to increased heat and mass transfer and thickened flames. For the methane/air flames, the richest flames may experience penetration by eddies even into the primary reaction zone of the flame.
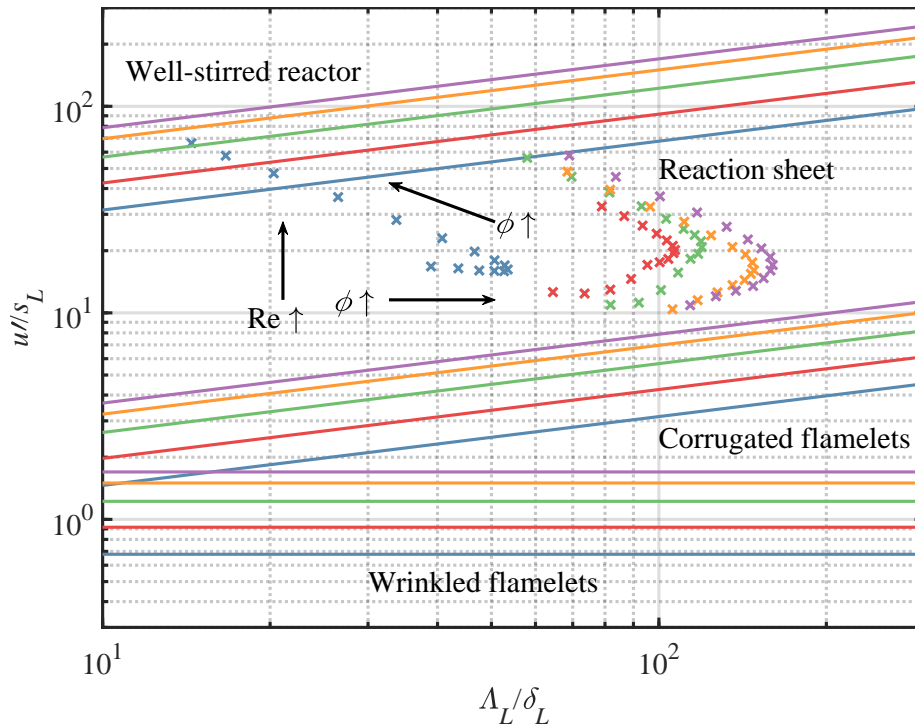
Figure B.3.: Borghi-Peters diagram blow-off experiment. Because of the lack of laminar burning velocities, operating points with equivalence ratios smaller than $\phi=0.8$ are not displayed. ■ Methane/air; ■ Methanol/air; ■ Ethanol/air; ■ 2-Propanol/air; ■ 2-Butanol/air.

Figure B.4 shows the flamelength experiment's flames in the Borghi-Peters diagram. Almost all flames appear to be affected by small eddy penetration to a certain extent in their preheating

zone. Only the richest mixture's flames are at the boundary to the corrugated flamelets, where an influence by turbulence and chemistry is expected.
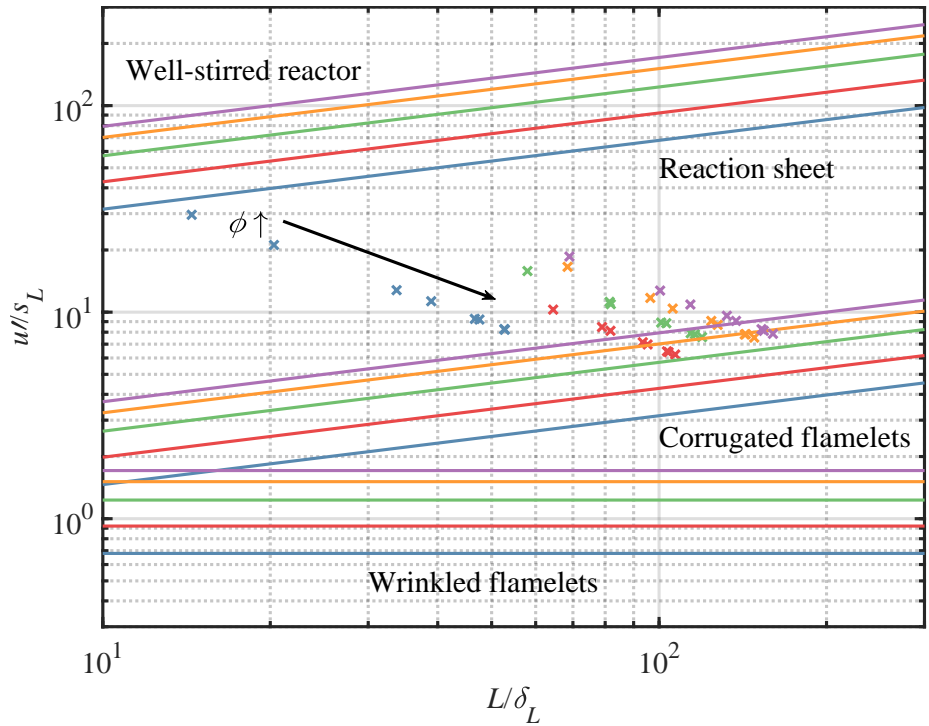
Figure B.4.: Borghi-Peters diagram Flamelength experiment. ■ Methane/air; ■ Methanol/air; ■ Ethanol/air; ■ 2-Propanol/air; ■ 2-Butanol/air.

Lastly, Figure B.5 shows that all of the flame topology experiment's flames should be situated in the corrugated flamelets regime. While some preheating zone effects might be expected in the most turbulent regions of the methane/air flames, the overall influence should be quite minor and is considered to be negligible.
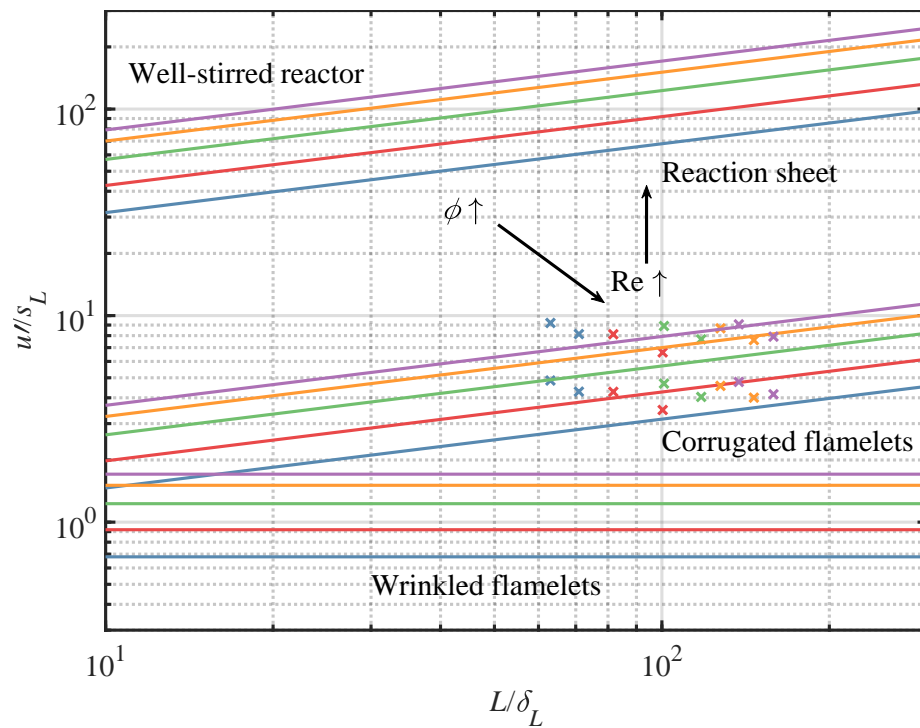
Figure B.5.: Borghi-Peters diagram flame topology experiment. ■ Methane/air; ■ Methanol/air; ■ Ethanol/air; ■ 2-Propanol/air; ■ 2-Butanol/air.

B.1.2.2. Thermochemical State Experiment

Figure B.6 presents the chosen operating points of the thermochemical state experiments in the Borghi-Peters diagram. As described above, the diagram is again derived from numerical calculations, and the limitations of this approach are discussed at the end of Section 5.2.3.
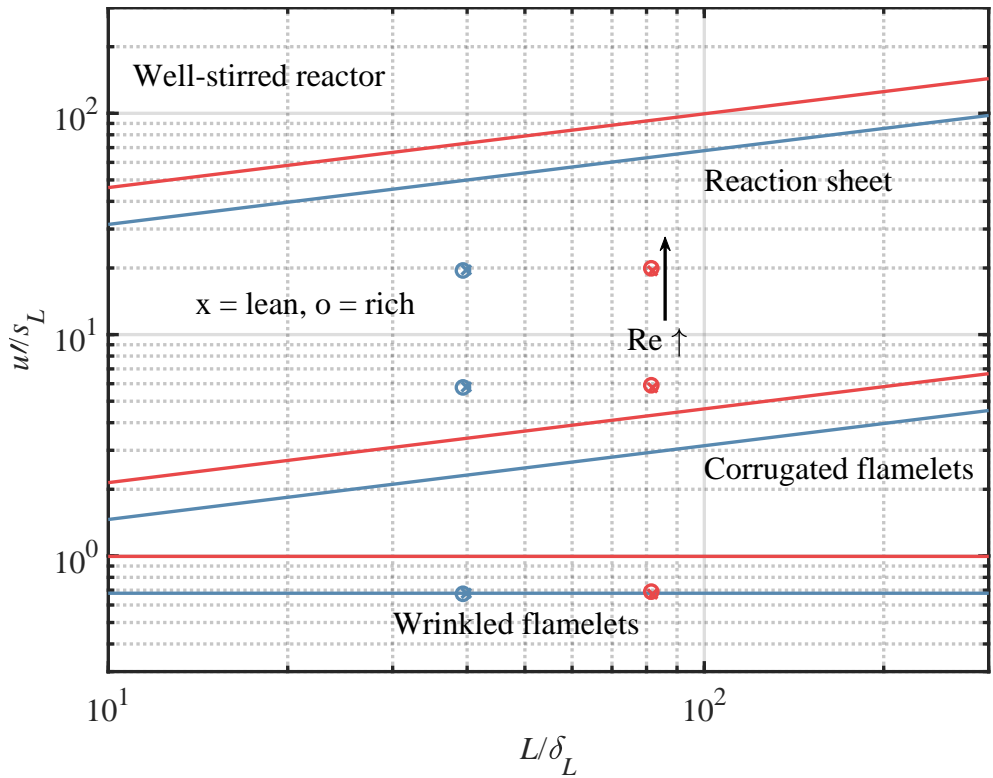
Figure B.6.: Borghi-Peters diagram of the turbulent flame experiment. ■ Methane/air; ■ Methanol/air; ■ Ethanol/air

As can be seen, the lowest bulk Reynolds number is located in the wrinkled flame regime, where no turbulence-chemistry interaction is expected. The two higher ones are located in the reaction sheet regime, which offers the prospect of finding turbulence-chemistry interaction effects. The distance between them should also offer enough room to find differences. Within the same bulk Reynolds number, the two equivalence ratios are very close, resulting from the same laminar burning velocity and similar laminar flame thicknesses.

However, as described in Section 6.7.2.1, it could only be realized a posteriori that the ethanol/air equivalence ratios were not accurately set during the experiment. Figure B.7 shows the approximate location of the flames in the Borghi-Peters diagram when accounting for this error.
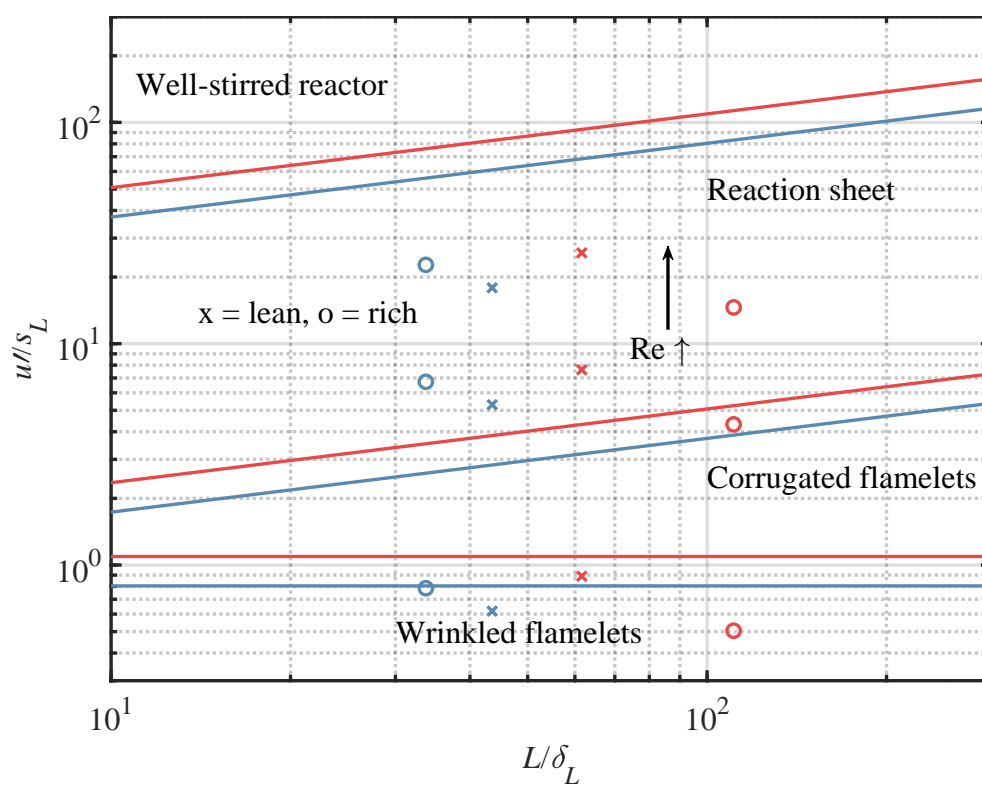
Figure B.7.: Borghi-Peters diagram of the turbulent flame experiment with the measured false equivalence ratios.
■ Methane/air; ■ Methanol/air; ■ Ethanol/air; x = lean ϕ (CH$_4$: 0.85 C$_2$H$_5$: 0.7), o = rich ϕ (CH$_4$: 1.3 C$_2$H$_5$: 1.25).

B.2. Study of Small Scale Radii

This section describes a study to quantitatively describe the smallest structures in the flame topology study in Section 5.4.3.

Thereby, two characteristic curvature values are taken from the complete flame curvature PDFs and inverted to retrieve the respective radii. Thereby, quantitative differences among the fuel-specific feature development on a micro-scale can be identified. On the PDF's negative side, the *small-scale negative radii* (r_{ss-}) are extracted at the fifth percentile. At the 95th percentile on the PDF's positive side, the *small-scale positive radii* (r_{ss+}) are extracted.

Notably, all of the obtained radii are larger than the Siemens star-derived detection system optical resolution. Furthermore, the radii are on the order of multiples of the laser sheet thickness. Both factors make it a robust parameter available from the given measurement technique.

Results are presented in Figure B.8, where slightly lean and rich flames ($\phi=0.9$ and 1.05) at a $Re_{bulk}=12000$ bulk Reynolds number are shown as exemplary cases.
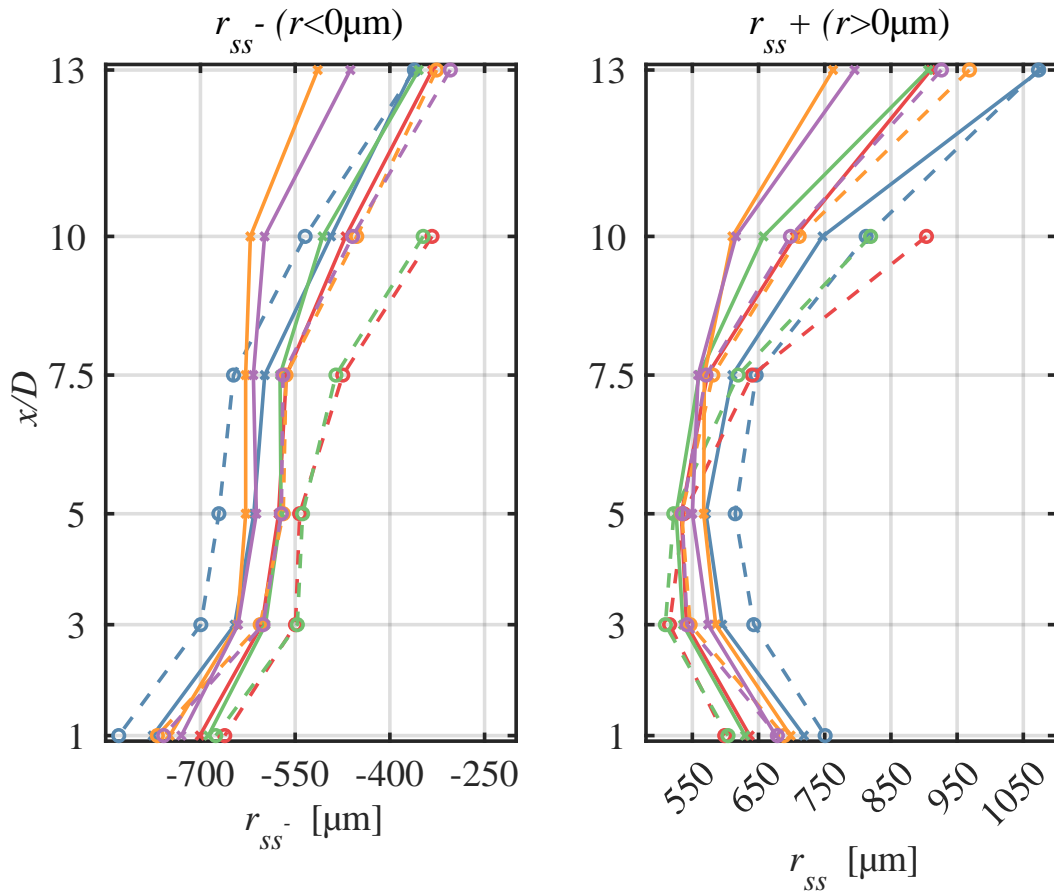
Figure B.8.: Small scale radii of the flames at $Re_{bulk}=12000$ for two equivalence ratios, $\phi=0.9$ (solid) and $\phi=1.05$ (dashed). ■ Methane/air; ■ Methanol/air; ■ Ethanol/air; ■ 2-Propanol/air; ■ 2-Butanol/air

Up to $x/D{=}5$ both positively and negatively curved features exhibit increasingly smaller radii (r_{ss}), which is attributed to the smaller eddy development and increased fluctuations within the shear-driven turbulence. Further downstream, the negatively-curved flame front regions show a continuous r_{ss-} progression towards even more decreasing magnitudes.

The continuing decrease is due to an increased probability of smaller unburned mixture pockets being located in burned gas areas (compare methanol/air single-shot at $x/D{\approx}10$ in Figure 5.9). This pocket development can be visualized as reactant-point sinks consumed in the axial direction by progressing flame fronts around them. In contrast, the small-scale positive radii r_{ss+} increase again in magnitude above $x/D{=}5$. This is because both the intersecting flame's left and right branches start to merge again as the unburned core flow vanishes towards the flame tip.

In the larger flame contours' connected segments, negatively shaped cusps grow to the positive bulges' expense, which flattens them and therefore increases their radii. This phenomenon was already discussed in light of the curvature PDFs, referring to the Landau-propagation [82, pg. 400ff]. Regarding the equivalence ratio change (dashed lines) the same effects discussed for the curvature PDF skewnesses applies.

B.3. Ethanol Response Function and Crosstalk Polynomial Determination From Electric Heater Measurements

This section describes how temperature-dependent response functions and crosstalks for ethanol are derived from spectra previously transferred from S.A. to S.B. (procedure in Section 6.2.3.3). To start with, Figure B.9 (top) shows the transferred ethanol spectrum at the extrapolated temperature of 343 K.
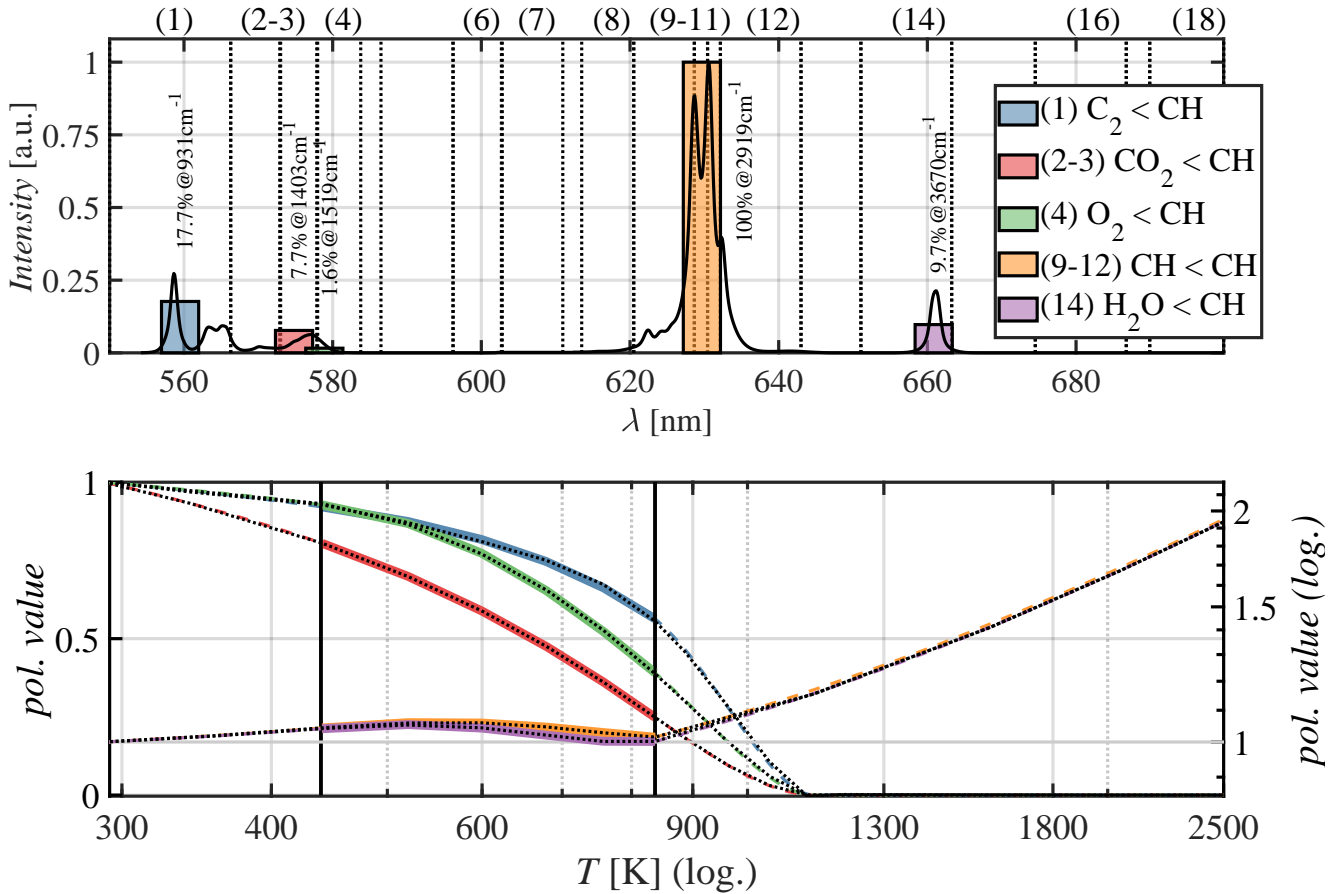
Figure B.9.: Ethanol response function development derived from electric heater measurements. While the ethanol spectra transferred from Spectrometer A to Spectrometer B at 343 K are shown in the upper graph, the lower graph shows the polynomial extrapolations derived from the available heater data.

Vertical color coded bars indicate the crosstalk magnitudes, to which the multiplier values correspond, in the predefined channels (Section 6.2.3.2 and 6.2.3.4). Thereby, the bar location on the abscissa is a reference to the *balance point* of the integrated surface between the channel boundaries. While the precise location will be lost in the experiment due to hardware binning, the wavenumber shift location is still relevant for the harmonic oscillator approximation applied below. The response functions of ethanol and its crosstalks, which are derived with the procedure described in the following, are shown in the lower graph of Figure B.9.

1. Initial analysis shows that ethanol crosstalks with relevant magnitude are onto C_2, carbon dioxide, oxygen, and water.

2. Within those channels' boundaries and the hydrocarbons channel, the transferred spectra are integrated at the available experimental temperatures.

3. The calculated values are inspected and the paths they likely take below and above the measured temperatures are estimated:

   a) The crosstalks onto C_2, carbon dioxide and oxygen have a strongly decreasing trend, which is almost linear. On the assumption that the trend continues and the cross-section will have a continuous trace towards zero, a smooth spline function is fitted near the approximate zero-crossing. The result is visible in Figure B.9 (bottom). The small extrapolation region towards lower temperatures is linearly extrapolated.

   b) The ethanol response function (hydrocarbons channel) and the crosstalks onto water both show a different behavior in the inspected temperature range. They increase slightly, before dropping below unity and recovering afterwards. Here, it is assumed that the recovery will proceed towards values above unity in a non-linear fashion. An extrapolation is less straight forward in this case.

   The chosen approach is the common assumption that for diatomic molecules at non-elevated temperatures, the polarizability acts as a *simple harmonic oscillator* [64]. Thereby, the ethanol molecule complexity is massively reduced to behave similar as a diatomic molecule and disregarding an-harmonic perturbations completely [57]. This is a drastic step, which is only taken here due to lack of viable alternatives at the present stage.

4. Lastly, as the MI is coded in that way, the temperature dependent response curves and crosstalks need to be approximated by polynomials. In this work, they are fitted to the extrapolated cold, the experimentally derived medium and the extrapolated higher temperature regions with splines and harmonic oscillator functions. Polynomials of 9th order with twelve to 14 individually positioned anker points were necessary to mimic the response function and cross talk shapes.

Table B.1 summarizes the polynomial parameters. As usual, the crosstalks by hydrocarbons are on the order of the main species multipliers, but inverse. The crosstalk multipliers are calculated in percent-wise relation to the CH-stretch region signal (compare Figure B.9).

Alternatively, rather than from transferred S.A. spectra, the crosstalk multiplier can be derived from binned S.B. images of ethanol in Raman-inactive helium carrier gas. The resulting crosstalk magnitudes obtained from a 200 laser shot-mean are also noted in Table B.1. The difference between the two ways of crosstalk multiplier calculation are neglected, as the multipliers are only a first guess and are refined by the in-situ derived calibration coefficients.

After implementing the above derived polynomials into the data presented in Section 6.5.4, a meaningless result is obtained. For the reasons also described in Section 6.2.4, this solution is therefore discarded.

Table B.1.: Definition of ethanol response function and its cross talks for matrix inversion implementation. The values were derived from temperature-dependent stick spectra by Dieter et al. [33], which were convoluted with this work's spectrometer transfer function, extrapolated to lower and high temperatures and integrated between the previously defined Raman channels.

Response function/ cross talk	Multiplier	Anker points	polynome order														
C₂H₅OH 290	4.4544e-06	13	9	365	440	441	520	599	679	758	837	1137	1591	2046	2500		
1				1.019	1.043	1.043	1.060	1.059	1.046	1.029	1.015	1.156	1.408	1.670	1.936		
C₂<<<C₂H₅OH 290	3.9736e+04	15	9	342	441	520	599	679	758	837	887	965	1044	1122	1200	2000	2500
1				0.973	0.921	0.875	0.817	0.746	0.663	0.563	0.465	0.275	0.099	0.003	0	0	0
CO₂<<<C₂H₅OH 290	1.7286e+04	15	9	342	441	520	599	679	758	837	887	965	1044	1122	1200	2000	2500
1				0.933	0.805	0.700	0.590	0.475	0.361	0.250	0.182	0.094	0.030	0.001	0	0	0
O₂<<<C₂H₅OH 290	3.5920e+03	15	9	342	441	520	599	679	758	837	887	965	1044	1122	1200	2000	2500
1				0.975	0.928	0.868	0.774	0.654	0.522	0.391	0.302	0.166	0.057	0.002	0	0	0
H₂O<<<C₂H₅OH 290	2.1776e+04	13	9	365	440	441	520	599	679	758	837	1137	1591	2046	2500		
1				1.019	1.043	1.041	1.060	1.059	1.046	1.029	1.015	1.156	1.408	1.670	1.936		

C. Further Information

C.1. Point Mask Target

During this work, a second point mask was purchased in order to streamline the calibration process while using the LTOJ. The original point mask design was thereby replicated and is shown in the technical drawing displayed in Figure C.1.

C.2. New Flat Flame

A cross-sectional drawing of the new flat flame burner is shown in Figure C.2. The sealing concept was adopted from Heilbronn [66]. The flame stabilizing sinter metal sizes and the coflow are identical to the old flat flame burner [20, 123].
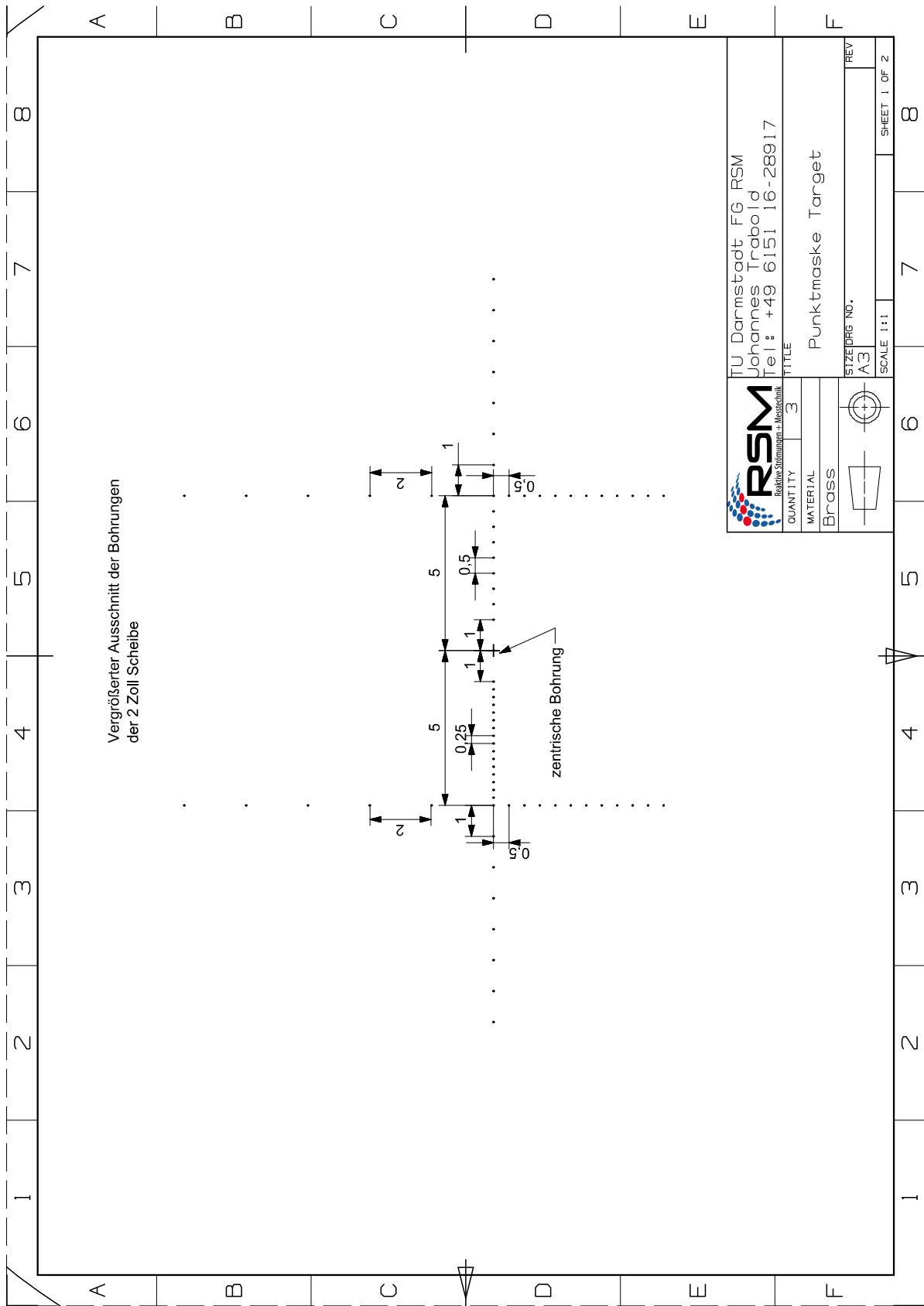
Figure C.1.: Point mask target technical drawing.

SECTION B-B

SHEET 2 OF 2

REV

SIZE DRG NO.
A4

SCALE 1:1

TITLE

asm_Brenner

TU Darmstadt FG RSM
Alexander Mueller

RSM
Reaktive Strömungen + Messtechnik

QUANTITY
1

MATERIAL

B

B
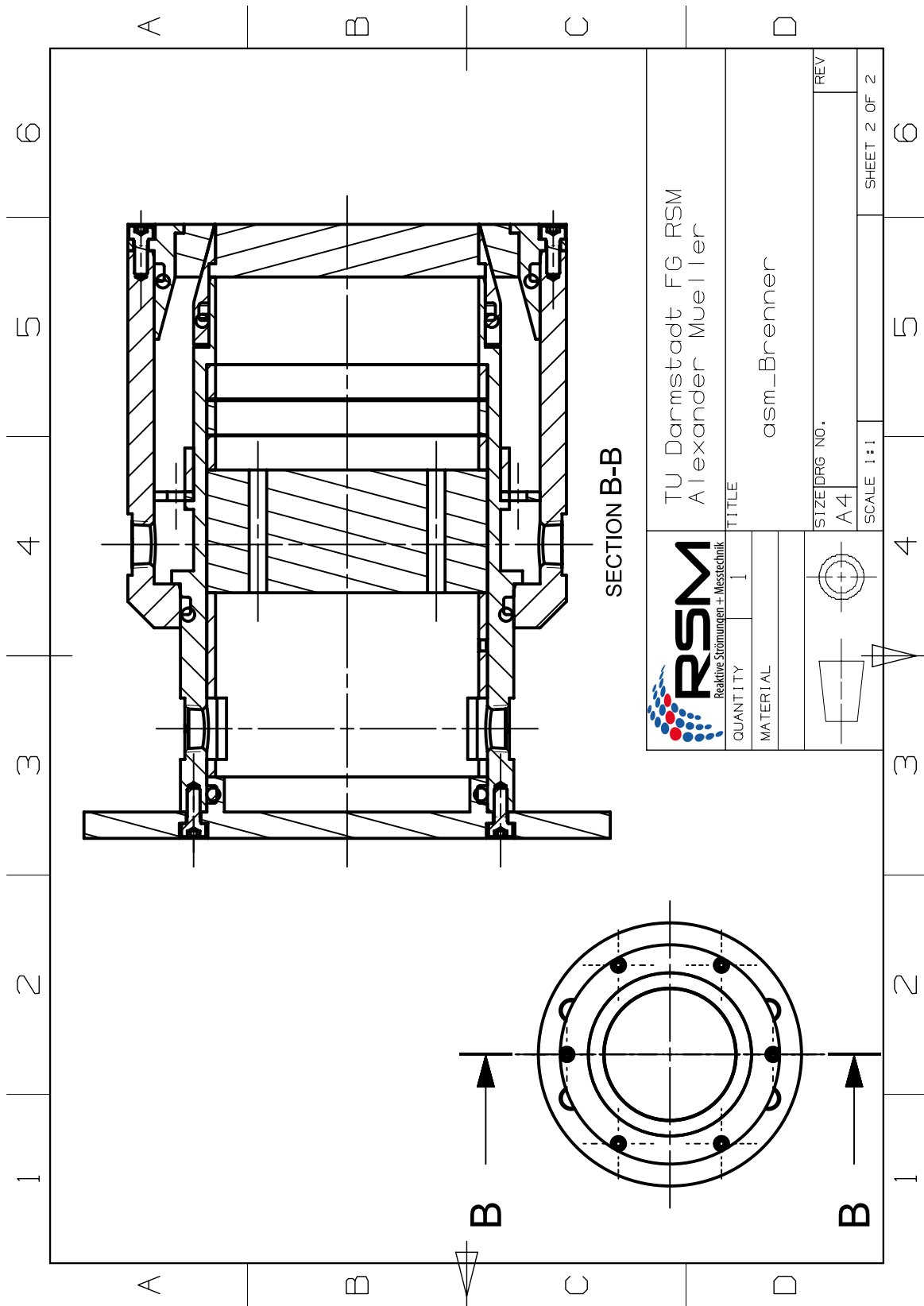
Figure C.2.: Technical drawing of the newly developed flat flame.

D. Permission by Journals and Co-authors to Reuse Articles for this Dissertation

D.1. Springer

I fully acknowledge the permission by Springer to reuse the article that I created with colleagues [141]. The title is: *Fuel effects in turbulent premixed pre-vaporized alcohol/air jet flames*

Information regarding the rights can be extracted from the publishers website: https://link.springer.com/article/10.1007/s10494-020-00166-6#rightslink, accessed on May 30th, 2023.

The relevant piece is the following: "Creative Commons. This is an open access article distributed under the terms of the Creative Commons CC BY license, which permits unrestricted use, distribution, and reproduction in any medium, provided the original work is properly cited. You are not required to obtain permission to reuse this article."

Furthermore, the co-authors have signed the following contribution declaration of the mentioned paper.

Declaration on the contribution to the scientific publication
Erklärung zum Eigenanteil der wissenschaftlichen Veröffentlichung
Ph.D. candidate, Johannes Trabold, M.Sc.

Co-Authors:	Sandra Hartl, Dr.-Ing.
	Steffen Walther, M.Sc.
	Ayane Johchi, Dr.-Ing.
	Andreas Dreizler, Prof. Dr. habil.
	Dirk Geyer, Prof. Dr.-Ing.

Scientific contribution of the Ph.D. candidate Johannes Trabold:

Installed the burner and pre-vaporization equipment with the support of Steffen Walther. Operated it during the OH-PLIF experiments.

Set up the OH-PLIF excitation and detection under the supervision of Ayane Johchi.

Calculated the alcohol/air mixtures' effective Lewis numbers numerically with the support of Sandra Hartl.

Wrote OH-PLIF evaluation code with the initial support of Ayane Johchi to retrieve a flame wrinkling merit, the flame surface density. Interpreted the results with the support of Andreas Dreizler and Dirk Geyer.

Designed the blow-off and flame length experiments in cooperation with Steffen Walther and Dirk Geyer. Wrote evaluation code for chemiluminescent images to retrieve flame lengths.

Numerically estimated the pilot flame's influence on extinction strain rates and thus blow-off with the support of Sandra Hartl. Calculated laminar burning velocities with the support of Sandra Hartl. Interpreted the flame length and blow-off results with the support of Andreas Dreizler and Dirk Geyer.
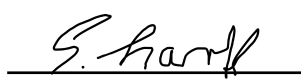
Analytically investigated and interpreted results regarding hydrodynamic instabilities.

Wrote the manuscript, took responsibility for correction and revision in the journal review process with the support of all other co-authors.

Entire contribution: The leading role in experiments, data analysis and writing of the manuscript.

All work was started and completed during the Ph.D. The publication is not the subject of any further ongoing or completed dissertation.

_____
(Johannes Trabold)

_____
(Sandra Hartl)

_____
(Steffen Walther)

_____
(Ayane Johchi)

_____
(Andreas Dreizler)

_____
(Dirk Geyer)

D.2. Elsevier

I fully acknowledge the permission by Elsevier to reuse the article that I created with colleagues [142]. The title is: *Fast shutter line-imaging system for dual-dispersion Raman spectroscopy in ethanol and OME flames*

Information regarding the rights can be extracted from the publishers website: https://www.elsevier.com/about/policies/copyright, accessed on May 30th, 2023.

The relevant piece is the following: "Authors can use their articles, in full or in part, for a wide range of scholarly, non-commercial purposes as outlined below: [...] Inclusion in a thesis or dissertation (provided that this is not to be published commercially). [...]"

Furthermore, the co-authors have signed the following contribution declaration of the mentioned paper.

Declaration on the contribution to the scientific publication

Erklärung zum Eigenanteil der wissenschaftlichen Veröffentlichung

Ph.D. candidate, Johannes Trabold, M.Sc.

Co-Authors:	David Butz, Dr.-Ing. Silvan Schneider, Dr.-Ing. Kevin Dieter, M.Eng. Robert Barlow, Phd. Andreas Dreizler, Prof. Dr.-Ing. habil. Dirk Geyer, Prof. Dr.-Ing.
Scientific contribution of the Ph.D. candidate Johannes Trabold:	Identified key intermediate species based upon numerical simulations.

Planned and performed all modifications to the existing Raman spectrometer test rig under supervision by Andreas Dreizler, Dirk Geyer, and Robert Barlow. The original system was planned and built by Silvan Schneider, David Butz, and Ph.D. candidate himself (during master thesis and the beginning of PhD), again under supervision of Andreas Dreizler, Dirk Geyer and Robert Barlow.

Studied optical spectrometer performance with the help of Silvan Schneider (during master thesis). This section is part of Silvan Schneider's completed dissertation and is referenced as such in the present work.

Selected spectral regions of interest with support of Kevin Dieter and Dirk Geyer.

Designed and built the laminar temperature-controlled opposed jet burner with the support of Dirk Geyer. Selected flame operating conditions and operated all systems during experiments.

Wrote code to process and display all data. Evaluated uncertainties and SNR.

Connected the experimental results with a strain-rate fitted numerical 1D simulation to gain more information (e.g. temperature, species, etc.).

Designed layout of all result graphs. Discussed them with Andreas Dreizler and Dirk Geyer.

Wrote the manuscript, took responsibility for correction and revision in the journal review process with the support of all other co-authors.

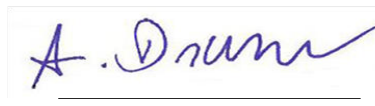**Entire contribution:**   The leading role in experiments, data analysis and writing of the manuscript.

Unless otherwise specified above, all work was started and completed during the Ph.D. and the publication contents are not the subject of any further ongoing or completed dissertation.
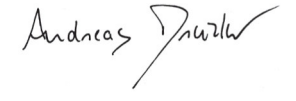
J. Trabold	*David Butz*	*S. Schneider*
(Johannes Trabold)	(David Butz)	(Silvan Schneider)

Kevin Dieter	*Robert Barlow*	*Andreas Dreizler*	*D. Geyer*
(Kevin Dieter)	(Robert Barlow)	(Andreas Dreizler)	(Dirk Geyer)

Bibliography

[1] R. Addabbo, J. K. Bechtold, and M. Matalon. Wrinkling of spherically expanding flames. *Proceedings of the Combustion Institute*, 29(2):1527–1535, 2002. ISSN 15407489. doi: 10.1016/S1540-7489(02)80187-0.

[2] A. K. Agarwal and H. Valera. *Greener and scalable e-fuels for decarbonization of transport*. Energy, environment, and sustainability. Springer, Singapore. ISBN 978-981-16-8344-2.

[3] H. Ajrouche, A. Lo, P. Vervisch, and A. Cessou. Assessment of a fast electro-optical shutter for 1D spontaneous Raman scattering in flames. *Measurement Science and Technology*, 26(7):075501, 2015. ISSN 0957-0233. doi: 10.1088/0957-0233/26/7/075501.

[4] A. Alqallaf, M. Klein, and N. Chakraborty. Effects of Lewis Number on the Evolution of Curvature in Spherically Expanding Turbulent Premixed Flames. *Fluids*, 4(1):12, 2019. doi: 10.3390/fluids4010012.

[5] S. Armbruster, S. F. Karnapp, C. Winter, L. Biesalski, and A. Keil. Advanced Design Project: Entwicklung eines schnellen mechanischen Verschlusses für das Raman-Rayleigh Spektrometer, RSM Institut, TU Darmstadt.

[6] R. S. Barlow. Laser diagnostics and their interplay with computations to understand turbulent combustion. *Proceedings of the Combustion Institute*, 31(1):49–75, 2007. ISSN 15407489. doi: 10.1016/j.proci.2006.08.122.

[7] R. S. Barlow and P. C. Miles. A shutter-based line-imaging system for single-shot raman scattering measurements of gradients in mixture fraction. *Proceedings of the Combustion Institute*, 28(1):269–277, 2000. ISSN 15407489. doi: 10.1016/S0082-0784(00)80220-9.

[8] R. S. Barlow, G.-H. Wang, P. Anselmo-Filho, M. S. Sweeney, and S. Hochgreb. Application of Raman/Rayleigh/LIF diagnostics in turbulent stratified flames. *Proceedings of the Combustion Institute*, 32(1): 945–953, 2009. ISSN 15407489. doi: 10.1016/j.proci.2008.06.070.

[9] R. S. Barlow, S. Meares, G. Magnotti, H. Cutcher, and A. R. Masri. Local extinction and near-field structure in piloted turbulent CH4/air jet flames with inhomogeneous inlets. *Combustion and Flame*, 162(10):3516–3540, 2015. ISSN 00102180. doi: 10.1016/j.combustflame.2015.06.009.

[10] R. S. Barlow, G. Magnotti, H. C. Cutcher, and A. R. Masri. On defining progress variable for Raman/Rayleigh experiments in partially-premixed methane flames. *Combustion and Flame*, 179:117–129, 2017. ISSN 00102180. doi: 10.1016/j.combustflame.2017.01.027.

[11] C. Becker. Erste Charakterisierung eines Versuchsbrenners für regenerative Brennstoffe mittels optischer und laserbasierter Lumineszenzmethoden, Masterthesis, Hoschschule Darmstadt, Maschinenbau und Kunststofftechnik.

[12] C. Becker and S. Rongstock. Chemilumineszenzmessungen der Flammen am Temperature Controlled Piloted Jet Burner (TCPJB), IFP Projekt, Hoschschule Darmstadt, Maschinenbau und Kunststofftechnik.

[13] J. H. Bell and R. D. Mehta. Contraction Design for Small Low-Speed Wind Tunnels. *Joint Institute for Aeronautics and Acoustics*, 1988. URL https://ntrs.nasa.gov/search.jsp?R=19890004382.

[14] J. M. Bergthorson, S. D. Salusbury, and P. E. Dimotakis. Experiments and modelling of premixed laminar stagnation flame hydrodynamics. *Journal of Fluid Mechanics*, 681:340–369, 2011. ISSN 0022-1120. doi: 10.1017/jfm.2011.203.

Bibliography

[15] R. W. Bilger, S. H. Starner, and R. J. Kee. On reduced mechanisms for methane-air combustion in nonpremixed flames. *Combustion and Flame*, 80(2):135–149, 1990. ISSN 00102180. doi: 10.1016/0010-2180(90)90122-8.

[16] D. Bok. Master thesis: Entwicklung, Aufbau und Inbetriebnahme der Erweiterung eines Transmissionsspektrometers, RSM Institut, TU Darmstadt.

[17] K. N. C. Bray. Studies of the Turbulent Burning Velocity. *Proceedings of the Royal Society A: Mathematical, Physical and Engineering Sciences*, 431(1882):315–335, 1990. ISSN 1364-5021. doi: 10.1098/rspa.1990.0133.

[18] A. Brockhinke, M. Letzgus, S. Rinne, and K. Kohse-Höinghaus. Energy transfer in the d3Pi(g)-a3Pi(u) (0-0) Swan bands of C2: implications for quantitative measurements. *The journal of physical chemistry. A*, 110(9): 3028–3035, 2006. doi: 10.1021/jp055553g.

[19] H. J. Burbano, J. Pareja, and A. A. Amell. Laminar burning velocities and flame stability analysis of H2/CO/air mixtures with dilution of N2 and CO2. *International Journal of Hydrogen Energy*, 36(4):3232–3242, 2011. ISSN 03603199. doi: 10.1016/j.ijhydene.2010.11.089.

[20] D. Butz. Experimentelle Untersuchung turbulenter regimeübergreifender Flammen. Dissertation, 2020.

[21] D. Butz, S. Hartl, S. Popp, S. Walther, R. S. Barlow, C. Hasse, A. Dreizler, and D. Geyer. Local flame structure analysis in turbulent CH4/air flames with multi-regime characteristics. *Combustion and Flame*, 210:426–438, 2019. ISSN 00102180. doi: 10.1016/j.combustflame.2019.08.032.

[22] L. Cai, S. Jacobs, R. Langer, F. vom Lehn, K. A. Heufer, and H. Pitsch. Auto-ignition of oxymethylene ethers (OMEn, n = 2–4) as promising synthetic e-fuels from renewable electricity: shock tube experiments and automatic mechanism generation. *Fuel*, 264:116711, 2020. ISSN 00162361. doi: 10.1016/j.fuel.2019.116711.

[23] F. Carbone, J. L. Smolke, A. M. Fincham, and F. N. Egolfopoulos. Comparative behavior of piloted turbulent premixed jet flames of C1-C8 hydrocarbons. *Combustion and Flame*, 180:88–101, 2017. ISSN 00102180. doi: 10.1016/j.combustflame.2017.02.030.

[24] A. Cessou, F. Guichard, H. Ajrouche, and A. Lo. 1D single-shot thermography by Spontaneous Raman Scattering in turbulent, spray or oxyfuel flames. In *Imaging and Applied Optics 2018 (3D, AO, AIO, COSI, DH, IS, LACSEA, LS&C, MATH, pcAOP)*, page LTu2C.1, Washington, D.C. OSA. ISBN 978-1-943580-44-6. doi: 10.1364/LACSEA.2018.LTu2C.1.

[25] Y.-C. Chen and M. S. Mansour. Measurements of Scalar Dissipation in Turbulent Hydrogen Diffusion Flames and Some Implications on Combustion Modeling. *Combustion Science and Technology*, 126(1-6):291–313, 1997. ISSN 0010-2202. doi: 10.1080/00102209708935678.

[26] P. Clavin and F. A. Williams. Effects of molecular diffusion and of thermal expansion on the structure and dynamics of premixed flames in turbulent flows of large scale and low intensity. *Journal of Fluid Mechanics*, 116:251–282, 1982. ISSN 0022-1120. doi: 10.1017/S0022112082000457.

[27] B. Coriton, S.-K. Im, M. Gamba, and J. H. Frank. Flow Field and Scalar Measurements in a Series of Turbulent Partially-Premixed Dimethyl Ether/Air Jet Flames. *Combustion and Flame*, 180:40–52, 2017. ISSN 00102180. doi: 10.1016/j.combustflame.2017.02.014.

[28] F. Creta, R. Lamioni, P. E. Lapenna, and G. Troiani. Interplay of Darrieus-Landau instability and weak turbulence in premixed flame propagation. *Physical review. E*, 94(5-1):053102, 2016. doi: 10.1103/PhysRevE.94.053102.

[29] H. C. Cutcher, R. S. Barlow, G. Magnotti, and A. R. Masri. Turbulent flames with compositionally inhomogeneous inlets: Resolved measurements of scalar dissipation rates. *Proceedings of the Combustion Institute*, 36(2):1737–1745, 2017. ISSN 15407489. doi: 10.1016/j.proci.2016.07.093.

[30] K. Dabov, A. Foi, V. Katkovnik, and K. Egiazarian. Image denoising with block-matching and 3D filtering. In E. R. Dougherty, J. T. Astola, K. O. Egiazarian, N. M. Nasrabadi, and S. A. Rizvi, editors, *Image Processing: Algorithms and Systems, Neural Networks, and Machine Learning*, SPIE Proceedings, page 606414. SPIE, 2006. doi: 10.1117/12.643267.

220

[31] R. W. Dibble, W. Kollmann, and R. W. Schefer. Conserved scalar fluxes measured in a turbulent nonpremixed flame by combined laser Doppler velocimetry and laser Raman scattering. *Combustion and Flame*, 55(3):307–321, 1984. ISSN 00102180. doi: 10.1016/0010-2180(84)90170-6.

[32] R. W. Dibble, A. R. Masri, and R. W. Bilger. The spontaneous raman scattering technique applied to nonpremixed flames of methane. *Combustion and Flame*, 67(3):189–206, 1987. ISSN 00102180. doi: 10.1016/0010-2180(87)90095-2.

[33] K. Dieter, K. Koschnick, J. Lill, G. Magnotti, A. Weinmann, A. Dreizler, and D. Geyer. Development of a Raman spectrometer for the characterization of gaseous hydrocarbons at high temperatures. *Journal of Quantitative Spectroscopy and Radiative Transfer*, 277:107978, 2022. ISSN 00224073. doi: 10.1016/j.jqsrt.2021.107978.

[34] K. Dieter, M. Richter, J. Trabold, K. Koschnick, F. Schael, A. Dreizler, and D. Geyer. Temperature dependent Raman spectra of pure, gaseous formaldehyde for combustion diagnostics. *Proceedings of the Combustion Institute*, 2022. ISSN 15407489. doi: 10.1016/j.proci.2022.08.049.

[35] N. Docquier, S. Belhalfaoui, F. Lacas, N. Darabiha, and C. Rolon. Experimental and numerical study of chemiluminescence in methane/air high-pressure flames for active control applications. *Proceedings of the Combustion Institute*, 28(2):1765–1774, 2000. ISSN 15407489. doi: 10.1016/S0082-0784(00)80578-0.

[36] J. M. Donbar, J. F. Driscoll, and C. D. Carter. Reaction zone structure in turbulent nonpremixed jet flames—from CH-OH PLIF images. *Combustion and Flame*, 122(1-2):1–19, 2000. ISSN 00102180. doi: 10.1016/S0010-2180(00)00098-5.

[37] J. F. Driscoll. Turbulent premixed combustion: Flamelet structure and its effect on turbulent burning velocities. *Progress in Energy and Combustion Science*, (34):91–134, 2008. ISSN 03601285.

[38] M. J. Dunn and R. S. Barlow. Effects of preferential transport and strain in bluff body stabilized lean and rich premixed CH4/air flames. *Proceedings of the Combustion Institute*, 34(1):1411–1419, 2013. ISSN 15407489. doi: 10.1016/j.proci.2012.06.070.

[39] M. J. Dunn, A. R. Masri, and R. W. Bilger. A new piloted premixed jet burner to study strong finite-rate chemistry effects. *Combustion and Flame*, 151(1-2):46–60, 2007. ISSN 00102180. doi: 10.1016/j.combustflame.2007.05.010.

[40] M. J. Dunn, A. Macfarlane, R. S. Barlow, D. Geyer, K. Dieter, and A. R. Masri. Spontaneous Raman–LIF–CO–OH measurements of species concentration in turbulent spray flames. *Proceedings of the Combustion Institute*, 38 (1):1779–1786, 2021. ISSN 15407489. doi: 10.1016/j.proci.2020.07.037.

[41] P. Durdevic. Entwicklung einer Traversierung und Untersuchung der Flammen erneuerbarer Brennstoe, Masterthesis, Hoschschule Darmstadt, Maschinenbau und Kunststofftechnik, .

[42] P. Durdevic. Implementierung einer Temperatursteuerungseinheit in LabVIEW und erste experimentelle Untersuchungen eines laminaren Gegenstrombrenners, IFWP Projekt, Hoschschule Darmstadt, Maschinenbau und Kunststofftechnik, .

[43] P. Durdevic. Konstruktion, Aufbau und Inbetriebnahme einer Temperatursteuerungseinheit für einen laminaren Gegenstrmobrenner, IFP Projekt, Hoschschule Darmstadt, Maschinenbau und Kunststofftechnik, .

[44] A. C. Eckbreth. *Laser diagnostics for combustion temperature and species*, volume 3 of *Combustion science and technology book series*. Taylor and Francis, New York, 1996. ISBN 9789056995324.

[45] F. N. Egolfopoulos and C. K. Law. Chain mechanisms in the overall reaction orders in laminar flame propagation. *Combustion and Flame*, 80(1):7–16, 1990. ISSN 00102180. doi: 10.1016/0010-2180(90)90049-W.

[46] F. Eitel, J. Pareja, A. Johchi, B. Böhm, D. Geyer, and A. Dreizler. Temporal evolution of auto-ignition of ethylene and methane jets propagating into a turbulent hot air co-flow vitiated with NO x. *Combustion and Flame*, 177: 193–206, 2017. ISSN 00102180. doi: 10.1016/j.combustflame.2016.12.009.

[47] I. Ekoto and R. Barlow. Development of a Raman spectroscopy technique to detect alternate transportation fuel hydrocarbon intermediates in complex combustion environments.

[48] A. Z. Farida, K. Kumaran, U. S. Shet, and T. Sundararajan. Stability of Partially Premixed Tubular Burner Flames with Co-Flow and External Swirl-Air. *5th Asia-Pacific Conference on Combustion*, 2005.

[49] S. A. Filatyev, J. F. Driscoll, C. D. Carter, and J. M. Donbar. Measured properties of turbulent premixed flames for model assessment, including burning velocities, stretch rates, and surface densities. *Combustion and Flame*, 141(1-2):1–21, 2005. ISSN 00102180. doi: 10.1016/j.combustflame.2004.07.010.

[50] D. Fischer and T. Förster. Konstruktion eines CoFlows für das Brennlabor der h_da, IFP Projekt, Hoschschule Darmstadt, Maschinenbau und Kunststofftechnik.

[51] A. Frassoldati, R. Grana, T. Faravelli, E. Ranzi, P. Oßwald, and K. Kohse-Höinghaus. Detailed kinetic modeling of the combustion of the four butanol isomers in premixed low-pressure flames. *Combustion and Flame*, 159 (7):2295–2311, 2012. ISSN 00102180. doi: 10.1016/j.combustflame.2012.03.002.

[52] F. Fuest. *1D Raman/Rayleigh-scattering and CO-LIF measurements in laminar and turbulent jet flames of dimethyl ether using a hybrid data reduction strategy: Dissertation*. Darmstadt, 2011. URL http://tuprints.ulb.tu-darmstadt.de/2773/.

[53] F. Fuest, R. S. Barlow, D. Geyer, F. Seffrin, and A. Dreizler. A hybrid method for data evaluation in 1-D Raman spectroscopy. *Proceedings of the Combustion Institute*, 33(1):815–822, 2011. ISSN 15407489. doi: 10.1016/j.proci.2010.06.064.

[54] F. Fuest, R. S. Barlow, J.-Y. Chen, and A. Dreizler. Raman/Rayleigh scattering and CO-LIF measurements in laminar and turbulent jet flames of dimethyl ether. *Combustion and Flame*, 159(8):2533–2562, 2012. ISSN 00102180. doi: 10.1016/j.combustflame.2011.11.001.

[55] F. Fuest, R. Barlow, A. Dreizler, and J. Sutton. Towards quantitative concentration measurement of acetylene in rich hydrocarbon flames using 1D Raman/Rayleigh scattering. In *51st AIAA Aerospace Sciences Meeting including the New Horizons Forum and Aerospace Exposition*, Reston, Virigina, 2013. American Institute of Aeronautics and Astronautics. ISBN 978-1-62410-181-6. doi: 10.2514/6.2013-558.

[56] F. Fuest, R. S. Barlow, G. Magnotti, A. Dreizler, I. W. Ekoto, and J. A. Sutton. Quantitative acetylene measurements in laminar and turbulent flames using 1D Raman/Rayleigh scattering. *Combustion and Flame*, 162(5): 2248–2255, 2015. ISSN 00102180. doi: 10.1016/j.combustflame.2015.01.021.

[57] D. Geyer, A. Kempf, A. Dreizler, and J. Janicka. Scalar dissipation rates in isothermal and reactive turbulent opposed-jets: 1-D-Raman/Rayleigh experiments supported by LES. *Proceedings of the Combustion Institute*, 30 (1):681–689, 2005. ISSN 15407489. doi: 10.1016/j.proci.2004.08.216.

[58] D. G. Goodwin, H. K. Moffat, I. Schoegl, R. L. Speth, and B. W. Weber. Cantera: An Object-oriented Software Toolkit for Chemical Kinetics, Thermodynamics, and Transport Processes, 2022.

[59] M. A. Gregor, F. Seffrin, F. Fuest, D. Geyer, and A. Dreizler. Multi-scalar measurements in a premixed swirl burner using 1D Raman/Rayleigh scattering. *Proceedings of the Combustion Institute*, 32(2):1739–1746, 2009. ISSN 15407489. doi: 10.1016/j.proci.2008.06.133.

[60] T. F. Guiberti, H. Cutcher, W. L. Roberts, and A. R. Masri. Influence of Pilot Flame Parameters on the Stability of Turbulent Jet Flames. *Energy & Fuels*, 31(3):2128–2137, 2017. ISSN 0887-0624. doi: 10.1021/acs.energyfuels.6b02052.

[61] T. F. Guiberti, M. Juddoo, D. A. Lacoste, M. J. Dunn, W. L. Roberts, and A. R. Masri. Fuel effects on the stability of turbulent flames with compositionally inhomogeneous inlets. *Proceedings of the Combustion Institute*, 36(2): 1777–1784, 2017. ISSN 15407489. doi: 10.1016/j.proci.2016.08.051.

[62] T. F. Guiberti, Y. Krishna, W. R. Boyette, C. Yang, W. L. Roberts, and G. Magnotti. Single-shot imaging of major species and OH mole fractions and temperature in non-premixed H2/N2 flames at elevated pressure. *Proceedings of the Combustion Institute*, 2020. ISSN 15407489. doi: 10.1016/j.proci.2020.06.252.

[63] Ö. L. Gülder and G. J. Smallwood. Flame surface densitites in premixed combustion at medium to high turbulence intensities. *Combustion Science and Technology*, (179):191–206, 2007. ISSN 0010-2202.

[64] R. K. Hanson, R. M. Spearrin, and C. S. Goldenstein. *Spectroscopy and Optical Diagnostics for Gases*. Springer International Publishing, Cham, 2016. ISBN 978-3-319-23251-5. doi: 10.1007/978-3-319-23252-2.

[65] S. Hartl, D. Geyer, A. Dreizler, G. Magnotti, R. S. Barlow, and C. Hasse. Regime identification from Raman/Rayleigh line measurements in partially premixed flames. *Combustion and Flame*, 189:126–141, 2018. ISSN 00102180. doi: 10.1016/j.combustflame.2017.10.024.

[66] D. Heilbronn. Development and design of a pressurized calibration flame at the EKT/RSM single sector combustor: Master thesis.

[67] G. Jomaas, C. K. Law, and J. K. Bechtold. On transition to cellularity in expanding spherical flames. *Journal of Fluid Mechanics*, 583:1–26, 2007. ISSN 0022-1120. doi: 10.1017/S0022112007005885.

[68] F. Joos. *Technische Verbrennung: Verbrennungstechnik, Verbrennungsmodellierung, Emissionen*. Springer, Berlin [u.a.], [online-ausg.] edition, 2006. ISBN 3-540-34333-4.

[69] G. Joulin and T. Mitani. Linear stability analysis of two-reactant flames. *Combustion and Flame*, 40:235–246, 1981. ISSN 00102180. doi: 10.1016/0010-2180(81)90127-9.

[70] M. M. Kamal, R. S. Barlow, and S. Hochgreb. Conditional analysis of turbulent premixed and stratified flames on local equivalence ratio and progress of reaction. *Combustion and Flame*, 162(10):3896–3913, 2015. ISSN 00102180. doi: 10.1016/j.combustflame.2015.07.026.

[71] M.-r. Kang, H.-y. Song, F.-x. Jin, and J. Chen. Synthesis and physicochemical characterization of polyoxymethylene dimethyl ethers. *Journal of Fuel Chemistry and Technology*, 45(7):837–845, 2017. ISSN 18725813. doi: 10.1016/S1872-5813(17)30040-3.

[72] A. N. Karpetis and R. S. Barlow. Measurements of scalar dissipation in a turbulent piloted methane/air jet flame. *Proceedings of the Combustion Institute*, 29(2):1929–1936, 2002. ISSN 15407489. doi: 10.1016/S1540-7489(02)80234-6.

[73] M. Klein, H. Nachtigal, M. Hansinger, M. Pfitzner, and N. Chakraborty. Flame Curvature Distribution in High Pressure Turbulent Bunsen Premixed Flames. *Flow, Turbulence and Combustion*, 101(4):1173–1187, 2018. ISSN 1386-6184. doi: 10.1007/s10494-018-9951-1.

[74] J. Kojima and Q.-V. Nguyen. Measurement and simulation of spontaneous Raman scattering in high-pressure fuel-rich H 2 –air flames. *Measurement Science and Technology*, 15(3):565–580, 2004. ISSN 0957-0233. doi: 10.1088/0957-0233/15/3/009.

[75] J. Kojima, Y. Ikeda, and T. Nakajima. Spatially resolved measurement of OH*, CH*, and C2* chemiluminescence in the reaction zone of laminar methane/air premixed flames. *Proceedings of the Combustion Institute*, 28(2):1757–1764, 2000. ISSN 15407489. doi: 10.1016/S0082-0784(00)80577-9.

[76] K. Koschnick. Detektion temperaturabhängiger Raman-Spektren von intermediären Spezies bei der Ethanol-Verbrennung.

[77] K. Koschnick and D. Hutcheson. Konstruktion eines laminaren Gegenstrombrenners für die Kalibrierung eines Raman-Rayleigh-Spektroskops, IFP Projekt, Hoschschule Darmstadt, Maschinenbau und Kunststofftechnik, .

[78] K. Koschnick and D. Hutcheson. Montage und Inbetriebnahme eines laminaren Gegenstrombrenners, IFWP Projekt, Hoschschule Darmstadt, Maschinenbau und Kunststofftechnik, .

[79] G. Kuenne, F. Seffrin, F. Fuest, T. Stahler, A. Ketelheun, D. Geyer, J. Janicka, and A. Dreizler. Experimental and numerical analysis of a lean premixed stratified burner using 1D Raman/Rayleigh scattering and large eddy simulation. *Combustion and Flame*, 159(8):2669–2689, 2012. ISSN 00102180. doi: 10.1016/j.combustflame.2012.02.010.

[80] J. C. Lagarias, J. A. Reeds, M. H. Wright, and P. E. Wright. Convergence Properties of the Nelder–Mead Simplex Method in Low Dimensions. *SIAM Journal on Optimization*, 9(1):112–147, 1998. ISSN 1052-6234. doi: 10.1137/S1052623496303470.

[81] R. Lamioni, P. E. Lapenna, G. Troiani, and F. Creta. Flame Induced Flow Features in the Presence of Darrieus-Landau Instability. *Flow, Turbulence and Combustion*, 101(4):1137–1155, 2018. ISSN 1386-6184. doi: 10.1007/s10494-018-9936-0.

[82] C. Law and C. Sung. Structure, aerodynamics, and geometry of premixed flamelets. *Progress in Energy and Combustion Science*, 26(4-6):459–505, 2000. ISSN 03601285. doi: 10.1016/S0360-1285(00)00018-6.

[83] C. K. Law. *Combustion physics*. Cambridge University Press, Cambridge, 1. paperback ed. edition, 2010. ISBN 9780521154215.

[84] G. G. Lee, K. Y. Huh, and H. Kobayashi. Measurement and analysis of flame surface density for turbulent premixed combustion on a nozzle-type burner. *Combustion and Flame*, 122(1-2):43–57, 2000. ISSN 00102180. doi: 10.1016/S0010-2180(00)00102-4.

[85] B. Lewis and Guenther von Elbe. *Combustion, Flames and Explosions of Gases: Third Edition*. Academic Press, Inc., 1987.

[86] J. Li, Z. Zhao, A. Kazakov, M. Chaos, F. L. Dryer, and J. J. Scire. A comprehensive kinetic mechanism for CO, CH 2 O, and CH 3 OH combustion. *International Journal of Chemical Kinetics*, 39(3):109–136, 2007. ISSN 05388066. doi: 10.1002/kin.20218.

[87] G. Magnotti and R. S. Barlow. Effects of high shear on the structure and thickness of turbulent premixed methane/air flames stabilized on a bluff-body burner. *Combustion and Flame*, 162(1):100–114, 2015. ISSN 00102180. doi: 10.1016/j.combustflame.2014.06.015.

[88] G. Magnotti and R. S. Barlow. Dual-resolution Raman spectroscopy for measurements of temperature and twelve species in hydrocarbon–air flames. *Proceedings of the Combustion Institute*, 36(3):4477–4485, 2017. ISSN 15407489. doi: 10.1016/j.proci.2016.06.128.

[89] G. Magnotti, D. Geyer, and R. S. Barlow. Interference free spontaneous Raman spectroscopy for measurements in rich hydrocarbon flames. *Proceedings of the Combustion Institute*, 35(3):3765–3772, 2015. ISSN 15407489. doi: 10.1016/j.proci.2014.05.076.

[90] G. Magnotti, U. KC, P. L. Varghese, and R. S. Barlow. Raman spectra of methane, ethylene, ethane, dimethyl ether, formaldehyde and propane for combustion applications. *Journal of Quantitative Spectroscopy and Radiative Transfer*, 163:80–101, 2015. ISSN 00224073. doi: 10.1016/j.jqsrt.2015.04.018.

[91] A. R. Masri, R. W. Dibble, and R. S. Barlow. The structure of turbulent nonpremixed flames revealed by Raman-Rayleigh-LIF measurements. *Progress in Energy and Combustion Science*, 22(4):307–362, 1996. ISSN 03601285. doi: 10.1016/S0360-1285(96)00009-3.

[92] M. Matalon. The Darrieus–Landau instability of premixed flames. *Fluid Dynamics Research*, 50(5):051412, 2018. doi: 10.1088/1873-7005/aab510.

[93] M. Matalon and B. J. Matkowsky. Flames as gasdynamic discontinuities. *Journal of Fluid Mechanics*, 124(-1):239, 1982. ISSN 0022-1120. doi: 10.1017/S0022112082002481.

[94] H. D. Matthews and K. Caldeira. Stabilizing climate requires near-zero emissions. *Geophysical Research Letters*, 35(4), 2008. ISSN 0094-8276. doi: 10.1029/2007GL032388.

[95] R. L. McCreery. *Raman Spectroscopy for Chemical Analysis*. John Wiley & Sons, Inc, Hoboken, NJ, USA, 2000. ISBN 9780471721642. doi: 10.1002/0471721646.

[96] S. Meares, V. N. Prasad, G. Magnotti, R. S. Barlow, and A. R. Masri. Stabilization of piloted turbulent flames with inhomogeneous inlets. *Proceedings of the Combustion Institute*, 35(2):1477–1484, 2015. ISSN 15407489. doi: 10.1016/j.proci.2014.05.071.

[97] W. Meier and O. Keck. Laser Raman scattering in fuel-rich flames: background levels at different excitation wavelengths. *Measurement Science and Technology*, 13(5):741–749, 2002. ISSN 0957-0233. doi: 10.1088/0957-0233/13/5/312.

[98] K. Menger. Charakterisierung zweier Gasprüfstände, Masterthesis, Hoschschule Darmstadt, Maschinenbau und Kunststofftechnik.

[99] P. C. Miles and R. S. Barlow. A fast mechanical shutter for spectroscopic applications. *Measurement Science and Technology*, 11(4):392–397, 2000. ISSN 0957-0233. doi: 10.1088/0957-0233/11/4/308.

[100] T. Morel. Comprehensive Design of Axisymmetric Wind Tunnel Contractions. *Journal of Fluids Engineering*, 97 (2):225–233, 1975. ISSN 0098-2202. doi: 10.1115/1.3447255.

[101] D. W. Naegeli and W. D. Weatherford. Practical ignition limits for low molecular weight alcohols. *Fuel*, 68(1): 45–48, 1989. ISSN 00162361. doi: 10.1016/0016-2361(89)90009-4.

[102] S. P. Nandula, T. M. Brown, and R. W. Pitz. Measurements of scalar dissipation in the reaction zones of turbulent nonpremixed H2-air flames. *Combustion and Flame*, 99(3-4):775–783, 1994. ISSN 00102180. doi: 10.1016/0010-2180(94)90073-6.

[103] A. Nauert. *Laseroptische Untersuchungen an verdrallten Vormischflammen: Fortschritt-Berichte VDI Reihe 6, Energietechnik*, volume 585. VDI-Verl., Düsseldorf, 2009. ISBN 978-3-18-358506-9.

[104] P. A. Nooren, M. Versluis, T. H. van der Meer, R. S. Barlow, and J. H. Frank. Raman-Rayleigh-LIF measurements of temperature and species concentrations in the Delft piloted turbulent jet diffusion flame. *Applied Physics B*, 71(1):95–111, 2000. ISSN 0946-2171. doi: 10.1007/s003400000278.

[105] C. Olm, T. Varga, É. Valkó, S. Hartl, C. Hasse, and T. Turányi. Development of an Ethanol Combustion Mechanism Based on a Hierarchical Optimization Approach. *International Journal of Chemical Kinetics*, 48(8):423–441, 2016. ISSN 05388066. doi: 10.1002/kin.20998.

[106] E. S. Oran. A tribute to Dr. George H. Markstein (1911–2011). *Combustion and Flame*, 162(1):1–2, 2015. ISSN 00102180. doi: 10.1016/j.combustflame.2014.07.005.

[107] G. Paczko, P. M. Lefdal, and N. Peters. Reduced reaction schemes for methane, methanol and propane flames. *Symposium (International) on Combustion*, 21(1):739–748, 1988. doi: 10.1016/S0082-0784(88)80306-0.

[108] J. Pareja, H. J. Burbano, A. Amell, and J. Carvajal. Laminar burning velocities and flame stability analysis of hydrogen/air premixed flames at low pressure. *International Journal of Hydrogen Energy*, 36(10):6317–6324, 2011. ISSN 03603199. doi: 10.1016/j.ijhydene.2011.02.042.

[109] N. Peters. Fifteen Lectures on Laminar and Turbulent Combustion: Ercoftac Summer School Aachen, .

[110] N. Peters. Combustion Theory: CEFRC Summer School Princeton, .

[111] N. Peters. A spectral closure for premixed turbulent combustion in the flamelet regime. *Journal of Fluid Mechanics*, 242:611–629, 1992. ISSN 0022-1120. doi: 10.1017/S0022112092002519.

[112] D. V. Petrov. Raman Spectrum of Methane in the Range 20–40oC. *Journal of Applied Spectroscopy*, 84(3): 420–424, 2017. ISSN 0021-9037. doi: 10.1007/s10812-017-0486-3.

[113] T. Poinsot and D. Veynante. *Theoretical and numerical combustion*. The authors, Toulouse Cedex, 3rd ed. edition, 2012. ISBN 978-2-7466-3990-4.

Bibliography

[114] S. B. Pope. *Turbulent flows*. Cambridge University Press, Cambridge and New York, 2000. ISBN 9780521598866.

[115] S. Popp, F. Hunger, S. Hartl, D. Messig, B. Coriton, J. H. Frank, F. Fuest, and C. Hasse. LES flamelet-progress variable modeling and measurements of a turbulent partially-premixed dimethyl ether jet flame. *Combustion and Flame*, 162(8):3016–3029, 2015. ISSN 00102180. doi: 10.1016/j.combustflame.2015.05.004.

[116] P.R. Shukla, J. Skea, R. Slade, A. Al Khourdajie, R. van Diemen, D. McCollum, M. Pathak, S. Some, P. Vyas, R. Fradera, M. Belkacemi, A. Hasija, G. Lisboa, S. Luz, J. Malley,. IPCC, 2022: Climate Change 2022: Mitigation of Climate Change. Contribution of Working Group III to the Sixth Assessment Report of the Intergovernmental Panel on Climate Change. URL https://www.ipcc.ch/report/ar6/wg3/about/how-to-cite-this-report/.

[117] G. Pretzier. A New Method for Numerical Abel-Inversion. *Zeitschrift für Naturforschung A*, 46(7):639–641, 1991. ISSN 0932-0784. doi: 10.1515/zna-1991-0715.

[118] J. Rogelj, M. Schaeffer, M. Meinshausen, R. Knutti, J. Alcamo, K. Riahi, and W. Hare. Zero emission targets as long-term global goals for climate protection. *Environmental Research Letters*, 10(10):105007, 2015. doi: 10.1088/1748-9326/10/10/105007.

[119] J. C. Rolon, D. Veynante, J. P. Martin, and F. Durst. Counter jet stagnation flows. *Experiments in Fluids*, 11(5):313–324, 1991. ISSN 0723-4864. doi: 10.1007/BF00194863.

[120] R. Sadanandan, M. Stöhr, and W. Meier. Simultaneous OH-PLIF and PIV measurements in a gas turbine model combustor. *Applied Physics B*, 90(3-4):609–618, 2008. ISSN 0946-2171. doi: 10.1007/s00340-007-2928-8.

[121] J. M. Samaniego, F. N. Egolfopoulos, and C. T. Bowman. CO2* Chemiluminescence in Premixed Flames. *Combustion Science and Technology*, 109(1-6):183–203, 1995. ISSN 0010-2202. doi: 10.1080/00102209508951901.

[122] B. G. Sarnacki, G. Esposito, R. H. Krauss, and H. K. Chelliah. Extinction limits and associated uncertainties of nonpremixed counterflow flames of methane, ethylene, propylene and n-butane in air. *Combustion and Flame*, 159(3):1026–1043, 2012. ISSN 00102180. doi: 10.1016/j.combustflame.2011.09.007.

[123] S. Schneider. Auswirkungen der Wasserstoff-Zumischung auf die Flammenstruktur turbulenter stratifizierter Methan-Luft-Flammen, 2017. URL http://tuprints.ulb.tu-darmstadt.de/6977/.

[124] S. Schneider, D. Geyer, G. Magnotti, M. J. Dunn, R. S. Barlow, and A. Dreizler. Structure of a stratified CH4 flame with H2 addition. *Proceedings of the Combustion Institute*, 37(2):2307–2315, 2019. ISSN 15407489. doi: 10.1016/j.proci.2018.06.205.

[125] F. Seffrin. *Geschwindigkeits- und Skalarfeld-Charakterisierung turbulenter stratifizierter Vormischflammen*. Cuvillier, Göttingen, 1. aufl. edition, 2011. ISBN 9783869556499.

[126] I. G. Shepherd. Flame surface density and burning rate in premixed turbulent flames. *Symposium (International) on Combustion*, 26(1):373–379, 1996. doi: 10.1016/S0082-0784(96)80238-4.

[127] T. Shimanouchi. *Tables of molecular vibrational frequencies. Consolidated vol. 1*. NSRDS, Washington DC, USA, nsrds-nbs 39 edition, 1972.

[128] G. I. Sivashinsky. Instabilities, Pattern Formation, and Turbulence in Flames. *Annual Review of Fluid Mechanics*, 15(1):179–199, 1983. ISSN 0066-4189. doi: 10.1146/annurev.fl.15.010183.001143.

[129] G. Smith, T. Bowman, and M. Frenklach. GRI30. URL http://combustion.berkeley.edu/gri-mech/.

[130] J. Smolke, S. Lapointe, L. Paxton, G. Blanquart, F. Carbone, A. M. Fincham, and F. N. Egolfopoulos. Experimental and numerical studies of fuel and hydrodynamic effects on piloted turbulent premixed jet flames. *Proceedings of the Combustion Institute*, 36(2):1877–1884, 2017. ISSN 15407489. doi: 10.1016/j.proci.2016.07.127.

[131] S. H. Sohrab, Z. Y. Ye, and C. K. Law. An experimental investigation on flame interaction and the existence of negative flame speeds. *Symposium (International) on Combustion*, 20(1):1957–1965, 1985. doi: 10.1016/S0082-0784(85)80695-0.

[132] T. Stahler, D. Geyer, G. Magnotti, P. Trunk, M. J. Dunn, R. S. Barlow, and A. Dreizler. Multiple conditioned analysis of the turbulent stratified flame A. *Proceedings of the Combustion Institute*, 36(2):1947–1955, 2017. ISSN 15407489. doi: 10.1016/j.proci.2016.08.070.

[133] D. Steinsberger and K. Luley. Aufbau und Inbetriebnahme eines temperierten Brenners für vorverdampfte Brennstoffe, IFP Projekt, Hoschschule Darmstadt, Maschinenbau und Kunststofftechnik.

[134] S. H. Strner, R. W. Bilger, R. W. Dibble, and R. S. Barlow. Some raman/rayleigh/lif measurements in turbulent propane flames. *Symposium (International) on Combustion*, 23(1):645–651, 1991. doi: 10.1016/S0082-0784(06)80312-7.

[135] W. Sun, G. Wang, S. Li, R. Zhang, B. Yang, J. Yang, Y. Li, C. K. Westbrook, and C. K. Law. Speciation and the laminar burning velocities of poly(oxymethylene) dimethyl ether 3 (POMDME3) flames: An experimental and modeling study. *Proceedings of the Combustion Institute*, 36(1):1269–1278, 2017. ISSN 15407489. doi: 10.1016/j.proci.2016.05.058.

[136] M. S. Sweeney, S. Hochgreb, M. J. Dunn, and R. S. Barlow. A comparative analysis of flame surface density metrics inpremixed and stratified flames. *Proceedings of the Combustion Institute*, 33(1):1419–1427, 2011. ISSN 15407489. doi: 10.1016/j.proci.2010.05.069.

[137] M. S. Sweeney, S. Hochgreb, M. J. Dunn, and R. S. Barlow. The structure of turbulent stratified and premixed methane/air flames I: Non-swirling flows. *Combustion and Flame*, 159(9):2896–2911, 2012. ISSN 00102180. doi: 10.1016/j.combustflame.2012.06.001.

[138] M. S. Sweeney, S. Hochgreb, M. J. Dunn, and R. S. Barlow. The structure of turbulent stratified and premixed methane/air flames II: Swirling flows. *Combustion and Flame*, 159(9):2912–2929, 2012. ISSN 00102180. doi: 10.1016/j.combustflame.2012.05.014.

[139] P. Tamadonfar and Ö. L. Gülder. Flame brush characteristics and burning velocities of premixed turbulent methane/air Bunsen flames. *Combustion and Flame*, 161(12):3154–3165, 2014. ISSN 00102180. doi: 10.1016/j.combustflame.2014.06.014.

[140] P. Tamadonfar and Ö. L. Gülder. Effects of mixture composition and turbulence intensity on flame front structure and burning velocities of premixed turbulent hydrocarbon/air Bunsen flames. *Combustion and Flame*, 162(12):4417–4441, 2015. ISSN 00102180. doi: 10.1016/j.combustflame.2015.08.009.

[141] J. Trabold, S. Hartl, S. Walther, A. Johchi, A. Dreizler, and D. Geyer. Fuel Effects in Turbulent Premixed Prevaporised Alcohol/Air Jet Flames. *Flow, Turbulence and Combustion*, 106(2):547–573, 2021. ISSN 1386-6184. doi: 10.1007/s10494-020-00166-6.

[142] J. Trabold, D. Butz, S. Schneider, K. Dieter, R. Barlow, A. Dreizler, and D. Geyer. Fast shutter line-imaging system for dual-dispersion Raman spectroscopy in ethanol and OME flames. *Combustion and Flame*, page 111864, 2022. ISSN 00102180. doi: 10.1016/j.combustflame.2021.111864.

[143] A. Trouvé and T. Poinsot. The evolution equation for the flame surface density in turbulent premixed combustion. *Journal of Fluid Mechanics*, 278:1–31, 1994. ISSN 0022-1120. doi: 10.1017/S0022112094003599.

[144] K. C. Utsav and P. L. Varghese. Accurate temperature measurements in flames with high spatial resolution using Stokes Raman scattering from nitrogen in a multiple-pass cell. *Applied optics*, 52(20):5007–5021, 2013. doi: 10.1364/AO.52.005007.

[145] P. S. Veloo, Y. L. Wang, F. N. Egolfopoulos, and C. K. Westbrook. A comparative experimental and computational study of methanol, ethanol, and n-butanol flames. *Combustion and Flame*, 157(10):1989–2004, 2010. ISSN 00102180. doi: 10.1016/j.combustflame.2010.04.001.

[146] D. Veynante, A. Trouvé, K. N. C. Bray, and T. Mantel. Gradient and counter-gradient scalar transport in turbulent premixed flames. *Journal of Fluid Mechanics*, 332:263–293, 1997. ISSN 0022-1120. doi: 10.1017/S0022112096004065.

[147] G. M. Watson, P. Versailles, and J. M. Bergthorson. NO formation in rich premixed flames of C1-C4 alkanes and alcohols. *Proceedings of the Combustion Institute*, 36(1):627–635, 2017. ISSN 15407489. doi: 10.1016/j.proci. 2016.06.108.

[148] T. Yu, C. Yang, P. Sharma, A. S. AlRamadan, and G. Magnotti. Fiber-bundle-based 2D Raman and Rayleigh imaging for major species and temperature measurement in laminar flames. *Optics letters*, 47(15):3764–3767, 2022. ISSN 0146-9592. doi: 10.1364/OL.467713.

[149] J. Zhao. Image Curvature Correction and Cosmic Removal for High-Throughput Dispersive Raman Spectroscopy. *Applied Spectroscopy*, 57(11):1368–1375, 2003.

Curriculum Vitae

Name	Johannes Ludwig Trabold	
Date of Birth	24. April 1989	
Place of Birth	Waiblingen, Germany	
School Education	09/2005 – 06/2008	**Technisches Gymnasium Buchen** Buchen, Germany Allgemeine Hochschulreife
Higher Education	10/2008 – 12/2015	**Technische Universität Darmstadt** Darmstadt, Germany Mechanical and Process Engineering Bachelor and Master of Science
	2012/2013	**University of Colorado Boulder** Boulder (CO), USA Study abroad
	2014/2015	**Kungliga Tekniska Högskolan** Stockholm, Sweden Study abroad
Research Association	06/2016 – 03/2022	**Technische Universität Darmstadt** Darmstadt, Germany Institute of Reactive Flows and Diagnostics

Journal Publications

2022 **Cellular structures of laminar lean premixed H_2/CH_4/air polyhedral flames**
Co-Author, *Applications in Energy and Combustion Science*

2022 **Fast shutter line-imaging system for dual-dispersion Raman spectroscopy in ethanol and OME flames**
First Author, *Combustion and Flame*

2022 **Temperature dependent Raman spectra of pure, gaseous formaldehyde for combustion diagnostics**
Co-Author, *Proceedings of the Combustion Institute*

2020 **Fuel effects in turbulent premixed pre-vaporized alcohol/air jet flames**
First Author, *Flow, Turbulence and Combustion*

Conference Contributions

2019 **Dual-auflösendes Raman Spektrometer zur simultanen hochaufgelösten Messung der Kohlenwasserstoff-Zwischenprodukte und Hauptspezies in vorgemischten Ethanolflammen**
Paper and Poster, *29. Deutscher Flammentag*, Bochum, Germany

2019 **Dual-resolution Raman spectroscopy of HC intermediates in laminar premixed ethanol/air flames**
Poster, *Laser Diagnostics in Energy and Combustion Sciences*, Les Diablerets, Switzerland

2018 **Experimental study on global and local turbulent premixed flame characteristics of alcohols**
Paper and Poster, *Joint Meeting of the German and Italian Sections of the Combustion Institute*, Sorrento, Italy

2017 **Flame structure of turbulent premixed methane and alcohol flames flames inferred from 2D OH-PLIF**
Poster, *International Bunsen Discussion Meeting on Chemistry and Diagnostics for Clean Combustion*, Bielefeld, Germany

2017 **Turbulent premixed flames fueled by methane and alcohols stabilized on a novel temperature controlled piloted jet burner (TCPJB)**
Paper and Poster, *8th European Combustion Meeting*, Dubrovnik, Croatia